Scaling up the Detail in Particle Collisions

Factorization and resummation for predictions
of multi-differential cross sections

Gillian Lustermans

Scaling up the Detail
in Particle Collisions

Factorization and resummation for predictions
of multi-differential cross sections

ACADEMISCH PROEFSCHRIFT

ter verkrijging van de graad van doctor
aan de Universiteit van Amsterdam
op gezag van de Rector Magnificus
prof. dr. ir. K.I.J. Maex
ten overstaan van een door het College voor Promoties ingestelde
commissie, in het openbaar te verdedigen in de Aula der Universiteit
op vrijdag 29 november 2019, te 11:00 uur

door

Gillian Hendrik Hubertus Lustermans

geboren te Maastricht

Promotiecommissie:

Promotor:	prof. dr. E.L.M.P. Laenen	Universiteit van Amsterdam
Copromotor:	dr. W.J. Waalewijn	Universiteit van Amsterdam
Overige leden:	prof. dr. W.J.P. Beenakker	Universiteit van Amsterdam
	prof. dr. P.J.G. Mulders	Vrije Universiteit Amsterdam
	prof. dr. E. Pallante	Rijksuniversiteit Groningen
	prof. dr. W. Verkerke	Universiteit van Amsterdam
	dr. C. Weniger	Universiteit van Amsterdam
	dr. L. Zeune	Johannes Gutenberg Universität Mainz

Faculteit der Natuurwetenschappen, Wiskunde en Informatica

The material presented in this thesis is based on the following publications:

[1] G. Lustermans, W. J. Waalewijn and L. Zeune
Joint transverse momentum and threshold resummation beyond NLL
Phys. Lett. B762 (2016) 447; arXiv: 1605.02740 [hep-ph]

[2] G. Lustermans, J. K. L. Michel, F. J. Tackmann and W. J. Waalewijn
Joint two-dimensional resummation in q_T and 0-jettiness at NNLL
JHEP 03 (2019) 124; arXiv: 1901.03331 [hep-ph]

[3] G. Lustermans, J. K. L. Michel and F. J. Tackmann
Generalized threshold factorization with full collinear dynamics
arXiv: 1908.00985 [hep-ph]

[4] G. Lustermans, A. Papaefstathiou and W. J. Waalewijn
How much joint resummation do we need?
JHEP 10 (2019) 130; arXiv: 1908.07529 [hep-ph]

Contents

<div style="text-align: right">

1

</div>

Introduction

Ever since the start of recorded history, mankind has been curious about the ultimate constituents of nature. A great number of scientific theories and discoveries, stretched out over thousands of years, eventually led to the conclusion that matter is composed of tiny particles, called atoms. Atoms were thought to be the most fundamental particles in nature for quite some time. However, experiments conducted around the beginning of the 20th century [5,6] showed that atoms actually consist of a positively charged nucleus surrounded by a cloud of negatively charged particles, now known as electrons. The atomic nucleus was later found to contain positively charged protons and electrically neutral particles called neutrons [7]. Although electrons are presently still considered to be indivisible elementary particles, protons and neutrons have both been found to be composed of three so-called quarks [8–10]. Quarks appear in two types, called up and down. Protons consist of two up quarks and one down quark, while neutrons carry two down quarks and a single up quark. In both cases the quarks are bound together through the exchange of gluons, the force-carriers of the strong interaction [11].

As of today, all known elementary particles and interactions between them are contained in a single theory known as the Standard Model (SM) [12–14]. Apart from the up quark, down quark and electron, the matter sector of the SM also includes the (nearly) massless neutrino [15,16]. These four elementary particles make up what is known as the first generation of matter. There are two additional generations, containing the same types of particles but with higher masses. The various interactions between the matter particles arise through the exchange of force-carrying bosons. The electromagnetic force is carried by the photon, which couples to all particles with electric charge. The quarks in the SM also carry a so-called color charge, to which the aforementioned gluon couples. The crucial difference between the gluon and the photon is the fact that the gluon itself carries a color charge as well, so that gluons also couple to one another. The third interaction in the SM, the weak interaction, governs the radioactive decay of atoms and is transferred by $W^{\pm}$ and Z bosons.

The final particle in the theory is the Higgs boson [17, 18], the discovery of which [19, 20] was announced in 2012. Through interactions with the Higgs field, the various particles of the SM obtain their respective masses.
Despite its many successes, the SM is not the ultimate theory of nature. For example, the theory does not provide a dark matter candidate, neutrino oscillations are absent in the SM and gravity is not included at all. Various experiments being conducted at the Large Hadron Collider (LHC) are aimed at searching for traces of physics from beyond the Standard Model. These experiments compare the results of measured observables against the SM predictions with increasing precision, looking for slight deviations that might indicate the presence of new physics. From the theoretical side, this requires increasingly accurate predictions of the SM processes.

At the LHC, beams of protons are accelerated in opposite directions in a circular tunnel to almost the speed of light. When these protons collide, their constituents (the quarks and gluons) can interact with one another. These interactions are characterized by a dimensionless number, known as a coupling constant, which encodes the strength of the corresponding force. Each of the three forces in the SM is represented by a different coupling constant. Despite their names, the numerical values of these coupling constants actually depend on the energy at which the corresponding interactions occur. Since the LHC collides protons against one another, interactions between quarks and gluons are numerous. Because of this, and because it has the largest coupling constant, processes involving the interactions governed by the strong force are of key importance.
If the strong coupling constant α_s is small enough, which seems to be the predominant case in nature, the cross section σ (proportional to the probability) of a general strong process may be written as a perturbative series

$$\sigma = \sigma_0 + \alpha_s\,\sigma_1 + \alpha_s^2\,\sigma_2 + \alpha_s^3\,\sigma_3 + \ldots. \tag{1.1}$$

Terms involving a higher number of interactions, i.e. terms with a higher power of α_s, are increasingly more difficult to calculate. On the other hand, each term in this series is also numerically smaller than the previous term by a factor of α_s. The series thus converges for $\alpha_s \ll 1$, and may be truncated at any desired order in the coupling constant to obtain predictions at the corresponding level of accuracy. The first (non-vanishing) term in the series is called the leading order (LO) and higher-order terms are known as the next-to-leading order (NLO), next-to-next-to-leading order (NNLO) and so on. This method, known as perturbation theory, provides a way to calculate cross sections, provided that every σ_n in eq. (1.1) is roughly of the same size as the previous σ_{n-1}, or smaller.

Processes of interest at the LHC, such as the production of a Higgs boson, are typically accompanied by an enormous amount of additional radiation, mostly composed of gluons. Since these gluons are massless, their energy may be arbitrarily small, theoretically even zero, which is known as the soft limit. Furthermore, the angle between two radiated particles may be so small that they are essentially indistinguishable from one another, in which case the particles are called collinear. The radiation at colliders, such as the LHC, tends to be dominated by these soft and collinear particles, to which most measurements that can be performed on the final state are highly sensitive.

Inclusive processes, for which no additional measurements are imposed on the final-state particles, usually involve only a single energy scale. At the LHC, this is typically the invariant mass Q of the quarks or gluons that are extracted from the protons and interact with each other. Performing a measurement of an observable quantity on the final state will in general introduce a dependence on an additional energy scale m to the cross section. If the measurement is sensitive to both collinear and soft emissions, series of logarithms of the ratio of the two scales will appear in every term, leading to the schematic expression

$$\sigma_n = \# \ln^{2n}\left(\frac{m}{Q}\right) + \# \ln^{2n-1}\left(\frac{m}{Q}\right) + \ldots + \# \ln\left(\frac{m}{Q}\right) + \#\,, \qquad (1.2)$$

where all the, in principle different, constants are denoted by $\#$. Measurements that are only sensitive to collinear radiation give rise to a similar series, except that the highest power of the logarithm that occurs at any σ_n is equal to n instead of $2n$.

When the scale m becomes very small with respect to Q, the logarithms can grow large enough to cancel the suppression by α_s that each term in eq. (1.1) has compared to the previous term, spoiling the convergence of the series. In order to still be able to obtain reliable predictions for the cross section, the series has to be reorganized in a procedure known as resummation.

As the problem arises due to the simultaneous consideration of both m and Q, a logical first step is to disentangle the physics at these different energy scales. One method of achieving this separation is through the use of effective field theories (EFTs), which will be discussed in more detail in chap. 3. An EFT can be obtained from a theory (known in this context as the 'full theory') by expanding its Lagrangian $\mathcal{L}_{\text{full}}$ in the small ratio m/Q as

$$\mathcal{L}_{\text{full}} = \mathcal{L}_{\text{EFT}}^{(0)} + \mathcal{L}_{\text{EFT}}^{(1)} + \mathcal{L}_{\text{EFT}}^{(2)} + \ldots\,, \qquad \text{with} \qquad \mathcal{L}_{\text{EFT}}^{(n)} = \sum_i C_i^{(n)} O_i^{(n)}. \quad (1.3)$$

The operators $O_i^{(n)}$ in the EFT Lagrangians are in principle different from the operators in the full theory and each is multiplied by an unknown coefficient $C_i^{(n)}$, known as a Wilson coefficient. By dedicated calculations of certain

processes in both the EFT and the full theory, and demanding the results to be equal in the limit $m/Q \to 0$, these Wilson coefficients may be determined order-by-order in α_s.

Due to the expansion in m/Q, the operators in the EFT no longer depend on Q. All dependence on this scale is instead contained in the Wilson coefficients, which in turn are independent of the scale m. Considering for simplicity the case in which a full theory operator O_{full} is described by a single operator in the EFT, this leads to the expression

$$O_{\text{full}}(Q, m) = C_{\text{EFT}}(Q, \mu) \, O_{\text{EFT}}(m, \mu) + \mathcal{O}\left(\frac{m}{Q}\right). \qquad (1.4)$$

Both the Wilson coefficient and the EFT operator obtain an additional dependence on the scale μ, which is a consequence of the renormalization of the EFT, described in more detail in secs. 2.2 and 3.7.2. By defining the functions $H(Q, \mu)$ and $F(m, \mu)$ as the squares of the Wilson coefficient and the operator respectively, the cross section can be seen to factorize as

$$\sigma \sim |O_{\text{full}}(Q, m)|^2 = |C_{\text{EFT}}(Q, \mu)|^2 \, |O_{\text{EFT}}(m, \mu)|^2 \equiv H(Q, \mu) \, F(m, \mu), \quad (1.5)$$

up to corrections of $\mathcal{O}(m/Q)$. The functions $H(Q, \mu)$ and $F(m, \mu)$ are both perturbative expansions in α_s in their own respect, each containing a series of logarithms analogous to eq. (1.2) at every order. However, the arguments of the logarithms occurring in $H(Q, \mu)$ and $F(m, \mu)$ are instead given by μ/Q and m/μ respectively. Although μ may be chosen freely, it appears in both functions, so that there is no choice that can be made such that both types of logarithms are minimized. The dependence of the functions on the scale μ can be made explicit through their derivatives

$$\mu \frac{\mathrm{d}H(Q, \mu)}{\mathrm{d}\mu} = \gamma_H(Q, \mu) \, H(Q, \mu),$$

$$\mu \frac{\mathrm{d}F(m, \mu)}{\mathrm{d}\mu} = \gamma_F(m, \mu) \, F(m, \mu), \qquad (1.6)$$

which are known as renormalization group equations (RGEs). Here $\gamma_H(Q, \mu)$ and $\gamma_F(m, \mu)$, called anomalous dimensions[1], are perturbative expansions in α_s as well. The solutions to these first-order differential equations are obtained

---

[1] Actually, for factorization formulas involving only two functions, the anomalous dimensions can only depend on μ. However, the specific logarithmic structure shown in eq. (1.2) only arises when considering anomalous dimensions that additionally depend on variables such as Q and m.

by separating the variables and integrating over μ and are given by

$$H(Q,\mu) = \exp\left[\int_{\mu_H}^{\mu} \frac{d\mu'}{\mu'} \gamma_H(Q,\mu')\right] H(Q,\mu_H) \equiv U_H(Q,\mu_H,\mu)\, H(Q,\mu_H),$$

$$F(m,\mu) = \exp\left[\int_{\mu_F}^{\mu} \frac{d\mu'}{\mu'} \gamma_F(m,\mu')\right] F(m,\mu_F) \equiv U_F(m,\mu_F,\mu)\, F(m,\mu_F), \quad (1.7)$$

where $U_H(Q,\mu_H,\mu)$ and $U_F(m,\mu_F,\mu)$ are known as evolution functions. These solutions then connect the functions at some scale μ_H or μ_F to the same functions at a different scale μ. As the scales μ_H and μ_F are arbitrary integration boundaries, they may be chosen freely. In particular, this means that the functions may be evaluated at the scales $\mu_H = Q$ and $\mu_F = m$, where all the logarithms are minimized, and then evolved to a common scale μ. In the factorized cross section, the evolution functions then combine into an overall evolution function, given by

$$U(Q,m) = U_H(Q,\mu_H = Q,\mu)\, U_F(m,\mu_F = m,\mu)$$
$$= \exp\left[\sum_{n=1}^{\infty} \# \alpha_s^n\, L^{n+1} + \sum_{n=1}^{\infty} \# \alpha_s^n\, L^n + \sum_{n=1}^{\infty} \# \alpha_s^n\, L^{n-1} + \ldots\right], \quad (1.8)$$

where $L \equiv \ln(m/Q)$. When a Taylor series of this exponential is performed, the first sum will reproduce the term containing the highest power of the logarithm in eq. (1.2) at every order in α_s, i.e. $\alpha_s^n L^{2n}$. Likewise, every next sum will reproduce all terms with logarithms of one power less than the previous sum. These sets of terms are collectively known as the leading logarithms (LL), next-to-leading logarithms (NLL), next-to-next-to-leading logarithms (NNLL) and so on. As the series in the exponential exhibits convergent behavior for $m \ll Q$, it may be truncated at any desired order to obtain reliable predictions for the cross section.

The main topic of this thesis is the resummation of the various logarithms that arise in cross sections of scattering processes subjected to multiple, simultaneous measurements. The origin of the soft and collinear radiation, due to which these logarithms emerge, is describe by the theory of the strong interaction. In chap. 2, an overview of this theory, known as Quantum Chromodynamics (QCD), is provided. After a brief discussion of renormalization and the resulting energy-dependence of the coupling constant, the effect of soft and collinear particles at colliders such as the LHC is addressed.

Since the resummation techniques in this thesis are based in the usage of EFTs, chap. 3 starts by describing the general philosophy and ideas behind these theories, as well as their main features. The rest of the chapter is dedicated to the

Soft-Collinear Effective Theory (SCET) and serves as an introduction to the subject. SCET is an EFT that describes the soft and collinear limits of QCD and the results in all subsequent chapters are obtained by making use of it.

In chap. 4 the simultaneous resummation of logarithms involving two distinct observables is performed. The process under consideration is called Drell-Yan ($pp \to \ell^+\ell^-$) and the two measurements are the transverse momentum q_T of the outgoing lepton pair and 0-jettiness (or beam thrust) $\mathcal{T}$, which quantifies to what degree a certain event looks like an event with no jets in the final state. The process and measurements are described in more detail in sec. 4.1.3. The methods developed in order to achieve the resulting resummed predictions in this chapter may be applicable to many other analyses as well.

Chap. 5 focusses on measuring the transverse momentum of heavy color-singlets (like the Higgs boson) that are produced near their kinematic threshold. Cross sections of such processes involve threshold logarithms in addition to logarithms of the transverse momentum. A novel framework that resums both types of logarithms is developed in this chapter. In contrast with earlier work, this method is not limited to any specific logarithmic accuracy. Currently all ingredients required for resummation at N^3LL accuracy are available.

The subject of chap. 6 is the derivation of a generalized factorization formula for processes at hadron colliders in the limit where almost all the available energy is used for the production of a color-singlet. This factorization contains a much larger set of contributions than the traditional soft threshold factorization formulas and may consequently be used to improve theoretical predictions for many processes.

Although chaps. 4 and 5 deal with the simultaneous resummation of two independent variables, one can of course consider even more measurements. As these measurements all depend on the momenta of the particles in the final state, many of them are correlated in some way. The work in chap. 7 aims to investigate to what degree a process subjected to a certain measurement might benefit from the resummation of a set of other measurements.

The conclusions drawn from the results obtained in each of these chapters are summarized in chap. 8. At the very end of this thesis, a summary intended for a broad audience is provided in both English and Dutch.

2

Quantum Chromodynamics

The quantum field theory that describes the strong interactions between quarks and gluons is known as Quantum Chromodynamics (QCD). This chapter starts in sec. 2.1 with a brief overview of the steps involved in the derivation of the QCD Lagrangian. Beyond the leading order in perturbation theory, divergences appear at both high and low energies. The former are treated through a renormalization process, discussed in sec. 2.2, which introduces the notions of the running coupling, asymptotic freedom and confinement. The divergences appearing at low energies are addressed in sec. 2.3. Here, the concepts of infrared-safety, factorization and evolution, which are of importance for the rest of this thesis, are explored.

2.1 The QCD Lagrangian

The Lagrangian of a quantum field theory describing the behavior of a certain type of fermions can be obtained by demanding its invariance under a local gauge transformation of the fermion fields

$$\psi(x) \ \longrightarrow \ U(x)\,\psi(x)\,. \tag{2.1}$$

The space in which this transformation is performed is the space corresponding to some internal degree of freedom of the fermion. The gauge transformation that is used depends on the representation of this space, which corresponds to the number of independent components of the internal degree of freedom. An example of an internal degree of freedom with only a single component is electric charge. The space corresponding to electric charge is one-dimensional, meaning that the fermion field $\psi(x)$ in this space transforms by acquiring a complex phase. Since observable quantities will involve the absolute value of the field (and never the field itself), the Lagrangian should be invariant under transformations that change the complex phase of the field. These types of transformations form an Abelian Lie group called $U(1)$, and writing down

all possible Lorentz-invariant terms of mass-dimension four that are invariant under these transformations (and under parity and time-reversal) leads to the Lagrangian of Quantum Electrodynamics (QED).

The internal degree of freedom that gives rise to the theory of strong interactions is called color and has three independent components. The fermion field in this color space (called the quark field) is then described by a triplet and its transformations can be represented by 3×3 matrices. The transformations of the quark fields (under which the Lagrangian is demanded to be invariant) are rotations in the complex three-dimensional color space and form a non-Abelian Lie group called $SU(3)$. These transformations can be written as

$$\psi(x) \longrightarrow \exp\left[i\phi^a(x)T^a\right]\psi(x)\,, \tag{2.2}$$

where $\phi^a(x)$ is an arbitrary function, the T^a are the generators of the group and a summation over $a = 1, \ldots, 8$ is implied. The generators obey the commutation relation

$$[T^a, T^b] = if^{abc}T^c\,, \tag{2.3}$$

where f^{abc} are called the structure constants of the group. The normalization of the generators is defined through

$$\mathrm{Tr}[T^aT^b] = T_F\,\delta^{ab}\,, \tag{2.4}$$

where $T_F = 1/2$ is chosen. The Casimir operators C_F and C_A in the fundamental and adjoint representation respectively are defined through

$$(T^aT^a)_{ij} = C_F\,\delta_{ij} \qquad \text{and} \qquad f^{acd}f^{bcd} = C_A\,\delta^{ab}\,, \tag{2.5}$$

where a summation over repeated indices is implied. For an $SU(N)$ group, the Casimir operators are given by

$$C_F = \frac{N^2 - 1}{2N} \qquad \text{and} \qquad C_A = N\,, \tag{2.6}$$

which for QCD ($N = 3$) evaluate to $C_F = 4/3$ and $C_A = 3$.

In order to be able to write down terms that are invariant under eq. (2.2) and involve the derivative of the quark field, the covariant derivative is defined as

$$D_\mu = \partial_\mu - ig_sA_\mu^a(x)T^a\,, \tag{2.7}$$

where g_s is known as the coupling constant and $A_\mu^a(x)$ is identified as the gluon gauge field. Kinetic terms for the gauge field can be obtained by considering the field strength

$$F_{\mu\nu}^a = \partial_\mu A_\nu^a - \partial_\nu A_\mu^a + g_s f^{abc} A_\mu^b A_\nu^c \,, \tag{2.8}$$

where the dependence on x has been left implicit. The final term in eq. (2.8) is special to non-Abelian gauge theories and leads to interactions between the gauge fields. Writing down all possible renormalizable, Lorentz-invariant terms that are gauge-invariant under $SU(3)$ and that conserve parity and time-reversal then leads to the Yang-Mills Lagrangian [11]

$$\mathcal{L}_{\text{YM}} = \bar{\psi}(i\slashed{D} - m)\psi - \frac{1}{4}(F_{\mu\nu}^a)^2 \,, \tag{2.9}$$

where m denotes the mass of the quark field and all fields should be understood to depend on x. Analogous to QED, the expression for the two-point function (the propagator) of the gluon that one obtains from the gauge-fixed Lagrangian for a Yang-Mills theory is not unique. This ambiguity expresses itself in the form of a gauge parameter ζ that can be chosen freely. In non-Abelian gauge theories, two additional terms are present in the Lagrangian, namely a gauge-fixing term and a term involving ghost fields [21], denoted by c. The ghosts serve as negative-signature degrees of freedom, i.e. they cancel the contributions of the unphysical (time-like and longitudinally polarized) states of the gluons. Including these terms and accommodating for multiple quark flavors f with different masses m_f, the Lagrangian that describes QCD is given by [22]

$$\mathcal{L}_{\text{QCD}} = \sum_f \bar{\psi}_f(i\slashed{D} - m_f)\psi_f - \frac{1}{4}(F_{\mu\nu}^a)^2 - \frac{1}{2\zeta}(\partial^\mu A_\mu^a)^2 - \bar{c}^a(\partial^\mu D_\mu^{ab})c^b \,, \tag{2.10}$$

where the covariant derivative in the adjoint representation is given by

$$D_\mu^{ab} = \delta^{ab}\partial_\mu + g_s f^{acb} A_\mu^c \,. \tag{2.11}$$

The QCD Lagrangian depends on only a few free parameters: the masses of the quarks m_f and the coupling constant g_s, which is more commonly expressed as $\alpha_s = g_s^2/(4\pi)$. Throughout this thesis all quarks will be taken as massless unless noted otherwise and the top quark will not be considered.

2.2 Ultraviolet divergences

Integrals over the momenta of virtual particles in loops often diverge in the region where the momenta grow large. These ultraviolet (UV) divergences indicate that the theory under consideration should not be considered valid in this

region of large momenta (small distances). In order to obtain finite predictions from the theory, the UV divergences have to be regulated in some way, after which they can be absorbed in redefinitions of the parameters of the theory in a process known as renormalization. The renormalized parameters depend on the scale that is introduced through the renormalization procedure. The requirement that the bare parameters (before renormalization) are independent of this scale leads to so-called renormalization group equations (RGEs), describing the behavior of the renormalized parameters as a function of the scale.

2.2.1 Regularization

Loop diagrams in quantum field theories involve at least one internal momentum p^μ that is not constrained by the external momenta. Since the computation of cross sections involves summing over all possibilities for unobserved quantities, the internal momenta have to be integrated over an in-principle infinite range. These types of integrals are often divergent and require a regularization procedure. The perhaps physically most intuitive method of regularization is to simply cut off these integrals at some large value Λ_{UV}. The regulated integrals will then lead to results involving divergences such as $\ln(\Lambda_{\mathrm{UV}})$. Since these divergences are due to high-momentum modes they are called UV divergences. Their presence indicates that the theory should not be assumed valid for very large momenta (corresponding to very small distances). Although imposing a momentum cutoff has the advantage of being very clear and intuitive, it also has a serious downside in that it does not preserve Ward identities.

A different method of regulating four-dimensional integrals, called dimensional regularization [23, 24], is to instead evaluate them in $d = 4 - 2\epsilon$ dimensions by replacing

$$\int \frac{\mathrm{d}^4 p}{(2\pi)^4} \longrightarrow \int \frac{\mathrm{d}^d p}{(2\pi)^d} \, . \tag{2.12}$$

The d-dimensional integration measure can be written as

$$\mathrm{d}^d p = \mathrm{d}\Omega_d \, \mathrm{d}p \, p^{d-1} \, , \tag{2.13}$$

where $\int \mathrm{d}\Omega_d$ is the surface area of a d-dimensional unit sphere given by

$$\int \mathrm{d}\Omega_d = \frac{2\pi^{d/2}}{\Gamma(d/2)} \, . \tag{2.14}$$

By splitting the d-dimensional integral this way, the UV divergences reside solely in the one-dimensional integral over $\mathrm{d}p$ and will manifest themselves as simple $1/\epsilon$ poles.

The main reason for the frequent use of dimensional regularization in the literature is the fact that it preserves gauge and Lorentz symmetries and therefore also Ward identities. Another often-appreciated property is the fact that scaleless integrals vanish in dimensional regularization, i.e.

$$\int \frac{\mathrm{d}^d p}{(2\pi)^d} \, (p^2)^n = 0 \,, \tag{2.15}$$

for any n [25]. Dimensional regularization regulates not only the UV divergences, but also divergences related to small momenta, known as infrared (IR) divergences. Both will manifest themselves as $1/\epsilon$ poles and some scaleless integrals only vanish because of cancellations between infrared and ultraviolet divergences. For the renormalization procedure described in the next section, it is important to distinguish between these types of divergences.

Unless noted otherwise, the method of dimensional regularization will be used throughout this thesis.

2.2.2 Renormalization

Although UV divergences must always cancel in observable quantities [26], it pays to remove them already at the level of the Lagrangian in a procedure known as renormalization. The Lagrangian given in eq. (2.10) is called the bare Lagrangian and involves bare parameters (masses and coupling constants) that differ from the parameters actually measured in experiments. The Lagrangian can be written in terms of the latter instead of the former by explicitly splitting off the infinite (but unobservable) shifts between the two and grouping them in what are known as counterterms. Besides the divergent parts from the bare parameters, one has the freedom to absorb additional (finite) terms into these counterterms. Any such choice is called a renormalization scheme and gives a precise definition of the renormalized parameters. The scheme in which only the divergences are absorbed into the counterterms is known as the minimal subtraction (MS) scheme [27, 28].

When using dimensional regularization, the mass-dimension of the Lagrangian changes from 4 to d, but the dimension of the gluon field is still equal to 1. Dimensional analysis of the interaction term in eq. (2.10) then reveals that the coupling constant g_s obtains a mass dimension of $2 - d/2 = \epsilon$. To enforce the coupling to be dimensionless, the MS scheme includes the replacement

$$g_s \longrightarrow g_s \, \mu^\epsilon \,. \tag{2.16}$$

Here μ is an arbitrary parameter of mass dimension 1 known as the renormalization scale.

The scheme that is most often used is a variation of the MS scheme called the modified minimal subtraction ($\overline{\text{MS}}$) scheme, which amounts to absorbing some extra terms that arise in each loop integral into the counterterms by making the change

$$\mu^2 \longrightarrow \mu^2 \, \frac{e^{\gamma_E}}{4\pi} \, , \tag{2.17}$$

where $\gamma_E \approx 0.577$ is the Euler-Mascheroni constant. Unless noted otherwise, the $\overline{\text{MS}}$ scheme will be used throughout this thesis as the method of choice for renormalization. In this scheme, the relation between the bare coupling constant α_s^{bare} and the renormalized coupling constant α_s can be expressed as

$$\alpha_s^{\text{bare}}(\epsilon) = \mu^{2\epsilon} \, Z_\alpha(\epsilon, \mu) \, \alpha_s(\mu) \, , \tag{2.18}$$

where the scaling factor Z_α represents a combination of field-strength renormalizations that is related to the counterterm by $\delta_\alpha = Z_\alpha - 1$.

2.2.3 Running coupling

Since the renormalization procedure gives definite meaning to the renormalized parameters by introducing an arbitrary energy scale, the renormalized coupling constant will depend on this renormalization scale. As indicated explicitly in eq. (2.18) for the case of $\overline{\text{MS}}$, the bare coupling depends on the regulator, but does not depend on the renormalization scale. This independence can be exploited by writing

$$0 = \frac{\mathrm{d}\alpha_s^{\text{bare}}}{\mathrm{d}\ln\mu} = \mu^{2\epsilon} \, Z_\alpha(\epsilon, \mu) \, \alpha_s(\mu) \left[2\epsilon + \frac{1}{Z_\alpha(\epsilon, \mu)} \frac{\mathrm{d}Z_\alpha(\epsilon, \mu)}{\mathrm{d}\ln\mu} + \frac{1}{\alpha_s(\mu)} \frac{\mathrm{d}\alpha_s(\mu)}{\mathrm{d}\ln\mu} \right] , \tag{2.19}$$

so that the rate at which the renormalized coupling constant changes with the energy scale μ is encoded by

$$\beta(\alpha_s(\mu), \epsilon) \equiv \frac{\mathrm{d}\alpha_s(\mu)}{\mathrm{d}\ln\mu} = \alpha_s(\mu) \left[-2\epsilon - \frac{1}{Z_\alpha(\epsilon, \mu)} \frac{\mathrm{d}Z_\alpha}{\mathrm{d}\ln\mu} \right]$$

$$= -2\epsilon \, \alpha_s(\mu) - 2\alpha_s(\mu) \sum_{n=0}^{\infty} \beta_n \Big(\frac{\alpha_s(\mu)}{4\pi} \Big)^{n+1} , \tag{2.20}$$

which is called the beta-function of QCD. It can be calculated perturbatively by applying the Callan-Symanzik equation [29, 30] to appropriately chosen

Green's functions. Since the beta-function is related to the counterterms that cancel the UV divergences, its exact form (beyond two loops) depends on the employed renormalization scheme. The 1-loop coefficient of the beta-function in $\overline{\text{MS}}$ is found to be

$$\beta_0 = \frac{11}{3}C_A - \frac{4}{3}T_F\,n_f\,, \tag{2.21}$$

where n_f represents the number of active quark flavors, given by the number of quarks whose mass is smaller than the energy scale under consideration, i.e. $m_q \lesssim Q$. The results at 2 and 3 loops can be found in app. C.2. The leading-order RGE of the coupling constant is then given by

$$\frac{\mathrm{d}\alpha_s(\mu)}{\mathrm{d}\ln\mu} = -2\beta_0\,\frac{\alpha_s(\mu)^2}{4\pi}\,, \tag{2.22}$$

which can be solved by separation of variables and integration from some reference scale μ_0 up to the scale μ to obtain

$$\alpha_s(\mu) = \frac{\alpha_s(\mu_0)}{1 + \alpha_s(\mu_0)\frac{\beta_0}{2\pi}\ln\left(\frac{\mu}{\mu_0}\right)}\,. \tag{2.23}$$

If the coupling constant is measured at some scale μ_0, its value at any other scale can be determined by using eq. (2.23) or its higher-order equivalents, which can be found in app. C.2 up to three loops. One commonly used reference scale is the mass of the Z boson m_Z, at which $\alpha_s(m_Z) = 0.1181$ [31]. A coupling that depends on the energy scale at which it is measured, like $\alpha_s(\mu)$, is called a 'running coupling'. Throughout the rest of this thesis the dependence of the running coupling on the scale μ will often be suppressed for the sake of readability.

The beta-function of QCD is negative[1], indicating that the strong coupling constant is large at small energy scales μ and decreases towards zero as the energy scale increases, as shown in fig. 2.1. At high energy scales, the interactions in QCD can be described by a perturbation series in the coupling constant, leading to the quarks and gluons behaving like free, weakly-interacting particles. This behavior is called asymptotic freedom [32, 33] and it can be shown that all non-Abelian gauge theories are asymptotically free if only renormalizable quantum field theories in four space-time dimensions are considered [34, 35]. At low energy scales, the strong coupling constant becomes large and can no longer be used as an expansion parameter. The theory becomes non-perturbative and quarks and gluons can no longer be described as free, individual particles. The asymptotic states of the theory consist of singlets in

---

[1]For a number of flavors $n_f < 17$.
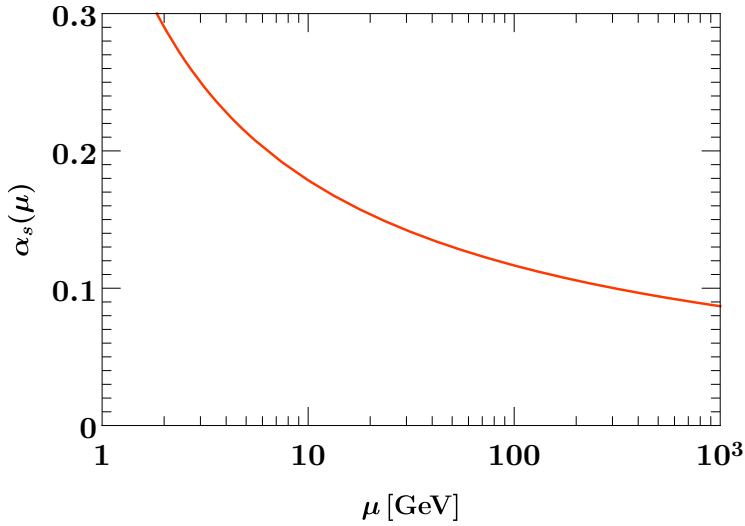
Figure 2.1 The running of the coupling constant $\alpha_s(\mu)$ in the $\overline{\text{MS}}$ renormalization scheme, at 3-loop accuracy with five active flavors.

color, called mesons and baryons (collectively known as hadrons). The former are composed of a quark and an antiquark with the same (but opposite) color charge, whereas the latter are made up of three quarks with different color charges. This process of quarks and gluons combining into colorless hadrons is known as confinement and explains why free quarks and gluons are not encountered in nature. The scale at which QCD becomes nonperturbative is the scale at which the denominator in eq. (2.23) vanishes, which at 1-loop accuracy is given by

$$\Lambda_{\text{QCD}} = \mu_0 \exp\left[-\frac{2\pi}{\beta_0 \alpha_s(\mu_0)}\right]. \tag{2.24}$$

This scale is actually independent of the scale μ_0 that appears on the right-hand side, but does depend on the renormalization scheme and the number of active flavors. It has a numerical value around $\Lambda_{\text{QCD}} \approx 200\,\text{MeV}$.

2.3 Infrared divergences

Apart from the UV divergences arising at very high energies, there are also IR divergences, originating from the low-energy regime. These divergences may arise in loop integrals of Feynman diagrams and in the phase space integral required to obtain cross sections from amplitudes. When all virtual corrections and all real radiation matrix elements are considered, these IR divergences will
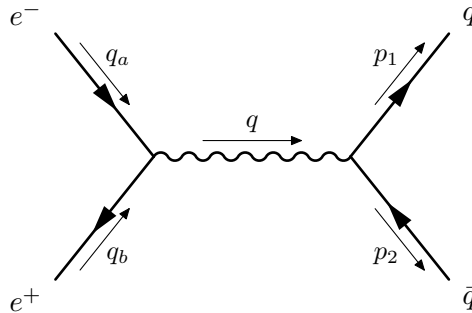
Figure 2.2 The leading-order diagram for the process $e^+e^- \to q\bar{q}$. The process is considered at $E_{\text{cm}} \ll m_Z$ so that the same diagram with a virtual Z boson is highly suppressed.

cancel, rendering the total cross section finite. At lepton colliders, the sum over all energy-degenerate initial and final states can be performed. At hadron colliders, however, the incoming particles cannot be described in perturbation theory, preventing the summation over all initial states. This leads to uncanceled IR divergences that have to be absorbed by the non-perturbative description of the hadrons in a procedure similar to the renormalization procedure used to treat UV divergences. The non-perturbative parton distribution functions, describing the extraction of a parton from the proton, become scale-dependent through this procedure. The resulting RGE then connects the parton distribution functions at various energy scales to one another.

2.3.1 Lepton colliders

Since quarks and antiquarks are electrically charged, they can be created at electron-positron colliders through the QED process

$$e^+e^- \longrightarrow \gamma^*/Z \longrightarrow q\bar{q}. \qquad (2.25)$$

As only the final state will receive higher-order QCD corrections, this process provides an ideal environment to study the properties of QCD. Assuming that this process happens far away from the Z-resonance, i.e. for center-of-mass energies $E_{\text{cm}} \ll m_Z$, the contribution from the Z-boson is highly suppressed and the leading-order (LO) Feynman diagram in fig. 2.2 leads to the cross section

$$\sigma^{(0)} = \frac{N_c(e^2 Q_q)^2 \mu^{2\epsilon}}{4\pi E_{\text{cm}}^2} \left(\frac{4\pi\mu^2}{E_{\text{cm}}^2} \right)^\epsilon \frac{(1-\epsilon)^2}{(3-2\epsilon)} \frac{\Gamma(1-\epsilon)}{\Gamma(2-2\epsilon)}, \qquad (2.26)$$
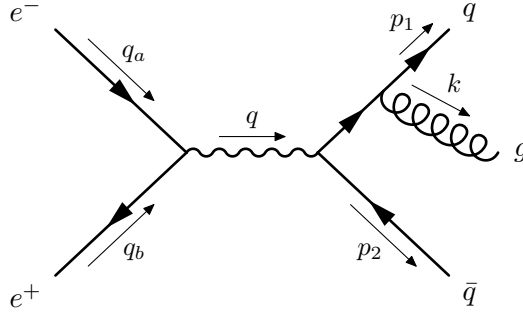
Figure 2.3 A radiative QCD correction to the leading-order process shown in fig. 2.2. The diagram in which the gluon is emitted from the antiquark instead is not shown explicitly.

where N_c is the number of colors, e is the electric unit charge, Q_q is the electric charge of the outgoing quark in units of e and all particles have been taken as massless.

A lowest-order QCD correction to the Born process can be obtained by considering the situation in which the outgoing quark radiates an additional gluon into the final state, as shown in fig. 2.3. The scattering amplitude of this diagram is given by

$$i\mathcal{M} = \frac{-ig_s T^a Q_q e^2}{q^2} \bar{v}(q_b)\gamma_\mu u(q_a)\, \bar{u}(p_1)\slashed{\epsilon}^*(k)\frac{(\slashed{p}_1 + \slashed{k})}{2k \cdot p_1}\gamma^\mu v(p_2)\,. \tag{2.27}$$

In the limit where the momentum k^μ is small (i.e. the Eikonal approximation), the factor describing the outgoing state can be seen to scale as

$$\bar{u}(p_1)\slashed{\epsilon}^*(k)\frac{(\slashed{p}_1 + \slashed{k})}{2k \cdot p_1}\gamma^\mu v(p_2) \sim \frac{1}{E_k(1 - \cos\theta)}\,, \tag{2.28}$$

where E_k is the energy of the outgoing gluon and θ the angle between the quark and the gluon. This expression diverges in the limit where the gluon becomes soft, i.e. $E_k \to 0$, as well as the limit $\theta \to 0$, in which the gluon becomes collinear to the quark. These soft and collinear divergences are universal in the sense that they are independent of the interactions that precede the emission of the gluon by the outgoing quark. Collectively, they are known as infrared (IR) divergences.

By also including the diagram in which the gluon is emitted from the antiquark instead, the cross section corresponding to the $\mathcal{O}(\alpha_s)$ corrections due to real radiation is given by

$$\sigma_{q\bar{q}}^{\mathrm{R}} = \sigma^{(0)}\frac{\alpha_s C_F}{2\pi}\left(\frac{4\pi\mu^2}{E_{\mathrm{cm}}^2}\right)^\epsilon \frac{\Gamma(1-\epsilon)^2}{\Gamma(1-3\epsilon)}\left[\frac{2}{\epsilon^2} + \frac{3}{\epsilon} + \frac{19}{2} + \mathcal{O}(\epsilon)\right]. \tag{2.29}$$
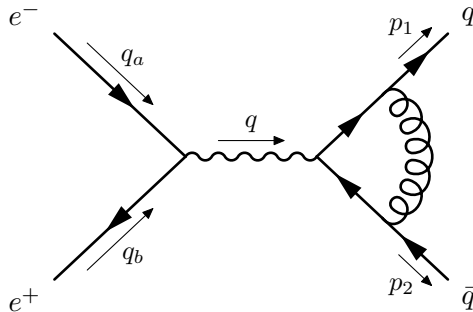
Figure 2.4 The one-loop virtual QCD correction to the leading-order process shown in fig. 2.2.

The IR divergences manifest themselves in this expression as $1/\epsilon$ poles. The $1/\epsilon^2$ pole reflects the region in which the gluon becomes both soft and collinear. For a consistent evaluation of the cross section at $\mathcal{O}(\alpha_s)$, the interference between the Born amplitude and its 1-loop QCD correction shown in fig. 2.4 has to be taken into account as well[2]. The cross section due to this virtual correction is given by

$$\sigma_{q\bar{q}}^{\mathrm{V}} = -\sigma^{(0)} \frac{\alpha_s C_F}{2\pi} \left(\frac{4\pi\mu^2}{E_{\mathrm{cm}}^2} \right)^{\epsilon} \frac{\Gamma(1-\epsilon)^2}{\Gamma(1-3\epsilon)} \left[\frac{2}{\epsilon^2} + \frac{3}{\epsilon} + 8 + \mathcal{O}(\epsilon) \right], \qquad (2.30)$$

which contains no UV divergences so that all $1/\epsilon$ poles correspond to IR divergences. As can be seen from eqs. (2.29) and (2.30) the IR divergences cancel between the real and virtual contributions and the resulting cross section at $\mathcal{O}(\alpha_s)$ is finite.

The reason behind this cancellation is that, in the IR limit, final states with any amount of real radiation are indistinguishable from the same final states without that radiation. This leads to the conclusion that final states with a fixed number of massless particles are actually ill-defined and that one always has to include both virtual corrections and real radiation diagrams in order to obtain finite results for the cross section of any process.

For the case of QED, the cancellation can experimentally be explained by the fact that each detector has a finite resolution, below which individual particles cannot be detected. This suggests that the phase-space integration for a measured process should actually only include the sensitivity range of the detector. If one of the particles in a process with an n-particle final state then has a momentum below this sensitivity range, it will remain undetected and instead contribute to the same process with a final state consisting of $n-1$

---

[2]The self-energy diagrams are not discussed explicitly, but have the effect of transforming the UV divergence that the diagram in fig. 2.4 gives rise to into an IR divergence.

particles. From this point of view, the singularities present in eq. (2.29) (which would arise from particles below the sensitivity range of the detector) are explicitly paired with the equal but opposite singularities in eq. (2.30). In QCD, the outgoing radiation will hadronize before reaching the detector, so that the asymptotic final states are massive. If the resolution of the detector is larger than the energy scale of the hadrons, these particles can still escape detection. For experiments that are sensitive enough to detect these massive particles, the phase space is instead cut off by the scale of nonperturbative physics.

The cancellation of soft and collinear divergences in measurable quantities is ensured by the Kinoshita-Lee-Nauenberg (KLN) theorem [36–38], which implies that physical quantities that are obtained by summing over sufficiently inclusive initial and final states are free of IR divergences to all orders in perturbation theory. The total hadronic cross section $e^+e^- \rightarrow X$ is an example of a sufficiently inclusive physical quantity that is guaranteed to be IR-finite (for QCD corrections) by the KLN theorem.

More exclusive cross sections subject to final-state measurements can be considered, as long as those measurements are IR-safe, meaning that they have to be insensitive to the addition of an arbitrary amount of infinitesimally soft or collinear particles.

2.3.2 Hadron colliders

The perturbative expansion in quantum field theory that allows for the calculation of cross sections depends on the assumption that external particles can be considered as free particles for timescales much longer than the timescale at which the interaction takes place. At lepton colliders, the accelerated beams are composed of the same particles that initiate the scattering processes, so they can be regarded as free particles prepared at $t = -\infty$. At colliders where instead beams of hadrons are used, the quarks and gluons (collectively called partons) that initiate the scattering processes are confined inside the hadrons. Focussing on proton-proton colliders such as the Large Hadron Collider (LHC), the general picture of a collision is schematically depicted in fig. 2.5. Here, two partons i and j are extracted from the incoming protons before initiating the hard interaction that leads to a generic final state labeled X. The extracted partons can be considered collinear to the incoming protons to good approximation and their momenta can thus be written as longitudinal fractions of the full momenta of the protons as

$$q_a^\mu = x_a P_a^\mu \qquad \text{and} \qquad q_b^\mu = x_b P_b^\mu \,, \tag{2.31}$$
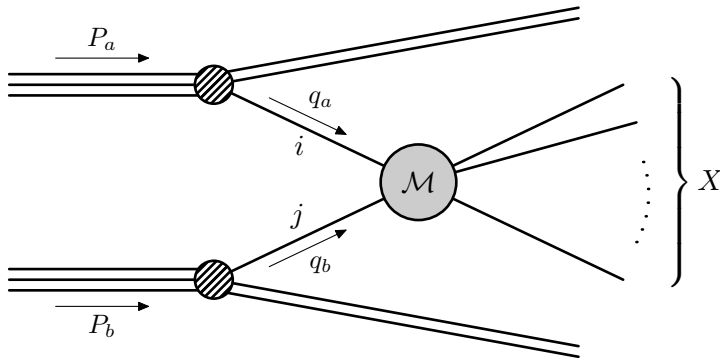
Figure 2.5 A schematic representation of a proton-proton collision. The partons i and j, which can be (anti)quarks or gluons, are extracted from the protons with momenta q_a^μ and q_b^μ respectively and initiate the hard interaction labeled by $\mathcal{M}$. The final state X may consist of any number of particles.

where $0 \leq x_{a,b} \leq 1$. The hadronic cross section $\sigma_{pp \to X}$ can be obtained at tree-level by multiplying the partonic cross section[3] $\hat{\sigma}_{ij \to X}$ of the underlying partonic process occurring at some x_a and x_b by the probability of extracting parton i with momentum fraction x_a and parton j with momentum fraction x_b from the protons and integrating over both momentum fractions.

The probability of extracting a parton i with momentum fraction x from the proton is encoded in a so-called Parton Distribution Function (PDF) $f_i(x)$. Since the intrinsic energy scale of the proton is of the order of Λ_{QCD}, these PDFs cannot be calculated in perturbation theory, but have to be determined from experiment (see for example refs. [39–41]) or by using lattice QCD [42–44]. Consequently, the hadronic cross section can be written as [45]

$$\sigma_{pp \to X}(P_a, P_b) = \int_0^1 \mathrm{d}x_a \int_0^1 \mathrm{d}x_b \sum_{i,j} f_i(x_a)\, f_j(x_b)\, \hat{\sigma}_{ij \to X}(x_a P_a, x_b P_b)\,, \quad (2.32)$$

where the sum runs over all partons and the dependence on E_{cm} has been left implicit. This formula represents the so-called parton model [46, 47] and is only the leading-order term in an expansion in Λ_{QCD}/Q, where Q denotes the energy scale of the hard scattering process. For values of Q much larger than Λ_{QCD}, the extraction of the partons from the protons can be considered to take place at a time long before the partons initiate the hard interaction. This allows one to regard the partons as free particles and subsequently validates the use of perturbation theory to calculate the partonic cross section.

---

[3]Partonic cross sections will be denoted by a hat to distinguish them from their hadronic counterparts.
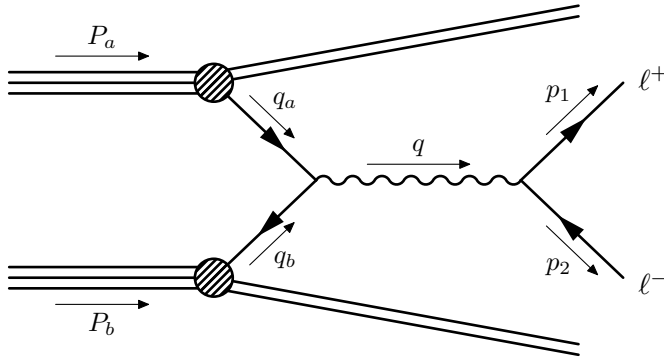
Figure 2.6 A schematic picture of the Drell-Yan process. A quark and an antiquark are extracted from the incoming protons and form a virtual photon (or Z boson) that subsequently decays into a lepton pair.

Eq. (2.32) then effectively separates the nonperturbative physics at the scale Λ_{QCD} encoded by the PDFs from the perturbative physics at the scale Q in the partonic cross section and is sometimes called the collinear factorization formula.

Although the perturbative calculation of the partonic cross section will in general depend on partonic variables, physical quantities will always be measured in terms of hadronic variables and it is often necessary to translate partonic results to their hadronic counterparts. The relations between partonic and hadronic quantities of import to this thesis can be obtained by considering the Drell-Yan process [48], given by

$$pp \longrightarrow Z/\gamma^* \longrightarrow \ell^+\ell^- \, . \tag{2.33}$$

In this process, shown in fig. 2.6, a quark and an antiquark extracted from the incoming protons form a virtual photon or Z boson that subsequently decays into a pair of leptons. In a sense, it is the (reversed) hadronic version of the process considered in sec. 2.3.1. The energy scale of the process is set by the invariant mass of the lepton pair, i.e.

$$Q^2 = q^2 \, . \tag{2.34}$$

Since the transverse momentum of the partons is negligibly small, the transverse momentum of the intermediate vector boson (at tree-level) is also small. Its longitudinal momentum, however, might in general be substantial. It can be conveniently parametrized by the rapidity, defined as

$$Y = \frac{1}{2}\ln\left(\frac{E_q + q_z}{E_q - q_z}\right). \tag{2.35}$$

In the center-of-mass (CM) frame of the incoming protons, the four-momentum of the intermediate vector boson is given by

$$q^\mu = \frac{E_{\text{cm}}}{2}\left(x_a + x_b, 0, 0, x_a - x_b\right).$$ (2.36)

The (partonic) invariant mass can be related to the CM energy by

$$Q^2 = 2q_a \cdot q_b = x_a x_b E_{\text{cm}}^2,$$ (2.37)

where the high-energy limit has been adopted so that the protons can be considered massless. The rapidity can be expressed in terms of the momentum fractions as

$$Y = \frac{1}{2}\ln\left(\frac{x_a}{x_b}\right).$$ (2.38)

The (partonic) momentum fractions can then be written in terms of the hadronic quantities as

$$x_a = \frac{Q}{E_{\text{cm}}}e^{+Y} \qquad \text{and} \qquad x_b = \frac{Q}{E_{\text{cm}}}e^{-Y},$$ (2.39)

allowing for a translation between the momentum fractions x_a and x_b and the experimentally accessible observables Q and Y.

2.3.3 Parton Evolution

The cancellation of soft and collinear divergences is guaranteed by the KLN theorem as long as all initial and final states with the same total energy are summed over. In proton-proton collisions, the sum over energy-degenerate initial states cannot be performed because the protons cannot be described by perturbation theory. As a result, the KLN theorem cannot be readily relied upon to cancel all IR divergences.

Since the sum over final states can still be performed for processes at hadron colliders, the divergences corresponding to soft and collinear splittings from final-state particles will cancel between the real and virtual diagrams as was the case for $e^+e^- \to X$ in sec. 2.3.1. The initial state, however, will in general give rise to IR divergences, which can originate from partons that undergo collinear splittings between their extraction from the protons and their initiation of the hard interaction process[4]. Although these collinear divergences may seem troublesome at first, they can be dealt with in a consistent way as

---

[4]It turns out that the divergences from soft radiation emitted by the initial state cancel exactly against the corresponding virtual contributions.
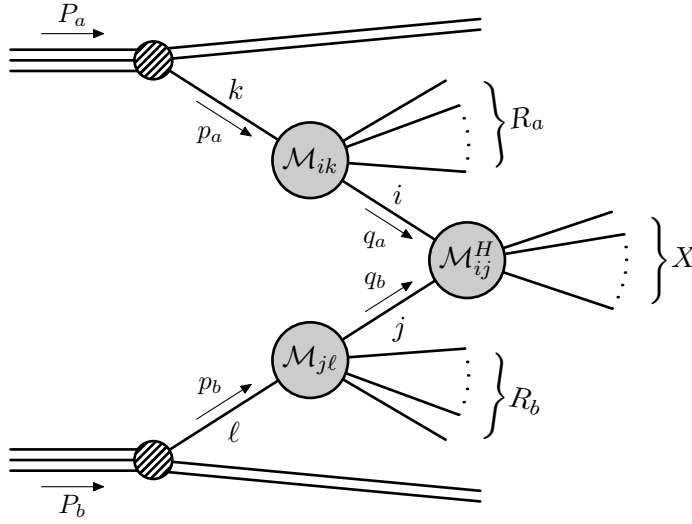
Figure 2.7 A schematic representation of a proton-proton collision including initial-state radiation. Two partons k and ℓ are extracted form the protons with momenta p_a^μ and p_b^μ respectively. In general, these partons will transition into particles i and j by emitting collinear radiation into the final state.

will be described in detail in this section. First, the part of the partonic cross section describing the collinear splittings is shown to be independent of the hard scattering process. This so-called transition function $T_{ik}(z)$ describes the transition of some parton k extracted from the proton into some other particle i. A next-to-leading order (NLO) calculation of this transition function is performed, leading to an uncanceled collinear divergence in the partonic cross section. Next, it is shown that this divergence may be absorbed into the PDF, which contains an equal but opposite IR divergence that is canceled by this procedure. Since the PDF is scaleless, this IR divergence exactly canceled a UV divergence in dimensional regularization. After absorbing the IR divergence from the transition function, the PDF thus contains an explicit UV divergence that has to be treated through a renormalization procedure.

The process of extracted partons emitting initial-state radiation before initiating the hard process is schematically depicted in fig. 2.7. Here, partons k and ℓ are extracted from the protons with momenta given by $p_a^\mu = \xi_a P_a^\mu$ and $p_b^\mu = \xi_b P_b^\mu$ respectively. These partons undergo collinear interactions, encoded by $\mathcal{M}_{ik}$ and $\mathcal{M}_{j\ell}$, through which they transition into partons i and j respectively. The momenta of these particles, which will initiate the hard interaction

$\mathcal{M}_{ij}^H$, are then given by

$$q_a^\mu = x_a P_a^\mu = \frac{x_a}{\xi_a} p_a^\mu \equiv z_a p_a^\mu \qquad \text{and} \qquad q_b^\mu = x_b P_b^\mu = \frac{x_b}{\xi_b} p_b^\mu \equiv z_b p_b^\mu, \quad (2.40)$$

where $z_{a,b} = x_{a,b}/\xi_{a,b}$ has been defined. Since the momenta $q_{a,b}^\mu$ enter the hard scattering process, they have been defined as to agree with the definition in eq. (2.31). The partonic cross section of the process shown in fig. 2.7, containing the hard interaction as well as the transitions of the incoming partons, is given by

$$\hat{\sigma}_{k\ell \to X}(p_a, p_b) = \frac{1}{4|\vec{v}_a - \vec{v}_b|E_a E_b} \int d\Pi_{R_a + R_b + X} \langle |\mathcal{M}|^2 \rangle$$
$$\times (2\pi)^4 \delta(p_a + p_b - p_{R_a} - p_{R_b} - p_X), \qquad (2.41)$$

where $\vec{v}_{a,b}$ are the velocities of the incoming beams, $E_{a,b}$ the energies of the partons extracted from the protons and $\langle |\mathcal{M}|^2 \rangle$ the squared amplitude of the complete partonic process $k\ell \to X + R$ (including both parton transitions and the hard interaction), averaged over all possible quantum numbers (spin and color) of the initial-state particles and summed over all possible quantum numbers of the final-state particles. The integral over $d\Pi_{R_a + R_b + X}$ is understood to cover the phase space of the entire final state, including R_a, R_b and X, whose momenta are given by $p_{R_a}^\mu$, $p_{R_b}^\mu$ and p_X^μ respectively.

The transition that a parton undergoes between its extraction from the proton and the initiation of the hard interaction can be described by a perturbative series in its own respect. At leading order, there are no splittings and partons i and j are simply equal to partons k and ℓ. In this case, X makes up the complete final state. The partonic cross section can then schematically be written as

$$\hat{\sigma}_{ij \to X}(q_a, q_b) = \hat{\sigma}_{ij \to X}^{H,(0)}(q_a, q_b), \qquad (2.42)$$

where $\hat{\sigma}_{ij \to X}^{H,(0)}(q_a, q_b)$ indicates the leading order of the perturbative expansion

$$\hat{\sigma}_{ij \to X}^H(q_a, q_b) = \hat{\sigma}_{ij \to X}^{H,(0)}(q_a, q_b) + \left(\frac{\alpha_s}{4\pi}\right) \hat{\sigma}_{ij \to X}^{H,(1)}(q_a, q_b) + \dots, \qquad (2.43)$$

representing the cross section resulting solely from $\mathcal{M}_{ij}^H$ (without any transitions of the partons).

At NLO, either the hard interaction might be evaluated at the next order, or one of the partons extracted from the protons might undergo a single collinear splitting. Although the transitions of both partons have to be taken into account, only $\mathcal{M}_{ik}$ will be considered here for simplicity. The treatment of the

matrix element $\mathcal{M}_{j\ell}$ follows the exact same logic. In the partonic CM frame, the four-momentum of parton k after its extraction from the proton is given by

$$p_a^\mu = \left(E_a, 0, 0, E_a\right). \tag{2.44}$$

Parton i, which emerges after the collinear radiation and initiates the hard interaction, obtains a fraction z_a of the longitudinal momentum of parton k, so that its four-momentum reads

$$q_a^\mu = \left(E_{q_a}, q_{a,x}, q_{a,y}, z_a E_a\right) \equiv \left(E_{q_a}, \vec{q}_{a\perp}, z_a E_a\right), \tag{2.45}$$

where $\vec{q}_{a\perp} \equiv (q_{a,x}, q_{a,y})$ defines the two-dimensional transverse momentum vector. The four-momentum of the single on-shell particle that makes up R_a when the transition matrix element is considered at NLO follows from momentum conservation and is given by

$$k_a^\mu = \left(E_{k_a}, -\vec{q}_{a\perp}, (1 - z_a)E_a\right), \tag{2.46}$$

where its energy $E_{k_a} = \sqrt{q_{a\perp}^2 + (1 - z_a)^2 E_a^2}$ is fixed by the fact that the particle is created on shell. Using factorization of the squared amplitude in the collinear limit, the partonic cross section in eq. (2.41) can then explicitly be written as

$$\hat{\sigma}_{kj \to X}(p_a, q_b) = \frac{1}{4|\vec{v}_a - \vec{v}_b|E_a E_{q_b}} \int \frac{\mathrm{d}k_{a,z}\, \mathrm{d}^{d-2}\vec{k}_{a\perp}}{(2\pi)^{d-1}} \int \mathrm{d}\Pi_X \frac{1}{2E_{k_a}} \sum_i \langle|\mathcal{M}_{ik}|^2\rangle$$
$$\times \left(\frac{1}{q_a^2}\right)^2 \langle|\mathcal{M}_{ij}^H|^2\rangle (2\pi)^4 \delta(p_a + q_b - k_a - p_X), \tag{2.47}$$

where dimensional regularization is used to regulate the phase space integral over the region R_a (containing only a single particle). Expanding to leading power in $\vec{q}_\perp$ and changing variables according to $\mathrm{d}k_{a,z}\, \mathrm{d}^{d-2}\vec{k}_{a\perp} = E_a\, \mathrm{d}z_a\, \mathrm{d}^{d-2}\vec{q}_{a\perp}$, the partonic cross section becomes

$$\hat{\sigma}_{kj \to X}(p_a, q_b) = \int \frac{\mathrm{d}^{d-2}\vec{q}_{a\perp}}{(2\pi)^{d-1}} \int_0^1 \mathrm{d}z_a \frac{z_a(1 - z_a)}{2q_{a\perp}^4} \sum_i \langle|\mathcal{M}_{ik}|^2\rangle\, \hat{\sigma}_{ij \to X}^H(z_a p_a, q_b), \tag{2.48}$$

where the cross section corresponding solely to the hard interaction is defined by

$$\hat{\sigma}_{ij \to X}^H(q_a, q_b) = \frac{1}{4|\vec{v}_1 - \vec{v}_2|E_{q_a} E_{q_b}} \int \mathrm{d}\Pi_X \langle|\mathcal{M}_{ij}^H|^2\rangle (2\pi)^4 \delta(q_a + q_b - p_X). \tag{2.49}$$

The $(d-2)$-dimensional integral over the transverse momentum can be translated into a one-dimensional integral by using eq. (2.13), after which the partonic cross section takes the form

$$\hat{\sigma}_{kj\to X}(p_a, q_b) = \frac{1}{\Gamma(1-\epsilon)} \frac{1}{(4\pi)^2} (4\pi)^\epsilon \int_0^\infty \frac{\mathrm{d}q_{a\perp}^2}{(q_{a\perp}^2)^\epsilon} \int_0^1 \mathrm{d}z_a \frac{z_a(1-z_a)}{q_{a\perp}^4}$$
$$\times \sum_i \langle |\mathcal{M}_{ik}|^2 \rangle \, \hat{\sigma}_{ij\to X}^H(z_a p_a, q_b) \,. \tag{2.50}$$

The matrix elements $\mathcal{M}_{ik}$, describing the transition of particle k into particle i, are independent of the hard scattering process and are found to be

$$\langle |\mathcal{M}_{ik}|^2 \rangle = \frac{g_s^2 \, \mu^{2\epsilon} q_{a\perp}^2}{z_a(1-z_a)} \, P_{ik}^{(0)}(z_a) \,, \tag{2.51}$$

where $P_{ik}^{(0)}(z)$ depends on the identity of the incoming and outgoing particles. For the various possibilities, they are given by

$$P_{qq}^{(0)}(z) = 2C_F \, \theta(z) P_{qq}(z) \,, \qquad P_{gq}^{(0)}(z) = 2C_F \, \theta(z) P_{gq}(z) \,, \tag{2.52}$$
$$P_{qg}^{(0)}(z) = 2T_F \, \theta(z) P_{qg}(z) \,, \qquad P_{gg}^{(0)}(z) = 2C_A \, \theta(z) P_{gg}(z) + \beta_0 \, \delta(1-z) \,.$$

The $P_{ij}(z)$ appearing in these coefficients are called the Altarelli-Parisi splitting functions. As the splitting functions only depend on the longitudinal momentum fraction z, the transverse momentum dependence of a transition from particle k to particle i is universal, i.e. it does not depend on the nature of the particles involved. Since collinear splittings with a large transverse momentum should actually be considered part of the hard scattering process instead of the transition amplitude, the integral over $\mathrm{d}q_{a\perp}^2$ can naturally be cut off at the invariant mass Q^2 of the process[5]. Performing this integral then finally leads to the NLO expression

$$\hat{\sigma}_{kj\to X}(p_a, q_b) = \frac{\alpha_s}{4\pi} \left[-\frac{1}{\epsilon} + \ln\left(\frac{Q^2 e^{\gamma_E}}{4\pi\mu^2}\right) \right] \int_0^1 \mathrm{d}z_a \sum_i P_{ik}^{(0)}(z_a) \, \hat{\sigma}_{ij\to X}^H(z_a p_a, q_b) \,. \tag{2.53}$$

The partonic cross section can then in general be expressed as

$$\hat{\sigma}_{kj\to X}(p_a, q_b) = \int_0^1 \mathrm{d}z_a \sum_i T_{ik}(z_a) \, \hat{\sigma}_{ij\to X}^H(z_a p_a, q_b) \,, \tag{2.54}$$

---

[5] Other cutoffs of a similar size are possible as well.

where the transition function $T_{ik}(z)$ has a perturbative expansion in α_s, given by

$$T_{ik}(z) = T_{ik}^{(0)}(z) + \left(\frac{\alpha_s}{4\pi}\right)T_{ik}^{(1)}(z) + \dots , \qquad (2.55)$$

where higher-order terms represent a higher number of collinear splittings. The LO and NLO results for the transition function can be read off from eqs. (2.42) and (2.53) and are given by

$$T_{ik}^{(0)}(z) = \delta_{ik}\, \delta(1-z) ,$$
$$T_{ik}^{(1)}(z) = \left[-\frac{1}{\epsilon} + \ln\left(\frac{Q^2 e^{\gamma_E}}{4\pi\mu^2}\right)\right] P_{ik}^{(0)}(z) . \qquad (2.56)$$

At NLO and beyond, the integral over $\mathrm{d}z_a$ in eq. (2.54) can only be performed when a particular pair of particles k and i is considered. For the case $k = i = q$, in which a quark gets extracted from the proton, radiates a gluon into the final state R_a and then enters the hard process, a naive calculation would lead to the splitting function

$$P_{qq}^{\mathrm{naive}}(z) = \frac{1+z^2}{1-z} , \qquad (2.57)$$

which has a soft divergence as $z \to 1$. The correct way of treating this divergence can be seen from the sum rule

$$\sum_i \int_0^1 \mathrm{d}z\, T_{ik}(z) = 1 , \qquad (2.58)$$

which simply states that the probability of particle k to transition into anything has to be equal to 1. Since the lowest-order transition function $T_{qq}^{(0)}(z)$ already integrates to unity, all higher-order contributions must vanish upon integration over $\mathrm{d}z$. In particular this means that the quark-quark splitting function must integrate to zero, which is accomplished by including the so-called plus prescription in its definition as

$$P_{qq}(z) = \left[\frac{1+z^2}{1-z}\right]_+ . \qquad (2.59)$$

A formal definition of the plus distribution, as well as a number of its properties, can be found in app. A. Here, the plus distribution of a function $f(z)$ is defined such that it agrees with its argument for all values $z < 1$, and that its integral against any smooth function $g(z)$ is given by

$$\int_x^1 \mathrm{d}z\, \left[f(z)\right]_+ g(z) = \int_x^1 \mathrm{d}z\, f(z)\left(g(z) - g(1)\right) - g(1) \int_0^x \mathrm{d}z\, f(z) . \qquad (2.60)$$

In particular, picking $g(z) = 1$ as a constant, this means that the plus distribution integrates to zero over the interval $0 \leq z \leq 1$. The remaining splitting functions, encoding the transitions of quarks into gluons, gluons into quarks and gluons into gluons, can be found in app. B.2.

The $1/\epsilon$ pole still left in eq. (2.53) is clearly not canceled by the splitting functions, nor will it be canceled by any virtual diagram. This divergence has its origin in the collinear limit $q_{a\perp}^2 \to 0$ and appears universally for any particles k and i. Although this left-over divergence might seem troublesome at first, it appears at the level of the partonic cross section, which is not a physical observable. Explicitly writing the observable, hadronic cross section defined in eq. (2.32) at NLO yields

$$
\sigma_{pp \to X}(P_a, P_b) = \sum_{k,j} \int_0^1 \mathrm{d}\xi_a \int_0^1 \mathrm{d}x_b\, f_k(\xi_a)\, f_j(x_b)
$$

$$
\times \left[\hat{\sigma}_{kj \to X}^{H,(0)}(\xi_a P_a, x_b P_b) + \frac{\alpha_s}{4\pi}\, \hat{\sigma}_{kj \to X}^{H,(1)}(\xi_a P_a, x_b P_b) \right.
$$

$$
+ \frac{\alpha_s}{4\pi} \ln\!\left(\frac{Q^2 e^{\gamma_E}}{4\pi\mu^2}\right) \sum_i \int_0^1 \mathrm{d}z_a\, P_{ik}^{(0)}(z_a)\, \hat{\sigma}_{ij \to X}^{H,(0)}(z_a \xi_a P_a, x_b P_b)
$$

$$
\left. - \frac{1}{\epsilon} \frac{\alpha_s}{4\pi} \sum_i \int_0^1 \mathrm{d}z_a\, P_{ik}^{(0)}(z_a)\, \hat{\sigma}_{ij \to X}^{H,(0)}(z_a \xi_a P_a, x_b P_b) \right]. \quad (2.61)
$$

Since the $1/\epsilon$ divergence appears completely independent of the underlying process, it can be absorbed into the PDF. This can be achieved by renaming the integration variable $\xi_a \to x_a$ and swapping the dummy indices $k \leftrightarrow i$ only on the first three lines and changing variables to $x_a = z_a \xi_a$ only on the last line. Doing so leads to the expression

$$
\sigma_{pp \to X}(P_a, P_b) = \sum_{i,j} \int_0^1 \mathrm{d}x_a \int_0^1 \mathrm{d}x_b\, f_j(x_b) \left[f_i(x_a)\, \hat{\sigma}_{ij \to X}^{H,(0)}(x_a P_a, x_b P_b) \right. \quad (2.62)
$$

$$
+ \frac{\alpha_s}{4\pi}\, f_i(x_a)\, \hat{\sigma}_{ij \to X}^{H,(1)}(x_a P_a, x_b P_b) + \frac{\alpha_s}{4\pi} \ln\!\left(\frac{Q^2 e^{\gamma_E}}{4\pi\mu^2}\right) f_i(x_a)
$$

$$
\times \sum_k \int_0^1 \mathrm{d}z_a\, P_{ki}^{(0)}(z_a)\, \hat{\sigma}_{kj \to X}^{H,(0)}(z_a x_a P_a, x_b P_b)
$$

$$
\left. - \frac{1}{\epsilon} \frac{\alpha_s}{4\pi} \sum_k \int_{x_a}^1 \frac{\mathrm{d}\xi_a}{\xi_a}\, f_k(\xi_a)\, P_{ik}^{(0)}\!\left(\frac{x_a}{\xi_a}\right) \hat{\sigma}_{ij \to X}^{H,(0)}(x_a P_a, x_b P_b) \right],
$$

up to corrections of $\mathcal{O}(\alpha_s^2)$. The PDFs can be defined as hadron matrix elements of the operators that count the number of quarks or gluons with a certain

momentum fraction. By an explicit calculation of their partonic counterparts (the distributions of certain partons within a parton), they are found to contain both UV and IR divergences, which cancel in dimensional regularization since the PDF is scaleless [45, 49]. The absorption of the IR divergence from eq. (2.62) into the PDF cancels its IR divergence exactly. The UV divergence that is left is thus equal in structure to the absorbed IR divergence and can be treated through a renormalization procedure. This entails considering the PDFs in eq. (2.62) to be bare quantities and defining the renormalized PDFs as an infinite shift from their bare counterparts. Using the $\overline{\text{MS}}$ scheme, only the pole is absorbed into the PDF, but the renormalization scale μ is redefined as given in eq. (2.17). The renormalized PDF at 1-loop accuracy, using $\overline{\text{MS}}$, is then given by

$$f_i(x, \mu) = f_i^{\text{bare}}(x) - \frac{1}{\epsilon} \frac{\alpha_s}{4\pi} \sum_k \int_x^1 \frac{d\xi}{\xi} \, f_k(\xi) \, P_{ik}^{(0)}\left(\frac{x}{\xi}\right). \tag{2.63}$$

The terms remaining after the renormalization procedure are collectively defined as the total partonic cross section

$$\hat{\sigma}_{ij \to X}(q_a, q_b, \mu) = \hat{\sigma}_{ij \to X}^{H,(0)}(q_a, q_b) + \frac{\alpha_s}{4\pi} \, \hat{\sigma}_{ij \to X}^{H,(1)}(q_a, q_b)$$
$$+ \frac{\alpha_s}{4\pi} \ln\left(\frac{Q^2}{\mu^2}\right) \sum_k \int_0^1 dz_a \, P_{ki}^{(0)}(z_a) \, \hat{\sigma}_{kj \to X}^{H,(0)}(z_a q_a, q_b), \tag{2.64}$$

which now no longer contains any divergences. The hadronic cross section then simply reads

$$\sigma_{pp \to X}(P_a, P_b) = \int_0^1 dx_a \int_0^1 dx_b \sum_{i,j} f_i(x_a, \mu) \, f_j(x_b, \mu) \, \hat{\sigma}_{ij \to X}(x_a P_a, x_b P_b, \mu),$$
$$\tag{2.65}$$

where now both the PDFs and the partonic cross section depend on the renormalization scale μ. A possible issue due to this scale dependence manifests itself when the PDFs used to calculate hadronic cross sections are measured at some scale $\mu_0 \ll Q$. For such scales, the logarithm in eq. (2.64), that will appear at every order at the same power as α_s, grows large and spoils the convergence of the perturbative series. Instead of measuring the PDFs at a different scale whenever a process at a different invariant mass Q is considered, there is a more sophisticated solution. The scale dependence of the PDF at $\mathcal{O}(\alpha_s)$ is explicitly given by

$$\frac{df_i(x, \mu)}{d\ln \mu} = \frac{\alpha_s}{2\pi} \sum_k \int_x^1 \frac{d\xi}{\xi} \, P_{ik}^{(0)}\left(\frac{x}{\xi}\right) f_k(\xi, \mu), \tag{2.66}$$

which is known as the Dokshitzer-Gribov-Lipatov-Altarelli-Parisi (DGLAP) equation [50–52]. Although no exact analytic solution to this integro-differential equation is known, it can be solved at a given order in perturbation theory either numerically or in Mellin space, after which an inverse Mellin transformation has to be performed. The solution to the DGLAP equation then relates PDFs at some scale μ to PDFs at some reference scale μ_0. Using this solution, a PDF measured at some scale μ_0 can be evolved to the scale μ, which can freely be chosen as $\mu \sim Q$ to minimize the logarithm in eq. (2.64) and to guarantee the convergence of the perturbative series of the partonic cross section.

In this chapter some general aspects of QCD have been reviewed. Many of these concepts, such as renormalization group equations and the appearance of infrared divergences play a key part throughout the rest of this thesis. The next chapter aims to give an insight in an effective theory that is particularly well-suited for the description of QCD in the IR limit.

3

Soft-Collinear Effective Theory

Energetic collisions at particle colliders are always accompanied by both soft and collinear radiation. A correct and adequate description of this infrared radiation is vital in order to study the details of the underlying hard interaction. Soft-Collinear Effective Theory (SCET) is an effective field theory that employs distinct soft and collinear fields to describe the infrared regime of QCD. The main advantage of this approach is that the separation of the various physical processes occurring at different energy scales allows each to be calculated individually, without being complicated by the others.

After a general introduction to effective field theories in sec. 3.1, this chapter will be dedicated to SCET, starting in sec. 3.2 with a summary of the various aspects of the theory, providing the reader with an overview of the topics that are discussed in the rest of the chapter. The various degrees of freedom in the theory are discussed in sec. 3.3 and the SCET Lagrangian is derived in sec. 3.4, while the topic of gauge symmetry is covered in sec. 3.5. The separation of the various sectors in the Lagrangian is shown in secs. 3.6 and 3.7 and the resulting factorization of cross sections is described in sec. 3.8. Finally, two slightly more involved versions of SCET that play a role in the rest of thesis are briefly discussed in secs. 3.9 and 3.10.

3.1 Effective field theories

Most phenomena in nature can be described using a theory that is valid only for specific energy ranges and do not require any detailed knowledge about some underlying, more general theory. Houses may be built without any knowledge of the interactions between the elementary particles that bricks are made of and the orbit of the moon around the earth can be calculated without resorting to quantum gravity. Effective theories implement this intuitive idea in a mathematically consistent way and provide a method of approximating complicated, or even unknown, theories by focussing only on the degrees of

freedom relevant to a given situation.

3.1.1 The philosophy of effective field theories

For virtually every physical quantity there exists a vast range of scales at which interesting phenomena occur in nature. In cosmology, dynamical processes are studied that take place over times of the order of the Hubble time[1], around 10^{17} seconds, while the lifetime of the top quark studied in particle physics is about 10^{-25} seconds. In terms of length scales, the study of large-scale structures involves the size of the observable universe, around 10^{26} meters, while the search for grand unified theories such as string theory is conducted at sizes of the order of the Planck length, around 10^{-35} meters.

Despite the large variety of scales at which interesting physics exists, the importance of any individual phenomenon is very often limited to a much smaller range of orders of magnitude. From a theoretical point of view, this amounts to the statement that the details that are required to describe the universe at some high energy scale are often not necessary to describe events occurring at a much lower energy scale. Theories at high scales are often more general than theories at low scales and may in principle be used to describe processes at both scales. In practice though, high-energy theories are often much more complicated than their low-energy counterparts (which are valid exclusively at low scales) and actual calculations are usually much easier to perform when using the latter. For example, although special relativity and classical (Newtonian) mechanics are in principle both suited to describe the motion of a thrown ball, the latter is much easier to use in practice. Classical mechanics can be considered as an expansion of special relativity in the limit where velocities are much smaller than the speed of light and serves as an example of a much wider class of theories known as Effective Field Theories (EFTs).

The philosophy behind an EFT is to focus on the physics at a particular energy scale by expanding a more general but more complicated theory, known as the 'full theory', in some small parameter so that all the details that are less relevant will appear in higher-order corrections [53–55]. For field theories this means that the Lagrangian of the full theory can be written as

$$\mathcal{L}_{\text{full}} = \sum_n \mathcal{L}_{\text{EFT}}^{(n)} \, , \tag{3.1}$$

where the superscript n denotes the nth order in an expansion in some small parameter λ. In general there are two ways in which EFTs are used, top-down

---

[1]The age that the universe would have had if its expansion had been linear.

and bottom-up.

In top-down types of EFTs, the high-energy theory is known, but overly complicated for calculations at lower energies. The operators in the EFT Lagrangian will in general contain coefficients that can be fixed by performing calculations of certain processes in both the full theory and the EFT and comparing the results. Classical mechanics is an example of a top-down EFT, where special relativity is considered as the full theory.

In bottom-up types of EFTs, the high-energy theory is not known. In this case, the Lagrangian of the EFT is constructed by writing down the most general set of operators consistent with the symmetries that the EFT is supposed to exhibit. The unknown coefficients in the Lagrangian of these types of theories have to be determined by experiments. An example of a bottom-up EFT is the Standard Model Effective Field Theory (SMEFT) [56–60], of which the lowest order is the Standard Model and higher orders contain higher-dimensional operators.

Effective field theories exist in many different varieties. Some EFTs arise when certain degrees of freedom are integrated out from theories. For example, integrating out the electron field from QED gives rise to the Euler-Heisenberg Lagrangian [61], which contains an effective coupling between photons. Another example is the Fermi theory of weak interactions [62], which is obtained from the electroweak sector of the Standard Model by integrating out the heavy $W^{\pm}$ bosons, leading to a direct coupling between four fermions.

Other EFTs are expansions in different types of parameters. In Heavy Quark Effective Theory (HQET) [63–66], for example, a heavy particle is approximated as a static source and an expansion around its small velocity is performed. Non-Relativistic QED [67] is set up in a similar fashion and describes the interactions of electrons with velocities much smaller than the speed of light with the (quantized) electromagnetic field.

Although all previous examples focus on particle physics, EFTs are used in many other branches of physics as well. Among countless others, these include effective field theories for inflation [68], gravitational inspirals [69] and EFTs describing excitations of the Fermi surface [70–73].

3.1.2 Setting up an EFT

Most EFTs are set up according to very similar methods, regardless of the actual physical system or phenomenon they are designed to describe. After deciding on a specific energy regime to focus on and figuring out the small parameter in which to expand the full theory, the degrees of freedom and symmetries of the EFT have to be determined. It is important to make sure that

all of the relevant propagating degrees of freedom are included, since their propagators in the perturbative expansion give rise to the poles that have to reproduce the complete analytic structure of the full theory in the low-energy limit. In general, the symmetries of the EFT do not have to be the same as those in the full theory as new symmetries might appear upon expanding.

The Lagrangian of the EFT is then obtained by considering all the operators containing the relevant degrees of freedom that are in accordance with the symmetries, up to some desired order in the expansion parameter. Each of these operators will in general carry an unknown coefficient, known as a Wilson coefficient, that can be determined by comparing processes in the EFT with the corresponding processes in the full theory to some desired order of precision. This procedure is known as matching.

The way in which this general approach to setting up an EFT works in practice can be shown best by means of an example. Consider a toy theory containing a heavy scalar ϕ and a light Dirac fermion ψ interacting through a Yukawa coupling as the full theory. Indicating the four-scalar coupling and the Yukawa coupling by g_4 and g_Y respectively, the Lagrangian of this full theory is given by

$$\mathcal{L}_{\text{full}} = \frac{1}{2}\partial^\mu\phi\,\partial_\mu\phi - \frac{1}{2}M^2\phi^2 - g_4\phi^4 + \bar{\psi}(i\slashed{\partial} - m)\psi - g_Y\bar{\psi}\phi\psi\,, \qquad (3.2)$$

where M is the mass of the scalar and m the mass of the fermion. The expansion parameter used to describe the low-energy regime of this full theory is given by $1/M^2$ and the only degree of freedom that the EFT contains is the fermion field ψ, leading to the Lagrangian

$$\mathcal{L}_{\text{EFT}} = \bar{\psi}(i\slashed{\partial} - m)\psi - \frac{C_4}{M^2}(\bar{\psi}\psi)^2 + \mathcal{O}\Big(\frac{1}{M^4}\Big)\,. \qquad (3.3)$$

The Wilson coefficient C_4 multiplying the four-fermion interaction can then be determined by for example calculating the s-channel amplitude of the process $\bar{\psi}\psi \to \bar{\psi}\psi$ in both the full theory and the EFT. The leading-order representation of this process in the EFT is shown in the left-hand diagram in fig. 3.1. The corresponding amplitude that is obtained by connecting the fermion lines in an s-channel configuration is given by

$$i\mathcal{M}_{\text{EFT}}^{(0)} = -i\frac{C_4}{M^2}\,\bar{v}(p_2)u(p_1)\,\bar{u}(p_3)v(p_4)\,. \qquad (3.4)$$

The lowest-order s-channel diagram of this process in the full theory, as depicted on the right-hand side in fig. 3.1, leads to the amplitude

$$i\mathcal{M}_{\text{full}}^{(0)} = -i\,\bar{v}(p_2)u(p_1)\frac{g_Y^2}{(p_1 + p_2)^2 - M^2}\bar{u}(p_3)v(p_4)\,. \qquad (3.5)$$
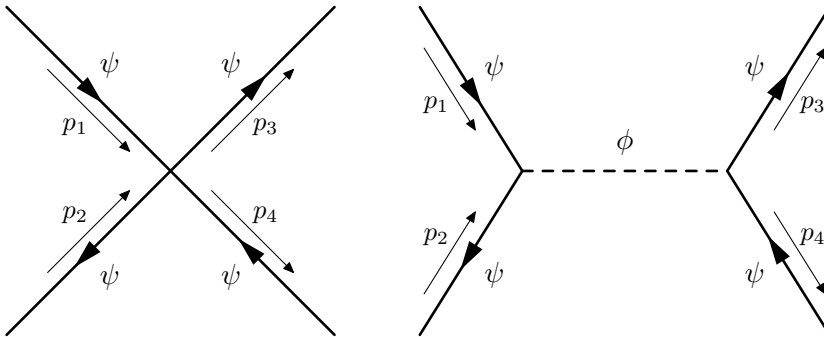
Figure 3.1 Feynman diagrams representing the process $\psi\psi \to \psi\psi$ at leading order in the effective theory (left) and the full theory (right).

Assuming that the external momenta are small, so that $(p_1^2 + p_2^2)^2 \ll M^2$, expanding the full theory result in $1/M^2$, and demanding the result to be equal to the amplitude from the EFT yields the leading-order matching equation

$$C_4 = -g_Y^2 + \mathcal{O}(g_Y^4)\,. \tag{3.6}$$

Now the complete EFT Lagrangian (at leading power) is known and can be used to calculate any other process without having to resort to the full theory again.

The matching procedure that was carried out at tree-level in the considered example gave rise to a particularly simple result. Carrying out the matching at higher orders in principle follows the same logic, but is often considerably more difficult and can only be performed after both the full theory and the EFT have been renormalized. Loop diagrams in the EFT may be carried out using the same techniques that are employed to calculate loop diagrams in the full theory, even though there are some caveats. For example, it is important to pick a mass-independent regulator (such as dimensional regularization), so that terms from different orders in the expansion are not mixed and the power counting is preserved[2].

3.1.3 Running operators in EFTs

Matching an EFT that is supposed to describe the behavior of some physical system at an energy scale μ_1 to a full theory induces a dependence of the

---

[2]Mass-dependent regulators are in principle also possible, but they complicate the procedure considerably.
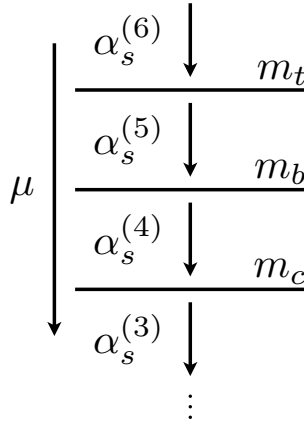
Figure 3.2 A pictorial representation of matching and running between different theories. The energy scale decreases according to the long vertical arrow and the horizontal lines represent the masses of various quarks. The short arrows stand for the running of the coupling constant with the indicated number of active flavors.

parameters of the EFT, such as coupling constants, on the scale μ_1. The renormalization group equations of these operators can then be used to determine their behavior at some other scale [74], in complete analogy to the running of the strong coupling constant $\alpha_s(\mu)$ described in sec. 2.2.3.

Many EFTs can themselves be expanded in a small parameter, leading to a new EFT valid at some lower scale $\mu_2 \ll \mu_1$. The parameters of the former EFT then have to be run down to the scale μ_2 before they can be matched to the new EFT at that scale.

A familiar example of this general procedure of matching and running can be found by considering the dependence of the strong coupling constant on the number of active flavors. By starting with a full theory containing six flavors of quarks and subsequently integrating out the heaviest quark, a chain of EFTs valid at progressively lower energy scales is obtained.

The full theory is matched to the EFT with five active flavors by demanding the continuity of physical quantities (such as S-matrices) at a scale $\mu \sim m_t$. The leading-order relation between the coupling constants from the two theories simply amounts to

$$\alpha_s^{(5)}(\mu_t) = \alpha_s^{(6)}(\mu_t) \left[1 + \mathcal{O}\big(\alpha_s^{(6)}(\mu_t)\big)\right]. \tag{3.7}$$

The higher-order corrections come from diagrams that are exclusive to the full theory, such as diagrams containing loops involving the top quark. These will

lead to a discontinuity in α_s that ensures the continuity of physical quantities across the threshold at $\mu \sim m_t$. The coupling constant in the EFT with five active flavors is then run down to the scale $\mu \sim m_b$, where it is matched to the EFT with four active flavors by again demanding continuity of physical quantities. This iterative procedure, schematically shown in fig. 3.2, represents the general method of matching and running according to which most EFTs are set up.

3.2 Overview of SCET

Soft-Collinear Effective Theory was developed as a top-down EFT of QCD through a series of papers including refs. [75–85], among many others. Apart from the field of heavy-flavor physics in which context it was originally considered, SCET has been applied to many other (sub)fields such as jet physics, electroweak corrections, heavy-ion collisions, top quark physics, physics beyond the Standard Model, dark matter and gravitational waves.
Some pedagogical introductions to SCET are available, the most notable of which are refs. [86, 87]. The structure of the current chapter mostly follows that of [86], supplemented by the original literature. The aim of this section is to provide the reader with a summary of the most prevalent features and aspects of SCET that are discussed in this chapter.

Unlike many other EFTs, such as the example considered in sec. 3.1.2, SCET is not obtained by integrating out heavy particles. The expansion parameter λ of SCET instead arises from the specific scaling of the momentum components of the relevant degrees of freedom, which are most conveniently expressed in terms of lightcone coordinates (see sec. 3.3.1). The degrees of freedom include collinear and (ultra)soft modes, the hierarchy between which depends on the process and measurement under consideration, giving rise to two distinct theories: $\mathrm{SCET_I}$ and $\mathrm{SCET_{II}}$, whose modes are discussed in sec. 3.3.2 and sec. 3.3.3 respectively. The next few sections solely involve $\mathrm{SCET_I}$ and a detailed discussion of $\mathrm{SCET_{II}}$ is left until sec. 3.9.

The scaling of the collinear and ultrasoft quark and gluon fields in $\mathrm{SCET_I}$ in terms of λ is determined in sec. 3.4.2, leading to the conclusion that, to leading power in λ, the QCD quark field is equal to the collinear quark field in SCET (see eq. (3.40)). The analogous expansion for the gluon field is given in eq. (3.43) and still involves a single momentum component of the ultrasoft gluon field at leading power.

In order to assign a definite scaling to both the gauge field and the derivatives of the quark field, a multipole expansion is performed in momentum space in sec. 3.4.3 by using a method known as the label formalism. This effectively splits each momentum into a large, discrete component (the label momentum) with collinear scaling and a small, continuous component (the residual momentum) with ultrasoft scaling. The former is included as a label on the collinear quark field, after which the field is Fourier transformed to position space only in the residual momentum. The operator that extracts the label momentum from a field, known as the label operator, can then be employed to obtain the quark and gluon fields given in eqs. (3.55) and (3.58) respectively.

Through its action on the collinear quark field, the partial derivative is split into a large (label) part and a residual piece in eq. (3.69), paving the way for the expansion of the covariant derivative to leading power in λ, given in eq. (3.72). The SCET_I collinear quark and gluon Lagrangians in eqs. (3.73) and (3.79) then follow from expanding all fields and derivatives in the corresponding QCD Lagrangian. The ultrasoft Lagrangian is simply equal to the Lagrangian of QCD with ultrasoft fields.

The simplest hard scattering processes involve a current, e.g. $e^+e^- \to$ dijets. Currents in SCET are in general not invariant under the collinear gauge transformations discussed in sec. 3.5.1. To restore collinear gauge invariance, each collinear quark field has to be accompanied by a collinear Wilson line, as given in eq. (3.108). This object represents the unsuppressed interactions between an n-collinear quark and any possible number of $\bar{n}$-collinear gluons (or between an $\bar{n}$-collinear quark and n-collinear gluons). Since collinear quark fields and Wilson lines always appear together, this motivates the definition of their combination as the quark jet field in eq. (3.146). The gluon jet field is defined analogously in eq. (3.147).

Ultrasoft Wilson lines, representing interactions between a collinear quark and any possible number of ultrasoft gluons, can be defined in a way similar to the collinear Wilson line (see eq. (3.131)). By making the Bauer-Pirjol-Stewart field redefinitions in eq. (3.135), all the ultrasoft gluons can be moved from the SCET_I collinear quark Lagrangian into the currents, obtaining the complete factorization of ultrasoft and collinear degrees of freedom. This allows one to write the cross section as a product (or convolution) of hard, collinear and soft matrix elements.

One of the subtleties of SCET is that the Wilson coefficients that are required for the matching onto QCD are included in the currents through a convolution instead of a multiplication. To perform the matching, the Feynman diagrams

representing a relevant process have to be determined in both the effective theory and the full theory, both having been renormalized. As SCET describes the infrared behavior of QCD, both results should agree in the IR limit. The difference between the two results determines the Wilson coefficients. Details on the matching procedure in SCET, as well as an explicit example for the case of $e^+e^- \to$ dijets, are described in sec. 3.7. Due to the renormalization procedure, the Wilson coefficients obtain a scale-dependence that leads to an RGE. The solution of this RGE serves to relate Wilson coefficients at different scales to one another and allows for the resummation of logarithms of the ratios of these scales, as described in sec. 3.7.3 for the case of the previously mentioned example of $e^+e^- \to$ dijets.

Since the various degrees of freedom in SCET are already factorized at the level of the Lagrangian, factorization theorems for differential cross sections can be readily obtained by also factorizing the contribution of each degree of freedom to the measurement under consideration. An example of this procedure for the measurement of thrust in $e^+e^- \to$ dijets is shown in sec. 3.8.1, resulting in the factorization formula in eq. (3.181). As is described in sec. 3.8.2, each resulting sector in a factorization formula can be calculated independently and will in general contain logarithms involving ratios of its inherent, natural scale and the common scale μ. Each of these functions adheres to an RGE, whose solution allows the evaluation of the function at its natural scale, after which it can be evolved to the common scale μ, resumming the logarithms in the process. This method of obtaining factorization formulas for cross sections differential in one or more variables and resumming the occurring logarithms is the main application of SCET used in this thesis.

An outline of the derivation of SCET_II and its main features are given in sec. 3.9. This EFT contains soft instead of ultrasoft degrees of freedom, whose perpendicular[3] momentum component is parametrically equal to the perpendicular component of the collinear modes. This makes SCET_II the correct theory to describe (among other things) measurements of observables sensitive to transverse momenta.

Finally, sec. 3.10 introduces yet another version of SCET, known as SCET_+, which involves collinear-soft modes in addition to the familiar (ultra)soft and collinear modes. SCET_+ is required when cross sections subject to multiple measurements are considered and plays an important role throughout this thesis.

---

[3]Perpendicular to the collinear directions n and $\bar{n}$, which are often chosen along the beam axis.

3.3 Degrees of freedom in SCET

The exact hierarchy between the soft and collinear degrees of freedom that SCET describes depends on the details of the process under consideration. The contribution of soft and collinear particles to a particular measurement is dictated by the properties of the measured observable and determines the relative scaling of the degrees of freedom. There are two main classes of observables leading to two distinct versions of the EFT, called $\mathrm{SCET_I}$ and $\mathrm{SCET_{II}}$. The former describes the infrared regime of QCD for processes subjected to measurements involving momentum components along preferred collinear directions, while a large class of examples described by $\mathrm{SCET_{II}}$ includes observables sensitive to momentum components perpendicular to such directions. These collinear directions might for example be the directions of the incoming beams, or those of outgoing jets.

3.3.1 Lightcone coordinates

The soft and collinear nature of the degrees of freedom in SCET can be described in a particularly convenient way through the usage of lightcone coordinates. In this set of coordinates, vectors are projected onto two light-like vectors n and $\bar{n}$ that satisfy

$$n^2 = \bar{n}^2 = 0 \qquad \text{and} \qquad n \cdot \bar{n} = 2 \,. \tag{3.8}$$

Two explicit vectors that adhere to these conditions are given by

$$n^\mu = \big(1, 0, 0, 1\big) \qquad \text{and} \qquad \bar{n}^\mu = \big(1, 0, 0, -1\big) \,, \tag{3.9}$$

and will be used for definiteness from here on. This choice is far from unique and the reinstatement of the freedom lost due to using this particular choice will be addressed in sec. 3.5.4. Any vector p^μ can be projected onto these light-like vectors as

$$p^+ \equiv n \cdot p = p^0 - p^3 \qquad \text{and} \qquad p^- \equiv \bar{n} \cdot p = p^0 + p^3 \,, \tag{3.10}$$

so that an on-shell particle moving in the positive $\hat{z}$-direction has a small p^+ and large p^- component. By defining the two-dimensional vector

$$p_\perp^\mu \equiv \big(0, p^1, p^2, 0\big) \equiv \big(0, \vec{p}_\perp, 0\big) \,, \tag{3.11}$$

as was already done in eq. (2.45), any vector can be decomposed as

$$p^\mu = \frac{\bar{n}^\mu}{2} p^+ + \frac{n^\mu}{2} p^- + p_\perp^\mu \,. \tag{3.12}$$
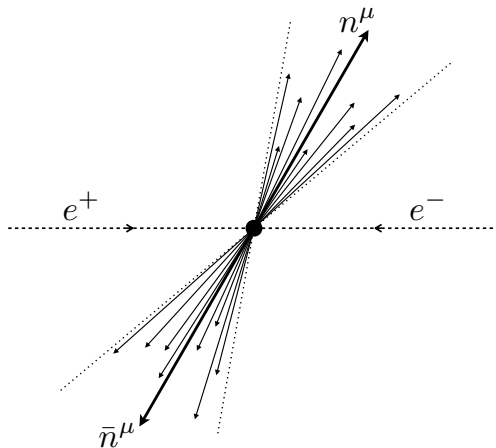
Figure 3.3 A schematic representation of the process $e^+e^- \to$ dijets in the center-of-mass frame. The directions n^μ and $\bar{n}^\mu$ of the jets are indicated explicitly.

When using lightcone coordinates, it is customary to denote vectors by $p^\mu = (p^+, p^-, \vec{p}_\perp)$, where the last entry contains the Euclidean (two-dimensional) perpendicular momentum, which differs from its Minkowski counterpart by $\vec{p}_\perp^2 = -p_\perp^2$. The product of two vectors p^μ and q^μ in lightcone coordinates is found to be

$$p \cdot q = \frac{1}{2}(p^+q^- + p^-q^+) + p_\perp \cdot q_\perp = \frac{1}{2}(p^+q^- + p^-q^+) - \vec{p}_\perp \cdot \vec{q}_\perp . \qquad (3.13)$$

Other objects can be decomposed into plus, minus and perpendicular components as well. The metric, for example, can be written as

$$g^{\mu\nu} = \frac{1}{2}(n^\mu \bar{n}^\nu + \bar{n}^\mu n^\nu) + g_\perp^{\mu\nu} . \qquad (3.14)$$

3.3.2 Modes in SCET$_\mathrm{I}$

The quarks in the final state of the process $e^+e^- \to q\bar{q}$, described in sec. 2.3.1, will in general undergo multiple splittings and eventually form two jets. The momentum of the intermediate vector boson in the center-of-mass frame of the collision is given by

$$q^\mu = \big(Q, 0, 0, 0\big) , \qquad (3.15)$$

and momentum conservation forces the two jets to be (approximately) back-to-back, as shown in fig. 3.3. One of the jets will be taken along the n-direction[4]

---

[4]In this sloppy notation, 'direction' always refers to the three spatial directions of the four-vector.
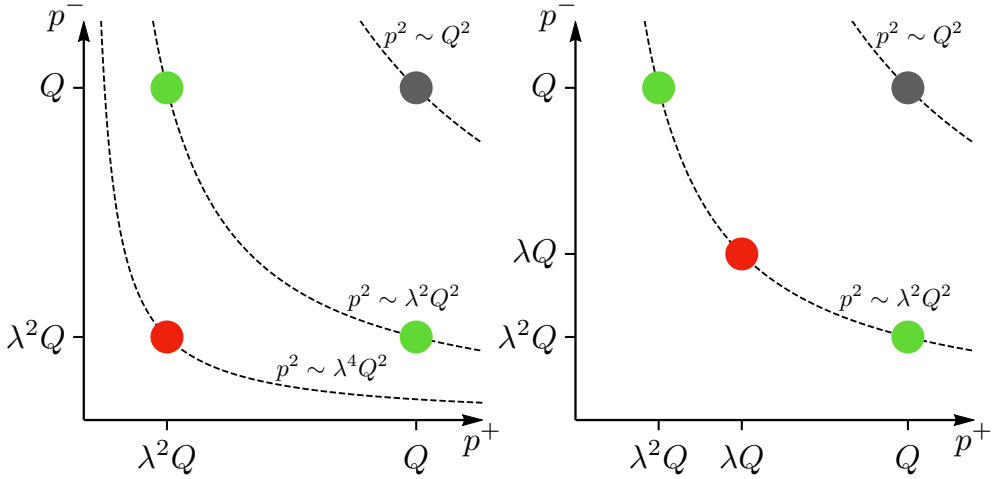
Figure 3.4 The plus and minus lightcone components of the various modes in SCET$_{\text{I}}$ (left-hand plot) and SCET$_{\text{II}}$ (right-hand plot). The hard, collinear and (ultra)soft modes are colored gray, green and red respectively.

with momentum p_n^μ and the other along the $\bar{n}$-direction with momentum $p_{\bar{n}}^\mu$. The large component of the momentum of each jet has to be of order Q to guarantee energy-momentum conservation, so $p_n^- \sim p_{\bar{n}}^+ \sim Q$.

The jets may still carry a transverse momentum due to possible recoil against radiation outside of the jets. The size of this transverse momentum must be parametrically smaller than Q to adhere to the definition of a jet, so $p_\perp \ll Q$, where $p_\perp$ denotes the absolute value of $p_\perp^\mu$. The small components of the jet momenta can be obtained by using the on-shell condition[5] $p^+ p^- \sim p_\perp^2$, leading to

$$p_n^\mu \sim \left(\frac{p_\perp^2}{Q}, Q, p_\perp \right) \sim Q\left(\lambda^2, 1, \lambda \right),$$

$$p_{\bar{n}}^\mu \sim \left(Q, \frac{p_\perp^2}{Q}, p_\perp \right) \sim Q\left(1, \lambda^2, \lambda \right), \tag{3.16}$$

where $\lambda = p_\perp / Q \ll 1$ in this case. Although the exact definition of λ will differ depending on the process and observables under consideration, this parametric hierarchy of the various components in terms of λ is what defines collinear modes in general.

---

[5]Although the jet itself in general carries a mass, the scaling of this condition still applies because every individual particle contained in the jet is on-shell.

To determine the parametric scaling of the soft radiation, an explicit observable has to be specified. As an example, consider the hemisphere mass: The invariant mass of all the particles in one of the two (symmetric) hemispheres combined. Picking the hemisphere into which the n-collinear jet propagates for definiteness, this observable is formally defined by

$$m_n^2 = \left(\sum_i p_i^\mu\right)^2, \tag{3.17}$$

where the sum runs over all particles in the aforementioned hemisphere. Since almost all the momentum is carried by the jet, the hemisphere mass must be of the order of the invariant mass of the jet (i.e. of the order of the n-collinear degree of freedom), so $m_n^2 \sim p_\perp^2$, which gives the constraint

$$p_\perp^2 \sim m_n^2 \sim (p_n^\mu + p_{us}^\mu)^2 = p_n^2 + p_{us}^2 + 2\, p_n \cdot p_{us}, \tag{3.18}$$

where p_{us}^μ represents the total soft momentum in the hemisphere containing the n-collinear jet. Since soft radiation does not have a preferred direction, the scaling of the soft degrees of freedom must be homogeneous, i.e. all lightcone components must be of the same parametric size. Writing the dot product in lightcone coordinates through eq. (3.13), the final term reduces to $2\, p_n \cdot p_{us} \sim p_n^- p_{us}^+ + \mathcal{O}(p_\perp)$. Since the collinear component scales as $p_n^- \sim Q$, the soft component is restricted to scale as $p_{us}^+ \sim p_\perp^2/Q$ in order to ensure the correct scaling of m_n^2. The homogeneous nature of the soft degrees of freedom then leads to the parametric scaling

$$p_{us}^\mu \sim \left(\frac{p_\perp^2}{Q}, \frac{p_\perp^2}{Q}, \frac{p_\perp^2}{Q}\right) \sim Q\left(\lambda^2, \lambda^2, \lambda^2\right). \tag{3.19}$$

As long as $m_n \sim m_{\bar n}$, the same reasoning holds for soft radiation entering the opposite hemisphere, so that the scaling in eq. (3.19) is the universal scaling of the soft degrees of freedom. Because their scaling is equal to the scaling of the small component of either collinear mode, the soft modes are able to interact with both jets but can never change the scaling of the collinear degrees of freedom. Soft modes scaling in this fashion are usually named ultrasoft modes and the version of the EFT in which they occur is known as SCET$_\text{I}$. The relative scaling of the plus and minus components of the ultrasoft and collinear modes is shown in the left-hand plot in fig. 3.4, while their perpendicular components are fixed by the on-shell condition as mentioned before. The dashed hyperbolas in this plot are lines of fixed virtuality, depicting the hierarchy between the ultrasoft and collinear degrees of freedom by placing the former on a lower hyperbola [83]. The hard modes are described by the hyperbola in the upper-right corner, parametrized by $p^2 \sim Q^2$.

3.3.3 Modes in SCET$_{\text{II}}$

Consider the decay of a B meson into a D meson and a pion[6]. The B and D meson both contain one very heavy quark (the bottom and charm quark respectively) that carries nearly all of their momentum. All the other components (the valence up or down quark and the sea quarks and gluons) are necessarily soft and their momenta must scale as the internal energy scale of the mesons, so

$$p_s^\mu \sim \left(\Lambda_{\text{QCD}}, \Lambda_{\text{QCD}}, \Lambda_{\text{QCD}}\right). \tag{3.20}$$

In the rest frame of the B meson, the light pion in the final state of the decay process is highly boosted and will be described by a collinear mode. Picking this boost along the $\hat{z}$-axis for concreteness and taking the parametric size of the pion momentum in the rest frame of the B meson to be of the size Q then sets the momentum component $p_n^- \sim Q$. As the virtuality must scale as $p^2 \sim \Lambda_{\text{QCD}}^2$, the scaling of the other components of the collinear mode can be determined through the on-shell condition, yielding

$$p_n^\mu \sim \left(\frac{\Lambda_{\text{QCD}}^2}{Q}, Q, \Lambda_{\text{QCD}}\right) \sim Q\left(\lambda^2, 1, \lambda\right), \tag{3.21}$$

where in this case $\lambda = \Lambda_{\text{QCD}}/Q \ll 1$. In terms of this small parameter, the soft degrees of freedom then scale as

$$p_s^\mu \sim Q\left(\lambda, \lambda, \lambda\right). \tag{3.22}$$

In contrast with the soft modes found in eq. (3.19), these soft degrees of freedom have the same virtuality as the collinear degrees of freedom, leading to a different version of the EFT, known as SCET$_{\text{II}}$. The relative hierarchy between the soft and collinear modes in this theory is shown in the right-hand plot in fig. 3.4, where both degrees of freedom are now described by the same hyperbola in contrast to the modes of SCET$_{\text{I}}$.

3.4 The SCET$_{\text{I}}$ Lagrangian

SCET describes the infrared behavior of the quark and gluon fields from QCD by splitting both into separate collinear and soft fields. The relative scaling of these fields may be used to expand the Lagrangian of QCD in the small parameter λ that characterizes the hierarchy between the momentum components of

---

[6] B and D mesons are bound states of an up or a down quark with a bottom quark and a charm quark respectively. Pions are bound states of up and down quarks.

the various degrees of freedom. The first term in this expansion is known as the leading-order Lagrangian of SCET$_\mathrm{I}$ and gives rise to a set of Feynman rules that may be used to calculate scattering processes in SCET.

Power corrections that were dropped in obtaining the leading-order result can be regained through a multipole expansion. Although multipole expansions are often carried out in position space, the label formalism that will be discussed in sec. 3.4.3 allows the inclusion of these power corrections to be implemented in momentum space instead.

3.4.1 Collinear spinors

The spinors representing collinear degrees of freedom in SCET can be derived from the (massless) QCD spinors by an expansion in the small expansion parameter. The QCD spinors in Dirac representation are given by

$$u(\vec{p}, s) = \sqrt{p^0} \begin{pmatrix} u^s \\ \frac{\vec{\sigma}\cdot\vec{p}}{p^0} u^s \end{pmatrix} \qquad \text{and} \qquad v(\vec{p}, s) = \sqrt{p^0} \begin{pmatrix} \frac{\vec{\sigma}\cdot\vec{p}}{p^0} v^s \\ v^s \end{pmatrix}, \qquad (3.23)$$

where s denotes the spin and the basis spinors are taken to be

$$u^1 = v^2 = \begin{pmatrix} 1 \\ 0 \end{pmatrix} \qquad \text{and} \qquad u^2 = v^1 = \begin{pmatrix} 0 \\ 1 \end{pmatrix}. \qquad (3.24)$$

For spinors corresponding to n-collinear momenta $p_n^\mu \sim Q(\lambda^2, 1, \lambda)$ and $\bar{n}$-collinear momenta $p_{\bar{n}}^\mu \sim Q(1, \lambda^2, \lambda)$, an expansion in λ amounts to

$$p_n^0 = \frac{p_n^-}{2} + \mathcal{O}(\lambda^2) \qquad \text{and} \qquad p_{\bar{n}}^0 = \frac{p_{\bar{n}}^+}{2} + \mathcal{O}(\lambda^2), \qquad (3.25)$$

for their respective zeroth components and

$$\vec{\sigma} \cdot \vec{p}_n = \sigma^3 \frac{p_n^-}{2} + \mathcal{O}(\lambda) \qquad \text{and} \qquad \vec{\sigma} \cdot \vec{p}_{\bar{n}} = -\sigma^3 \frac{p_{\bar{n}}^+}{2} + \mathcal{O}(\lambda), \qquad (3.26)$$

for the dot product with the Pauli spin matrices. These expansions then lead to the n-collinear spinors

$$u_n(p, s) = \sqrt{\frac{p_n^-}{2}} \begin{pmatrix} u^s \\ \sigma^3 u^s \end{pmatrix} \qquad \text{and} \qquad v_n(p, s) = \sqrt{\frac{p_n^-}{2}} \begin{pmatrix} \sigma^3 v^s \\ v^s \end{pmatrix}, \qquad (3.27)$$

and the $\bar{n}$-collinear spinors

$$u_{\bar{n}}(p, s) = \sqrt{\frac{p_{\bar{n}}^+}{2}} \begin{pmatrix} u^s \\ -\sigma^3 u^s \end{pmatrix} \qquad \text{and} \qquad v_{\bar{n}}(p, s) = \sqrt{\frac{p_{\bar{n}}^+}{2}} \begin{pmatrix} -\sigma^3 v^s \\ v^s \end{pmatrix}, \qquad (3.28)$$

up to corrections of order λ. Acting on these collinear spinors with the lightlike vectors n^μ and $\bar{n}^\mu$ contracted with the gamma matrices can be seen to yield

$$\slashed{n}\, u_n(p,s) = \slashed{n}\, v_n(p,s) = \slashed{\bar{n}}\, u_{\bar{n}}(p,s) = \slashed{\bar{n}}\, v_{\bar{n}}(p,s) = 0\,, \qquad (3.29)$$

in analogy to the massless Dirac equation for the QCD spinors. These identities inspire the definition of two projection operators

$$P_n \equiv \frac{\slashed{n}\slashed{\bar{n}}}{4} = \frac{1}{2}\begin{pmatrix} \mathbb{1} & \sigma^3 \\ \sigma^3 & \mathbb{1} \end{pmatrix} \qquad \text{and} \qquad P_{\bar{n}} \equiv \frac{\slashed{\bar{n}}\slashed{n}}{4} = \frac{1}{2}\begin{pmatrix} \mathbb{1} & -\sigma^3 \\ -\sigma^3 & \mathbb{1} \end{pmatrix}\,, \quad (3.30)$$

that project onto either of the two lightlike vectors as

$$P_n\,\slashed{n} = \slashed{n}\,, \qquad P_{\bar{n}}\,\slashed{\bar{n}} = \slashed{\bar{n}} \qquad \text{and} \qquad P_n\,\slashed{\bar{n}} = P_{\bar{n}}\,\slashed{n} = 0\,, \qquad (3.31)$$

and obey the relations $P_n^2 = P_n$ and $P_{\bar{n}}^2 = P_{\bar{n}}$. Their effect on the various collinear spinors is found to be

$$\begin{aligned} P_n\, u_n(p,s) &= u_n(p,s)\,, & P_n\, v_n(p,s) &= v_n(p,s)\,, \\ P_{\bar{n}}\, u_{\bar{n}}(p,s) &= u_{\bar{n}}(p,s)\,, & P_{\bar{n}}\, v_{\bar{n}}(p,s) &= v_{\bar{n}}(p,s)\,, \end{aligned} \qquad (3.32)$$

and all other combinations vanish. Since the momentum components of the soft degrees of freedom scale homogenously, no expansion in λ will provide a simplification of the QCD spinors.

3.4.2 Collinear and ultrasoft quark and gluon fields

As a first step towards the field content of SCET$_\text{I}$, the quark field in QCD is split into a collinear piece and an ultrasoft piece. The relative scaling of these two components can be found by considering their 2-point correlation functions. For ultrasoft quarks with a momentum scaling as $p_{us}^2 \sim \lambda^4 Q^2$ this gives

$$\langle 0|\, T\{\psi_{us}(x)\bar{\psi}_{us}(0)\}\, |0\rangle = \int \mathrm{d}^4 p_{us}\, e^{-i p_{us}\cdot x}\, \frac{i\slashed{p}_{us}}{p_{us}^2 + i\epsilon} \sim \lambda^6 Q^3\,, \qquad (3.33)$$

so that the ultrasoft quark field scales as $\psi_{us} \sim \lambda^3 Q^{3/2}$.
The collinear quark field is first split further into an n- and an $\bar{n}$-collinear component[7] by [75]

$$\psi_c(x) = (P_n + P_{\bar{n}})\, \psi_c(x) \equiv \hat{\xi}_n(x) + \phi_{\bar{n}}(x)\,, \qquad (3.34)$$

---

[7] Note that both fields carry momenta in the same collinear direction. The subscripts n and $\bar{n}$ refer to the directions of the spin components of the fields.

where the collinear quark fields are defined as

$$\hat{\xi}_n \equiv P_n \psi_c \qquad \text{and} \qquad \phi_{\bar{n}} \equiv P_{\bar{n}} \psi_c \,. \tag{3.35}$$

Here the dependence of the fields on x has been suppressed, a practice that will be maintained throughout most of this thesis for the sake of readability. The projection operators for the collinear spinors also serve as projection operators for the collinear quark fields through the identities

$$P_n \hat{\xi}_n = \hat{\xi}_n \,, \qquad P_{\bar{n}} \phi_{\bar{n}} = \phi_{\bar{n}} \qquad \text{and} \qquad P_n \phi_{\bar{n}} = P_{\bar{n}} \hat{\xi}_n = 0 \,. \tag{3.36}$$

Analogous identities for the conjugate spinors can be obtained by realizing that $\bar{P}_n = P_{\bar{n}}$. Using these projection relations, the 2-point correlation function of the $\phi_{\bar{n}}$ field can be expressed as

$$\langle 0 | \, T\{\phi_{\bar{n}}(x)\bar{\phi}_{\bar{n}}(0)\} \, | 0 \rangle = \langle 0 | \, T\{P_{\bar{n}}\psi_c(x)\bar{\psi}_c(0)P_n\} \, | 0 \rangle$$
$$= \int \mathrm{d}^4 p_c \, e^{-ix \cdot p_c} \, P_{\bar{n}} \, \frac{i \slashed{p}_c}{p_c^2 + i\epsilon} \, P_n \,. \tag{3.37}$$

By anticommuting $\slashed{p}_c$ towards the left and using the properties of the lightlike vectors n^μ and $\bar{n}^\mu$ from eq. (3.8), this propagator can be simplified to

$$\langle 0 | \, T\{\phi_{\bar{n}}(x)\bar{\phi}_{\bar{n}}(0)\} \, | 0 \rangle = \int \mathrm{d}^4 p_c \, e^{-ix \cdot p_c} \, \frac{i}{p_c^2 + i\epsilon} \, \frac{p_c^+ \slashed{\bar{n}}}{2} \,, \tag{3.38}$$

which for an n^μ-collinear momentum $p_c^\mu = p_n^\mu \sim Q(\lambda^2, 1, \lambda)$ with a small plus component leads to the parametric scaling $\phi_{\bar{n}} \sim \lambda^2 Q^{3/2}$. Doing the same type of manipulations for the $\hat{\xi}_n$ field yields the 2-point correlator

$$\langle 0 | \, T\{\hat{\xi}_n(x)\bar{\hat{\xi}}_n(0)\} \, | 0 \rangle = \int \mathrm{d}^4 p_c \, e^{-ix \cdot p_c} \, \frac{i}{p_c^2 + i\epsilon} \, \frac{p_c^- \slashed{n}}{2} \,, \tag{3.39}$$

which now involves the large minus component of the collinear momentum so that the field scales as $\hat{\xi}_n \sim \lambda Q^{3/2}$. The relative scaling of these three fields then allows an expansion of the QCD quark field as

$$\psi_{\rm QCD} = \hat{\xi}_n + \mathcal{O}(\lambda^2) \,, \tag{3.40}$$

so that for each collinear direction only one collinear quark field and no ultrasoft quark fields need to be considered at leading power.

Since the gluon field and the partial derivative both appear in the covariant derivative in eq. (2.7), the two must have the same scaling. In particular,

this means that the gluon field scales as its momentum does. The parametric scaling of the collinear and ultrasoft gluon modes is thus simply given by

$$A_n^\mu \sim Q\big(\lambda^2, 1, \lambda\big) \qquad \text{and} \qquad A_{us}^\mu \sim Q\big(\lambda^2, \lambda^2, \lambda^2\big)\,, \qquad (3.41)$$

and the total gluon field is defined as their sum

$$A_{\text{QCD}}^\mu = A_n^\mu + A_{us}^\mu\,. \qquad (3.42)$$

The relative scaling of the individual components of the ultrasoft and collinear fields then leads to the expansion

$$A_{\text{QCD}}^\mu \sim \big(A_n^+ + A_{us}^+, A_n^-, \vec{A}_{n\perp}\big) + \mathcal{O}(\lambda)\,, \qquad (3.43)$$

so that only the plus component of the ultrasoft gluon field remains at leading power.

3.4.3 The label formalism

To be able to regain all the power corrections that were dropped in the expansion in λ, a multipole expansion, similar to the multipole expansion of an electrostatic potential for a charge distribution in electromagnetism, may be performed. This multipole expansion can be carried out in position space [84, 88], but suffers from the drawback that the familiar Feynman rules are given in momentum space. Alternatively, the multipole expansion may be carried out in momentum space through a method known as the label formalism [75–78], which will be the method of choice in this thesis. The collinear quark field in momentum space is obtained by Fourier transforming its position space counterpart

$$\tilde{\hat{\xi}}_n(p) = \int \frac{\mathrm{d}^4 x}{(2\pi)^4}\, e^{ip\cdot x}\, \hat{\xi}_n(x)\,, \qquad (3.44)$$

where the x- and p-dependence of the fields has been made explicit for clarity. The momentum of this field can be split into two pieces

$$p^\mu = p_\ell^\mu + p_r^\mu\,, \qquad (3.45)$$

where

$$p_\ell^\mu \sim Q\big(0, 1, \lambda\big) \qquad \text{and} \qquad p_r^\mu \sim Q\big(\lambda^2, \lambda^2, \lambda^2\big)\,, \qquad (3.46)$$

are called the label momentum and the residual momentum respectively. The parametrically small residual momentum will be treated as a continuous quantity, but the large label momentum is regarded in a discrete fashion. A pictorial
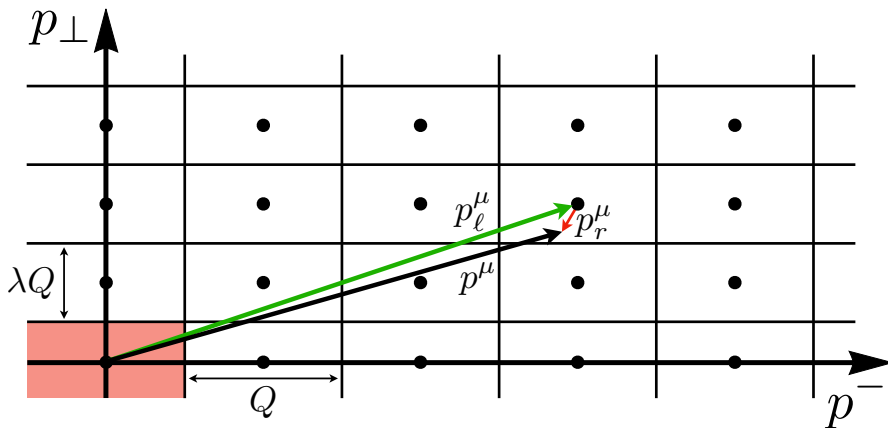
Figure 3.5 A representation of the decomposition of a general momentum (the black arrow) into a label momentum component (the green arrow) and a residual momentum component (the red arrow). The red box in the lower left corner is the 0-bin, containing all ultrasoft momenta.

representation of the decomposition into label and residual momenta is shown in fig. 3.5. Each box in this $(p^-, p_\perp)$-plane[8] corresponds to a different label momentum and the steps between boxes are discrete. As the scaling of the label momentum shows, the size of the boxes in the horizontal p^- direction is Q, while their size in the vertical $p_\perp$ direction is λQ. The exact position within any box with respect to the center of the box is determined by the continuous residual momentum so that any total momentum p^μ is uniquely described by one label momentum and one residual momentum.

Collinear momenta contain both label and residual components, whereas the parametric scaling of ultrasoft momenta ensures that they solely consist of a residual momentum. This means that all ultrasoft momenta reside in the $(0,0)$-box (shaded red in fig. 3.5), often called the zero-bin, and that integrals over ultrasoft momenta can simply be changed to integrals over residual components

$$\int \mathrm{d}^4 p_{us} \longrightarrow \int \mathrm{d}^4 p_r \,. \tag{3.47}$$

---

[8]As before, the remaining p^+ component is redundant since it follows from the on-shell relation $p^+ p^- \sim p_\perp^2$.

Integrals over collinear momenta turn into a combination of a discrete sum over label momenta and a continuous integral over residual momenta as

$$\int \mathrm{d}^4 p_n \longrightarrow \sum_{p_\ell \neq 0} \int \mathrm{d}^4 p_r \,, \tag{3.48}$$

where the sum runs over all boxes except the zero-bin [83]. As this zero-bin is populated by ultrasoft modes, it has to be excluded here to avoid double-counting.

Because of the discrete nature of the label momentum, it is common practice to include it as a label on the collinear quark field, which then only explicitly depends on the residual momentum, i.e.

$$\tilde{\hat{\xi}}_n(p) \longrightarrow \tilde{\hat{\xi}}_{n,p_\ell}(p_r) \,. \tag{3.49}$$

Fourier transforming back to position space solely in the residual momentum then leads to a hybrid field

$$\xi_{n,p_\ell}(x) = \int \mathrm{d}^4 p_r \, e^{-ip_r \cdot x} \, \tilde{\hat{\xi}}_{n,p_\ell}(p_r) \,, \tag{3.50}$$

which is described in momentum space for the label momentum and in position space for the residual momentum. Using this procedure, the collinear quark field $\hat{\xi}_n(x)$ can be written in terms of the hybrid field as

$$\hat{\xi}_n(x) = \int \mathrm{d}^4 p \, e^{-ip \cdot x} \, \tilde{\hat{\xi}}_n(p) = \sum_{p_\ell \neq 0} \int \mathrm{d}^4 p_r \, e^{-ip_\ell \cdot x} \, e^{-ip_r \cdot x} \, \tilde{\hat{\xi}}_{n,p_\ell}(p_r)$$

$$= \sum_{p_\ell \neq 0} e^{-ip_\ell \cdot x} \, \xi_{n,p_\ell}(x) \,, \tag{3.51}$$

where the argument x on the left-hand side is the complete position variable, conjugate to the complete momentum of the field. The argument x on the right-hand side, however, represents the position variable conjugate to the residual momentum component of the field.

Although this derivation is explicitly performed for the case of quarks, a similar treatment for the antiquark modes will differ only by a sign in the exponential on the right-hand side of eq. (3.51). The complete collinear quark field (including the antiquark modes) can then be obtained by extending the sum over label momenta to negative labels, i.e.

$$\hat{\xi}_n(x) = \hat{\xi}_n^+(x) + \hat{\xi}_n^-(x) = \sum_{p_\ell \neq 0} e^{-ip_\ell \cdot x} \left(\xi_{n,p_\ell}^+(x) + \xi_{n,-p_\ell}^-(x) \right)$$

$$\equiv \sum_{p_\ell \neq 0} e^{-ip_\ell \cdot x} \, \xi_{n,p_\ell}(x) \,, \tag{3.52}$$

where the superscripts $+$ and $-$ correspond to the quark and antiquark modes of the field respectively.

For positive values of the label momentum, the field $\xi_{n,p_\ell}(x)$ annihilates particles and for negative values it creates particles. It then seems useful to define an operator that extracts the label momentum from a collinear quark field as

$$\mathcal{P}^\mu \, \xi_{n,p_\ell}(x) = p_\ell^\mu \, \xi_{n,p_\ell}(x) \qquad \text{and} \qquad \mathcal{P}^\mu \, \xi_{n,p_\ell}^\dagger(x) = -p_\ell^\mu \, \xi_{n,p_\ell}^\dagger(x) \,, \qquad (3.53)$$

where $\mathcal{P}^\mu$ is called the label operator and scales as the label momentum

$$\mathcal{P}^\mu \sim Q\big(0, 1, \lambda\big) \,. \qquad (3.54)$$

The label operator can be used to rewrite eq. (3.51) to

$$\hat{\xi}_n(x) = e^{-i\mathcal{P}\cdot x} \sum_{p_\ell \neq 0} \xi_{n,p_\ell}(x) \equiv e^{-i\mathcal{P}\cdot x}\, \xi_n(x) \,, \qquad (3.55)$$

where the field $\xi_n(x)$ is defined to implicitly contain the sum over all label momenta as

$$\xi_n(x) \equiv \sum_{p_\ell \neq 0} \xi_{n,p_\ell}(x) \,. \qquad (3.56)$$

A similar analysis, involving a Fourier transform to position space, decomposing the momentum in a label and a residual piece and Fourier transforming back only in the residual momentum, can be done for the collinear gluon field. The analog of eq. (3.55) for the collinear gluon field then reads

$$\hat{A}_n^\mu(x) = e^{-i\mathcal{P}\cdot x} \sum_{p_\ell \neq 0} A_{n,p_\ell}^\mu(x) \equiv e^{-i\mathcal{P}\cdot x} A_n^\mu(x) \,, \qquad (3.57)$$

where the definition

$$A_n^\mu(x) \equiv \sum_{p_\ell \neq 0} A_{n,p_\ell}^\mu(x) \,, \qquad (3.58)$$

has been used. The sum again includes both positive and negative values of the label momentum.

3.4.4 The collinear quark Lagrangian

The kinetic term for the massless, collinear quark field in the QCD Lagrangian, given by

$$\mathcal{L}_c = \bar{\psi}_c \, i\slashed{D} \, \psi_c \,, \qquad (3.59)$$

can be rewritten by splitting the field according to eq. (3.34) and writing the covariant derivative in lightcone coordinates following eq. (3.12), to yield

$$\mathcal{L}_c = \bar{\hat{\xi}}_n \frac{\slashed{\bar{n}}}{2} i D^+ \hat{\xi}_n + \bar{\hat{\xi}}_n \, i\slashed{D}_\perp \hat{\xi}_n + \bar{\hat{\xi}}_n \, i\slashed{D}_\perp \phi_{\bar{n}} + \bar{\phi}_{\bar{n}} \, i\slashed{D}_\perp \hat{\xi}_n$$
$$+ \bar{\phi}_{\bar{n}} \frac{\slashed{n}}{2} i D^- \phi_{\bar{n}} + \bar{\phi}_{\bar{n}} \, i\slashed{D}_\perp \phi_{\bar{n}} \,, \tag{3.60}$$

where a number of terms have vanished due to the relations

$$\slashed{n} \, \hat{\xi}_n = 0 \,, \qquad \slashed{\bar{n}} \, \phi_{\bar{n}} = 0 \,, \qquad \bar{\hat{\xi}}_n \, \slashed{n} = 0 \qquad \text{and} \qquad \bar{\phi}_{\bar{n}} \, \slashed{\bar{n}} = 0 \,. \tag{3.61}$$

This expression can be simplified further by making use of the projection operator and the fact that n^μ is perpendicular to $D_\perp^\mu$, so that the second term reads

$$\bar{\hat{\xi}}_n \, i\slashed{D}_\perp \hat{\xi}_n = \bar{\hat{\xi}}_n \, i\slashed{D}_\perp P_n \, \hat{\xi}_n = \frac{1}{4} \bar{\hat{\xi}}_n \, i\slashed{D}_\perp \slashed{n}\slashed{\bar{n}} \, \hat{\xi}_n = -\frac{1}{4} \bar{\hat{\xi}}_n \, \slashed{n} \, i\slashed{D}_\perp \slashed{\bar{n}} \, \hat{\xi}_n = 0 \,. \tag{3.62}$$

The final term vanishes by an analogous identity and the Lagrangian reduces to

$$\mathcal{L}_c = \bar{\hat{\xi}}_n \frac{\slashed{\bar{n}}}{2} i D^+ \hat{\xi}_n + \bar{\hat{\xi}}_n \, i\slashed{D}_\perp \phi_{\bar{n}} + \bar{\phi}_{\bar{n}} \, i\slashed{D}_\perp \hat{\xi}_n + \bar{\phi}_{\bar{n}} \frac{\slashed{n}}{2} i D^- \phi_{\bar{n}} \,. \tag{3.63}$$

Since the field $\phi_{\bar{n}}$ is subleading in the collinear limit, it will not appear in operators that represent hard interactions at leading power. The field $\phi_{\bar{n}}$ can thus be integrated out completely by using the equation of motion (the Euler-Lagrange equation) of its conjugate field

$$0 = \frac{\delta \mathcal{L}_c}{\delta \bar{\phi}_{\bar{n}}} = i\slashed{D}_\perp \hat{\xi}_n + \frac{\slashed{n}}{2} i D^- \phi_{\bar{n}} \,, \tag{3.64}$$

to obtain the relation

$$\phi_{\bar{n}} = \frac{1}{iD^-} i\slashed{D}_\perp \frac{\slashed{\bar{n}}}{2} \hat{\xi}_n \,. \tag{3.65}$$

Plugging this into eq. (3.63), the kinetic term for the massless quark field in the Lagrangian can be seen to equal

$$\mathcal{L}_c = \bar{\hat{\xi}}_n \left(iD^+ + i\slashed{D}_\perp \frac{1}{iD^-} i\slashed{D}_\perp \right) \frac{\slashed{\bar{n}}}{2} \hat{\xi}_n \,. \tag{3.66}$$

It is important to note that at this point no expansion has been done and this kinetic term is still exactly equal to the kinetic term for a massless collinear quark field in full QCD.

In order to be able to do an expansion and obtain the collinear quark Lagrangian in SCET$_\mathrm{I}$, it is necessary to determine the parametric scaling of the covariant derivative, defined in eq. (2.7) by

$$iD_\mu = i\partial_\mu + g_s \hat{A}_\mu \,, \tag{3.67}$$

where the abbreviation $\hat{A}_\mu \equiv \hat{A}_\mu^a T^a$ has been employed. The action of the partial derivative on the collinear quark field in eq. (3.51) is found to be

$$
\begin{aligned}
i\partial^\mu \hat{\xi}_n &= \sum_{p_\ell \neq 0} e^{-ip_\ell \cdot x} \left(p_\ell^\mu \xi_{n,p_\ell} + i\partial^\mu [\xi_{n,p_\ell}] \right) \\
&= e^{-i\mathcal{P}\cdot x} \sum_{p_\ell \neq 0} \left(\mathcal{P}^\mu + i\partial_r^\mu \right) \xi_{n,p_\ell} = e^{-i\mathcal{P}\cdot x} \left(\mathcal{P}^\mu + i\partial_r^\mu \right) \xi_n \,,
\end{aligned}
\tag{3.68}
$$

where ∂_r^μ denotes the partial derivative with respect to the position space variable conjugate to the residual momentum only. As the same identity holds for collinear gluon fields, it is possible to make the general symbolic identification

$$i\partial^\mu \longrightarrow e^{-i\mathcal{P}\cdot x} \left(\mathcal{P}^\mu + i\partial_r^\mu \right) , \tag{3.69}$$

where the left-hand side is understood to act on the 'hatted' fields in eqs. (3.51) and (3.57), whereas the right-hand side acts on the 'un-hatted' fields defined in eqs. (3.56) and (3.58).
Employing the splitting of the gluon field from eq. (3.42) then leads to the covariant derivative

$$iD^\mu = \mathcal{P}^\mu + i\partial_r^\mu + g_s A_n^\mu + g_s A_{us}^\mu \,, \tag{3.70}$$

where now the 'unhatted' gluon fields are used. The overall exponential has been omitted since it is already present in the Lagrangian due to the definition in eq. (3.55). Using the previously established power counting of the various ingredients, the leading power expansions of the minus and perpendicular components of the covariant derivative can be defined as

$$iD_n^- \equiv \mathcal{P}^- + g_s A_n^- \qquad \text{and} \qquad iD_{n\perp}^\mu \equiv \mathcal{P}_\perp^\mu + g_s A_{n\perp}^\mu \,, \tag{3.71}$$

and differ only by terms of $\mathcal{O}(\lambda^2)$ from iD^- and $iD_\perp^\mu$. No expansion can be done for the plus component since all (non-vanishing) terms are of equal parametric size. The covariant derivative expanded to leading power is then given by

$$iD_n^\mu = \frac{\bar{n}^\mu}{2}\left(i\partial_r^+ + g_s A_n^+ + g_s A_{us}^+\right) + \frac{n^\mu}{2}\left(\mathcal{P}^- + g_s A_n^-\right) + \mathcal{P}_\perp^\mu + g_s A_{n\perp}^\mu \,. \tag{3.72}$$

Using the expanded covariant derivative in eq. (3.66), the n-collinear quark Lagrangian in SCET$_\mathrm{I}$, at leading power, is found to be [76]

$$\mathcal{L}_{n\xi}^{(0)} = e^{-i\mathcal{P}\cdot x} \, \bar{\xi}_n \left[iD^+ + i\slashed{D}_{n\perp} \frac{1}{iD_n^-} i\slashed{D}_{n\perp} \right] \frac{\slashed{\bar{n}}}{2} \xi_n \,. \tag{3.73}$$

3.4.5 The collinear gluon Lagrangian

The kinetic term for an n-collinear gauge field can be derived from the kinetic term in the QCD Lagrangian given by

$$\mathcal{L}_{g,\text{kin}} = -\frac{1}{4}(F_{\mu\nu}^a)^2 = -\frac{1}{2}\,\text{Tr}[F_{\mu\nu}F^{\mu\nu}]\,, \tag{3.74}$$

where the abbreviation $F_{\mu\nu} \equiv F_{\mu\nu}^a T^a$ for the field strength tensor defined in eq. (2.8) has been introduced. Using the relation between the field strength tensor and the covariant derivative, given by

$$[D_\mu, D_\nu] = -ig_s F_{\mu\nu}^a T^a\,, \tag{3.75}$$

and expanding the covariant derivatives to leading power as given in eq. (3.72), the kinetic term for a collinear gluon field arises as

$$\mathcal{L}_{ng,\text{kin}} = \frac{1}{2g_s^2}\,\text{Tr}\big[[iD_n^\mu, iD_n^\nu]^2\big]\,. \tag{3.76}$$

To complete the Lagrangian for the collinear gauge field, the gauge-fixing term and the ghost term, given by

$$\mathcal{L}_{\text{gauge-fix}} = -\frac{1}{2\zeta}(\partial^\mu A_\mu^a)^2 \qquad \text{and} \qquad \mathcal{L}_{\text{ghost}} = -\bar{c}^a(\partial^\mu D_\mu^{ab})c^b\,, \tag{3.77}$$

have to be considered as well [78]. Both of these pieces involve partial derivatives, which are partial derivatives with respect to the position variable conjugate to the full momentum. In order to exclusively derive the collinear gluon Lagrangian without fixing the gauge of ultrasoft gluons, these partial derivatives must by replaced by

$$i\partial^\mu \longrightarrow i\mathcal{D}_{us}^\mu \equiv \frac{\bar{n}^\mu}{2}(i\partial_r^+ + g_s A_{us}^+) + \frac{n^\mu}{2}\mathcal{P}^- + \mathcal{P}_\perp^\mu\,, \tag{3.78}$$

which is equal to the full covariant derivative in eq. (3.72) after removing the collinear gluon fields. This definition slightly adjusts the partial derivatives so that they become covariant with respect to the ultrasoft gluon field, but are still partial derivatives with respect to the collinear gluon field. The collinear gluon Lagrangian at leading power in SCET$_\text{I}$ then reads

$$\mathcal{L}_{ng}^{(0)} = \frac{1}{2g_s^2}\,\text{Tr}\big[[iD_n^\mu, iD_n^\nu]^2\big] + \frac{1}{\zeta}\,\text{Tr}\big[[i\mathcal{D}_{us}^\mu, A_{n\mu}]^2\big] + 2\,\text{Tr}\big[\bar{c}_n[i\mathcal{D}_{us}^\mu, [iD_{n\mu}, c_n]]\big]\,. \tag{3.79}$$

3.4.6 Feynman rules

The combined SCET$_\text{I}$ Lagrangian contains a copy of the collinear quark and gluon Lagrangians from eqs. (3.73) and (3.79) for each distinct collinear direction and is further supplemented with an ultrasoft Lagrangian

$$\mathcal{L}^{(0)}_{\text{SCET}_\text{I}} = \sum_n \big[\mathcal{L}^{(0)}_{n\xi} + \mathcal{L}^{(0)}_{ng}\big] + \mathcal{L}^{(0)}_{us}\,. \tag{3.80}$$

The ultrasoft Lagrangian is a copy of the massless QCD Lagrangian involving ultrasoft fields

$$\mathcal{L}^{(0)}_{us} = \bar\psi_{us}\,i\slashed{D}_{us}\psi_{us} - \frac{1}{4}(F^a_{us,\mu\nu})^2 - \frac{1}{2\zeta_{us}}(\partial^\mu A^a_{us,\mu})^2 - \bar c^a_{us}(\partial^\mu D^{ab}_{us,\mu})c^b_{us}\,, \tag{3.81}$$

where $\zeta_{us} \neq \zeta$, the field strength tensor $F^a_{us,\mu\nu}$ is understood to contain ultrasoft gauge fields and the ultrasoft full covariant derivative is defined as

$$D^\mu_{us} = \partial^\mu - ig_s A^\mu_{us}\,, \tag{3.82}$$

and is not to be confused with the expanded $\mathcal{D}^\mu_{us}$. Since the ultrasoft Lagrangian mimics the full QCD Lagrangian, the Feynman rules for soft degrees of freedom are identical to the Feynman rules in full QCD.

The Feynman rules for collinear quarks can be read off from the Lagrangian after plugging in the definitions of the covariant derivatives and only keeping terms up to first order in the coupling constant

$$\mathcal{L}^{(0)}_{n\xi} = e^{-i\mathcal{P}\cdot x}\,\bar\xi_n\Big[i\partial^+_r + \slashed{\mathcal{P}}_\perp\frac{1}{\mathcal{P}^-}\slashed{\mathcal{P}}_\perp + g_s\Big(A^+_{us} + A^+_n + \slashed{\mathcal{P}}_\perp\frac{1}{\mathcal{P}^-}\slashed{A}_{n\perp}$$
$$- \slashed{\mathcal{P}}_\perp\frac{A^-_n}{(\mathcal{P}^-)^2}\slashed{\mathcal{P}}_\perp + \slashed{A}_{n\perp}\frac{1}{\mathcal{P}^-}\slashed{\mathcal{P}}_\perp\Big) + \mathcal{O}(g_s^2)\Big]\frac{\slashed{\bar n}}{2}\xi_n\,, \tag{3.83}$$

where the expansion

$$\frac{1}{iD^-_n} = \frac{1}{\mathcal{P}^-} - g_s\frac{A^-_n}{(\mathcal{P}^-)^2} + \mathcal{O}(g_s^2)\,, \tag{3.84}$$

has been used. After using the identifications $i\partial^\mu_r \to p^\mu_r$ and $\mathcal{P}^\mu \to p^\mu_\ell$, the terms of $\mathcal{O}(g_s^0)$ determine the 2-point correlation function of the collinear quark field in momentum space. The Feynman rule for the n-collinear quark propagator is then found to be
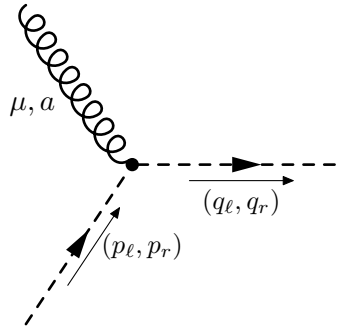
$$\underset{(p_\ell,\,p_r)}{\text{- - - -}\blacktriangleright\text{- - - -}} \quad = \quad \frac{i\slashed{\bar n}}{2}\frac{p^-_\ell}{p^+_r p^-_\ell + p^2_{\ell\perp} + i\epsilon}\,, \tag{3.85}$$

where the convention that collinear quarks will be denoted by dashed lines has been adopted. The same result can be obtained directly from the massless quark propagator in QCD, $i\not{p}/(p^2 + i\epsilon)$, by switching to lightcone coordinates and expanding the momentum to leading power as

$$\not{p} = \frac{\not{n}}{2}p_\ell^- + \mathcal{O}(\lambda) \qquad \text{and} \qquad p^2 = p_r^+ p_\ell^- + p_{\ell\perp}^2\,, \qquad (3.86)$$

where the plus components have been identified as residual momenta, since label momenta do not have a plus component, and the minus and perpendicular components as label momenta, since they are parametrically larger than their residual counterparts.

The first term of $\mathcal{O}(g_s)$ in eq. (3.83) describes the interaction between collinear quarks and ultrasoft gluons, which can be seen to lead to the Feynman rule
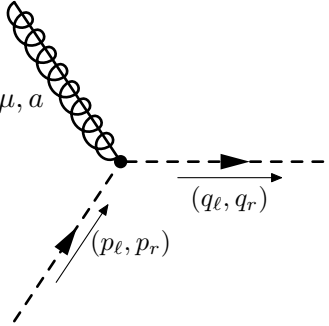
$$= \quad ig_s T^a n^\mu \frac{\not{\bar{n}}}{2}\,. \qquad (3.87)$$

The other four terms of $\mathcal{O}(g_s)$ give rise to an interaction between the collinear quark field and a collinear gluon. By explicitly decomposing the gluon field into lightcone components, it can be factored out to yield the interaction term

$$I_c = e^{-i\mathcal{P}\cdot x}\,\bar{\xi}_n\,g_s A_{n,\mu}\Big(n^\mu + \not{\mathcal{P}}_\perp \frac{1}{\mathcal{P}^-}\gamma_\perp^\mu - \not{\mathcal{P}}_\perp \frac{\bar{n}^\mu}{(\mathcal{P}^-)^2}\not{\mathcal{P}}_\perp + \gamma_\perp^\mu \frac{1}{\mathcal{P}^-}\not{\mathcal{P}}_\perp\Big)\frac{\not{\bar{n}}}{2}\xi_n\,. \qquad (3.88)$$

The collinear quark fields ξ_n and $\bar{\xi}_n$ will in general carry different label momenta. Calling these p_ℓ and q_ℓ respectively and acting with the label operators on the corresponding fields then yields the Feynman rule given by

$$= \; ig_s T^a \Big(n^\mu + \frac{\slashed{q}_{\ell\perp}\gamma_\perp^\mu}{q_\ell^-} + \frac{\gamma_\perp^\mu \slashed{p}_{\ell\perp}}{p_\ell^-}$$
$$- \frac{\slashed{q}_{\ell\perp}\slashed{p}_{\ell\perp}}{q_\ell^- \, p_\ell^-}\bar{n}^\mu \Big)\frac{\slashed{\bar{n}}}{2} \,, \quad (3.89)$$

where the collinear gluon is depicted by an ordinary gluon line crossed by a straight line. If the expansion in eq. (3.83) were to be continued to $\mathcal{O}(g_s^2)$, one additional interaction term would arise, leading to a Feynman rule for the 4-point interaction between two collinear gluons and two collinear quarks.

3.5 Gauge symmetry in SCET$_I$

The scaling of the allowed gauge transformations in SCET$_I$ can be either collinear or ultrasoft, leading to two distinct types of transformations for each ultrasoft and collinear quark and gluon field. As currents in SCET$_I$ are in general not invariant under collinear gauge transformations, the inclusion of a Wilson line containing collinear gluons is required to ensure gauge-invariance. An additional reason for the necessity of this Wilson line is the fact that it takes an arbitrary number of unsuppressed interactions between collinear gluons and quarks into account.

3.5.1 Collinear and ultrasoft gauge transformations

Under a general local gauge transformation in QCD, as given in eq. (2.2), the collinear quark fields transform as

$$\xi_{n,p_\ell} \longrightarrow \mathcal{U}(x)\,\xi_{n,p_\ell} \qquad \text{and} \qquad \bar{\xi}_{n,p_\ell} \longrightarrow \bar{\xi}_{n,p_\ell}\,\mathcal{U}^\dagger(x)\,, \qquad (3.90)$$

where the definition $\mathcal{U}(x) \equiv \exp[i\phi^a(x)T^a]$ has been introduced. Under this transformation, the first term in the collinear quark Lagrangian from eq. (3.83), involving the (residual) partial derivative, transforms into

$$e^{-i\mathcal{P}\cdot x}\,\bar{\xi}_n\,\mathcal{U}^\dagger(x)\,i\partial_r^+ \frac{\slashed{\bar{n}}}{2}\mathcal{U}(x)\,\xi_n = e^{-i\mathcal{P}\cdot x}\,\bar{\xi}_n\big(i\partial_r^+ - \partial_r^+[\phi^a(x)T^a]\big)\frac{\slashed{\bar{n}}}{2}\xi_n\,, \quad (3.91)$$

where the derivative in the second term should be understood to only act upon the terms within square brackets. The arbitrary function $\phi^a(x)$ can in principle be of $\mathcal{O}(\lambda^0)$, which would spoil the gauge invariance. To avoid this from happening, the allowed gauge transformations in SCET_I are limited to collinear and ultrasoft gauge transformations, denoted by $\hat{\mathcal{U}}_n(x)$ and $\mathcal{U}_{us}(x)$ respectively, which scale as

$$
\begin{aligned}
i\partial^\mu \hat{\mathcal{U}}_n(x) &\sim Q(\lambda^2, 1, \lambda)\, \hat{\mathcal{U}}_n(x)\,, \\
i\partial^\mu \mathcal{U}_{us}(x) &\sim Q(\lambda^2, \lambda^2, \lambda^2)\, \mathcal{U}_{us}(x)\,.
\end{aligned}
\tag{3.92}
$$

The collinear gauge transformation can be Fourier transformed to momentum space, decomposed into label and residual momenta and then Fourier transformed back in only the residual momentum in complete analogy with the collinear quark field in eq. (3.55), leading to [76–78]

$$
\hat{\mathcal{U}}_n(x) \equiv e^{-i\mathcal{P}\cdot x}\, \mathcal{U}_n(x) \equiv e^{-i\mathcal{P}\cdot x} \sum_{p_\ell \neq 0} \mathcal{U}_{n,p_\ell}(x)\,,
\tag{3.93}
$$

where x now only refers to the position conjugate to the residual momentum and will often be suppressed from here on. Although the local gauge transformations in eq. (3.90) are expressed in position space, the collinear gauge transformations involve the label momentum, which is not transformed back to position space. The multiplicative nature of the gauge transformations in position space would turn into a convolution in momentum space for continuous momenta. Since the label momenta are discrete, this convolution involves a sum rather than an integral, leading to

$$
\xi_n \longrightarrow \mathcal{U}_n \xi_n = \sum_{q_\ell \neq 0} \mathcal{U}_{n,p_\ell - q_\ell}\, \xi_{n,q_\ell} \equiv \mathcal{U}_{n,p_\ell - q_\ell}\, \xi_{n,q_\ell}\,,
\tag{3.94}
$$

as the transformation of the collinear gauge transformation from position space to label momentum space. In the final step, the convention that repeated label momenta are to be summed over has been introduced.

From the gauge transformation of the gluon field in QCD, given by

$$
A^\mu \longrightarrow \mathcal{U}\Big[A^\mu + \frac{i}{g_s}\partial^\mu\Big]\mathcal{U}^\dagger\,,
\tag{3.95}
$$

the collinear transformation of the collinear gauge field A_n^μ in SCET_I can be obtained by replacing $\partial^\mu \to \mathcal{D}_{us}^\mu$, as described in eq. (3.78), and restricting the collinear transformations to $\mathcal{U}_n$. Employing the same notation for discrete convolutions in the label momentum then leads to

$$
A_n^\mu \longrightarrow \mathcal{U}_{n,p_\ell - q_\ell}\Big[A_{n,q_\ell - k_\ell}^\mu + \frac{i}{g_s}\delta_{q_\ell, k_\ell}\mathcal{D}_{us}^\mu\Big]\mathcal{U}_{n,k_\ell}^\dagger\,,
\tag{3.96}
$$

where δ_{q_ℓ,k_ℓ} is the Kronecker delta forcing the two label momenta to be equal. The cumbersome notation for these discrete convolutions can be made more intuitive by defining the collinear gauge transformation matrix $\mathbb{U}_n(x)$ in label momentum space through its entries as

$$\mathbb{U}_n(x)_{p_\ell,q_\ell} \equiv \mathcal{U}_{n,p_\ell-q_\ell}(x)\,, \tag{3.97}$$

where p_ℓ and q_ℓ denote the row and column of the matrix respectively. In this notation the collinear quark field is regarded as a vector in label momentum space and the set of collinear gauge transformations of all the fields in SCET$_\mathrm{I}$ is given by

$$\xi_n(x) \xrightarrow{\ \mathcal{U}_n\ } \mathbb{U}_n(x)\,\xi_n(x)\,,$$

$$\psi_{us}(x) \xrightarrow{\ \mathcal{U}_n\ } \psi_{us}(x)\,,$$

$$A_n^\mu(x) \xrightarrow{\ \mathcal{U}_n\ } \mathbb{U}_n(x)\Big(A_n^\mu(x) + \frac{i}{g_s}\mathcal{D}_{us}^\mu\Big)\mathbb{U}_n^\dagger(x)\,,$$

$$A_{us}^\mu(x) \xrightarrow{\ \mathcal{U}_n\ } A_{us}^\mu(x)\,. \tag{3.98}$$

The ultrasoft gauge transformations involve only the position variables conjugate to the residual momenta, so they are analogous to the gauge transformations in QCD. As every field in SCET$_\mathrm{I}$ has a dependence on residual momenta, each field transforms under ultrasoft gauge transformations. The complete set of ultrasoft gauge transformations is given by

$$\xi_n(x) \xrightarrow{\ \mathcal{U}_{us}\ } \mathcal{U}_{us}(x)\,\xi_n(x)\,,$$

$$\psi_{us}(x) \xrightarrow{\ \mathcal{U}_{us}\ } \mathcal{U}_{us}(x)\,\psi_{us}(x)\,,$$

$$A_n^\mu(x) \xrightarrow{\ \mathcal{U}_{us}\ } \mathcal{U}_{us}(x)\,A_n^\mu(x)\,\mathcal{U}_{us}^\dagger(x)\,,$$

$$A_{us}^\mu(x) \xrightarrow{\ \mathcal{U}_{us}\ } \mathcal{U}_{us}(x)\Big(A_{us}^\mu(x) + \frac{i}{g}\partial_r^\mu\Big)\mathcal{U}_{us}^\dagger(x)\,. \tag{3.99}$$

The absence of a term involving the partial derivative in the transformation of the collinear gluon field reflects the fact that the ultrasoft fields describe physics at long distances, while the collinear fields correspond to smaller distances [78].

3.5.2 The collinear Wilson line

To study the consequences of the collinear gauge transformations, the proces in which a quark with flavor q' turns into a quark with flavor q may be considered.
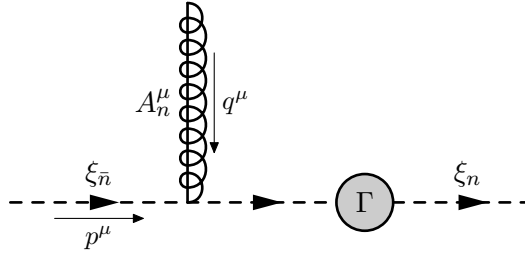
Figure 3.6 A single collinear gluon interacting with the incoming quark in the quark-to-quark current.

In full QCD, the current corresponding to this proces is given by

$$J_{qq'}^{\text{QCD},\mu} = \bar{\psi}_q \, \Gamma_i^{\mu} \, \psi_{q'} \,, \tag{3.100}$$

where $i = V, A$ refers to either a vector or an axial-vector coupling. By considering the situation in which the incoming quark is $\bar{n}$-collinear and the outgoing quark n-collinear, the corresponding SCET current is given by

 $\qquad \longrightarrow \qquad J_{qq',0}^{\mu} = \bar{\xi}_{q,n} \, \Gamma_i^{\mu} \, \xi_{q',\bar{n}} \,, \tag{3.101}$

where the shaded blob signifies the transition from the quark q' to the quark q. The corresponding subscripts q' and q on the collinear quark fields will be dropped from here on. Under ultrasoft gauge transformations, both fields transform in a similar way, so that the current is left invariant. The $\bar{n}$-collinear quark field is invariant under n-collinear gauge transformations, but the n-collinear quark field transforms according to eq. (3.98). Since an analogous reasoning holds for $\bar{n}$-collinear gauge transformations, the current as a whole does not appear to be invariant under collinear gauge transformations.

Apart from the apparent gauge-dependence of (for example) the quark-to-quark current, there is another issue with the current description of the fields in SCET. Consider adding an additional n-collinear gluon to the $\bar{n}$-collinear quark in the quark-to-quark current, leading to the diagram in fig. 3.6 and the current

$$J_{qq',1}^{\mu} = -g_s \bar{\xi}_n \, \Gamma_i^{\mu} \frac{\bar{\slashed{n}}}{2} \frac{p^+ + q^+}{(p^+ + q^+)(p^- + q^-) + (p_\perp + q_\perp)^2} A_n^- \frac{\slashed{n}}{2} \xi_{\bar{n}} \,. \tag{3.102}$$
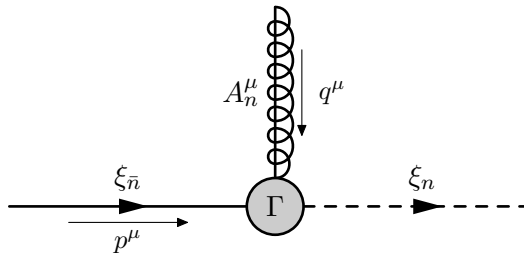
Figure 3.7 The correction to the quark-to-quark current by a single n-collinear gluon. The quark propagator from fig. 3.6 has been integrated out, moving the collinear gluon into an effective operator.

Keeping the terms of leading power in λ than yields

$$J^\mu_{qq',1} = \bar{\xi}_n \left[\frac{-g_s A^-_n}{q^-} \right] \Gamma^\mu_i \, \xi_{\bar{n}} \, . \tag{3.103}$$

The internal propagator has been integrated out and at leading power the addition of a collinear gluon to the quark-to-quark current can be described by an effective operator as shown in fig. 3.7. As the additional gluon in fig. 3.6 is n-collinear, its minus component appearing in eq. (3.103) is not suppressed and this diagram has to be taken into account already at leading power in λ. This observation can be extended to an arbitrary number of n-collinear gluons so that all diagrams involving all possible numbers of additional n-collinear gluons have to be taken into account. A general diagram of this sort, involving m additional n-collinear gluons, is shown in fig. 3.8. Iteratively using the result for the addition of a single gluon and summing over all permutations then leads to the quark-to-quark current in SCET [76]

$$J^\mu_{qq',m} = \bar{\xi}_n \left[\sum_\text{perms} \frac{(-g_s)^m}{m!} \frac{A^{a_1,-}_n A^{a_2,-}_n \ldots A^{a_m,-}_n}{(q^-_1)(q^-_1 + q^-_2) \ldots (\sum^m_{i=1} q^-_i)} T^{a_m} \ldots T^{a_2} T^{a_1} \right] \Gamma^\mu_i \, \xi_{\bar{n}} \, . \tag{3.104}$$

The position conjugate to the residual momentum, although suppressed in the notation, is the same for each field, reflecting the locality of an effective operator analogous to fig. 3.7, but with m gluons entering the vertex. The addition of any possible number of n-collinear gluons to the quark-to-quark current is then obtained by summing this expression over all possible m

$$J^\mu_{qq'} = \sum^\infty_{m=0} J^\mu_{qq',m} \equiv \bar{\xi}_n \, W_n \, \Gamma^\mu_i \, \xi_{\bar{n}} \, , \tag{3.105}$$
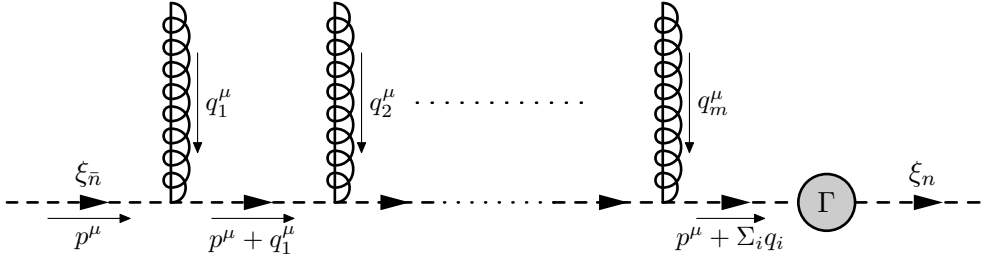
Figure 3.8 The quark-to-quark current with m additional n-collinear gluons attached to the incoming $\bar{n}$-collinear quark.

where the collinear Wilson line W_n in momentum space has been defined as

$$W_n \equiv \sum_{\text{perms}} \sum_{m=0}^{\infty} \sum_{q_1,\dots,q_m} \frac{(-g_s)^m}{m!} \frac{A_{n,q_1}^{a_1,-} A_{n,q_2}^{a_2,-} \dots A_{n,q_m}^{a_m,-}}{(q_1^-)(q_1^- + q_2^-)\dots(\sum_{i=1}^{m} q_i^-)} T^{a_m}\dots T^{a_2} T^{a_1} . \tag{3.106}$$

Here the sum over the label momenta of the gluon fields has been made explicit. Writing out the first few terms of the sum over m explicitly gives

$$W_n = \sum_{\text{perms}} \left[1 + \sum_{q_1} \frac{(-g_s)}{1!} \frac{1}{q_1^-} A_{n,q_1}^{-} \right.$$
$$\left. + \sum_{q_1,q_2} \frac{(-g_s)^2}{2!} \frac{1}{(q_1^- + q_2^-)} A_{n,q_2}^{-} \frac{1}{(q_1^-)} A_{n,q_1}^{-} + \dots \right], \tag{3.107}$$

so that each term is obtained by multiplying the previous term from the left by the gluon field and the momentum in the denominator from the next order in m. The momenta in the denominator of each term can be replaced by the label operator, which then acts on each field to its right. This then allows the Wilson line in (label) momentum space to be written as [76, 77]

$$W_n = \sum_{\text{perms}} \exp\left[-g_s \frac{1}{\mathcal{P}^-} A_n^{-} \right]. \tag{3.108}$$

All additions of all possible numbers of n-collinear gluons to the incoming $\bar{n}$-collinear quark field in the quark-to-quark current can thus be replaced by the insertion of a single n-collinear Wilson line. By the same reasoning all additions of $\bar{n}$-collinear gluons to the n-collinear quark can be taken into account through an $\bar{n}$-collinear Wilson line. In addition to accounting for an arbitrary number of unsuppressed collinear gluon attachments, the collinear Wilson line also serves to restore gauge invariance, which will be the topic of the next section. The

interaction between n-collinear gluons and n-collinear quarks (and between $\bar{n}$-collinear gluons and $\bar{n}$-collinear quarks) is already present in the Lagrangian in eq. (3.73) and does not require a treatment analogous to the one presented in this section.

3.5.3 Collinear gauge invariance

In (label) momentum space, the collinear Wilson line can be defined through the equation

$$0 = iD_n^- \, W_n = (\mathcal{P}^- + g_s A_n^-)\, W_n \,. \tag{3.109}$$

The action of the minus component of the collinear covariant derivative on the collinear Wilson line in combination with any other operators can be determined from this definition, leading to the identity

$$iD_n^- \, W_n = W_n \, \mathcal{P}^- \,. \tag{3.110}$$

The fact that the collinear Wilson line is a unitary operator then allows the label operator and its inverse to be written as

$$\mathcal{P}^- = W_n^\dagger \, iD_n^- \, W_n \qquad \text{and} \qquad \frac{1}{\mathcal{P}^-} = W_n^\dagger \, \frac{1}{iD_n^-} \, W_n \,. \tag{3.111}$$

The collinear Wilson line exclusively contains collinear gluon fields that transform under ultrasoft gauge transformations as given in eq. (3.99) so that the $\mathcal{U}_{us}$ and $\mathcal{U}_{us}^\dagger$ will cancel each other in between each pair of gluon fields, leading to an ultrasoft gauge transformation of the collinear Wilson line given by

$$W_n \xrightarrow{\;\mathcal{U}_{us}\;} \mathcal{U}_{us} \, W_n \, \mathcal{U}_{us}^\dagger \,, \tag{3.112}$$

mirroring the transformation of a single collinear gluon field.

The behavior of the minus component of the collinear gluon field under a collinear gauge transformation can be determined from eq. (3.98) and is explicitly given by

$$A_n^- \xrightarrow{\;\mathcal{U}_n\;} \mathbb{U}_n \left(A_n^- + \frac{1}{g_s} \mathcal{P}^- \right) \mathbb{U}_n^\dagger \,, \tag{3.113}$$

where the minus component of the ultrasoft covariant derivative defined in eq. (3.78) has been plugged in. Writing the transformation of the collinear Wilson line symbolically as $W_n \to W_n'$, its definition in eq. (3.109) transforms under a general collinear gauge transformation as

$$0 = iD_n^- \, W_n \;\longrightarrow\; \left(\mathbb{U}_n \mathbb{U}_n^\dagger \mathcal{P}^- + g_s \mathbb{U}_n A_n^- \mathbb{U}_n^\dagger + \mathbb{U}_n \mathcal{P}^- [\mathbb{U}_n^\dagger] \right) W_n' \,, \tag{3.114}$$

where the label operator in the final term is understood to only act upon the matrix in square brackets. Using the product rule for the label operator, the first and third term can be combined and lead to the transformation

$$0 = i D_n^- W_n \longrightarrow \mathbb{U}_n \left(\mathcal{P}^- + g_s A_n^- \right) \mathbb{U}_n^\dagger W_n' \,. \tag{3.115}$$

To satisfy this equation, the collinear Wilson line has to transform as

$$W_n \xrightarrow{\;\mathcal{U}_n\;} \mathbb{U}_n \, W_n \,, \tag{3.116}$$

under collinear gauge transformations. This transformation of the collinear Wilson line, which was included in the quark-to-quark current in eq. (3.105) in order to take all possible additions of all possible numbers of collinear gluons into account, then leaves the quark-to-quark current invariant under collinear gauge transformations. Accompanying collinear quark fields by a collinear Wilson line will in general ensure the invariance of all currents in SCET under collinear gauge transformations.

3.5.4 Reparametrization invariance

By making an explicit choice for the light-like vectors n^μ and $\bar{n}^\mu$ in eq. (3.9), the original Lorentz symmetry was broken. There are three possible transformations under which these explicit light-like vectors still obey their defining properties from eq. (3.8), given by [80, 89]

$$
\begin{aligned}
\text{I:} \quad & n^\mu \xrightarrow{\;\text{I}\;} n^\mu + r_\perp^\mu \quad \text{and} \quad \bar{n}^\mu \xrightarrow{\;\text{I}\;} \bar{n}^\mu \,, \\
\text{II:} \quad & n^\mu \xrightarrow{\;\text{II}\;} n^\mu \qquad\quad \text{and} \quad \bar{n}^\mu \xrightarrow{\;\text{II}\;} \bar{n}^\mu + \bar{r}_\perp^\mu \,, \\
\text{III:} \quad & n^\mu \xrightarrow{\;\text{III}\;} e^s \, n^\mu \qquad \text{and} \quad \bar{n}^\mu \xrightarrow{\;\text{III}\;} e^{-s} \, \bar{n}^\mu \,,
\end{aligned}
\tag{3.117}
$$

where the displacement vectors $r_\perp^\mu$ and $\bar{r}_\perp^\mu$ are perpendicular to both n^μ and $\bar{n}^\mu$. By multiplying the light-like vectors by an n-collinear momentum, transforming the product according to these three reparametrization transformations and demanding that the transformed expressions respect the n-collinear scaling $Q(\lambda^2, 1, \lambda)$ leads to the definite parametric scaling

$$r_\perp^\mu \sim \lambda \,, \qquad \bar{r}_\perp^\mu \sim 1 \qquad \text{and} \qquad s \sim 1 \,. \tag{3.118}$$

This means that for an n-collinear momentum only the displacement vector $r_\perp^\mu$ is restricted. Demanding that an arbitrary n-collinear momentum p_n^μ remains invariant under these reparametrization transformations then leads to

the transformations of the perpendicular component

$$
\begin{aligned}
\text{I:} \quad & p^\mu_{n\perp} \xrightarrow{\ \text{I}\ } p^\mu_{n\perp} - \frac{r^\mu_\perp}{2} p^-_n - \frac{\bar{n}^\mu}{2}(r_\perp \cdot p_{n\perp})\,, \\
\text{II:} \quad & p^\mu_{n\perp} \xrightarrow{\ \text{II}\ } p^\mu_{n\perp} - \frac{\bar{r}^\mu_\perp}{2} p^+_n - \frac{n^\mu}{2}(\bar{r}_\perp \cdot p_{n\perp})\,, \\
\text{III:} \quad & p^\mu_{n\perp} \xrightarrow{\ \text{III}\ } p^\mu_{n\perp}\,.
\end{aligned}
\tag{3.119}
$$

The SCET$_\text{I}$ Lagrangian is unique by power counting, gauge invariance and reparametrization inveriance (RPI), as can be shown by applying these general transformations to each term in the Lagrangian. Physically, transformation (I) corresponds to a (small) change in the direction of n^μ, which leaves the n-collinear momentum n-collinear. As the vector $\bar{n}^\mu$ acts only as an auxiliary vector in this case, transformation (II) can change its direction by a large amount. Transformation (III) can physically be interpreted as a boost in the $\hat{z}$-direction.

Another ambiguity was introduced by splitting the momentum in a label and a residual part in eq. (3.45). A small amount proportional to λ^2 may freely be shifted from the label momentum to the residual momentum or vice versa, as long as it has a vanishing plus component in order to preserve the power counting. This then describes a fourth reparametrization transformation as

$$
\mathcal{P}^\mu \xrightarrow{\ \text{IV}\ } \mathcal{P}^\mu + b^\mu \qquad \text{and} \qquad i\partial^\mu_r \xrightarrow{\ \text{IV}\ } i\partial^\mu_r - b^\mu\,,
\tag{3.120}
$$

with $b^+ \sim Q(0, \lambda^2, \lambda^2)$. The collinear quark field then transforms accordingly as

$$
(\mathcal{P}^\mu + i\partial^\mu_r)\,\xi_{n,p_\ell} \xrightarrow{\ \text{IV}\ } (\mathcal{P}^\mu + i\partial^\mu_r)\,e^{ib\cdot x}\,\xi_{n,p_\ell+b}\,.
\tag{3.121}
$$

Although the label operator and the residual partial derivative scale differently, they are tied together through this transformation so that the combined operator $\mathcal{P}^\mu + i\partial^\mu_r$ connects different orders in λ to one another. As the (full) partial derivative was identified by this combination in eq. (3.69), it makes sense to gauge the label operator and residual partial derivative as a combined operator. Since $\mathcal{P}^+ = 0$, the plus component of this combination can simply be gauged as

$$
[\mathcal{P}^+ + i\partial^+_r] \longrightarrow iD^+ = i\partial^+_r + g_s A^+_n + g_s A^+_{us}\,,
\tag{3.122}
$$

where the covariant derivative was given in eq. (3.70). To gauge the minus and perpendicular components, it is necessary to inspect the behavior of the various

covariant derivatives under gauge transformations. Collinear gauge transformations of the covariant derivatives can be read off from the transformations of the gluon fields and read

$$iD_n^- \xrightarrow{\mathcal{U}_n} \mathbb{U}_n \, iD_n^- \, \mathbb{U}_n^\dagger \,,$$

$$iD_{n\perp}^\mu \xrightarrow{\mathcal{U}_n} \mathbb{U}_n \, iD_{n\perp}^\mu \, \mathbb{U}_n^\dagger \,,$$

$$iD^+ \xrightarrow{\mathcal{U}_n} \mathbb{U}_n \, iD^+ \, \mathbb{U}_n^\dagger \,,$$

$$iD_{us}^\mu \xrightarrow{\mathcal{U}_n} iD_{us}^\mu \,. \tag{3.123}$$

Their transformations under ultrasoft gauge transformations can be found in a similar way and are given by

$$iD_n^- \xrightarrow{\mathcal{U}_{us}} \mathcal{U}_{us} \, iD_n^- \, \mathcal{U}_{us}^\dagger \,,$$

$$iD_{n\perp}^\mu \xrightarrow{\mathcal{U}_{us}} \mathcal{U}_{us} \, iD_{n\perp}^\mu \, \mathcal{U}_{us}^\dagger \,,$$

$$iD^+ \xrightarrow{\mathcal{U}_{us}} \mathcal{U}_{us} \, iD^+ \, \mathcal{U}_{us}^\dagger \,,$$

$$iD_{us}^\mu \xrightarrow{\mathcal{U}_{us}} \mathcal{U}_{us} \, iD_{us}^\mu \, \mathcal{U}_{us}^\dagger \,. \tag{3.124}$$

Simply identifying the label operator with iD_n^μ and the residual derivative with iD_{us}^μ does not work since they transform differently under collinear gauge transformations. This can be remedied by using the collinear Wilson line and its transformation properties so that the combined label operator and residual partial derivative can be gauged uniquely by [80, 89]

$$[\mathcal{P}^- + i\partial_r^-] \longrightarrow iD^- \equiv iD_n^- + W_n \, iD_{us}^- \, W_n^\dagger \,,$$

$$[\mathcal{P}_\perp^\mu + i\partial_{r\perp}^\mu] \longrightarrow iD_\perp^\mu \equiv iD_{n\perp}^\mu + W_n \, iD_{us\perp}^\mu \, W_n^\dagger \,. \tag{3.125}$$

3.6 Ultrasoft-collinear factorization

The SCET$_\mathrm{I}$ collinear quark and gluon Lagrangians from eqs. (3.73) and (3.79) still contain ultrasoft fields through the occurrence of the covariant derivatives. The ultrasoft and collinear fields can be completely decoupled from one another through a convenient field redefinition. The interactions between both types of infrared degrees of freedom are then moved from the Lagrangian into the currents and external operators, which will describe the hard scattering. This separation of the soft and collinear quarks and gluons at the level of the Lagrangian enables the derivation of factorization theorems for numerous processes.
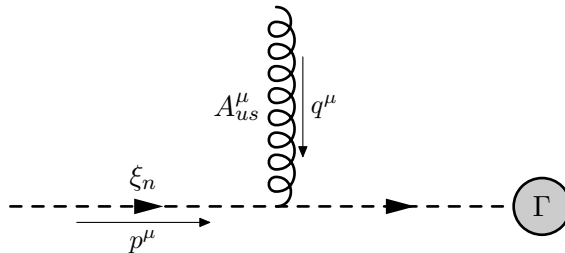
Figure 3.9 A single ultrasoft gluon interacting with an incoming collinear quark.

3.6.1 The ultrasoft Wilson line

The collinear Wilson line from eq. (3.108) incorporates all possible additions of collinear gluons to the SCET currents and restores the gauge invariance of these currents. The additions of ultrasoft gluons can be considered in a similar way by starting with the diagram in fig. 3.9, in which a single ultrasoft gluon is absorbed by a collinear quark that then enters the rest of the diagram, represented by Γ. The internal propagator of the collinear quark is given by eq. (3.85) and reads

$$\text{propagator} = \frac{i\slashed{n}}{2} \frac{p_\ell^-}{q_r^+ p_\ell^- + i\epsilon} \,, \tag{3.126}$$

where the fact that ultrasoft particles carry no label momentum and the on-shell condition for the external collinear quark have been used. The label momentum can be divided out, although depending on its sign this might change the sign of the $i\epsilon$. Using this expression and omitting the $i\epsilon$ for simplicity for the moment, the expression for the combined diagram can be obtained using the Feynman rule from eq. (3.87) and is given by

$$J_{c,1} = \Gamma\left[-g_s \frac{1}{q^+} A_{us}^+\right] \xi_n \,, \tag{3.127}$$

where the slashed light-like vectors have combined into a projection operator obeying $P_n \xi_n = \xi_n$ and the subscript on the residual momentum has been dropped since q^μ does not carry any label momentum.

Extending this to the addition of an arbitrary number of ultrasoft gluons, as shown in fig. 3.10, and correcting for all possible permutations then leads to
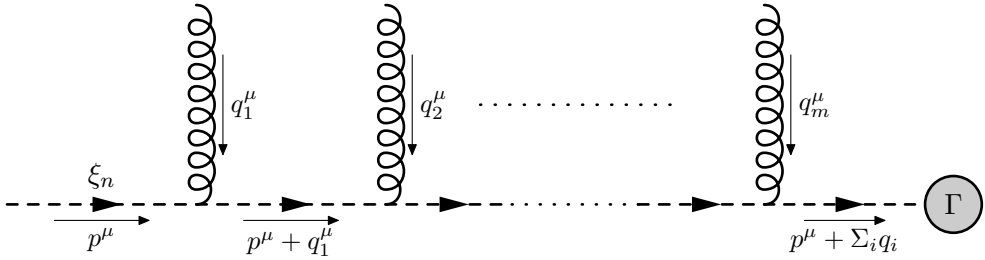
Figure 3.10 The addition of an arbitrary number of ultrasoft gluons to an external collinear quark.

the expression

$$
J_{c,m} = \Gamma \left[\sum_{\text{perms}} \frac{(-g_s)^m}{m!} \frac{A_{us}^{a_1,+}(q_1) A_{us}^{a_2,+}(q_2) \dots A_{us}^{a_m,+}(q_m)}{(q_1^+)(q_1^+ + q_2^+) \dots (\sum_{i=i}^m q_i^+)} T^{a_m} \dots T^{a_2} T^{a_1} \right] \xi_n \, .
$$
(3.128)

Adding all possible numbers of gluon additions and comparing to the result in eq. (3.106), an ultrasoft Wilson line [78] can be identified as

$$
Y_n \equiv \sum_{m=0}^{\infty} \sum_{\text{perms}} \frac{(-g_s)^m}{m!} \frac{A_{us}^{a_1,+}(q_1) A_{us}^{a_2,+}(q_2) \dots A_{us}^{a_m,+}(q_m)}{(q_1^+)(q_1^+ + q_2^+) \dots (\sum_{i=i}^m q_i^+)} T^{a_m} \dots T^{a_2} T^{a_1} \, ,
$$
(3.129)

in momentum space. For the collinear Wilson line W_n, the subscript n referred to the fact that n-collinear gluons were attached (to an $\bar{n}$-collinear quark), while here it refers to the collinear direction of the quark that the Wilson line follows. As the ultrasoft Wilson line exclusively involves residual momenta, which are Fourier transformed back to position space in the SCET framework, a position space expression for the Wilson line itself is natural as well and is given by

$$
\tilde{Y}_n(x) = \mathrm{P} \, \exp \left[i g_s \int_{-\infty}^{0} \mathrm{d}s \, A_{us}^{a,+}(x + sn) T^a \right] ,
$$
(3.130)

where the P denotes path ordering and the dependence on x has been made explicit for clarity. Making this dependence implicit again, the ultrasoft Wilson line in position space obeys the identities

$$
\tilde{Y}_n^\dagger \tilde{Y}_n = 1 \qquad \text{and} \qquad i D_{us}^+ \tilde{Y}_n = 0 \, .
$$
(3.131)

The Eikonal propagator in eq. (3.126), from which the structure of the ultrasoft Wilson line follows, will be slightly different for other types of external particles,

leading to slightly different Wilson lines. The complete set of ultrasoft Wilson lines in position space is given by

$$\tilde{Y}_{n+} = \mathrm{P} \exp\left[ig_s \int_{-\infty}^{0} \mathrm{d}s\, A_{us}^{+}(x+sn)\right] \qquad \text{for incoming quarks,}$$

$$\tilde{Y}_{n+}^{\dagger} = \mathrm{P} \exp\left[ig_s \int_{0}^{\infty} \mathrm{d}s\, A_{us}^{+}(x+sn)\right] \qquad \text{for outgoing quarks,}$$

$$\tilde{Y}_{n-}^{\dagger} = \bar{\mathrm{P}} \exp\left[-ig_s \int_{-\infty}^{0} \mathrm{d}s\, A_{us}^{+}(x+sn)\right] \qquad \text{for incoming antiquarks,}$$

$$\tilde{Y}_{n-} = \bar{\mathrm{P}} \exp\left[-ig_s \int_{0}^{\infty} \mathrm{d}s\, A_{us}^{+}(x+sn)\right] \qquad \text{for outgoing antiquarks,} \quad (3.132)$$

where $\bar{\mathrm{P}}$ denotes anti-path-ordering.

3.6.2 BPS field redefinitions

The fact that external collinear quarks will always be accompanied by an arbitrary amount of ultrasoft gluons motivates the redefinition [90, 91] of the collinear quark field as

$$\xi_{n,p_\ell} \longrightarrow \tilde{Y}_n\, \xi_{n,p_\ell}\,, \qquad (3.133)$$

so that the ultrasoft Wilson line is implicitly taken into account. A similar analysis can be done for external collinear gluons, leading to an ultrasoft Wilson line in the adjoint representation, $\tilde{Y}_{n,\mathrm{adj}}^{ab}$, which can be related to the ultrasoft Wilson line in the fundamental representation in eq. (3.130) by

$$\tilde{Y}_{n,\mathrm{adj}}^{ab} T^b = \tilde{Y}_n\, T^a\, \tilde{Y}_n^{\dagger}\,. \qquad (3.134)$$

From this, the complete set of redefinitions for the collinear fields, called the Bauer-Pirjol-Stewart (BPS) field redefinitions [78], is found to be

$$\begin{aligned}
\xi_{n,p_\ell} &\longrightarrow \tilde{Y}_n\, \xi_{n,p_\ell}\,, \\
A_{n,p_\ell}^{\mu} &\longrightarrow \tilde{Y}_n\, A_{n,p_\ell}^{\mu}\, \tilde{Y}_n^{\dagger}\,, \\
W_n &\longrightarrow \tilde{Y}_n\, W_n\, \tilde{Y}_n^{\dagger}\,, \\
c_{n,p_\ell} &\longrightarrow \tilde{Y}_n\, c_{n,p_\ell}\, \tilde{Y}_n^{\dagger}\,,
\end{aligned} \qquad (3.135)$$

where the transformation of the collinear Wilson line automatically follows from that of the collinear gluon field. The transformation of the ghost field will not be discussed but has been included for completeness.

Starting from the collinear quark Lagrangian from eq. (3.73), replacing the inverse covariant derivative using the identity in eq. (3.111) and plugging in the expressions for the remaining covariant derivatives leads to

$$
\mathcal{L}_{n\xi}^{(0)} = e^{-i\mathcal{P}\cdot x}\, \bar{\xi}_n \Big[iD_{us}^+ + g_s A_n^+ + (\mathcal{\slashed{P}}_\perp + g_s \slashed{A}_{n\perp}) W_n \frac{1}{\mathcal{P}^-} W_n^\dagger (\mathcal{\slashed{P}}_\perp + g_s \slashed{A}_{n\perp}) \Big] \frac{\slashed{\bar{n}}}{2} \xi_n \,,
$$
(3.136)

where $iD_n^+ = iD_{us}^+ + g_s A_n^+$ has been identified. Doing the BPS field redefinitions then introduces ultrasoft Wilson lines next to the collinear quark and gluon fields that mutually cancel trivially for all terms except the first, which involves the ultrasoft covariant derivative. The cancellation of the ultrasoft Wilson lines for this term can be obtained by using the defining equation from eq. (3.131) on on arbitrary operator, leading to the identity

$$
iD_{us}^+ \tilde{Y}_n = \tilde{Y}_n\, i\partial_r^+ \,,
$$
(3.137)

analogous to the one obtained for the collinear Wilson line in eq. (3.110). This equation can then be used to pull the ultrasoft Wilson line through the ultrasoft covariant derivative, after which it cancels against its conjugate from the other collinear quark field. The BPS field redefinitions then finally lead to the collinear quark Lagrangian

$$
\mathcal{L}_{n\xi}^{(0)} = e^{-i\mathcal{P}\cdot x}\, \bar{\xi}_n \Big[i\partial_r^+ + g_s A_n^+ + (\mathcal{\slashed{P}}_\perp + g_s \slashed{A}_{n\perp}) W_n \frac{1}{\mathcal{P}^-} W_n^\dagger (\mathcal{\slashed{P}}_\perp + g_s \slashed{A}_{n\perp}) \Big] \frac{\slashed{\bar{n}}}{2} \xi_n \,,
$$
(3.138)

where all ultrasoft gluons have been removed. The exact same exercise can be done for the collinear gluon Lagrangian, after which the ultrasoft gluons will have been completely decoupled from the collinear fields. Since any field redefinition has to be done for all occurring instances of the fields, this process of ultrasoft-collinear factorization effectively moves the ultrasoft gluons from the Lagrangian into the currents. The quark-to-quark current from eq. (3.105), for example, will change under the BPS field redefinitions into

$$
J_{qq'}^\mu \longrightarrow [\bar{\xi}_n W_n]\, [\tilde{Y}_n^\dagger \tilde{Y}_{\bar{n}}]\, \Gamma_i^\mu\, [W_{\bar{n}}^\dagger \xi_{\bar{n}}] \,.
$$
(3.139)

Here, the attachment of all possible numbers of collinear gluons to the quarks are represented by the collinear Wilson lines W_n and $W_{\bar{n}}$ and the attachment of all possible ultrasoft gluons to both the collinear quarks and the collinear Wilson lines are taken into account by the ultrasoft Wilson lines $\tilde{Y}_n$ and $\tilde{Y}_{\bar{n}}$.

3.7 Hard-collinear factorization

Since SCET is an effective theory that only describes the infrared dynamics of QCD, the effect of any hard interaction has to be included through a matching procedure. In contrast with EFTs such as the Fermi theory of weak interactions, where the matching equations are multiplicative, SCET is matched to QCD through a convolution between the Wilson coefficients and the effective operators or currents.

Since SCET is a quantum field theory in its own respect, it requires a regularization and renormalization procedure to deal with UV divergences. The renormalization of the Wilson coefficients matching SCET to QCD leads to a renormalization group equation whose solution relates Wilson coefficients at different energy scales to one another and allows for the resummation of Sudakov logarithms [92].

3.7.1 Wilson coefficients

Just as any other effective field theory, SCET has to be matched onto a full theory (QCD in this case) through Wilson coefficients that encode the dynamics of the high-energy degrees of freedom from QCD that are not described by SCET. In order for the large momenta $p^\mu \sim Q$ on which the Wilson coefficients will in general depend to be gauge invariant, they must come from combinations of fields that are invariant under collinear gauge transformations, e.g. from the combination $\xi_n W_n$. To accomplish this, the Wilson coefficient has to depend on the label operator, which is able to extract the combined large label momentum from products of fields. Including such a Wilson coefficient, which is now itself an operator instead of a number, for the quark-to-quark current (before doing the BPS field redefinition) then gives

$$
\begin{aligned}
J_{qq'}^\mu &= C_{qq'}(-\mathcal{P}_n^-, -\mathcal{P}_{\bar{n}}^-)\,[\bar{\xi}_n W_n]\,\Gamma_i^\mu\,[W_{\bar{n}}\xi_{\bar{n}}] \\
&= [\bar{\xi}_n W_n]\,C_{qq'}(\mathcal{P}_n^{\dagger-}, \mathcal{P}_{\bar{n}}^{\dagger-})\,\Gamma_i^\mu\,[W_{\bar{n}}\xi_{\bar{n}}]\,,
\end{aligned}
\tag{3.140}
$$

where the inclusion of the minus signs is conventional. The Wilson coefficient can be turned back into a number by introducing an integration over the new label momenta ω_n and $\omega_{\bar{n}}$ as

$$
J_{qq'}^\mu = \int \mathrm{d}\omega_n\,\mathrm{d}\omega_{\bar{n}}\,C_{qq'}(\omega_n, \omega_{\bar{n}})\,[\bar{\xi}_n W_n]\,\delta(\omega_n - \mathcal{P}_n^{\dagger-})\,\Gamma_i^\mu\,\delta(\omega_{\bar{n}} - \mathcal{P}_{\bar{n}}^{\dagger-})\,[W_{\bar{n}}\xi_{\bar{n}}]\,.
\tag{3.141}
$$

Defining the delta functions to be part of the operator as

$$
\mathcal{O}_{qq'}^\mu(\omega_n, \omega_{\bar{n}}) \equiv [\bar{\xi}_n W_n]\,\delta(\omega_n - \mathcal{P}_n^{\dagger-})\,\Gamma_i^\mu\,\delta(\omega_{\bar{n}} - \mathcal{P}_{\bar{n}}^{\dagger-})\,[W_{\bar{n}}\xi_{\bar{n}}]\,,
\tag{3.142}
$$

then leads to

$$J^\mu_{qq'} = \int \mathrm{d}\omega_n \, \mathrm{d}\omega_{\bar{n}} \, C_{qq'}(\omega_n, \omega_{\bar{n}}) \, \mathcal{O}^\mu_{qq'}(\omega_n, \omega_{\bar{n}}) \,, \qquad (3.143)$$

where the hard and collinear degrees of freedom have completely factorized. The hard-collinear factorization can be obtained for any SCET operator by using the fact that eq. (3.110) leads to the more general identity

$$(iD^-_n)^k = W_n \, (\mathcal{P}^-)^k \, W^\dagger_n \,, \qquad (3.144)$$

for integer k, so that a general function f can always be written as [77, 78]

$$f(iD^-_n) = W_n \, f(\mathcal{P}^-) \, W^\dagger_n = \int \mathrm{d}\omega \, f(\omega) \left[W_n \, \delta(\omega - \mathcal{P}^-) \, W^\dagger_n \right]. \qquad (3.145)$$

As ultrasoft Wilson lines do not carry any label momentum, they commute with the label operator so that the BPS field redefinitions can be done either before or after the hard-collinear factorization.

After including the Wilson coefficients to match the SCET currents to QCD, collinear quark fields are always accompanied by a collinear Wilson line and the delta function that picks out the large momentum piece of the field. This then motivates the definition of the quark jet field as [76, 77]

$$\chi_{n,\omega} \equiv [\delta(\omega - \mathcal{P}^-) \, \chi_n] \equiv [\delta(\omega - \mathcal{P}^-) \, W^\dagger_n \, \xi_n] \,, \qquad (3.146)$$

where the label operator is defined to act only within the square brackets. In a similar way the gluon jet field[9] can be defined as

$$\mathcal{B}^\mu_{n\perp,\omega} \equiv [\mathcal{B}^\mu_{n\perp} \delta(\omega - \mathcal{P}^{\dagger-})] \equiv \frac{1}{g_s} \left[\frac{1}{\mathcal{P}^-} W^\dagger_n [iD^-_n, iD^\mu_{n\perp}] W_n \, \delta(\omega - \mathcal{P}^{\dagger-}) \right], \quad (3.147)$$

where again the derivatives act only within the (outer) square brackets. The two degrees of freedom of this gluon jet field can be associated with the two physical gluon polarizations.

It can be shown that all other possible collinear operators can be reduced to combinations of these quark and gluon jet fields and the label operator $\mathcal{P}^\mu_{n\perp}$ to all orders in λ [89], so that the complete set of collinear building blocks in SCET is given by

$$\text{Collinear building blocks:} \quad \chi_{n,\omega} \,, \quad \mathcal{B}^\mu_{n\perp,\omega} \,, \quad \text{and} \quad \mathcal{P}^\mu_{n\perp} \,. \qquad (3.148)$$

This set is to be supplemented by the ultrasoft operators in order to fully describe all SCET processes.

---

[9]In SCET$_{\mathrm{II}}$, these quark and gluon jet fields are instead called quark and gluon parton fields.

3.7.2 Matching $e^+e^- \to$ dijets at one loop

Beyond tree-level, the procedure of matching SCET to QCD, i.e. determining the Wilson coefficients, will involve integrals over the unconstrained loop momenta. The division of the momentum into a label momentum and a residual piece changes these integrals according to eqs. (3.47) and (3.48), which need to be recombined into a single integral in order to handle loop integrals of the form

$$I_{\text{loop}} = \int \mathrm{d}^d p \, f(p) \,, \tag{3.149}$$

where f is a general function of the momentum p. For a collinear momentum p_n that has been split up according to the label formalism, this function will look like $f(p_r^+, p_\ell^-, p_{\ell\perp})$, and loop integrals in the label formalism are given by

$$
\begin{aligned}
I_{\text{loop}}^{\text{LF}} &= \sum_{p_\ell \neq 0} \int \mathrm{d}^d p_r \, f(p_r^+, p_\ell^-, p_{\ell\perp}) \\
&= \sum_{p_\ell} \int \mathrm{d}^d p_r \, f(p_r^+, p_\ell^-, p_{\ell\perp}) - \int \mathrm{d}^d p_r \, f^{(0)}(p_r^+, 0, 0) \,, \tag{3.150}
\end{aligned}
$$

where the final term is called a zero-bin subtraction and ensures that the (0,0)-box in the grid shown in fig. 3.5 is not counted twice [83]. Since only the plus component of the residual momentum appears in the integrand and the boxes in the grid refer to a particular minus and perpendicular momentum, the function $f(p_r^+, p_\ell^-, p_{\ell\perp})$ must be constant throughout each box. The residual momentum integral can thus be evaluated at any place in the box, which is accomplished by a shift in the label momenta

$$
\begin{aligned}
\sum_{p_\ell} \int \mathrm{d}^d p_r \, f(p_r^+, p_\ell^-, p_{\ell\perp}) &= \sum_{p_\ell} \int \mathrm{d}^d p_r \, f(p_r^+, p_\ell^- + p_r^-, p_{\ell\perp} + p_{r\perp}) \\
&= \int \mathrm{d}^d p \, f(p) \,, \tag{3.151}
\end{aligned}
$$

where the original splitting of the momentum as $p^\mu = p_\ell^\mu + p_r^\mu$ has effectively been reversed. The zero-bin subtraction term can be shifted in the same way so that a general loop integral is found to be equal to

$$I_{\text{loop}}^{\text{LF}} = \int \mathrm{d}^d p \left(f(p) - f^{(0)}(p) \right). \tag{3.152}$$

The zero-bin subtraction term is obtained from the function f by first changing the scaling of the label momenta to $\mathcal{O}(\lambda^2)$ (the scaling of the ultrasoft modes)

and then keeping only terms up to the same order as in the original loop integration, taking into account that the integration measures $d^d p$ and $d^d p_r$ scale differently.

The process $e^+ e^- \to$ dijets, shown in fig. 3.3, provides an ideal example to study the procedure of matching SCET to QCD in more detail. In this process, the incoming leptons form a virtual photon or Z boson that subsequently decays into a quark and an antiquark that both undergo a cascade of collinear splittings, forming two jets of particles, each collinear to a different direction. The QCD current of this process is given by

$$J_{q\bar{q}}^{\mathrm{QCD},\mu} = \bar{\psi}_q \, \Gamma_i^\mu \, \psi_{\bar{q}} \,, \tag{3.153}$$

where the $i = V, A$ again either refers to a vector or an axial-vector coupling. The SCET current is simply the quark-to-quark current for $q\bar{q}$ and was already given in eq. (3.141). In terms of the quark jet fields it reads[10]

$$J_{q\bar{q}}^\mu = \int \mathrm{d}\omega_n \, \mathrm{d}\omega_{\bar{n}} \, C_{q\bar{q}}(\omega_n, \omega_{\bar{n}}) \, \bar{\chi}_{n,\omega_n} \, \Gamma_i^\mu \, \chi_{\bar{n},\omega_{\bar{n}}} \,. \tag{3.154}$$

The integration structure can be simplified by using the fact that the vectors n^μ and $\bar{n}^\mu$ must occur with equal powers within each operator, which is a consequence of RPI-III from eq. (3.117). This then implicates that ω_n and $\omega_{\bar{n}}$ can never occur individually, as only their product respects RPI-III, so that the Wilson coefficient reduces to $C_{q\bar{q}}(\omega_n, \omega_{\bar{n}}) \to C_{q\bar{q}}(\omega_n \omega_{\bar{n}})$. A final simplification follows from momentum conservation, which forces both integration measures to be equal to the invariant mass of the incoming particles Q. The SCET current then reads

$$J_{q\bar{q}}^\mu = C_{q\bar{q}}(Q^2) \, \bar{\chi}_n \, \Gamma_i^\mu \, \chi_{\bar{n}} \,. \tag{3.155}$$

The large momenta on which the Wilson coefficients depend will in general always be constrained by external kinematics as long as the current contains at most one collinear building block for each distinct collinear direction.

The Wilson coefficients are determined by calculating diagrams up to some desired order in both QCD and SCET. These results should agree in the IR regime, while their UV behavior will be different. The SCET calculation will in general lead to additional UV divergences that need to be removed through

---

[10]Although $e^+ e^- \to$ dijets is described by a single current in both QCD and SCET, there might in general be more Dirac structures representing the current in SCET, each accompanied by its own Wilson coefficient.
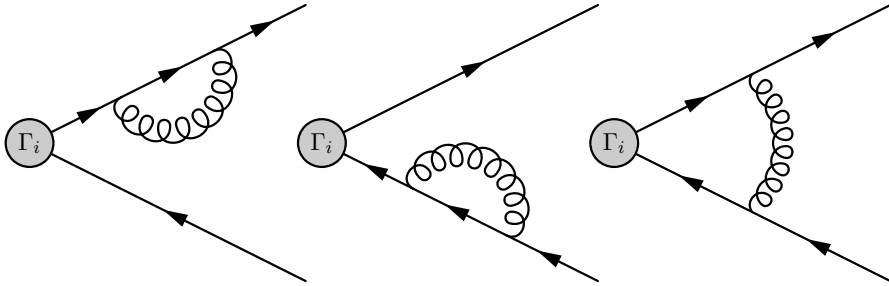
Figure 3.11 The three diagrams describing the QCD corrections at NLO to the process $e^+e^- \to$ dijets.

a renormalization procedure. The Wilson coefficients are then defined as the difference between the QCD result and the renormalized SCET result. Since the renormalization will introduce a scale-dependence, the Wilson coefficients will obtain a dependence on the renormalization scale in analogy with the scale-dependence of the coupling constant in eq. (2.18).

The tree-level diagrams for $e^+e^- \to$ dijets in QCD and SCET evaluate to the same result so that the leading-order Wilson coefficient is equal to

$$C_{q\bar{q}}(Q^2) = 1 + \mathcal{O}(\alpha_s).\tag{3.156}$$

The matching of the SCET current to QCD at 1-loop accuracy will be performed in Feynman gauge. To make a clear distinction between the UV and IR divergences in QCD, the former will be treated by dimensional regularization while the latter are regularized by considering the quark and antiquark as off-shell particles. After the renormalization procedure, the combined result of the three QCD diagrams shown in fig. 3.11 is given by

$$\mathcal{M}_{\text{QCD}} = \frac{\alpha_s C_F}{4\pi} \left[-2\ln^2\left(\frac{p^2}{Q^2}\right) - 4\ln\left(\frac{p^2}{Q^2}\right) - \ln\left(\frac{-Q^2}{\mu^2}\right) - \frac{2\pi^2}{3} \right] J_{q\bar{q}}^{\text{QCD}},\tag{3.157}$$

where $p^2 = p_1^2 = p_2^2 \neq 0$. The non-vanishing diagrams for this process in SCET, prior to performing the BPS field redefinitions, are shown in fig. 3.12 and are regulated in the same manner as the QCD diagrams. The diagrams on the second line represent the collinear vertex corrections that contain interactions between the collinear (anti)quark and the corresponding collinear Wilson line. The wavefunction renormalization diagrams, involving ultrasoft instead of collinear gluons, vanish since the Feynman rule in eq. (3.87) describing their interaction involves the light-like vector n^μ and $n \cdot n = 0$. Evaluating the SCET
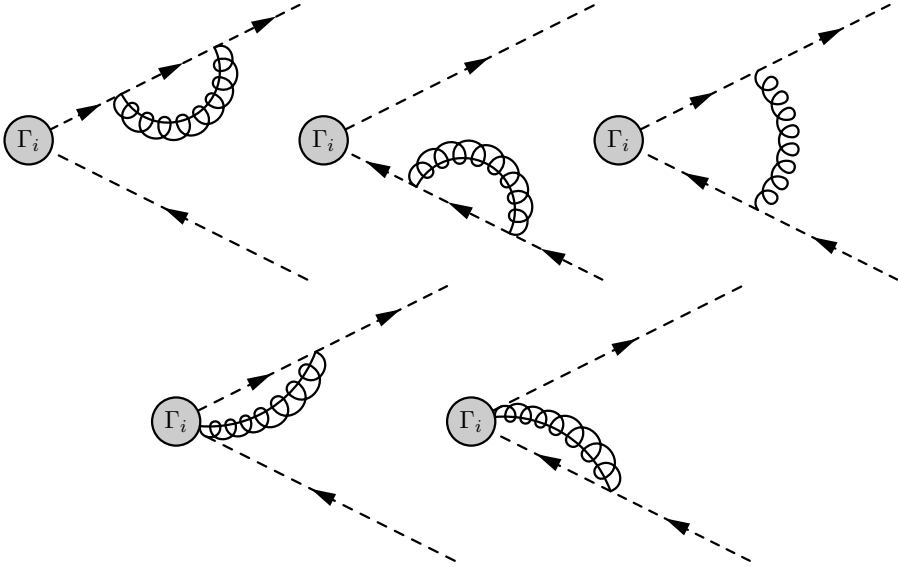
Figure 3.12 The nonvanishing diagrams describing the NLO corrections in SCET to the process $e^+e^- \to$ dijets, before the BPS field redefinitions are performed. The collinear gluons in the graphs on the second line are taken out of the collinear Wilson line.

loop integrals leads to the combined (bare) result [75, 76, 93]

$$\mathcal{M}_{\text{SCET}} = \frac{\alpha_s C_F}{4\pi} \left[\frac{2}{\epsilon^2} + \frac{3}{\epsilon} - \frac{2}{\epsilon} \ln\left(\frac{-Q^2}{\mu^2}\right) - 2\ln^2\left(\frac{p^2}{Q^2}\right) + \ln^2\left(\frac{-Q^2}{\mu^2}\right) \right.$$
$$\left. - 4\ln\left(\frac{p^2}{Q^2}\right) - 4\ln\left(\frac{-Q^2}{\mu^2}\right) + 8 - \frac{5\pi^2}{6} \right] J_{q\bar{q}}^{\text{QCD}}. \qquad (3.158)$$

The zero-bin that has been subtracted as part of the integration cf. eq. (3.152) is scaleless in this case and vanishes. However, as was already discussed in sec. 2.2.1, the reason that it vanishes is that the $1/\epsilon$ poles from the IR regime cancel against those related to the UV regime and subtracting the zero-bin effectively turns all $1/\epsilon$ divergences in SCET into UV divergences. In the difference between the QCD and SCET results, all the IR divergences regulated by the off-shellness $p^2 \neq 0$ cancel and the (bare) 1-loop Wilson coefficient is given by

$$C_{q\bar{q}}^{\text{bare}}(Q^2, \epsilon) = 1 + \frac{\alpha_s C_F}{4\pi} \left[-\frac{2}{\epsilon^2} - \frac{3}{\epsilon} + \frac{2}{\epsilon} \ln\left(\frac{-Q^2}{\mu^2}\right) - \ln^2\left(\frac{-Q^2}{\mu^2}\right) \right.$$
$$\left. + 3\ln\left(\frac{-Q^2}{\mu^2}\right) - 8 + \frac{\pi^2}{6} \right] + \mathcal{O}(\alpha_s^2), \qquad (3.159)$$

which can be seen to be independent of μ, as it should. This Wilson coefficient is then renormalized through[11]

$$C_{q\bar{q}}^{\text{bare}}(Q^2, \epsilon) = Z_{q\bar{q}}(Q^2, \epsilon, \mu)\, C_{q\bar{q}}(Q^2, \mu)\,, \tag{3.160}$$

where the scale factor, containing the counterterms, is given by

$$Z_{q\bar{q}} = 1 + \frac{\alpha_s C_F}{4\pi}\left[-\frac{2}{\epsilon^2} - \frac{3}{\epsilon} + \frac{2}{\epsilon}\ln\left(\frac{-Q^2}{\mu^2}\right)\right] + \mathcal{O}(\alpha_s)\,. \tag{3.161}$$

This then leads to the renormalized Wilson coefficient [93]

$$C_{q\bar{q}}(Q^2, \mu) = 1 + \frac{\alpha_s C_F}{4\pi}\left[-\ln^2\left(\frac{-Q^2}{\mu^2}\right) + 3\ln\left(\frac{-Q^2}{\mu^2}\right) - 8 + \frac{\pi^2}{6}\right]\,, \tag{3.162}$$

up to corrections of $\mathcal{O}(\alpha_s^2)$, matching the SCET current for $e^+e^- \to$ dijets to the QCD result at one loop.

3.7.3 Resummation of Sudakov logarithms

The scale-independence of the bare Wilson coefficient leads to the renormalization group equation

$$\mu\frac{\mathrm{d}C_{q\bar{q}}(Q^2, \mu)}{\mathrm{d}\mu} = \left[-Z_{q\bar{q}}^{-1}(Q^2, \epsilon, \mu)\,\mu\frac{\mathrm{d}Z_{q\bar{q}}(Q^2, \epsilon, \mu)}{\mathrm{d}\mu}\right]C_{q\bar{q}}(Q^2, \mu)\,, \tag{3.163}$$

in complete analogy to the scale-independence of the bare coupling constant that led to the beta function in eq. (2.20). The term in square brackets is known as the anomalous dimension $\gamma_{q\bar{q}}(Q^2, \mu)$ of the Wilson coefficient and is found to be equal to

$$\gamma_{q\bar{q}}(Q^2, \mu) = \frac{\alpha_s(\mu)C_F}{4\pi}\left[4\ln\left(\frac{-Q^2}{\mu^2}\right) - 6\right]\,. \tag{3.164}$$

The structure of this anomalous dimension is order-independent so that at each order there will be a single logarithm and a constant term.

If the Wilson coefficient is evaluated at a scale μ^2 that is significantly different from $-Q^2$, the first term in the anomalous dimension will dominate over the second term and the combination of the coupling constant α_s and the logarithm might be counted as an $\mathcal{O}(1)$ number. The expansion in α_s is then no

---

[11]In general, the effective theory has to be renormalized before it is matched onto the full theory. However, since QCD is already renormalized here, the matching may be performed before renormalizing the SCET result.

longer a sensible perturbative series and the more correct grouping of terms can schematically be visualized by

$$\gamma_{q\bar{q}}(Q^2, \mu) \sim [\alpha_s L] + [\alpha_s + \alpha_s^2 L] + [\alpha_s^2 + \alpha_s^3 L] + \dots , \tag{3.165}$$

where L stands for the logarithm in the anomalous dimension and each term might carry a different coefficient. The first term in this expansion is known as the leading logarithm (LL) and subsequent terms are known as next-to-leading logarithm (NLL), next-to-next-to-leading logarithm (NNLL) etc. From this expansion, it is immediately clear that at any desired order N^{n}LL, the term in the anomalous dimension containing the logarithm is required at $(n+1)$ loops, while the constant term is needed only at n loops.

The RGE for the Wilson coefficient at LL can then be expressed as

$$\frac{\mathrm{d}\ln(C_{q\bar{q}}(Q^2, \mu))}{\mathrm{d}\ln\mu} = \frac{2\alpha_s(\mu)C_F}{\pi} \ln\left(\frac{\omega}{\mu}\right) , \tag{3.166}$$

where $\omega^2 \equiv -Q^2$ has been defined for simplicity. This RGE, together with the RGE for the coupling constant at LL from eq. (2.22), forms a set of coupled differential equations. The latter can be used to rewrite the logarithm in the anomalous dimension as

$$\ln\left(\frac{\omega}{\mu}\right) = \int_{\mu'=\mu}^{\mu'=\omega} \mathrm{d}\ln\mu' = -\frac{2\pi}{\beta_0}\left(\frac{1}{\alpha_s(\mu)} - \frac{1}{\alpha_s(\omega)}\right) , \tag{3.167}$$

so that, after separating variables and integrating from the boundary scale μ_0 to the arbitrary scale μ, the RGE for the Wilson coefficient can be written as

$$\int_{\mu'=\mu_0}^{\mu'=\mu} \mathrm{d}\ln(C_{q\bar{q}}(Q^2, \mu')) = \frac{8\pi C_F}{\beta_0^2}\int_{\mu'=\mu_0}^{\mu'=\mu}\frac{\mathrm{d}\alpha_s(\mu')}{\alpha_s(\mu')}\left(\frac{1}{\alpha_s(\mu')} - \frac{1}{\alpha_s(\omega)}\right) , \tag{3.168}$$

where the definition of the beta function has again been used to change variables. Solving the integrals and shifting the coupling constant $\alpha_s(-Q)$ to $\alpha_s(\mu_0)$ using eq. (2.23) then yields

$$\frac{C_{q\bar{q}}(Q^2, \mu)}{C_{q\bar{q}}(Q^2, \mu_0)} = \exp\left[-\frac{8\pi C_F}{\beta_0^2\alpha_s(\mu_0)}\left(\frac{1}{r} - 1 + \frac{\alpha_s(\mu_0)}{\alpha_s(\omega)}\ln r\right)\right] , \tag{3.169}$$

where $r \equiv \alpha_s(\mu)/\alpha_s(\mu_0)$. Finally, the coupling constant at the scale ω can be shifted to the scale μ_0 at LL through the relation in eq. (2.23) so that the solution

$$\frac{C_{q\bar{q}}(Q^2, \mu)}{C_{q\bar{q}}(Q^2, \mu_0)} = \exp\left[-\frac{8\pi C_F}{\beta_0^2\alpha_s(\mu_0)}\left(\frac{1}{r} - 1 + \ln r\right)\right]\left(\frac{\omega}{\mu_0}\right)^{-\frac{4C_F}{\beta_0}\ln r} , \tag{3.170}$$

is obtained. This solution relates the Wilson coefficient at some scale μ to the result at some other scale μ_0. The structure of this solution can be seen more clearly by choosing the boundary scale $\mu_0 = \omega$, so that the only dependence on the scale ω left is through the strong coupling constant. Again writing $\alpha_s(\omega)$ in terms of $\alpha_s(\mu)$ and expanding for small α_s then gives the LL solution

$$\frac{C_{q\bar{q}}(Q^2,\mu)}{C_{q\bar{q}}(Q^2,\omega)} = \exp\left[-\frac{2C_F}{\pi}\sum_{n=1}^{\infty}K_n\,\alpha_s(\mu)^n\ln^{n+1}\left(\frac{\omega}{\mu}\right)\right], \tag{3.171}$$

where the constant is given by

$$K_n = \frac{(-1)^{n+1}}{n(n+1)}\left(\frac{\beta_0}{2\pi}\right)^{n-1}. \tag{3.172}$$

The result in eq. (3.171) is known as the Sudakov form factor at leading logarithm. Upon expanding the exponential, the term involving the logarithm with the highest power at each order in $\alpha_s(\mu)$ in the Wilson coefficient $C_{q\bar{q}}(Q^2,\mu)$ is recovered. This can be seen explicitly at $\mathcal{O}(\alpha_s)$ by a comparison with the term involving the squared logarithm in eq. (3.162).

Since the series in the argument of the exponential is simpler than the series obtained upon expansion of said exponential, the structure of the Wilson coefficient is most conveniently expressed by considering its logarithm. Performing a similar calculation at higher logarithmic accuracy will lead to the series shown schematically in fig. 3.13. This figure depicts the relation between the counting of terms with the same logarithmic accuracy and the original counting of terms with the same order in the coupling constant. The rows are composed of terms of the same order n in the N^nLO counting and the columns contain terms of the same order in the N^nLL counting.

If the Wilson coefficient is calculated directly at some arbitrary scale μ, its logarithms might be large and spoil the convergence of the perturbative series. The solution of the RGE can be used to instead calculate the Wilson coefficient at the scale ω (where the logarithms are minimized) and then evolve it to the scale μ using the Sudakov form factor, reproducing the most important logarithms at each order in α_s. This process is known as resummation [94,95].

3.8 Separation of scales

As a consequence of the disentanglement of the collinear and ultrasoft degrees of freedom in the SCET$_\text{I}$ Lagrangian, inclusive cross sections and decay widths

$$\ln\left(\frac{C_{q\bar{q}}(Q^2,\mu)}{C_{q\bar{q}}(Q^2,\omega)}\right) \sim \begin{array}{c} \text{LO} \quad \text{LL} \quad \text{NLL} \quad \text{NNLL} \\ \# + \alpha_s\Big[\ \#L^2 \ + \ \#L \ + \ \# \ \Big]\ \text{NLO} \\ + \alpha_s^2\Big[\ \#L^4 \ + \ \#L^3 \ + \ \#L^2 \ + \ \dots \Big]\text{NNLO} \\ + \alpha_s^3\Big[\ \#L^6 \ + \ \#L^5 \ + \ \#L^4 \ + \ \dots \Big]\text{N}^3\text{LO} \\ + \ \vdots \qquad \vdots \qquad \vdots \qquad \vdots \qquad \ddots \end{array}$$

Figure 3.13 A pictorial representation of the difference between fixed-order counting (blue dashed boxes) and resummation-order counting (red solid boxes). The potentially large logarithms are denoted by L and all possible coefficients and constants are indicated by occurrences of $\#$.

will also factorize into distinct sectors involving only a single type of modes. For differential cross sections representing measurements on the external state of a particular process, the contributions of the various modes to the measured observable have to be shown to factorize as well. The various functions representing the factorized sectors can be calculated[12] independently to some desired accuracy and are then multiplied or convolved with one another to form the differential cross section.

These functions are subject to a renormalization procedure analogous to that of the Wilson coefficient and lead to similar renormalization group equations. Each sector contains logarithms that can be minimized at a particular scale, after which the solutions to the RGEs can be used to evolve each function back to a common factorization scale, resumming all the logarithms in the cross section in the process.

3.8.1 Factorization theorems

Currents J^μ that describe scattering processes at lepton colliders appear in the cross section as squared transition amplitudes integrated over all intermediate states as

$$\sigma \sim \sum_X L_{\mu\nu}\,\langle 0|\bar{T}\{J^{\nu\dagger}\}|X\rangle\langle X|T\{J^\mu\}|0\rangle\,(2\pi)^4\delta(q-P_X)\,, \qquad (3.173)$$

where q^μ is the combined momentum of the incoming leptons and P_X^μ the total momentum of the outgoing particles in state X. The leptonic tensor

---

[12]In the case of non-perturbative regimes, they can be determined from experiment instead.

$L_{\mu\nu}$ describes any behavior of the incoming process not described by the current (such as the formation of the intermediate vector boson in the case of $e^+e^- \to$ dijets) and the T and $\bar{T}$ denote time-ordering and anti-time-ordering respectively. The sum over all intermediate states X is understood to be an integral for continuous variables and contains both the phase space integration and any kinematic restrictions relevant for the process under consideration.

After the BPS field redefinitions from eq. (3.135), the collinear and ultrasoft degrees of freedom in SCET completely factorize at the level of the Lagrangian, so that the Hamiltonian and therefore also the Hilbert space factorize into these distinct sectors as well. Taking an explicit outgoing state with two collinear sectors in addition to the ultrasoft sector, like the outgoing state for $e^+e^- \to$ dijets, this factorization of the Hilbert space is given by

$$|X\rangle = |X_n\rangle \, |X_{\bar{n}}\rangle \, |X_{us}\rangle , \qquad (3.174)$$

after which the symbolic sum over X in the cross section turns into three distinct sums over X_n, $X_{\bar{n}}$ and X_{us}. The various collinear and ultrasoft fields in the matched SCET current act only within their respective sectors so that a product of three different matrix elements arises. Each sector has to be a color singlet in its own respect. For example, the n-collinear matrix element reduces to

$$\langle 0|\chi_n^a|X_n\rangle\langle X_n|\bar{\chi}_n^b|0\rangle = \frac{\delta^{ab}}{N_c}\langle 0|\chi_n^c|X_n\rangle\langle X_n|\bar{\chi}_n^c|0\rangle , \qquad (3.175)$$

where a, b and c are color indices, N_c denotes the number of colors and a sum over repeated indices is implied. The Dirac structure that still connects different sectors can be rearranged by a Fierzing procedure to completely disconnect the soft and collinear matrix elements. For SCET currents involving two collinear quark fields, e.g. the current for $e^+e^- \to$ dijets, the only non-vanishing structure that the Fierzing procedure leads to is the vector current[13]. Sticking with the example of $e^+e^- \to$ dijets, the cross section after this factorization of the collinear and ultrasoft sectors in both spin and color takes the form [96, 97]

$$\sigma \sim A_0 \sum_{X_n, X_{\bar{n}}, X_{us}} |C_2(Q^2,\mu)|^2 \, (2\pi)^4 \delta(q - P_{X_n} - P_{X_{\bar{n}}} - P_{X_{us}})$$
$$\times \langle 0|\frac{\slashed{\bar{n}}}{4N_c}\chi_n|X_n\rangle\langle X_n|\bar{\chi}_n|0\rangle \, \langle 0|\bar{\chi}_{\bar{n}}|X_{\bar{n}}\rangle\langle X_{\bar{n}}|\frac{\slashed{n}}{4N_c}\chi_{\bar{n}}|0\rangle$$
$$\times \langle 0|\bar{T}\{Y_{\bar{n}}^\dagger Y_n\}|X_{us}\rangle\langle X_{us}|T\{Y_n^\dagger Y_{\bar{n}}\}|0\rangle , \qquad (3.176)$$

---

[13]This statement holds for unpolarized beams, more structures are possible when polarized beams are considered.

where the constant A_0 contains the leptonic tensor, the coefficient that the Fierz identity leads to and the sum over $i = V, A$. Each of the three distinct matrix elements is understood to be traced over color, spin, or both as appropriate. The light-like vectors $\not{n}$ and $\not{\bar{n}}$ appear in the collinear sectors after decomposing the gamma matrices in terms of lightcone coordinates.

The sums over the external states X_n, $X_{\bar{n}}$ and X_{us} involve the kinematic restrictions that ensure a particular configuration. For the case of $e^+e^- \to$ dijets, this entails forcing the outgoing state to contain exactly two jets. This restriction can be taken into account explicitly by measuring the hemisphere mass from eq. (3.17) of both hemispheres a and b and demanding the result to be small. If there would be more than a single direction per hemisphere along which collinear particles exit the hard process, the mass of that hemisphere would become sizable. The measurement of the hemisphere masses m_a^2 and m_b^2 can be implemented in the cross section by inserting

$$1 = \int \mathrm{d}m_a^2 \int \mathrm{d}m_b^2 \, \delta\big(m_a^2 - Q(k_n^+ + k_{us}^+)\big) \, \delta\big(m_b^2 - Q(k_{\bar{n}}^- + k_{us,b}^-)\big), \quad (3.177)$$

where the momenta inside the delta functions have been expanded to leading power and the large label momentum has been identified as $k_n^- = k_{\bar{n}}^+ = Q$. The integration measures can then be brought to the left-hand side to obtain a cross section differential in the hemisphere masses. After factorizing these measurement delta functions as well as the overall momentum-conserving delta function, the cross section will be completely factorized and each independent sector is connected to the others only through either a multiplication or a convolution. For the example of $e^+e^- \to$ dijets, the factorized cross section then takes the form [96]

$$\frac{\mathrm{d}\sigma}{\mathrm{d}m_a^2 \, \mathrm{d}m_b^2} \sim H_{ij}(Q, \mu) \int \mathrm{d}s_n \, \mathrm{d}s_{\bar{n}} \, \mathrm{d}k_{us,a}^+ \, \mathrm{d}k_{us,b}^- \, \delta(m_a^2 - s_n - Qk_{us,a}^+)$$
$$\times \, \delta(m_b^2 - s_{\bar{n}} - Qk_{us,b}^-) \, J_i(s_n) \, J_j(s_{\bar{n}}) \, S_{ij}^{\text{hemi}}(k_{us,a}^+, k_{us,b}^-), \quad (3.178)$$

where $s_n \equiv Qk_n^+$ and $s_{\bar{n}} \equiv Qk_{\bar{n}}^-$. An implicit sum over i and j, representing the relevant partonic channels, is to be understood. For the process under consideration, these are $\{i, j\} = \{q, \bar{q}\}$ and $\{i, j\} = \{\bar{q}, q\}$. The hard function $H_{ij}(Q, \mu)$ is defined as the squared absolute value of the Wilson coefficient, multiplied by the Born cross section. The jet functions $J_i(s_n)$ describe the particles in the final state collinear to the outgoing quark and antiquark. The hemisphere soft function $S_{ij}^{\text{hemi}}(k_{us,a}^+, k_{us,b}^-)$ encodes the contribution of the ultrasoft radiation to the measurement of both hemisphere invariant masses. Both the jet and soft functions are independent of the underlying hard interaction and can individually be calculated perturbatively. A global soft function can be obtained

from the hemisphere soft function through [96, 98]

$$S_{ij}(k) = \int \mathrm{d}k^+_{us,a}\, \mathrm{d}k^-_{us,b}\, S^{\mathrm{hemi}}_{ij}(k^+_{us,a}, k^-_{us,b})\, \delta(k - k^+_{us,a} - k^-_{us,b})\,. \qquad (3.179)$$

This soft function, often called the thrust soft function or inclusive soft function, is defined as the vacuum matrix element[14]

$$S_{q\bar{q}}(k) = \frac{1}{N_c} \mathrm{Tr}\Big[\langle 0| \bar{T}\{Y^\dagger_n(0) Y_{\bar{n}}(0)\}\, \delta(k - \mathcal{P}^+_a - \mathcal{P}^-_b)\, T\{Y^\dagger_{\bar{n}}(0) Y_n(0)\}\, |0\rangle\Big]\,,$$
$$(3.180)$$

where the trace is over color, N_c denotes the number of colors and the operators $\mathcal{P}^+_a$ and $\mathcal{P}^-_b$ serve to pick out the plus and minus component of the momenta going into hemispheres a and b respectively. This soft function will play a role in the combined resummation of transverse momentum and beam thrust in chap. 4. Using this inclusive soft function, the factorization in eq. (3.178) may be turned into the factorization for a cross section differential in the the variable known as thrust τ, which for the case of hemisphere invariant masses is given by $\tau = (m_a^2 + m_b^2)/Q^2$. The explicit form of this factorization is given by [96]

$$\frac{\mathrm{d}\sigma}{\mathrm{d}\tau} \sim H_{ij}(Q, \mu) \int \mathrm{d}k\, \mathrm{d}s_n\, \mathrm{d}s_{\bar{n}}\, J_i(s_n)\, J_j(s_{\bar{n}})\, S_{ij}(k)\, \delta\Big(\tau - \frac{k}{Q} - \frac{s_n + s_{\bar{n}}}{Q^2}\Big)\,.$$
$$(3.181)$$

In processes with other measurements, more differential soft and jet functions, involving the measurement of multiple momentum components, might be necessary. In proton-proton collisions, the partons that are extracted from the proton undergo collinear splittings before initiating the hard interaction, as was described in sec. 2.3.3. Due to the collinear nature of these interactions, the evolution of a parton from its extraction out of the proton until its initiation of the hard interaction is described in SCET by a collinear function called a beam function [99, 100]. The beam function is related to the parton distribution functions through the matching equation

$$B_i(t, x, \mu) = \sum_j \int_x^1 \frac{\mathrm{d}z}{z}\, \mathcal{I}_{ij}(t, z, \mu)\, f_j\Big(\frac{x}{z}, \mu\Big)\Big[1 + \mathcal{O}\Big(\frac{\Lambda^2_{\mathrm{QCD}}}{t}\Big)\Big]\,, \qquad (3.182)$$

where the sum runs over all possible partons. The matching coefficients $\mathcal{I}_{ij}$ can be determined perturbatively and at tree-level they are given by

$$\mathcal{I}_{ij}(t, z, \mu) = \delta_{ij}\, \delta(1 - z)\, \delta(t)\,, \qquad (3.183)$$

---

[14]This definition holds for both $i = q$ and $\bar{q}$ (and $j = \bar{q}$ or q respectively). The matrix element for $i = g$ differs only from eq. (3.180) by $N_c \to N_c^2 - 1$.

so that the beam function reduces to the conventional PDFs at leading order. The matching coefficients are known to $\mathcal{O}(\alpha_s^2)$ [101, 102] and can be found in app. B.2. As is the case for jet and soft functions, the measurement of additional components of the incoming partons leads to more differential beam functions, analogous to more generic PDFs such as the transverse-momentum-dependent PDF.

3.8.2 Resummation

After the renormalization procedure, the various functions that might appear in factorization formulas will depend on the common scale μ. A perturbative calculation of these functions will in general yield a result containing powers of logarithms (or the distributional analogs, plus distributions, which can be found in app. A) involving the scale μ. As the power of these logarithms grows at every order in α_s, the scale μ has to be picked such that the logarithms remain small to ensure the convergence of the perturbative expansion of each function. For the hard function in eq. (3.178), for example, logarithms of $-Q^2/\mu^2$ appear at each order in perturbation theory, as shown in eq. (3.162), so a viable choice for the scale would be $\mu \sim Q$. The scale at which the logarithms inside a particular function are minimized is called the natural or canonical scale of the function. Different functions will in general contain logarithms of different ratios and therefore have different canonical scales, so that no single choice of μ can minimize the logarithms in all the perturbative functions at once.

Each function F occurring in a particular factorization formula is renormalized according to the general equation

$$F^{\text{bare}}(t, \epsilon) = Z_F(t, \epsilon, \mu) \otimes F(t, \mu) \,, \tag{3.184}$$

where t represents a variable on which the function F depends and $\otimes$ refers to either a multiplication or a convolution. For the renormalization of the Wilson coefficient in eq. (3.160) this is an ordinary multiplication. For many perturbative functions the renormalization is done through a convolution as

$$F^{\text{bare}}(t, \epsilon) = \int \mathrm{d}t' \, Z_F(t - t', \epsilon, \mu) \, F(t', \mu) \,. \tag{3.185}$$

The fact that the bare function is scale-independent then leads to a renormalization group equation for the renormalized function, as was seen already for the renormalized coupling constant in eq. (2.20) and the renormalized Wilson coefficient in eq. (3.163). The general form of such an RGE is dictated by

$$\mu \frac{\mathrm{d}F(t, \mu)}{\mathrm{d}\mu} = \gamma_F(t, \mu) \otimes F(t, \mu) \,, \tag{3.186}$$

where γ_F is the anomalous dimension of the function F and $\otimes$ refers to the same type of multiplication or convolution structure as before. For a multiplicatively renormalized function, such as the Wilson coefficient, the RGE is therefore also multiplicative and the anomalous dimension takes the general form

$$\gamma_F(t,\mu) = a_F \, \Gamma^i_{\text{cusp}}(\alpha_s) \ln\left(\frac{t}{\mu}\right) + \gamma^i_F(\alpha_s)\,, \tag{3.187}$$

where the cusp anomalous dimension $\Gamma^i_{\text{cusp}}(\alpha_s)$ is a general factor that appears in all anomalous dimensions. Both the cusp and the non-cusp anomalous dimensions are expansions in α_s defined by

$$\Gamma^i_{\text{cusp}}(\alpha_s) = \sum_{n=0}^{\infty} \Gamma^i_n \left(\frac{\alpha_s}{4\pi}\right)^{n+1} \qquad \text{and} \qquad \gamma^i_X(\alpha_s) = \sum_{n=0}^{\infty} \gamma^i_{X,n} \left(\frac{\alpha_s}{4\pi}\right)^{n+1}\,, \tag{3.188}$$

where the superscript $i = q, g$ refers to anomalous dimensions involving either quarks or gluons respectively. The coefficients of the cusp anomalous dimension can be found up to three loops in eq. (C.33). The coefficients of the non-cusp anomalous dimension differ per function (indicated by the subscript X) and can also be found in app. C.2 for the various functions that occur in this thesis. The exact argument of the logarithm depends on the variable on which the function F depends.

Functions that are renormalized through a convolution structure will in general contain plus distributions and delta functions instead of logarithms and constants. The general expression for their anomalous dimension is given by the distributional analogue of eq. (3.187), namely

$$\gamma_F(t,\mu) = a_F \, \Gamma^i_{\text{cusp}}(\alpha_s)\mathcal{L}_0(t,\mu) + \gamma^i_F(\alpha_s)\delta(t)\,, \tag{3.189}$$

where $\mathcal{L}_0(t,\mu) \equiv \mathcal{L}_0(t/\mu)/\mu$ is the notation used to represent plus distributions as described in app. A.

The first step towards the general solution to a multiplicative RGE entails a separation of variables and integration from some fixed scale μ_0 to an arbitrary scale μ to obtain

$$\ln\left(\frac{F(t,\mu)}{F(t,\mu_0)}\right) = \int_{\ln\mu_0}^{\ln\mu} \mathrm{d}\ln\mu'\, \gamma_F(t,\mu')\,. \tag{3.190}$$

The definition of the beta function in eq. (2.20) can be used to rewrite the logarithm in the anomalous dimension according to

$$\ln\left(\frac{t}{\mu}\right) = \ln\left(\frac{t}{\mu_0}\right) - \int_{\ln\mu_0}^{\ln\mu} \mathrm{d}\ln\mu' = \ln\left(\frac{t}{\mu_0}\right) - \int_{\alpha_s(\mu_0)}^{\alpha_s(\mu)} \frac{\mathrm{d}y}{\beta(y)}\,. \tag{3.191}$$

Plugging the general form of the anomalous dimension in and again changing integration variables according to the definition of the beta function then yields

$$
\ln\!\left(\frac{F(t,\mu)}{F(t,\mu_0)}\right) = \left[a_F \ln\!\left(\frac{t}{\mu_0}\right)\eta_\Gamma^i(\mu_0,\mu) - a_F K_\Gamma^i(\mu_0,\mu) + K_{\gamma_F^i}(\mu_0,\mu)\right], \quad (3.192)
$$

where the evolution kernels have been defined as

$$
\eta_\Gamma^i(\mu_0,\mu) = \int_{\alpha_s(\mu_0)}^{\alpha_s(\mu)} \frac{\mathrm{d}x}{\beta(x)}\,\Gamma_{\mathrm{cusp}}^i(x)\,,
$$

$$
K_\Gamma^i(\mu_0,\mu) = \int_{\alpha_s(\mu_0)}^{\alpha_s(\mu)} \frac{\mathrm{d}x}{\beta(x)}\,\Gamma_{\mathrm{cusp}}^i(x) \int_{\alpha_s(\mu_0)}^{x} \frac{\mathrm{d}y}{\beta(y)}\,,
$$

$$
K_{\gamma_F^i}(\mu_0,\mu) = \int_{\alpha_s(\mu_0)}^{\alpha_s(\mu)} \frac{\mathrm{d}x}{\beta(x)}\,\gamma_F^i(x)\,. \quad (3.193)
$$

Explicit expressions for these evolution kernels can be found up to NNLL in app. C.2. The final result that relates the function $F(t,\mu)$ at a scale μ to the same function at some other scale μ_0 can then be found through exponentiation and reads

$$
F(t,\mu) = U_F(t,\mu_0,\mu)\,F(t,\mu_0)\,, \quad (3.194)
$$

where the evolution of the function F between the two different scales is described by the evolution function

$$
U_F(t,\mu_0,\mu) = \left(\frac{t}{\mu_0}\right)^{a_F \eta_\Gamma^i(\mu_0,\mu)} \exp\!\left[-a_F K_\Gamma^i(\mu_0,\mu) + K_{\gamma_F^i}(\mu_0,\mu)\right]. \quad (3.195)
$$

For the Wilson coefficient, this procedure was performed explicitly in sec. 3.7.3 at LL accuracy for the canonical value of the scale μ_0 at which all the logarithms are minimized.

Functions that are renormalized through a convolution lead to renormalization group equations of the form

$$
\mu \frac{\mathrm{d}F(t,\mu)}{\mathrm{d}\mu} = \int \mathrm{d}t'\,\gamma_F(t-t',\mu)\,F(t',\mu)\,, \quad (3.196)
$$

which can be changed to ordinary multiplicative RGEs by a transformation to for example Fourier space or Laplace space. The Laplace transform of a function $F(t,\mu)$ is defined analogous to the Fourier transform in eq. (A.19) as

$$
\hat{F}(s,\mu) = \int_0^\infty \mathrm{d}t\, e^{-st}\,F(t,\mu)\,, \quad (3.197)
$$

leading to a general expression for the anomalous dimension in Laplace space given by

$$\hat{\gamma}_F(s, \mu) = -a_F \, \Gamma^i_{\text{cusp}}(\alpha_s) \ln(s \, e^{\gamma_E} \mu) + \gamma^i_F(\alpha_s) \,. \tag{3.198}$$

Since both the RGE and the anomalous dimension now have the same form as their multiplicative counterparts, the solution (in Laplace space) to the RGE of a function renormalized through a convolution structure has the same form as eq. (3.194). The transformation of this solution back to momentum space leads to a convolution between the function F and the evolution function U_F given by

$$F(t, \mu) = \int \mathrm{d}t' \, U_F(t - t', \mu_0, \mu) \, F(t', \mu_0) \,. \tag{3.199}$$

The evolution function in momentum space can be found by an inverse Laplace transform and reads

$$U_F(t, \mu_0, \mu) = \frac{\exp\left[-a_F K^i_\Gamma(\mu_0, \mu) - a_F \gamma_E \, \eta^i_\Gamma(\mu_0, \mu) + K_{\gamma^i_F}(\mu_0, \mu)\right]}{\Gamma[1 + a_F \, \eta^i_\Gamma(\mu_0, \mu)]}$$
$$\times \left(a_F \, \eta^i_\Gamma(\mu_0, \mu) \mathcal{L}^{a_F \eta^i_\Gamma(\mu_0, \mu)}(t, \mu) + \delta(t) \right), \tag{3.200}$$

where the plus distribution of the form $\mathcal{L}^a(t, \mu)$ is defined in app. A.

Each function in a factorization formula has to be evaluated at the same scale μ, which might cause the logarithms inside the functions to grow large and spoil the perturbative convergence if μ differs significantly from the natural scale of the functions. The solution to the RGE of each function can be used to instead calculate every function at its own natural scale, where the logarithms are guaranteed to be small, and then evolve the functions to a common scale μ. For the factorization of $e^+e^- \to$ dijets in eq. (3.181), for example, this would lead to

$$\frac{\mathrm{d}\sigma}{\mathrm{d}\tau} \sim U^i_H(Q, \mu_H, \mu) \, H_{ij}(Q, \mu_H) \int \mathrm{d}k \, \mathrm{d}s_n \, \mathrm{d}s_{\bar{n}} \, \delta\left(\tau - \frac{k}{Q} - \frac{s_n + s_{\bar{n}}}{Q^2}\right)$$
$$\times \int \mathrm{d}s'_n \, U^i_J(s_n - s'_n, \mu_J, \mu) \, J_i(s'_n, \mu) \int \mathrm{d}s'_{\bar{n}} \, U^j_J(s_{\bar{n}} - s'_{\bar{n}}, \mu_J, \mu) \, J_j(s'_{\bar{n}}, \mu)$$
$$\times \int \mathrm{d}k' \, U^i_S(k - k', \mu_S, \mu) \, S_{ij}(k', \mu) \,. \tag{3.201}$$

In this way, all the logarithms in the cross section are resummed to some logarithmic accuracy determined by the order at which the various ingredients

Order	Functions	γ_X^i	Γ_{cusp}^i	β
LL	LO		1-loop	1-loop
NLL	LO	1-loop	2-loop	2-loop
NLL$'$	NLO	1-loop	2-loop	2-loop
NNLL	NLO	2-loop	3-loop	3-loop
NNLL$'$	NNLO	2-loop	3-loop	3-loop
N^{3}LL	NNLO	3-loop	4-loop	4-loop

Table 3.1 Overview of the required ingredients necessary for achieving a desired logarithmic accuracy. The columns denote the required order in α_s of the perturbative functions entering the factorization formula, the non-cusp and cusp anomalous dimensions and the beta function respectively.

(perturbative functions, anomalous dimensions and the beta function) are included. An overview of the required ingredients for the first few orders of logarithmic accuracy is given in table 3.1. In the primed-order counting [103], the fixed-order coefficients are included to one order higher compared to the conventional, unprimed orders.

Since the physical cross section does not depend on the common scale μ, it can be chosen freely. It is often convenient to pick this scale equal to the natural scale of one of the perturbative functions occurring in the factorization formula to avoid the evolution of that particular function. The independence of the cross section on the scale μ also leads to a consistency relation for the anomalous dimensions, requiring that they must add up to zero.

3.9 SCET$_{\text{II}}$

Since the contribution of ultrasoft radiation to observables sensitive to the transverse momentum is suppressed with respect to collinear radiation, SCET$_{\text{I}}$ does not provide a correct description for these types of observables. As some of the most interesting measurements (such as the transverse momentum spectrum of the Higgs boson) fall into this category of observables, a different version of the effective theory, in which the perpendicular components of the collinear and soft modes scale equally, is required. The modes of this theory, known as SCET$_{\text{II}}$, were already discussed briefly in sec. 3.3.3 and are equal in virtuality. The separation between soft and collinear modes is instead a separation in rapidity, which leads to singularities unregulated by dimensional regularization. The treatment of these singularities leads to a separate renormalization group equation connecting functions at various rapidities to one another.

3.9.1 Soft degrees of freedom

The parametric scaling of the n-collinear, $\bar{n}$-collinear and ultrasoft degrees of freedom appearing in SCET$_{\mathrm{I}}$ are given by

$$p_n^\mu \sim Q(\lambda^2, 1, \lambda), \qquad p_{\bar{n}}^\mu \sim Q(1, \lambda^2, \lambda) \qquad \text{and} \qquad p_{us}^\mu \sim Q(\lambda^2, \lambda^2, \lambda^2), \tag{3.202}$$

respectively. The small lightcone component of each of the collinear modes is of the same size as its counterpart from the ultrasoft mode, allowing for interactions between ultrasoft and collinear particles. As the other components of the collinear degrees of freedom dominate over those from the ultrasoft sector, the scaling of collinear particles remains unchanged under these interactions. The fact that the perpendicular component of the collinear radiation always dominates over the perpendicular component of the ultrasoft radiation prevents SCET$_{\mathrm{I}}$ from being the correct EFT to describe processes in which observables sensitive to the transverse momentum of soft radiation are measured. The correct version of the EFT, known as SCET$_{\mathrm{II}}$, contains the same collinear degrees of freedom as SCET$_{\mathrm{I}}$, but whereas the latter contains ultrasoft degrees of freedom, the former instead contains soft degrees of freedom that scale as

$$p_s^\mu \sim Q(\lambda, \lambda, \lambda). \tag{3.203}$$

The perpendicular component of the soft and collinear modes is now indeed of the same parametric size so that both will contribute to measurements involving the transverse momentum.

Soft particles in SCET$_{\mathrm{II}}$ change the scaling of collinear particles when the two interact, resulting in a mode with the parametric scaling $Q(\lambda, 1, \lambda)$, which is off-shell and needs to be integrated out. This situation is similar to the coupling of an n-collinear gluon to an $\bar{n}$-collinear quark in SCET$_{\mathrm{I}}$, as discussed in sec. 3.5.2, where the parametric scaling of the quark is changed to $Q(1, 1, \lambda)$ by the interaction. Taking an arbitrary number of interactions with n-collinear gluons into account and integrating out all the resulting off-shell propagators then led to an effective coupling involving the collinear Wilson line. The off-shell modes resulting from the soft-collinear interactions in SCET$_{\mathrm{II}}$ can be integrated out in a similar fashion, leading to a soft Wilson line given by

$$S_n(x) = \mathrm{P} \, \exp\left[ig_s \int_{-\infty}^{0} \mathrm{d}s \, A_s^+(x + sn) \right], \tag{3.204}$$

that has to be included to ensure gauge-invariance. A convenient procedure of matching SCET$_{\mathrm{II}}$ to QCD is to first match to SCET$_{\mathrm{I}}$, which then in turn gets
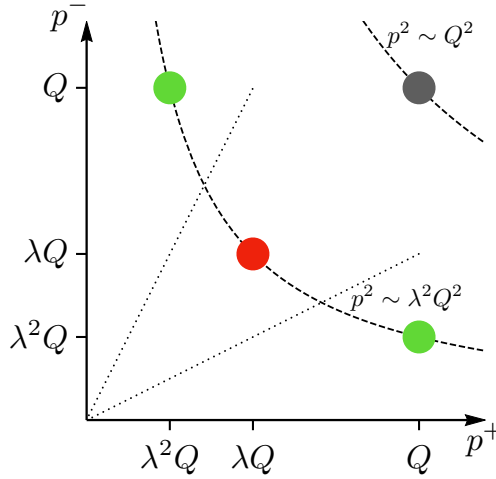
Figure 3.14 The degrees of freedom present in SCET_{II}. The hard, collinear and soft modes are colored gray, green and red respectively. The dotted straight lines represent the separation in rapidity between the collinear and soft modes.

matched to QCD [78, 104]. Consider the set of modes

$$p^{\mu}_{hn} \sim Q\big(\lambda, 1, \sqrt{\lambda}\big), \qquad p^{\mu}_{h\bar{n}} \sim Q\big(1, \lambda, \sqrt{\lambda}\big) \qquad \text{and} \qquad p^{\mu}_{s} \sim Q\big(\lambda, \lambda, \lambda\big), \tag{3.205}$$

where the latter is the soft mode from SCET_{II} and other two are known as hard-collinear modes. The soft modes have a virtuality equal to $p^2_s \sim \lambda^2 Q^2$, the hard-collinear modes have a virtuality of $p^2_{hn} \sim \lambda Q^2$ and their relative hierarchy is the characteristic SCET_{I} hierarchy. The hard-collinear and soft degrees of freedom can then be decoupled (factorized) in the usual way through the BPS field redefinitions in SCET_{I}, as described in sec. 3.6.2. The matching to SCET_{II} can be performed after the decoupling by lowering the virtuality of the hard-collinear modes to the virtuality of collinear modes $p^2_n \sim \lambda^2 Q^2$. As long as the product of operators representing the hard scattering in the SCET_{I} theory contains (for each collinear sector) at most a single operator that involves hard-collinear as well as soft fields, e.g. the current $J^{\mu}_{q\bar{q}}$, the matching procedure simply entails making the change from ultrasoft to soft Wilson lines, $Y_n \to S_n$. For time-ordered products with two or more such operators, the matching becomes more involved and will lead to a convolution between the SCET_{I} current and a Wilson coefficient in the usual way.

3.9.2 Rapidity divergences

To avoid counting infrared singularities twice when performing momentum integrals, the zero-bin has to be subtracted as described in sec. 3.7.2. The zero-bin in SCET$_{\text{I}}$ is obtained by changing the scaling of the collinear modes to an ultrasoft scaling, which entails scaling down the minus and the perpendicular component of the n-collinear momentum $p_n^\mu \sim Q(\lambda^2, 1, \lambda)$ to $Q\lambda^2$. In the (p^-, p^+)-plot on the left-hand side of fig. 3.4 this then corresponds to leaving the hyperbola described by $p^2 \sim \lambda^2 Q^2$ and ending up on the ultrasoft hyperbola described by $p^2 \sim \lambda^4 Q^2$.

In the case of SCET$_{\text{II}}$, the zero-bin is obtained by raising the plus component and lowering the minus component of the n-collinear momentum to the scale $Q\lambda$. This leaves the invariant mass $p^2 = p^+ p^-$ unchanged, as it should since the collinear and soft modes are not separated in virtuality (they lie on the same hyperbola in fig. 3.14). The separation between these two degrees of freedom is a separation in the ratio of their plus and minus components p^+/p^-, which is conventionally expressed as the rapidity

$$Y = \frac{1}{2} \ln\left(\frac{p^+}{p^-}\right), \tag{3.206}$$

which was already defined in eq. (2.35). The lines of constant rapidity that separate the soft and collinear modes in SCET$_{\text{II}}$ are then lines of constant p^+/p^- and are shown as dotted lines in fig. 3.14. As the rapidity is not boost invariant, regulators such as dimensional regularization that regulate Lorentz-invariant quantities like the invariant mass p^2 do not regulate any singularities corresponding to a separation of modes in their rapidity.

The rapidity singularities arise from the (Eikonal) denominators in the soft and collinear Wilson lines given in eqs. (3.108) and (3.204) and can be regulated through multiple methods. A method that is closely related to dimensional regularization is to use the so-called η-regulator [105,106] to modify the Wilson lines in momentum space by[15]

$$S_n(x) = \sum_{\text{perms}} \exp\left[\frac{-g_s}{\mathcal{P}^+} w \left(\frac{|\mathcal{P}^- - \mathcal{P}^+|}{\nu}\right)^{-\eta/2} A_n^+(x)\right]$$

$$W_n(x) = \sum_{\text{perms}} \exp\left[\frac{-g_s}{\mathcal{P}^-} w^2 \left(\frac{|\mathcal{P}^-|}{\nu}\right)^{-\eta} A_n^-(x)\right]. \tag{3.207}$$

The combination of $\mathcal{P}^- - \mathcal{P}^+$ in the soft Wilson line is equal to twice the momentum in the $\hat{z}$-direction. The plus component of the label operator in the

---

[15]These expression hold at one loop. At higher orders they are slightly more complicated [105].

collinear Wilson line is parametrically much smaller than its minus component, hence it can be dropped at leading power. The scale ν is analogous to the scale μ in dimensional regularization in that it ensures that the mass dimension of the expression as a whole remains unchanged. The power η is similar to the infinitesimal ϵ in dimensional regularization and will lead to poles of $1/\eta$. Finally, the parameter w plays the role of a fictitious coupling (it will eventually be set to unity), analogous to α_s, which is renormalized through

$$w^{\text{bare}} = w(\eta, \nu) \, \nu^{\eta/2}, \tag{3.208}$$

so that a rapidity renormalization group equation, similar to eq. (2.20), is obtained as

$$\nu \frac{\mathrm{d}}{\mathrm{d}\nu} w(\eta, \nu) = -\frac{\eta}{2} \, w(\eta, \nu) \,. \tag{3.209}$$

After this additional regularization procedure, perturbative functions in factorization theorems containing soft or collinear Wilson lines will contain divergences in both $1/\epsilon$ and $1/\eta$. The limit $\eta \to 0$ has to be taken first, with $\eta/\epsilon^n \to 0$ for all n. After also taking the limit $\epsilon \to 0$, the parameter w may be set to $w = 1$ and counterterms can be added to absorb the poles in both $1/\eta$ and $1/\epsilon$ to render the resulting perturbative function finite. Regulating and renormalizing rapidity divergences then introduces logarithms containing the scale ν in these functions in addition to the logarithms containing the scale μ. To ensure these logarithms remain small enough to render the perturbative expansion of the function valid, a procedure analogous to the one used to achieve the same goal for logarithms involving the scale μ in sec. 3.8.2 may be employed. Each function will thus obey both a μ-RGE and a ν-RGE with their respective anomalous dimensions schematically given by

$$\gamma_\mu = -Z^{-1}\mu \frac{\mathrm{d}Z}{\mathrm{d}\mu} \qquad \text{and} \qquad \gamma_\nu = -Z^{-1}\nu \frac{\mathrm{d}Z}{\mathrm{d}\nu} \,, \tag{3.210}$$

where Z denotes the combination of all relevant renormalization factors. Solving both RGEs will then lead to two evolution equations, one evolving the function from a scale μ_0 to another scale μ, as given in eq. (3.194) or eq. (3.199), and one evolving the function from a scale ν_0 to the scale ν. As the order of the μ and ν derivatives may be interchanged, the μ- and ν-anomalous dimensions are related through

$$\mu \frac{\mathrm{d}\gamma_\nu}{\mathrm{d}\mu} = \nu \frac{\mathrm{d}\gamma_\mu}{\mathrm{d}\nu} \,, \tag{3.211}$$

and the evolution is independent of the path chosen in the (μ, ν) plane. Picking
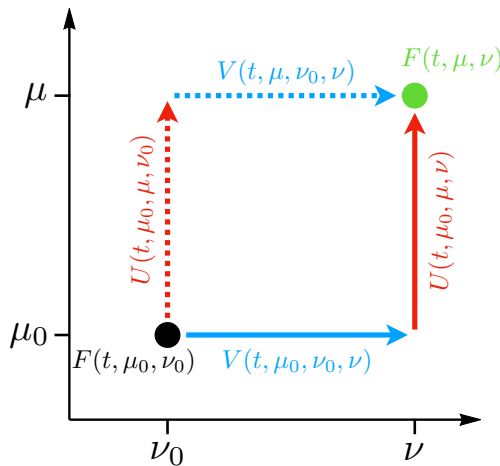
Figure 3.15 A pictorial representation of two possible ways of running a function from the scales μ_0 and ν_0 to the scales μ and ν. The running in μ and ν is represented by the red and blue arrows respectively.

the path shown by the solid arrows in fig. 3.15 for definiteness, the complete evolution of a function F from its natural scales μ_0 and ν_0 to a set of common scales μ and ν is then given by

$$F(t,\mu,\nu) = U_F(t,\mu_0,\mu,\nu) \otimes V_F(t,\mu_0,\nu_0,\nu) \otimes F(t,\mu_0,\nu_0)\,, \qquad (3.212)$$

where, as before, the $\otimes$ encodes either a multiplication or a convolution structure. The evolution function $V_F(t,\mu_0,\nu_0,\nu)$ evolves the function F from the scale ν_0 to the scale ν at fixed μ_0 and $U_F(t,\mu_0,\mu,\nu)$, given in eq. (3.195) or eq. (3.200), evolves the function from μ_0 to μ (at fixed ν). All rapidity divergences occurring in this thesis will be treated using the η-regulator described in this section.

3.10 SCET$_+$

The specific measurement under consideration determines the relevant degrees of freedom and therefore the version of SCET that is appropriate for the given situation. For measured variables depending on the plus or minus lightcone components, SCET$_\text{I}$ is the correct theory, while measurements depending on the transverse component are properly described by SCET$_\text{II}$. When both types of measurements are considered simultaneously, neither version of SCET fully describes the process and an additional set of degrees of freedom has to be included in order to provide a complete description [107, 108]. To see how
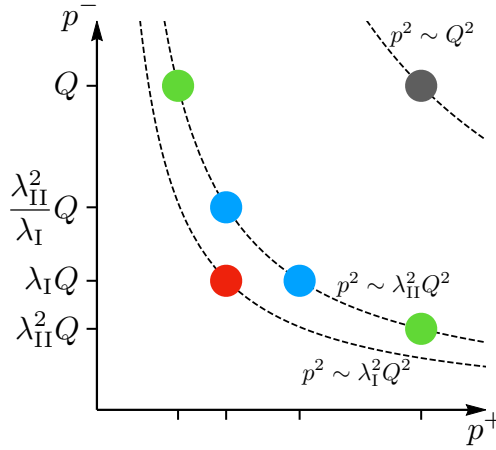
Figure 3.16 The relevant modes for SCET_+. The hard, collinear, collinear-soft and soft modes are colored gray, green, blue and red respectively.

these new modes arise, consider a SCET_{II}-type measurement M_{II} depending on the perpendicular lightcone component of the particles in the final state and a SCET_{I}-type measurement M_{I}, depending on their other two lightcone components. In the first case, the expansion parameter is given by $\lambda_{\text{II}} = M_{\text{II}}/Q$ and the collinear degrees of freedom are given by

$$
\begin{aligned}
p_n^\mu &\sim Q\big(\lambda_{\text{II}}^2, 1, \lambda_{\text{II}}\big) \sim \big(M_{\text{II}}^2/Q, Q, M_{\text{II}}\big)\,, \\
p_{\bar n}^\mu &\sim Q\big(1, \lambda_{\text{II}}^2, \lambda_{\text{II}}\big) \sim \big(Q, M_{\text{II}}^2/Q, M_{\text{II}}\big)\,.
\end{aligned}
\tag{3.213}
$$

The additional measurement of M_{I} leads to a second power counting in the expansion parameter $\lambda_{\text{I}} = M_{\text{I}}/Q$ and is sensitive to a new set of degrees of freedom with either a plus or minus component $p^\pm \sim Q\lambda_{\text{I}}$. Demanding that these modes also contribute to the measurement of M_{II} and are on-shell then completely fixes their scaling to

$$
\begin{aligned}
p_{ns}^\mu &\sim Q\big(\lambda_{\text{I}}, \lambda_{\text{II}}^2/\lambda_{\text{I}}, \lambda_{\text{II}}\big) \sim \big(M_{\text{I}}, M_{\text{II}}^2/M_{\text{I}}, M_{\text{II}}\big)\,, \\
p_{\bar ns}^\mu &\sim Q\big(\lambda_{\text{II}}^2/\lambda_{\text{I}}, \lambda_{\text{I}}, \lambda_{\text{II}}\big) \sim \big(M_{\text{II}}^2/M_{\text{I}}, M_{\text{I}}, M_{\text{II}}\big)\,,
\end{aligned}
\tag{3.214}
$$

for the case in which $\lambda_{\text{I}} \ll \lambda_{\text{II}}$. These modes are known as collinear-soft modes since their scaling is somewhere in between the scaling of the collinear and soft degrees of freedom. The complete set of modes describing SCET_+ is made up by the collinear, and collinear-soft degrees of freedom from eqs. (3.213) and (3.214), supplemented by the usual soft mode given by

$$
p_s^\mu \sim Q\big(\lambda_{\text{I}}, \lambda_{\text{I}}, \lambda_{\text{I}}\big) \sim \big(M_{\text{I}}, M_{\text{I}}, M_{\text{I}}\big)\,,
\tag{3.215}
$$

and is shown in fig. 3.16. These degrees of freedom can be seen to reduce to the usual $SCET_{II}$ and $SCET_I$ sets of modes in the regions where $\lambda_I \sim \lambda_{II}$ and $\lambda_{II} \sim \sqrt{\lambda_I}$ respectively. In the first case, the soft mode and the two collinear-soft modes join to form a single soft degree of freedom. In the second case the collinear-soft modes are absorbed by the collinear modes and the scaling of the soft mode reduces to the ultrasoft scaling from $SCET_I$.

The emission of an arbitrary number of n-collinear gluons from an $\bar{n}$-collinear quark field is captured by the collinear Wilson line W_n given in eq. (3.204). In $SCET_+$, a similar Wilson line describing the emission of an arbitrary number of n-collinear-soft gluons is defined as

$$ V_n(x) = \text{P} \exp\left[ig_s \int_{-\infty}^{0} \mathrm{d}s\, A_{ns}^-(x + s\bar{n}) \right]. \tag{3.216} $$

In $SCET_{II}$, the interactions between soft gluons and n-collinear quarks give rise to off-shell propagators that have to be integrated out and yield soft Wilson lines in a similar fashion. For $SCET_+$, the same situation occurs when collinear-soft degrees of freedom interact with the n-collinear quark, so that an additional collinear-soft Wilson line is required to ensure gauge-invariance. This second collinear-soft Wilson line is given by

$$ X_n(x) = \text{P} \exp\left[ig_s \int_{-\infty}^{0} \mathrm{d}s\, A_{ns}^+(x + sn) \right], \tag{3.217} $$

in complete analogy to the soft Wilson line in eq. (3.204). In addition to the soft and collinear gauge transformations considered in eqs. (3.98) and (3.99) respectively, the collinear-soft gluons occurring in $SCET_+$ give rise to collinear-soft gauge transformations. These transformations leave the quark fields $\chi_n(x)$ as well as the soft Wilson lines $S_n(x)$ invariant and only transform the collinear-soft Wilson lines as [108]

$$ V_n(x) \xrightarrow{\;\mathcal{U}_{ns}\;} \mathbb{U}_{ns}(x)\, V_n(x) \,, $$

$$ V_{\bar{n}}(x) \xrightarrow{\;\mathcal{U}_{ns}\;} V_{\bar{n}}(x) \,, $$

$$ X_n(x) \xrightarrow{\;\mathcal{U}_{ns}\;} \mathbb{U}_{ns}(x)\, X_n(x) \,, $$

$$ X_{\bar{n}}(x) \xrightarrow{\;\mathcal{U}_{ns}\;} X_{\bar{n}}(x) \,, \tag{3.218} $$

and similarly for $\bar{n}$-collinear-soft gauge transformations. The matrix $\mathbb{U}_{ns}(x)$ appearing here is the n-collinear-soft equivalent of eq. (3.97). From these transformations it is clear that the collinear-soft Wilson lines must always occur

in the combination $V_n^\dagger(x) X_n(x)$ and $X_{\bar{n}}^\dagger(x) V_{\bar{n}}(x)$ to ensure the collinear-soft gauge invariance of SCET_+ currents. The collinear-soft Wilson lines $V_n(x)$ and $X_n(x)$ do not transform under collinear gauge transformations and transform in the same way as collinear fields do under soft gauge transformations, i.e as

$$V_n(x) \xrightarrow{\;\mathcal{U}_s\;} \mathcal{U}_s(x)\, V_n(x)\, \mathcal{U}_s^\dagger(x)\,,$$

$$V_{\bar{n}}(x) \xrightarrow{\;\mathcal{U}_s\;} \mathcal{U}_s(x)\, V_{\bar{n}}(x)\, \mathcal{U}_s^\dagger(x)\,,$$

$$X_n(x) \xrightarrow{\;\mathcal{U}_s\;} \mathcal{U}_s(x)\, X_n(x)\, \mathcal{U}_s^\dagger(x)\,,$$

$$X_{\bar{n}}(x) \xrightarrow{\;\mathcal{U}_s\;} \mathcal{U}_s(x)\, X_{\bar{n}}(x)\, \mathcal{U}_s^\dagger(x)\,. \tag{3.219}$$

To completely decouple the various degrees of freedom in the SCET_+ Lagrangian, a field redefinition similar to the BPS field redefinition in eq. (3.135) can be performed by [107]

$$V_n(x) \longrightarrow S_n(x)\, V_n(x)\, S_n^\dagger(x)\,,$$

$$V_{\bar{n}}(x) \longrightarrow S_{\bar{n}}(x)\, V_{\bar{n}}(x)\, S_{\bar{n}}^\dagger(x)\,,$$

$$X_n(x) \longrightarrow S_n(x)\, X_n(x)\, S_n^\dagger(x)\,,$$

$$X_{\bar{n}}(x) \longrightarrow S_{\bar{n}}(x)\, X_{\bar{n}}(x)\, S_{\bar{n}}^\dagger(x)\,, \tag{3.220}$$

after which the soft, collinear and collinear-soft modes no longer interact with one another.

To ensure the regulation of rapidity divergences in SCET_+, the same regulator that is used for the soft Wilson line $S_n(x)$ in $\mathrm{SCET}_{\mathrm{II}}$ in eq. (3.207) can be employed for the collinear-soft Wilson lines, leading to

$$V_n(x) = \sum_{\text{perms}} \exp\left[\frac{-g_s}{\mathcal{P}^-} w \left(\frac{|\mathcal{P}^-|}{\nu}\right)^{-\eta/2} A_{ns}^-(x)\right],$$

$$X_n(x) = \sum_{\text{perms}} \exp\left[\frac{-g_s}{\mathcal{P}^-} w \left(\frac{|\mathcal{P}^-|}{\nu}\right)^{-\eta/2} A_{ns}^+(x)\right], \tag{3.221}$$

where the momentum operators in the regulator have been expanded to leading power.

4

Joint two-dimensional resummation in q_T and 0-jettiness

In scattering processes that are subjected to the measurement of multiple observables, various types of logarithms can appear and may grow large, depending on the exact hierarchy between the measurements. In this chapter, the process of Drell-Yan $pp \to Z/\gamma^* \to \ell^+\ell^-$ is considered with a simultaneous measurement of the transverse momentum q_T of the signal lepton pair and the hadronic resolution variable 0-jettiness $\mathcal{T}$, also known as beam thrust [99,109]. The different possible hierarchies between these two measurements lead to distinct descriptions of the corresponding regions in phase space, each being described in a different way and leading to a different factorization formula.

The framework that enables the resummation of all logarithms involving both q_T and $\mathcal{T}$ is developed in this chapter through the construction of appropriate two-dimensional profile scales that combine the various regimes. In addition, perturbative uncertainties are assessed and the cross section obtained in the EFT approach for small values of the measured observables is matched to full QCD at large q_T and $\mathcal{T}$. This setup is flexible in the sense that both the matching procedure and the estimation of uncertainties can be changed in a fairly straightforward way.

Although Drell-Yan is used as an example, the methods developed in this chapter apply equally well to any other color-singlet production process. The matching procedure is even more generic and can be used for any type of two-dimensional resummation for which the correct EFT description is known for each relevant region of phase space. Furthermore, the framework can be used at any order for which the relevant perturbative ingredients are available[1].

This chapter starts in sec. 4.1 with a motivation describing the various available methods of resummation and its importance in the case of the simultaneous measurement of q_T and $\mathcal{T}$. In sec. 4.2 the relevant parametric regimes and

---

[1] Some double-differential ingredients required at NNLL$'$ and N^{3}LL are already known [110].

their respective factorizations are discussed. The combination of these various regimes into a single cross section prediction is addressed in sec. 4.3 and the obtained numerical predictions for the fully resummed, two-dimensional $(q_T, \mathcal{T})$ spectrum, obtained at NNLL+NLO accuracy, can be found in sec. 4.4. The material presented in this chapter reflects the research published in ref. [2].

4.1 Motivation

The increasing accuracy of measurements at the LHC places high demands on the precision and versatility of theoretical predictions. Fixed-order perturbation theory has proven to be a powerful tool to describe a large number of LHC processes, provided the measurement is sufficiently inclusive. With increasing data sets, however, more fine-grained measurements become possible and increasingly differential quantities come into focus. These more exclusive cross sections often involve several physical scales set by the hard interaction and the differential measurements or cuts applied on the final state. When these scales are widely separated, the perturbative series at each order is dominated by logarithms of their ratios. The resummation of these logarithms to all orders is crucial in order to arrive at the best possible predictions.

4.1.1 Methods of resummation

The resummation of the large logarithms that arise due to the separation of the various relevant scales in scattering processes may be carried out either through numerical or analytical means. Numerical methods that achieve resummation for measurements sensitive to soft and collinear radiation are known as parton-shower Monte Carlo event generators. These parton showers provide fully exclusive final states so that in principle any desired measurements or cuts can be imposed on the generated events. Existing implementations of parton showers are only formally accurate at about leading-logarithmic level, depending on the evolution variable of the shower, the specific observables under consideration and other implementation details[2]. Furthermore, estimating the perturbative uncertainties of parton showers is challenging, which is in part due to their limited perturbative accuracy. Popular examples of parton-shower Monte Carlo event generators include `Pythia` [112,113], `Herwig` [114–116], and `Sherpa` [117].

There are various analytic methods available for the higher-order resummation of infrared-sensitive observables. These include the Collins-Soper-Sterman

---

[2]A recent detailed analysis can be found in ref. [111].

(CSS) formalism [45, 118, 119], seminumerical methods based on the coherent-branching formalism [120–123], and methods using renormalization group evolution in effective field theories of QCD, such as SCET, which is described in detail in chap. 3. The common drawback of analytic resummation methods is that they only apply after a sufficient amount of emissions have been integrated over, which is why they have been primarily used for the resummation of single-differential observables. Their crucial advantage is that they can be systematically extended to higher orders, and theoretical uncertainties can be addressed in a more reliable way.

4.1.2 Double-differential resummation

There has been much progress in extending analytic resummation methods to cases involving multiple variables. One of the most well-known examples is the joint resummation of transverse momentum q_T and threshold (large x) logarithms [1, 124–129] which will be the main focus of chap. 5. Other examples include the combined resummation of q_T and small x [130], N-jettiness (or jet mass) with dijet invariant masses [107, 131], two angularities [132, 133], jet mass and jet radius [134], jet vetoes and jet rapidity [135, 136], or threshold and jet radius in inclusive jet production [137, 138]. Another well-understood case is when an infrared-sensitive measurement is separated into its contributions from mutually exclusive regions of phase space [96, 98, 139]. Finally, different infrared-sensitive measurements performed in different regions of phase space may require the resummation of nonglobal logarithms [140–145].

Most of these examples either involve different variables that effectively resolve different subsequent emissions, or involve a primary resummation variable that is modified by an auxiliary measurement or constraint. In contrast, the methods developed in the current chapter are aimed at resolving emissions at the same level by simultaneously measuring two independent, infrared-sensitive observables. Extending analytic resummation to such genuinely multi-dimensional resolution variables is of key theoretical concern, as it allows for a more complete description of the emission pattern beyond LL, effectively filling a gap between analytic resummation methods and parton showers. So far, this has been achieved at NNLL for the case of simultaneously measuring two angularities in e^+e^- collisions [133].

4.1.3 Process and measurements

Although the framework developed in this chapter applies to any type of color-singlet production at hadron colliders, the Drell-Yan process, $pp \to Z/\gamma^* \to \ell^+\ell^-$, will be considered for concreteness. Drell-Yan production was already

discussed in sec. 2.3.2 and a schematic diagram of the process can be found in fig. 2.6. The corresponding cross section is taken to be differential in the total invariant mass Q and rapidity Y of the lepton pair (or, in general, the color-singlet final state), defined in eqs. (2.37) and (2.38) respectively. In addition, the process is subjected to the measurement of two distinct resolution variables. One of the observables of interest is the total transverse momentum[3] q_T of the color-singlet final state. The other measured variable is 0-jettiness $\mathcal{T}$ (also known as beam thrust) [98, 99, 109, 146], defined as

$$\mathcal{T} \equiv \mathcal{T}_0 = \sum_i \min\left\{ \frac{2q_a \cdot k_i}{Q_a}, \frac{2q_b \cdot k_i}{Q_b} \right\}, \qquad (4.1)$$

where the sum runs over all particles i with momentum k_i in the final state, excluding the color-singlet final state. The massless reference momenta q_a and q_b are given by

$$q_a^\mu = \frac{Qe^{+Y}}{2}\, n^\mu \qquad \text{and} \qquad q_b^\mu = \frac{Qe^{-Y}}{2}\, \bar{n}^\mu\,, \qquad (4.2)$$

in accordance with eq. (2.31). Different variations of 0-jettiness exist, depending on the exact definition of the measure factors Q_a and Q_b, which need to obey $Q_a Q_b = Q^2$. Although all numerical results in the current chapter are obtained using the leptonic definition $Q_a = Q_b = Q$, the developed framework applies equally well to other definitions, so the measure factors will be kept generic.

Since all lightcone components of soft degrees of freedom are small and energetic particles with small transverse momenta must have either a small plus or minus component, the minimum prescription eq. (4.1) ensures that both their contributions to 0-jettiness are parametrically small. On the other hand, the plus and minus components of energetic radiation with large transverse momentum must both be sizable, so that the value of $\mathcal{T}$ is dominated by these emissions. Requiring $\mathcal{T}$ to be small then ensures the absence of any energetic radiation with large transverse momentum and can thus be used to veto central jets. In contrast, an imposed cut on q_T will act as a general jet veto, making no distinction between central and more forward jets.

Achieving the combined resummation in both q_T and $\mathcal{T}$ is conceptually important because these observables are prototypes for two large classes of infrared-sensitive observables. The measurement of q_T constrains the transverse momentum of initial-state radiation, while the measurement of 0-jettiness constrains its virtuality. These two types of observables give rise to different types

---

[3]Transverse with respect to the axis of the incoming proton beams.

of logarithmic structures and each is described by a different version of SCET. The measurement of $\mathcal{T}$ is correctly described by SCET_I, while SCET_II is the appropriate theory to describe the q_T measurement, as discussed in sec. 3.9. Beyond providing a prototype for combining resummations performed using SCET_I and SCET_II, the joint resummation of q_T and $\mathcal{T}$ is also of direct phenomenological interest. First of all, both are important variables individually. The measurement of $\mathcal{T}$ in bins of q_T [147] can probe the so-called underlying event in hadron collisions, i.e. the interactions between the remnants of the protons after the extraction of the partons that initiate the hard interaction. Furthermore, the `Geneva` Monte Carlo event generator [148, 149] uses $\mathcal{T}$ as the underlying jet resolution variable for the event generation, achieving NNLL$'$+NNLO accuracy in $\mathcal{T}$ in conjunction with fully showered and hadronized events. While other observables, such as q_T, benefit from the underlying high resummation order, they do not enjoy the same level of formal accuracy in `Geneva` as $\mathcal{T}$ itself. The joint resummation of $\mathcal{T}$ and q_T to a given order enables extending the event generation in `Geneva` to also be accurate in q_T to the same order.

The double-differential factorization for transverse momentum and 0-jettiness was first considered in ref. [108]. There the regions of phase space described by SCET_I and SCET_II were identified, together with the appropriate intermediate effective theory SCET_+, described in sec. 3.10, that connects them. The goal of this chapter is to develop an explicit matching procedure that combines the three different theories, SCET_I, SCET_+, and SCET_II, such that the resummation structure of each is recovered in its respective region of phase space. As an additional condition, the method is required to enable the recovery of the single-differential resummation in either one variable upon integration over the other.

4.2 Resummation framework

The relative contribution of the various degrees of freedom to both q_T and $\mathcal{T}$ depends on the specific hierarchy between these imposed measurements. Each hierarchy corresponds to a distinct region in phase space and in each of these regions the cross section can be factorized in a different way. There are two regimes in which only logarithms involving one of the two measurements are resummed, while the other observable acts as an auxiliary variable, inducing no additional logarithms. The third relevant regime is described by two distinct expansion parameters and its factorization formula can be used to resum logarithms of both types of measurements.
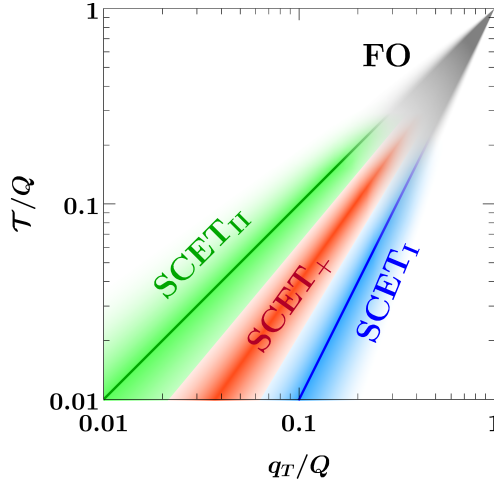
Figure 4.1 The relevant parametric regimes in the $(q_T, \mathcal{T})$ plane and their SCET descriptions. The solid lines correspond to the phase-space boundaries $q_T = \mathcal{T}$ (green) and $q_T = \sqrt{Q\mathcal{T}}$ (blue).

Extending the validity of these factorizations towards large values of the measurements requires matching them to fixed-order QCD results. Correctly describing this region entails turning off the resummation, which can be achieved through the use of profile scales. Certain variations of these profile scales and the common scale towards which all ingredients are evolved then allows one to estimate perturbative uncertainties due to both the resummation procedure and missing higher-order contributions.

4.2.1 Overview of parametric regimes

The various momentum scales relevant to the dynamical behavior of the initial-state radiation (ISR) are fixed through the simultaneous measurement of q_T and $\mathcal{T}$. The scale of the hard interaction is set by the invariant mass $Q \gg \Lambda_{\mathrm{QCD}}$ of the Drell-Yan lepton pair. The typical transverse momentum of emissions that recoil against the lepton pair is set by the measurement of $q_T \ll Q$. Soft or ultrasoft emissions can contribute to the measurement of $\mathcal{T} \ll Q$ at central rapidities ($|Y| \ll Y_{\mathrm{max}}$) via either of the projections onto q_a^μ and q_b^μ in eq. (4.1). The homogeneous scaling of their momentum components then implies that their characteristic transverse momentum is $p_s \sim \mathcal{T}$. In addition, collinear radiation with a typical energy $p_c^0 \sim Q$ can contribute to $\mathcal{T}$ through its small momentum component without upsetting the hierarchy $\mathcal{T} \ll Q$. These collinear emissions then have a typical transverse momentum $p_{c\perp} \sim \sqrt{Q\mathcal{T}}$.

The factorization and resummation structure of the cross section differential in both q_T and $\mathcal{T}$ depends on the parametric hierarchy between these scales. There are three relevant parametric regimes [108], which are illustrated in fig. 4.1.

In the first (blue) regime, representing the parametric hierarchy $\mathcal{T} \ll q_T \sim \sqrt{Q\mathcal{T}}$, ultrasoft emissions with transverse momentum $p_{us\perp} \sim \mathcal{T}$ and collinear emissions with transverse momentum $p_{c\perp} \sim \sqrt{Q\mathcal{T}}$ both contribute to the $\mathcal{T}$ measurement. Due to the parametric relation $p_{us\perp} \ll p_{c\perp}$, the q_T measurement is determined solely by collinear emissions. The appropriate EFT description for this regime is SCET$_\mathrm{I}$. It has the same renormalization group (RG) structure as the single-differential $\mathcal{T}$ spectrum, with q_T acting as an auxiliary variable. This SCET$_\mathrm{I}$ regime is discussed in more detail in sec. 4.2.2.

The opposite (green) regime corresponds to the hierarchy $\mathcal{T} \sim q_T \ll \sqrt{Q\mathcal{T}}$, in which both soft and collinear emissions have transverse momentum $p_{s\perp} \sim p_{c\perp} \sim q_T$ and thus contribute to the q_T measurement. On the other hand, only soft radiation at central rapidities contributes to $\mathcal{T}$, while the contribution from collinear radiation is suppressed. This regime is described by SCET$_\mathrm{II}$, whose RG structure is analogous to that of the single-differential q_T spectrum, with $\mathcal{T}$ as the auxiliary variable. This SCET$_\mathrm{II}$ regime is discussed in more detail in sec. 4.2.3.

The intermediate (red) regime in the "bulk", $\mathcal{T} \ll q_T \ll \sqrt{Q\mathcal{T}}$, shares features with both "boundary" cases. As in the SCET$_\mathrm{I}$ regime, central soft radiation contributes to $\mathcal{T}$, while, as in the SCET$_\mathrm{II}$ regime, collinear radiation contributes to q_T. This regime is described by two distinct expansion parameters, which gives rise to collinear-soft degrees of freedom that contribute to both measurements [108], as described in sec. 3.10. The relevant EFT description is provided by SCET$_+$, which in this case shares elements with both SCET$_\mathrm{I}$ and SCET$_\mathrm{II}$. The SCET$_+$ regime and its relation to the regimes on the two boundaries are discussed in sec. 4.2.4.

4.2.2 The SCET$_\mathrm{I}$ regime

In this regime, characterized by the hierarchy $\mathcal{T} \ll q_T \sim \sqrt{Q\mathcal{T}}$, both ultrasoft and collinear modes are constrained by $\mathcal{T}$, while only collinear modes can

contribute to q_T. The scaling of the relevant modes in this regime reads

$$n\text{-collinear:}\quad p_n^\mu \sim \left(\mathcal{T}, Q, \sqrt{Q\mathcal{T}}\right) \sim \left(\tfrac{q_T^2}{Q}, Q, q_T\right),$$

$$\bar{n}\text{-collinear:}\quad p_{\bar{n}}^\mu \sim \left(Q, \mathcal{T}, \sqrt{Q\mathcal{T}}\right) \sim \left(Q, \tfrac{q_T^2}{Q}, q_T\right),$$

$$\text{ultrasoft:}\quad p_{us}^\mu \sim \left(\mathcal{T}, \mathcal{T}, \mathcal{T}\right). \tag{4.3}$$

These degrees of freedom lead to a factorization formula for the cross section given by [99, 150]

$$\frac{\mathrm{d}\sigma_{\mathrm{I}}}{\mathrm{d}Q\,\mathrm{d}Y\,\mathrm{d}q_T\,\mathrm{d}\mathcal{T}} = H_{ij}(Q,\mu) \int \mathrm{d}t_a \int \mathrm{d}^2\vec{k}_a\, B_i(t_a, x_a, \vec{k}_a, \mu)$$

$$\times \int \mathrm{d}t_b \int \mathrm{d}^2\vec{k}_b\, B_j(t_b, x_b, \vec{k}_b, \mu) \int \mathrm{d}k\, S_{ij}(k, \mu)$$

$$\times \delta\big(q_T - |\vec{k}_a + \vec{k}_b|\big)\, \delta\Big(\mathcal{T} - \frac{t_a}{Q_a} - \frac{t_b}{Q_b} - k\Big), \tag{4.4}$$

which holds up to power corrections of the form [4]

$$\frac{\mathrm{d}\sigma}{\mathrm{d}Q\,\mathrm{d}Y\,\mathrm{d}q_T\,\mathrm{d}\mathcal{T}} = \frac{\mathrm{d}\sigma_{\mathrm{I}}}{\mathrm{d}Q\,\mathrm{d}Y\,\mathrm{d}q_T\,\mathrm{d}\mathcal{T}} \left[1 + \mathcal{O}\Big(\frac{\mathcal{T}}{Q}, \frac{q_T^2}{Q^2}, \frac{\mathcal{T}^2}{q_T^2}\Big)\right]. \tag{4.5}$$

The hard function $H_{ij}(Q,\mu)$ describes the short-distance scattering that produces the lepton pair through the off-shell γ^* or Z and is equal to the square of the matching coefficient determined in sec. 3.7.2, multiplied by the Born cross section given in eq. (B.3). In addition to Q, it depends on the partonic channel encoded by the subscripts i and j, which are implicitly summed over all relevant combinations of quark and antiquark flavors on the right-hand side of eq. (4.4).

The beam functions $B_i(t, x, \vec{k}_T, \mu)$ describe the extraction of a quark (or antiquark) from the proton with momentum fraction x, virtuality t, and transverse momentum $\vec{k}_T$. They are a more differential version of the beam functions described in eq. (3.182). The momentum fractions are directly related to Q and Y as given in eq. (2.39). The t and $\vec{k}_T$ encode the contribution of the collinear radiation to the measurement of $\mathcal{T}$ and q_T respectively, as captured by the measurement delta-functions on the last line of eq. (4.4). For $t \sim k_T^2 \gg \Lambda_{\mathrm{QCD}}^2$, these beam functions can be matched onto the PDFs [99, 100, 150] through

$$B_i(t, x, \vec{k}_T, \mu) = \sum_j \int_x^1 \frac{\mathrm{d}z}{z}\, \mathcal{I}_{ij}(t, z, \vec{k}_T, \mu)\, f_j\Big(\frac{x}{z}, \mu\Big) \left[1 + \mathcal{O}\Big(\frac{\Lambda_{\mathrm{QCD}}^2}{t}, \frac{\Lambda_{\mathrm{QCD}}^2}{k_T^2}\Big)\right].$$

$$\tag{4.6}$$

---

[4]Lorentz invariance suggests that power corrections in q_T always appear in terms of q_T^2.

The soft function $S_{ij}(k, \mu)$ was already mentioned in sec. 3.8.1. It encodes the contribution from soft radiation to the 0-jettiness measurement and depends on the color charge of the colliding partons. Explicit expressions for the hard, beam and soft functions can be found up to 1-loop accuracy in app. B.

The factorization in eq. (4.4) separates the physics at the canonical SCET$_\mathrm{I}$ scales given by

$$\mu_H^\mathrm{I} \sim Q, \qquad \mu_B^\mathrm{I} \sim \sqrt{Q\mathcal{T}}, \qquad \mu_S^\mathrm{I} \sim \mathcal{T}. \qquad (4.7)$$

By evaluating all the perturbative ingredients at their respective natural scales and evolving them to a common scale, all logarithms of $\mathcal{T}/Q \sim \mu_S^\mathrm{I}/\mu_H^\mathrm{I} \sim (\mu_B^\mathrm{I}/\mu_H^\mathrm{I})^2 \sim (\mu_S^\mathrm{I}/\mu_B^\mathrm{I})^2$ are resummed.

The hard and soft function in eq. (4.4) are the same as those appearing in the single-differential $\mathcal{T}$ spectrum and do not depend on q_T. The RG consistency of the cross section then implies that the RGE of the double-differential beam functions must also be independent of q_T, such that the overall RG structure of the cross section is equivalent to the single-differential case. This leads to the conclusion that q_T takes the role of an auxiliary measurement in the SCET$_\mathrm{I}$ resummation and no large logarithms of q_T will appear in the cross section as long as the parametric relation $q_T \sim \sqrt{Q\mathcal{T}}$ is satisfied.

The cross section in eq. (4.4) nevertheless provides a nontrivial and genuinely double-differential extension of the single-differential case. This is already visible from the structure of the power corrections in eq. (4.5). Furthermore, the q_T dependence does affect and is affected by the $\mathcal{T}$ resummation because the double-differential beam functions enter in a convolution with the beam and soft evolution functions. Physically, they account for the total q_T recoil from all collinear emissions that are being resummed in $\mathcal{T}$.

The factorization of the double-differential spectrum in eq. (4.4), and the factorization formulas in the following sections, do not account for effects from Glauber gluon exchanges, in which spectator partons interact with one another. These exchanges can connect partons from different hadrons and may spoil factorization. However, their perturbative contribution is expected to enter only at $\mathcal{O}(\alpha_s^4)$ (corresponding to N^{4}LL$'$) [151, 152], which is well beyond the precision of the currently available perturbative ingredients. If so desired, they may be included using the Glauber operator framework from ref. [153].

Due to the power corrections shown in eq. (4.5), the factorization theorem in eq. (4.4) breaks down for large $\mathcal{T} \sim q_T^2/Q \sim Q$. To extend the description of the cross section to be valid for these large values of the measured variables,
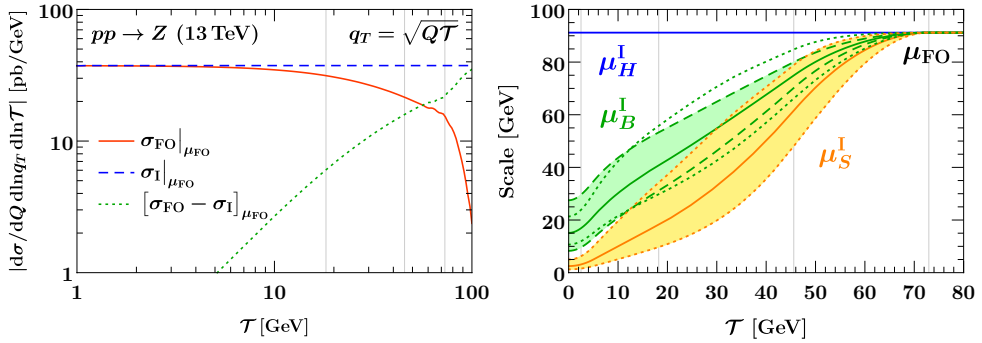
Figure 4.2 Left: Comparison of singular and nonsingular contributions to the fixed $\mathcal{O}(\alpha_s)$ double spectrum as a function of $\mathcal{T}$, with $q_T = \sqrt{Q\mathcal{T}}$ kept fixed. The solid red line shows the full QCD result and the dashed blue line the singular contributions contained in the SCET$_\mathrm{I}$ result eq. (4.4). The dotted green line shows their difference, which corresponds to the power corrections indicated in eq. (4.5). Right: SCET$_\mathrm{I}$ profile scales and their associated variations. The dotted lines (and the yellow band) indicate common up/down variations of μ_S^I and μ_B^I from varying α. The dashed lines (and the green band) are variations of β that only act on μ_B^I. In both plots, the thin vertical lines correspond to the transition points (x_0, x_1, x_2, x_3) given in the text.

the power corrections have to be reinstated. This can be achieved by matching to the full fixed-order result using a standard additive matching given by

$$\mathrm{d}\sigma_\mathrm{I}^{\mathrm{match}} = \mathrm{d}\sigma_\mathrm{I}\big|_{\mu^\mathrm{I}} + \big[\mathrm{d}\sigma_\mathrm{FO} - \mathrm{d}\sigma_\mathrm{I}\big]_{\mu_\mathrm{FO}}. \tag{4.8}$$

Here the abbreviation $\mathrm{d}\sigma \equiv \mathrm{d}\sigma/(\mathrm{d}Q\,\mathrm{d}Y\,\mathrm{d}q_T\,\mathrm{d}\mathcal{T})$ has been employed and $\mathrm{d}\sigma_\mathrm{FO}$ denotes the fixed-order cross section[5] in full QCD. The subscripts on the scales on the right-hand side indicate whether $\mathrm{d}\sigma_\mathrm{I}$ is RG evolved using the SCET$_\mathrm{I}$ resummation scales μ^I (whose precise definitions are discussed below in eq. (4.10)), or whether it is evaluated with all scales set to a common fixed-order scale μ_FO.

By construction, $\mathrm{d}\sigma_\mathrm{I}$ evaluated at a common scale μ_FO exactly reproduces the singular limit of $\mathrm{d}\sigma_\mathrm{FO}$, such that the term in square brackets in eq. (4.8) is a purely nonsingular power correction at small $\mathcal{T} \ll Q$, which can simply be added to the resummed cross section. This is checked explicitly at fixed $\mathcal{O}(\alpha_s)$ in the left panel of fig. 4.2. The full QCD result (solid red) is compared to the SCET$_\mathrm{I}$ singular limit (dashed blue) as a function of $\mathcal{T}$, while keeping $q_T = \sqrt{Q\mathcal{T}}$ fixed to ensure that all classes of power corrections in eq. (4.5)

---

[5]The cross section to a fixed, predetermined order in α_s, i.e. without any resummation.

uniformly vanish as $\mathcal{T} \to 0$. This is indeed satisfied, as the difference (dotted green) vanishes like a power.

For $\mathcal{T} \sim Q$, the SCET$_\mathrm{I}$ singular contribution and the power corrections are of the same size, implying that the resummation must be turned off to not upset the $\mathcal{O}(1)$ cancellation between them and correctly reproduce the fixed-order result. This is commonly achieved by using profile scales [103, 154], i.e. by having $\mu_B^\mathrm{I} \equiv \mu_B^\mathrm{I}(\mathcal{T})$ and $\mu_S^\mathrm{I} \equiv \mu_S^\mathrm{I}(\mathcal{T})$ transition from their canonical values from eq. (4.7) at small $\mathcal{T}$ to a common high scale for large $\mathcal{T}$. This is schematically represented by

$$\begin{aligned}
\mu_B^\mathrm{I}(\mathcal{T}) &\longrightarrow \mu_H^\mathrm{I} = \mu_\mathrm{FO} && \text{for} && \mathcal{T} \longrightarrow Q\,, \\
\mu_S^\mathrm{I}(\mathcal{T}) &\longrightarrow \mu_H^\mathrm{I} = \mu_\mathrm{FO} && \text{for} && \mathcal{T} \longrightarrow Q\,.
\end{aligned} \tag{4.9}$$

As a result, the first and third term in eq. (4.8) exactly cancel in this limit, so the matched result reproduces $\mathrm{d}\sigma_\mathrm{FO}$ as desired.

Due to the equivalent RG structure, the profile scales used for the single-differential structure may be employed in the double-differential case as well. The profile scales developed for the closely related case of SCET$_\mathrm{I}$-like jet vetoes in ref. [155] and used for the single-differential $\mathcal{T}$ resummation in `Geneva` [149] are given by

$$\mu_S^\mathrm{I} = \mu_\mathrm{FO}\, f_\mathrm{run}^\mathrm{I}\!\left(\frac{\mathcal{T}}{Q}\right), \qquad \mu_B^\mathrm{I} = \mu_\mathrm{FO} \left[f_\mathrm{run}^\mathrm{I}\!\left(\frac{\mathcal{T}}{Q}\right) \right]^{1/2} \qquad \text{and} \qquad \mu_H^\mathrm{I} = \mu_\mathrm{FO}\,, \tag{4.10}$$

with the profile function $f_\mathrm{run}^\mathrm{I}$ given by [156]

$$f_\mathrm{run}^\mathrm{I}(x) = \begin{cases} x_0\left(1 + \frac{x^2}{4x_0^2}\right) & x \le 2x_0\,, \\ x & 2x_0 < x \le x_1\,, \\ x + \frac{(2-x_2-x_3)(x-x_1)^2}{2(x_2-x_1)(x_3-x_1)} & x_1 < x \le x_2\,, \\ 1 - \frac{(2-x_1-x_2)(x-x_3)^2}{2(x_3-x_1)(x_3-x_2)} & x_2 < x \le x_3\,, \\ 1 & x_3 < x\,. \end{cases} \tag{4.11}$$

Based on fig. 4.2, the transition points governing the turn-off towards the fixed-order regime $x \sim 1$ are chosen as $(x_1, x_2, x_3) = (0.2, 0.5, 0.8)$. In addition, eq. (4.11) turns off the resummation in the nonperturbative region $x \lesssim 2x_0$, where $x_0 = 1\,\mathrm{GeV}/Q$ is chosen. For μ_FO itself, the central scale $\mu_\mathrm{FO} = Q$ is used. The central scale choices are illustrated as solid lines in the right panel

of fig. 4.2.

The perturbative uncertainties in $d\sigma_{\mathrm{I}}^{\mathrm{match}}$ are estimated by considering two different sources. The first uncertainty contribution, Δ_{I}, is inherent to the $\mathrm{SCET_I}$ resummation. It is estimated by varying the individual $\mathrm{SCET_I}$ scales while keeping μ_{FO} fixed, effectively probing the tower of higher-order logarithms that are being resummed. For this, the profile scale variations [155] defined by

$$\mu_S^{\mathrm{I}} = \mu_{\mathrm{FO}}\Big[f_{\mathrm{vary}}\Big(\frac{\mathcal{T}}{Q}\Big)\Big]^\alpha f_{\mathrm{run}}^{\mathrm{I}}\Big(\frac{\mathcal{T}}{Q}\Big)\,,$$

$$\mu_B^{\mathrm{I}} = \mu_{\mathrm{FO}}\bigg\{\Big[f_{\mathrm{vary}}\Big(\frac{\mathcal{T}}{Q}\Big)\Big]^\alpha f_{\mathrm{run}}^{\mathrm{I}}\Big(\frac{\mathcal{T}}{Q}\Big)\bigg\}^{1/2-\beta}\,, \tag{4.12}$$

are used. Here $\alpha = \beta = 0$ corresponds to the central scale choice in eq. (4.10) and the variation factor is defined as

$$f_{\mathrm{vary}}(x) = \begin{cases} 2(1 - x^2/x_3^2) & 0 \le x < x_3/2\,, \\ 1 + 2(1 - x/x_3)^2 & x_3/2 \le x < x_3\,, \\ 1 & x_3 \le x\,. \end{cases} \tag{4.13}$$

It approaches a factor of two in the resummation region at small x and reduces to unity toward the fixed-order regime at $x = x_3$, where the resummation is turned off. The estimate for Δ_{I} is obtained by computing $d\sigma_{\mathrm{match}}^{\mathrm{I}}$ for each of the four profile scale variations

$$(\alpha, \beta) = \big\{(+1, 0), (-1, 0), (0, +1/6), (0, -1/6)\big\}\,, \tag{4.14}$$

and taking the maximum absolute deviation from the central result. These variations are also indicated in the right panel of fig. 4.2. No explicit variations of the transition points are performed since they are found to have a subdominant effect.

For the second uncertainty contribution, Δ_{FO}, common variations of μ_{FO} up and down by a factor of two in all ingredients of eq. (4.8) are considered. Since μ_{FO} enters in all μ^{I} scales as a common overall factor, each inherits the same variation, which leaves all resummed logarithms invariant. Hence, the μ_{FO} variation effectively probes the effect of missing higher-order corrections in the fixed-order contributions. The final uncertainty estimate for $d\sigma_{\mathrm{I}}^{\mathrm{match}}$ is obtained by adding both contributions in quadrature,

$$\Delta_{\mathrm{total}}^{\mathrm{I}} = \Delta_{\mathrm{I}} \oplus \Delta_{\mathrm{FO}} \equiv \big(\Delta_{\mathrm{I}}^2 + \Delta_{\mathrm{FO}}^2\big)^{1/2}. \tag{4.15}$$

The matched result $d\sigma_{\mathrm{I}}^{\mathrm{match}}$ in eq. (4.8) on its own constitutes a prediction for the double-differential spectrum that covers the part of phase space described by the parametric relation $q_T \sim \sqrt{Q\mathcal{T}}$.

4.2.3 The SCET$_\mathrm{II}$ regime

In this regime, characterized by the hierarchy $\mathcal{T} \sim q_T \ll \sqrt{Q\mathcal{T}}$, both soft and collinear emissions are constrained by q_T. Only soft radiation is constrained by the $\mathcal{T}$ measurement, while collinear radiation remains unaffected by it. The relevant modes in this regime scale as

$$n\text{-collinear:} \quad p_n^\mu \sim \Big(\frac{q_T^2}{Q}, Q, q_T\Big)\,,$$

$$\bar{n}\text{-collinear:} \quad p_{\bar{n}}^\mu \sim \Big(Q, \frac{q_T^2}{Q}, q_T\Big)\,,$$

$$\text{ultrasoft:} \quad p_{us}^\mu \sim \big(q_T, q_T, q_T\big) \sim \big(\mathcal{T}, \mathcal{T}, \mathcal{T}\big)\,. \tag{4.16}$$

In this case, the cross section factorizes as [108]

$$\frac{\mathrm{d}\sigma_\mathrm{II}}{\mathrm{d}Q\,\mathrm{d}Y\,\mathrm{d}q_T\,\mathrm{d}\mathcal{T}} = H_{ij}(Q,\mu) \int \mathrm{d}^2\vec{k}_a\, B_i(\omega_a, \vec{k}_a, \mu, \nu) \int \mathrm{d}^2\vec{k}_b\, B_j(\omega_b, \vec{k}_b, \mu, \nu)$$

$$\times \int \mathrm{d}k \int \mathrm{d}^2\vec{k}_s\, S_{ij}(k, \vec{k}_s, \mu, \nu)$$

$$\times \delta\big(q_T - |\vec{k}_a + \vec{k}_b + \vec{k}_s|\big)\, \delta\big(\mathcal{T} - k\big)\,. \tag{4.17}$$

This factorization formula receives power corrections of the form

$$\frac{\mathrm{d}\sigma}{\mathrm{d}Q\,\mathrm{d}Y\,\mathrm{d}q_T\,\mathrm{d}\mathcal{T}} = \frac{\mathrm{d}\sigma_\mathrm{II}}{\mathrm{d}Q\,\mathrm{d}Y\,\mathrm{d}q_T\,\mathrm{d}\mathcal{T}} \left[1 + \mathcal{O}\Big(\frac{\mathcal{T}}{Q}, \frac{q_T^2}{\mathcal{T}Q}\Big)\right]\,. \tag{4.18}$$

The hard function $H_{ij}(Q,\mu)$ is the same as in eq. (4.4). The beam functions $B_i(\omega, \vec{k}_T, \mu, \nu)$ are the same transverse-momentum-dependent beam functions as in the single-differential q_T spectrum. The large momentum components ω in eq. (4.17) are given by

$$\omega_a = Qe^{+Y} = x_a E_\mathrm{cm} \qquad \text{and} \qquad \omega_b = Qe^{-Y} = x_b E_\mathrm{cm}\,, \tag{4.19}$$

and the trivial dependence of the beam function on E_cm is suppressed. For $k_T^2 \gg \Lambda_\mathrm{QCD}^2$, the beam functions satisfy a matching relation similar to the one in eq. (4.6) [49, 99, 105, 157–160], given by

$$B_i(\omega, \vec{k}_T, \mu, \nu) = \sum_j \int_x^1 \frac{\mathrm{d}z}{z}\, \mathcal{I}_{ij}(\omega, \vec{k}_T, z, \mu, \nu)\, f_j\Big(\frac{\omega}{zE_\mathrm{cm}}, \mu\Big) \left[1 + \mathcal{O}\Big(\frac{\Lambda_\mathrm{QCD}^2}{k_T^2}\Big)\right]\,. \tag{4.20}$$

The double-differential soft function $S_{ij}(k, \vec{k}_s, \mu, \nu)$ encodes the contribution of soft radiation to both $\mathcal{T}$ and q_T. The explicit expressions of the various perturbative ingredients are gathered in app. B.

The RG consistency of the cross section implies that both the μ and ν RGE of the double-differential soft function do not depend on $\mathcal{T}$. Hence, the overall RG structure of the double-differential cross section is equivalent to the single-differential q_T spectrum, with $\mathcal{T}$ acting as an auxiliary measurement. The factorization in eq. (4.17) separates the physics at the canonical SCET_{II} invariant-mass and rapidity scales

$$\mu_H^{\text{II}} \sim Q \,, \qquad \mu_B^{\text{II}} \sim q_T \,, \qquad \mu_S^{\text{II}} \sim q_T \,,$$
$$\nu_B^{\text{II}} \sim Q \,, \qquad \nu_S^{\text{II}} \sim q_T \,. \tag{4.21}$$

It has been known for a long time [161] that directly resumming the logarithms of q_T/Q in momentum space is challenging due to the vectorial nature of $\vec{q}_T$, though by now approaches for doing so exist [162, 163]. The same complications arise here for the double-differential spectrum. This issue can be bypassed, is as commonly done, by carrying out the resummation in a conjugate space known as impact parameter (b_T) space [94, 95, 157, 164]. The Fourier transform from $\vec{q}_T$ to $\vec{b}_T$ turns the vectorial convolutions in eq. (4.17) into simple products at $b_T \equiv |\vec{b}_T|$. The canonical SCET_{II} scales in b_T-space are then given by

$$\mu_H^{\text{II}} \sim Q \,, \qquad \mu_B^{\text{II}} \sim b_0/b_T \,, \qquad \mu_S^{\text{II}} \sim b_0/b_T \,,$$
$$\nu_B^{\text{II}} \sim Q \,, \qquad \nu_S^{\text{II}} \sim b_0/b_T \,, \tag{4.22}$$

where the inclusion of $b_0 \equiv 2e^{-\gamma_E} \approx 1.12291$ is conventional.

By evaluating the functions in the factorization theorem at their canonical scales and evolving them to a common scale in both μ and ν, all logarithms of $(b_0/b_T)/Q \sim \mu_B/\mu_H \sim \mu_S/\mu_H \sim \nu_S/\nu_B$ are resummed. In ref. [163] it was shown that the canonical resummation in b_T space is in fact equivalent to the exact solution of the RGE in momentum space, except for the fact that one effectively uses a shifted set of finite terms in the boundary conditions (similar to the difference between renormalization schemes).

A characteristic feature of the resummed q_T spectrum is that the rapidity anomalous dimension γ_ν^i depends on the scale μ through α_s and is thus itself perturbatively renormalized at its intrinsic scale μ_0, so that for scales $\mu \neq \mu_0$ it requires resummation [105]. Solving its RGE leads to the expression

$$\tilde{\gamma}_\nu^i(b_T, \mu) = -4\eta_\Gamma^i(\mu_0, \mu) + \tilde{\gamma}_{\nu,\text{FO}}^i(b_T, \mu_0) + \tilde{\gamma}_{\nu,\text{np}}^i(b_T) \,, \tag{4.23}$$

where all logarithms of μ/μ_0 are resummed inside the evolution kernel η_Γ^i defined in eq. (3.193). The canonical choice of μ_0 that eliminates all large logarithms in the fixed-order boundary condition $\tilde{\gamma}_{\nu,\text{FO}}(b_T, \mu_0)$ is given by

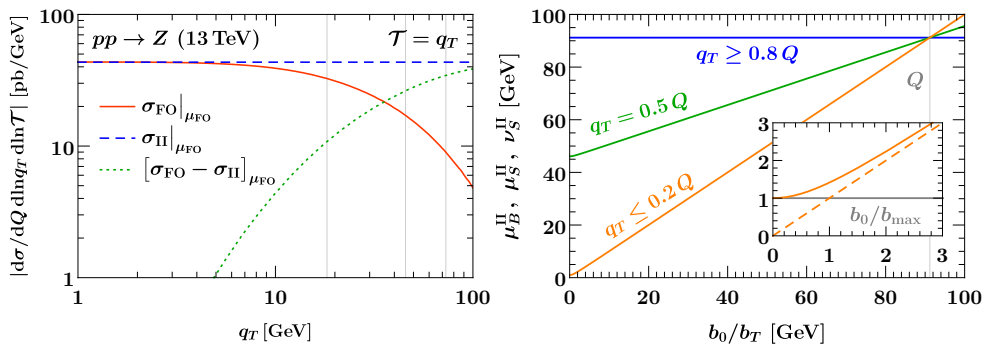$$\mu_0 \sim b_0/b_T \,. \tag{4.24}$$

Figure 4.3 Left: Comparison of singular and nonsingular contributions to the fixed $\mathcal{O}(\alpha_s)$ double spectrum as a function of q_T, with $\mathcal{T} = q_T$ kept fixed. The solid red line shows the full QCD result and the dashed blue line the singular contributions contained in the SCET$_{\rm II}$ result in eq. (4.17). The dotted green line shows their difference, which corresponds to the power corrections indicated in eq. (4.18). The thin vertical lines correspond to the transition points (x_1, x_2, x_3) given in the text. Right: SCET$_{\rm II}$ hybrid profile scales as a function of b_0/b_T for representative values of q_T. The inset shows the behavior of the profile in the nonperturbative region $b_0/b_T \sim \Lambda_{\rm QCD}$, where the dashed orange line indicates the canonical value of $\mu_B^{\rm II}, \mu_S^{\rm II}$ and $\nu_S^{\rm II}$.

By choosing μ_0 as a function of b_T such that it freezes out to a perturbative value at large b_T, the Landau pole at $b_T \sim 1/\Lambda_{\rm QCD}$ is avoided. The mismatch to the full result that this leads to can in principle be captured by a nonperturbative model $\tilde{\gamma}_{\nu,\rm np}^i(b_T)$, which can be extracted from experimental measurements at small q_T. Recently, it was shown that it could also be determined from lattice calculations [165]. For the purpose of this chapter it will be set to zero for simplicity. The explicit scale choice made for μ_0 is given in eq. (4.27).

The description of the cross section in eq. (4.17) can be extended to the fixed-order region $q_T \sim \mathcal{T} \sim Q$ through an additive matching given by

$$d\sigma_{\rm II}^{\rm match} = d\sigma_{\rm II}\big|_{\mu^{\rm II}} + \big[d\sigma_{\rm FO} - d\sigma_{\rm II}\big]_{\mu_{\rm FO}}, \qquad (4.25)$$

in analogy with the SCET$_{\rm I}$ case in eq. (4.8). Here the subscript $\mu^{\rm II}$ indicates that $d\sigma_{\rm II}$ is evaluated at the SCET$_{\rm II}$ resummation scales $\mu^{\rm II}$ (given below in eq. (4.27)) in b_T space, and then numerically Fourier transformed back to momentum space. The subscript $\mu_{\rm FO}$ indicates that it is instead evaluated at a common fixed-order scale $\mu_{\rm FO}$, which can be done directly in momentum space. Analogous to the discussion for SCET$_{\rm I}$, the term in square brackets in

eq. (4.25) is by construction a purely nonsingular power correction for small q_T. This is illustrated in the left panel of fig. 4.3, which shows that the difference (green dotted) between the full QCD result (solid red) and the SCET$_{\text{II}}$ singular result (dashed blue) indeed vanishes like a power as $q_T \to 0$ along the line of fixed $\mathcal{T} = q_T$.

Approaching $q_T \sim \mathcal{T} \sim Q$, the q_T resummation must again be turned off to ensure that the delicate cancellations between singular and nonsingular contributions occur and to properly recover the correct fixed-order result for the spectrum. This can be achieved by constructing hybrid profile scales that depend on both b_T and q_T, and undergo a continuous deformation away from the canonical b_T scales in eq. (4.21) as a function of the target q_T value. This is schematically represented by

$$\mu_{B,S}^{\text{II}}(q_T, b_T) \longrightarrow \mu_H^{\text{II}} = \mu_{\text{FO}} \qquad \text{for} \qquad q_T \longrightarrow Q\,,$$
$$\nu_{B,S}^{\text{II}}(q_T, b_T) \longrightarrow \mu_H^{\text{II}} = \mu_{\text{FO}} \qquad \text{for} \qquad q_T \longrightarrow Q\,. \tag{4.26}$$

The scale μ_0 does not need to asymptote to μ_{FO} towards large q_T because its effect on the matched result is already turned off as $\nu_S^{\text{II}} \to \nu_B^{\text{II}}$. In this limit, the first and last term in eq. (4.25) exactly cancel, leaving the fixed-order result $\mathrm{d}\sigma_{\text{FO}}$. A set of central scales that achieves the conditions in eq. (4.26) in a relatively simple way is given by

$$\mu_H^{\text{II}} = \nu_B^{\text{II}} = \mu_{\text{FO}}\,,$$
$$\mu_B^{\text{II}} = \mu_S^{\text{II}} = \nu_S^{\text{II}} = \mu_{\text{FO}}\, f_{\text{run}}^{\text{II}}\left(\frac{q_T}{Q}, \frac{b_0}{b^*(b_T)\, Q}\right),$$
$$\mu_0 = \frac{b_0}{b^*(b_T)}\,, \tag{4.27}$$

where $f_{\text{run}}^{\text{II}}$ is a hybrid profile function given by

$$f_{\text{run}}^{\text{II}}(x, y) = 1 + g_{\text{run}}(x)(y - 1)\,. \tag{4.28}$$

This function controls the amount of resummation by adjusting the slope of the scales in b_T space as a function of q_T/Q via the function

$$g_{\text{run}}(x) = \begin{cases} 1 & 0 < x \le x_1\,, \\ 1 - \frac{(x-x_1)^2}{(x_2-x_1)(x_3-x_1)} & x_1 < x \le x_2\,, \\ \frac{(x-x_3)^2}{(x_3-x_1)(x_3-x_2)} & x_2 < x \le x_3\,, \\ 0 & x_3 \le x\,. \end{cases} \tag{4.29}$$

As a result, for $q_T \le x_1 Q$ the slope is equal to unity, yielding the canonical resummation, while for $q_T \ge x_3 Q$, the slope vanishes so the resummation is

fully turned off. In between, the slope smoothly transitions from one to zero, which transitions the resummation from being canonical to being turned off. This is illustrated in the right panel of fig. 4.3. The same transition points as for SCET$_\mathrm{I}$ are used, i.e. $(x_1, x_2, x_3) = (0.2, 0.5, 0.8)$, which is supported by fig. 4.3. This approach differs from the hybrid profile scales introduced in ref. [166]. While the latter also satisfy the requirements in eq. (4.26), they do not reproduce the exact canonical b_T-space scales for $q_T \ll Q$ because they introduce a profile shape directly in b_T space.

As discussed below eq. (4.24), a nonperturbative prescription is required when the canonical value of μ_0 (or μ_S^II, or μ_B^II) approaches the Landau pole at $b_0/b_T \sim \Lambda_\mathrm{QCD}$. This is achieved by evaluating the hybrid scales at $b^*(b_T)$, defined by

$$b^*(b_T) = \frac{b_T}{\sqrt{1 + b_T^2/b_\mathrm{max}^2}} \,, \tag{4.30}$$

rather than at b_T itself. Here $b_0/b_\mathrm{max} \gtrsim \Lambda_\mathrm{QCD}$ ensures that all scales are canonical for small $b_T \approx b^*$, but remain perturbative for large b_T where $b^* \to b_\mathrm{max}$, as shown in the inset in the right panel of fig. 4.3. In line with the choice of nonperturbative turn-off parameter in the SCET$_\mathrm{I}$ case, the value

$$b_0/b_\mathrm{max} = 1\,\mathrm{GeV} \,, \tag{4.31}$$

is adopted. The functional form of eq. (4.30) is the same as in the standard b^* prescription [95, 164], although any other functional form with the same asymptotic behavior is also viable. It must be stressed, however, that b^* in the current setup only affects the scales, so it essentially serves the same purpose as the x_0 nonperturbative cutoff in the SCET$_\mathrm{I}$ scales in eq. (4.11). By contrast, the standard b^* prescription corresponds to a *global* replacement of b_T by b^*, including the measurement itself. For the single-differential q_T spectrum, this global replacement induces power corrections of $\mathcal{O}(b_T^2/b_\mathrm{max}^2)$ that scale like a generic nonperturbative contribution. While these might complicate the extraction of nonperturbative model parameters from data [167], they are not a critical issue.

For the double-differential case, however, the standard b^* prescription does in fact not work. This is because substituting b^* for b_T in the physical measurement, at least at fixed-order, renders Fourier integrals of the double-differential SCET$_\mathrm{II}$ soft function divergent. This can be seen from eqs. (B.36) and (B.37), which only depend on $x = b_T \mathcal{T}$. Substituting $b_T \to b^*$ makes them asymptote to a constant for any $\mathcal{T}$, upsetting their required asymptotic behavior $\sim 1/x^2$.

The resummation uncertainties for $\mathrm{d}\sigma_\mathrm{II}^\mathrm{match}$ are estimated by adopting the set of profile scale variations introduced for the SCET$_\mathrm{II}$-like jet veto in ref. [156].
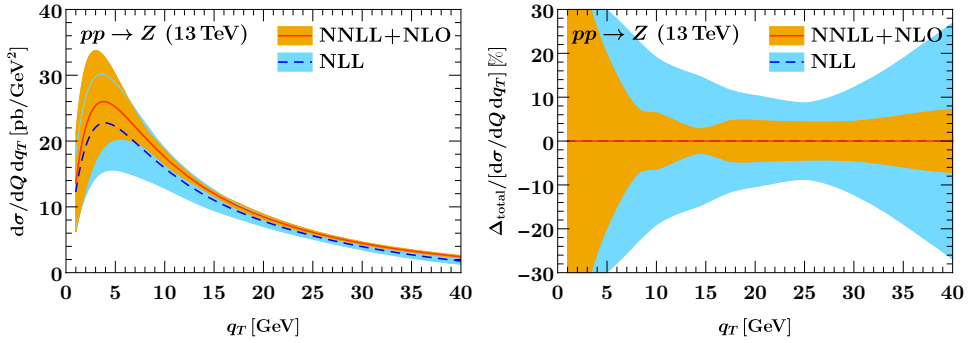
Figure 4.4 The single-differential q_T spectrum at NLL (blue) and NNLL+NLO (red with orange band), using the q_T resummation method described in the text. The bands indicate $\Delta_{\mathrm{II}} \oplus \Delta_{\mathrm{FO}}$. In the right panel, the uncertainties are shown as percent differences relative to the central result at each order.

They are given by

$$
\mu_S^{\mathrm{II}} = \mu_{\mathrm{FO}} \left[f_{\mathrm{vary}}\left(\frac{q_T}{Q}\right) \right]^{v_{\mu_S}} f_{\mathrm{run}}^{\mathrm{II}}\left(\frac{q_T}{Q}, \frac{b_0}{b^* Q}\right),
$$
$$
\nu_S^{\mathrm{II}} = \mu_{\mathrm{FO}} \left[f_{\mathrm{vary}}\left(\frac{q_T}{Q}\right) \right]^{v_{\nu_S}} f_{\mathrm{run}}^{\mathrm{II}}\left(\frac{q_T}{Q}, \frac{b_0}{b^* Q}\right),
$$
$$
\mu_B^{\mathrm{II}} = \mu_{\mathrm{FO}} \left[f_{\mathrm{vary}}\left(\frac{q_T}{Q}\right) \right]^{v_{\mu_B}} f_{\mathrm{run}}^{\mathrm{II}}\left(\frac{q_T}{Q}, \frac{b_0}{b^* Q}\right),
$$
$$
\nu_B^{\mathrm{II}} = \mu_{\mathrm{FO}} \left[f_{\mathrm{vary}}\left(\frac{q_T}{Q}\right) \right]^{v_{\nu_B}}, \tag{4.32}
$$

where each of the four variation exponents can be $v_i = \{+1, 0, -1\}$, and f_{vary} was given in eq. (4.13). The central scale choice corresponds to

$$
(v_{\mu_S}, v_{\nu_S}, v_{\mu_B}, v_{\nu_B}) = (0, 0, 0, 0), \tag{4.33}
$$

and there are in principle 80 possible different combinations of the v_i. Since the arguments of the resummed logarithms are ratios of scales, some combinations of scale variations will lead to variations of these arguments that are larger than a factor of two, and should therefore be excluded [156]. After dropping these combinations, only 36 different scale variations for the $\mathrm{SCET_{II}}$ regime are left. To probe the uncertainty in the nonperturbative prescription, two independent variations of $b_0/b_{\mathrm{max}} = \{0.5\,\mathrm{GeV}, 2\,\mathrm{GeV}\}$ are added to these, after which the $\mathrm{SCET_{II}}$ resummation uncertainty Δ_{II} is determined as the maximum absolute deviation from the central result among all 38 variations. Variations of the

transition points are not considered since their contribution is again found to be subdominant.

As for SCET$_\text{I}$, Δ_FO is estimated by overall variations of μ_FO by a factor of two, which is inherited by all the SCET$_\text{II}$ scales, so it probes the fixed-order uncertainties while leaving the resummed logarithms invariant. The total uncertainty estimate for $d\sigma_\text{II}^\text{match}$ is then obtained as

$$\Delta_\text{total}^\text{II} = \Delta_\text{II} \oplus \Delta_\text{FO} \,. \tag{4.34}$$

The matched result $d\sigma_\text{II}^\text{match}$ in eq. (4.25) provides a prediction for the double-differential spectrum that covers the part of phase space where $\mathcal{T} \sim q_T$.

Since this is a novel method of performing the q_T resummation, it makes sense to inspect its impact on the single-differential q_T spectrum as well. In fig. 4.4, the q_T spectrum at both NNLL+NLO and NLL are shown, both with the uncertainties estimated as described above. The results look very reasonable, providing an indication that the q_T resummation procedure described above performs as intended. Note that there is a slight pinch in the uncertainty bands around $q_T = 15\,\text{GeV}$, indicating that the uncertainties there are likely a bit underestimated. This is an artifact of scale variations that is not unusual to be seen in resummed spectrum predictions.

4.2.4 The SCET$_+$ regime

This regime is characterized by the hierarchy $\mathcal{T} \ll q_T \ll \sqrt{Q\mathcal{T}}$ and involves two distinct expansion parameters, leading to intermediate collinear-soft modes. As described in sec. 3.10, these collinear-soft modes contribute to both the q_T and the $\mathcal{T}$ measurement, which uniquely fixes their scaling. Central soft modes only contribute to $\mathcal{T}$ as in SCET$_\text{I}$, while the energetic collinear modes only contribute to q_T as in SCET$_\text{II}$. The modes in this regime then scale as

$$n\text{-collinear:} \quad p_n^\mu \sim \left(\frac{q_T^2}{Q}, Q, q_T \right),$$

$$n\text{-collinear-soft:} \quad p_{ns}^\mu \sim \left(\mathcal{T}, \frac{q_T^2}{\mathcal{T}}, q_T \right),$$

$$\bar{n}\text{-collinear:} \quad p_{\bar{n}}^\mu \sim \left(Q, \frac{q_T^2}{Q}, q_T \right),$$

$$\bar{n}\text{-collinear-soft:} \quad p_{\bar{n}s}^\mu \sim \left(\frac{q_T^2}{\mathcal{T}}, \mathcal{T}, q_T \right),$$

$$\text{ultrasoft:} \quad p_{us}^\mu \sim \left(\mathcal{T}, \mathcal{T}, \mathcal{T} \right). \tag{4.35}$$

The collinear-soft modes have the same virtuality as the collinear modes, $p_{cs}^2 \sim p_c^2 \sim q_T^2$, but have a more central rapidity $e^{|y|} \sim q_T/\mathcal{T}$, which is small compared

to the rapidity $e^{|y|} \sim Q/q_T$ of the collinear modes. Hence, the two have a SCET$_{\text{II}}$-like relation and become a single collinear mode in the SCET$_{\text{I}}$ limit $q_T \sim \sqrt{Q\mathcal{T}}$. At the same time, the collinear-soft and soft modes have a SCET$_{\text{I}}$-like relation, being separated in virtuality, and become a single soft mode in the SCET$_{\text{II}}$ limit $\mathcal{T} \sim q_T$. In this way, SCET$_+$ is able to smoothly connect the SCET$_{\text{I}}$ and SCET$_{\text{II}}$ regimes. This is similar to the collinear-soft mode originally introduced in ref. [107], which instead connected two SCET$_{\text{I}}$ theories. The cross section in SCET$_+$ factorizes as [108]

$$
\frac{\mathrm{d}\sigma_+}{\mathrm{d}Q\,\mathrm{d}Y\,\mathrm{d}q_T\,\mathrm{d}\mathcal{T}} = H_{ij}(Q,\mu) \int \mathrm{d}^2\vec{k}_a\,B_i(\omega_a,\vec{k}_a,\mu,\nu) \int \mathrm{d}^2\vec{k}_b\,B_j(\omega_b,\vec{k}_b,\mu,\nu)
$$
$$
\times \int \mathrm{d}\ell_a^+ \int \mathrm{d}^2\vec{\ell}_a\,\mathscr{S}_i(\ell_a^+,\vec{\ell}_a,\mu,\nu) \int \mathrm{d}\ell_b^- \int \mathrm{d}^2\vec{\ell}_b\,\mathscr{S}_j(\ell_b^-,\vec{\ell}_b,\mu,\nu)
$$
$$
\times \int \mathrm{d}k\,S_{ij}(k,\mu)\,\delta\big(q_T - |\vec{k}_a + \vec{k}_b + \vec{\ell}_a + \vec{\ell}_b|\big)
$$
$$
\times \delta\Big(\mathcal{T} - \frac{\omega_a\ell_a^+}{Q_a} - \frac{\omega_b\ell_b^-}{Q_b} - k\Big), \tag{4.36}
$$

which holds up to power corrections

$$
\frac{\mathrm{d}\sigma}{\mathrm{d}Q\,\mathrm{d}Y\,\mathrm{d}q_T\,\mathrm{d}\mathcal{T}} = \frac{\mathrm{d}\sigma_+}{\mathrm{d}Q\,\mathrm{d}Y\,\mathrm{d}q_T\,\mathrm{d}\mathcal{T}} \left[1 + \mathcal{O}\Big(\frac{q_T^2}{\mathcal{T}Q}, \frac{\mathcal{T}^2}{q_T^2}\Big)\right]. \tag{4.37}
$$

The hard function is again the same as before. The beam functions are the q_T-dependent beam functions from SCET$_{\text{II}}$, while the soft function is the $\mathcal{T}$-dependent soft function from SCET$_{\text{I}}$. The new ingredient is the double-differential collinear-soft function $\mathscr{S}_i(k,\vec{k}_T,\mu,\nu)$, which encodes the contributions of the collinear-soft modes to both q_T and $\mathcal{T}$. Like the soft function in eq. (3.180), it is defined as a matrix element of Eikonal Wilson lines, but like the beam functions, it describes radiation that goes into a definite hemisphere. The explicit expression of this collinear-soft function to 1-loop order can be found in app. B.4.

The factorization formula in eq. (4.36) can be interpreted as a refactorization of either of the double-differential SCET$_{\text{I}}$ and SCET$_{\text{II}}$ cross sections [108], which precisely reflects the relation between the degrees of freedom described above. On the one hand, the SCET$_{\text{I}}$ double-differential beam function can be expanded in the SCET$_+$ limit $q_T \ll \sqrt{Q\mathcal{T}}$, upon which it factorizes into the

SCET$_{II}$ beam function and the collinear-soft function as

$$B_i(\omega k, \omega/E_{cm}, \vec{k}_T, \mu) = \int d^2\vec{\ell}_T\, B_i(\omega, \vec{k}_T - \vec{\ell}_T, \mu, \nu)\, \mathscr{S}_i(k, \vec{\ell}_T, \mu, \nu)$$
$$\times \left[1 + \mathcal{O}\left(\frac{k_T^2}{\omega k}\right)\right]. \tag{4.38}$$

The dependence on the rapidity scale ν of the two terms on the right-hand side must cancel, while their μ-dependence must combine into that of the left-hand side. This allows the derivation of the RGEs for the collinear-soft function as given in eqs. (C.21) and (C.22).

Similarly, expanding the SCET$_{II}$ double-differential soft function in the SCET$_+$ limit $\mathcal{T} \ll q_T$, it factorizes into the SCET$_I$ soft function and the two n-collinear-soft and $\bar{n}$-collinear-soft functions as

$$S_{ij}(k, \vec{k}_T, \mu, \nu) = \int d^2\vec{\ell}_T \int d\ell_a^+\, \mathscr{S}_i(\ell_a^+, \vec{\ell}_T, \mu, \nu) \int d\ell_b^-\, \mathscr{S}_j(\ell_b^-, \vec{k}_T - \vec{\ell}_T, \mu, \nu)$$
$$\times S_{ij}\left(k - \frac{\omega_a \ell_a^+}{Q_a} - \frac{\omega_b \ell_b^-}{Q_b}, \mu\right)\left[1 + \mathcal{O}\left(\frac{k^2}{k_T^2}\right)\right]. \tag{4.39}$$

Since the left-hand side does not depend on $\omega_{a,b}$ and $Q_{a,b}$, this dependence must also drop out on the right-hand side, and therefore in the whole SCET$_+$ cross section in eq. (4.36). This can be achieved explicitly by recalling that $\omega_a\omega_b = Q_a Q_b = Q^2$ and rewriting

$$d\ell_a^+\, \mathscr{S}_i(\ell_a^+, \vec{\ell}_a, \mu, \nu)\, d\ell_b^-\, \mathscr{S}_j(\ell_b^-, \vec{\ell}_b, \mu, \nu)\, \delta\left(\mathcal{T} - \frac{\omega_a\ell_a^+}{Q_a} - \frac{\omega_b\ell_b^-}{Q_b} - k\right)$$
$$= dk_a^+\, \mathscr{S}_i\left(k_a^+, \vec{\ell}_a, \mu, \frac{Q_a\nu}{\omega_a}\right) dk_b^-\, \mathscr{S}_j\left(k_b^-, \vec{\ell}_b, \mu, \frac{Q_b\nu}{\omega_b}\right) \delta(\mathcal{T} - k_a^+ - k_b^- - k)$$
$$= dk_a^+\, \mathscr{S}_i(k_a^+, \vec{\ell}_a, \mu, \nu)\, dk_b^-\, \mathscr{S}_j(k_b^-, \vec{\ell}_b, \mu, \nu)\, \delta(\mathcal{T} - k_a^+ - k_b^- - k), \tag{4.40}$$

where in the first step, a change of variables from $\ell_{a,b}^\pm$ to $k_a^+ = \omega_a\ell_a^+/Q_a$ and $k_b^- = \omega_b\ell_b^-/Q_b$ has been made. In the second step, an evolution in rapidity from $\nu_{a,b} \equiv Q_{a,b}\nu/\omega_{a,b}$ back to a common ν at fixed μ has been performed, for which the rapidity evolution factors exactly cancel because

$$\ln\left(\frac{\nu_a}{\nu}\right) + \ln\left(\frac{\nu_b}{\nu}\right) = \ln\left(\frac{Q_a Q_b}{\omega_a \omega_b}\right) = 0. \tag{4.41}$$

The SCET$_+$ factorization in eq. (4.36) fully disentangles the physics at the canonical SCET$_+$ scales given by:

$$\mu_H^+ \sim Q, \qquad \mu_B^+ \sim q_T, \qquad \mu_{\mathscr{S}}^+ \sim q_T, \qquad \mu_S^+ \sim \mathcal{T},$$
$$\nu_B^+ \sim Q, \qquad \nu_{\mathscr{S}}^+ \sim q_T^2/\mathcal{T}. \tag{4.42}$$

As for SCET_{II}, the q_T resummation is performed in impact parameter space, transforming the vectorial convolutions in eq. (4.36) into simple products. In b_T space, the canonical SCET_+ scales read

$$\mu_H^+ \sim Q\,, \qquad \mu_B^+ \sim b_0/b_T\,, \qquad \mu_{\mathscr{S}}^+ \sim b_0/b_T\,, \qquad \mu_S^+ \sim \mathcal{T}\,,$$
$$\nu_B^+ \sim Q\,, \qquad\qquad \nu_{\mathscr{S}}^+ \sim (b_0/b_T)^2/\mathcal{T}\,. \qquad (4.43)$$

By evaluating all functions at their natural scales and evolving them to common scales, all logarithms of large ratios of the scales in the problem, given by

$$\frac{(b_0/b_T)^2}{Q\mathcal{T}} \sim \frac{\nu_{\mathscr{S}}^+}{\nu_B^+}\,, \qquad \frac{\mathcal{T}}{b_0/b_T} \sim \frac{\mu_S^+}{\mu_{\mathscr{S}}^+}\,,$$
$$\frac{b_0/b_T}{Q} \sim \frac{\mu_B^+}{\mu_H^+} \sim \frac{\mu_{\mathscr{S}}^+}{\mu_H^+} \qquad \text{and} \qquad \frac{\mathcal{T}}{Q} \sim \frac{\mu_S^+}{\mu_H^+}\,, \qquad (4.44)$$

are resummed. The logarithms of the first ratio appear in the double-differential SCET_{I} beam function in the limit $q_T \ll \sqrt{Q\mathcal{T}}$, and are resummed in SCET_+ by the additional ν evolution in the refactorization in eq. (4.38). Similarly, logarithms of the second ratio appear in the double-differential SCET_{II} soft function in the limit $\mathcal{T} \ll q_T$, and are resummed in SCET_+ by the additional μ evolution in eq. (4.39).

4.2.5 Outer space

There are two additional regions of phase-space that are left blank in fig. 4.1. The region above the SCET_{II} regime is characterized by the hierarchy $q_T \ll \mathcal{T} \ll \sqrt{Q\mathcal{T}}$, while the region to the right of the SCET_{I} regime corresponds to $\mathcal{T} \ll \sqrt{Q\mathcal{T}} \ll q_T$. Both of these regions are power suppressed.

As discussed in sec. 4.2.3, only soft radiation contributes to the $\mathcal{T}$ measurement in SCET_{II}, as the collinear contributions are power suppressed. However, in the regime in which $q_T \ll \mathcal{T}$, even the soft contribution to $\mathcal{T}$ becomes power suppressed. In this hierarchy, a single real emission at fixed $\mathcal{O}(\alpha_s)$ is kinematically impossible both in SCET_{II} as well as in full QCD. Soft emissions at higher orders can populate this region of phase space as long they are approximately back-to-back such that their transverse momenta largely cancel. The cross section in this regime is then power suppressed by $\mathcal{O}(q_T^2/\mathcal{T}^2)$. Equivalently, expanding the SCET_{II} factorization of the double-differential cross section in the limit $q_T \ll \mathcal{T}$ reduces it to the single-differential q_T spectrum with an overall $\delta(\mathcal{T})$, which is exploited in the numerical implementation cf. eq. (B.32). Physically, this means that by integrating the double spectrum in SCET_{II} up to some $\mathcal{T}_{\text{cut}} \gg q_T$, the single-differential q_T spectrum is recovered, while the

effect of the cut is power suppressed in this limit. Note that there is also a contribution from double-parton scattering [168–171] in this region, where the two jets produced in the second interaction alongside the Z boson are naturally back-to-back and not power suppressed. This contribution is still not expected to exceed the single-parton scattering contribution by much because double-parton scattering itself is power suppressed by $\mathcal{O}(\Lambda_{\text{QCD}}^2/\mathcal{T}^2)$, with $\mathcal{T}$ setting the scale of the second hard scattering producing the back-to-back jets.

Similarly, in the limit $\sqrt{Q\mathcal{T}} \ll q_T$, even the contribution from collinear radiation to q_T becomes power suppressed in SCET$_{\text{I}}$ (cf. eq. (B.17)) and at leading power, the single-differential $\mathcal{T}$ spectrum with an overall $\delta(q_T)$ is recovered. An additional subtlety for $\sqrt{Q\mathcal{T}} \ll q_T$ is that very energetic forward radiation with energy $\sim q_T^2/\mathcal{T}$ can theoretically contribute [108], pushing the hard scale up to $q_T^2/\mathcal{T} \gg Q$. However, the cross section in this kinematic configuration is very strongly suppressed by the PDFs, allowing for its description at fixed-order in this framework.

The above analysis justifies focusing on the shaded regions of phase space in fig. 4.1, corresponding to the main SCET$_{\text{I}}$, SCET$_{\text{II}}$, and SCET$_+$ regimes.

4.3 Matching effective theories

The various factorization formulas described in the previous section need to be matched to each other and the fixed-order result in order to obtain a single expression for the cross section differential in both q_T and $\mathcal{T}$. Since the intermediate regime contains an additional expansion with respect to both boundary regimes, matching the former to the latter can be done in a way analogous to the matching of the SCET$_{\text{I}}$ or SCET$_{\text{II}}$ factorizations to the fixed-order in eqs. (4.8) and (4.25).

The SCET$_+$ factorization formula describing the bulk region in phase space reduces to the SCET$_{\text{I}}$ and SCET$_{\text{II}}$ factorizations in the respective characteristic kinematical regions. Most of the canonical SCET$_+$ scales, however, do not agree with the canonical scales of both boundary theories. The canonical rapidity scale of the collinear-soft function is even different from both corresponding canonical boundary scales. To remedy this, profile scales are needed that pick out the correct canonical scale in each region according to the hierarchy between $\mathcal{T}$ and q_T (or its conjugate b_T). Between the canonical values, the profile scales must then ensure a smooth interpolation.

By picking all canonical scales in terms of the profile functions defined in eqs. (4.11) and (4.28), turning off the resummation towards the fixed-order region is automatically included. This method ensures that any scale varia-
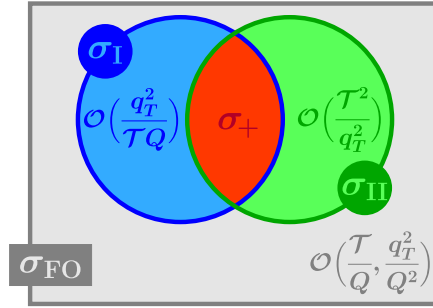
Figure 4.5 Venn diagram of power corrections to the factorized double-differential spectrum. SCET$_\text{I}$ (blue) and SCET$_\text{II}$ (green) each capture a set of power corrections that is expanded away in the SCET$_+$ factorization (red) and the opposite boundary regime. A third class of power corrections to the overall soft-collinear limit is captured by the fixed-order calculation in full QCD (gray).

tions performed for the boundary theories will automatically propagate into the matched cross section. In addition to these inherited uncertainties, the points at which the interpolated profile scales initiate and end the transition from one canonical scale to the next are also arbitrary to some extent. To assess this uncertainty in the matching procedure, the transition points of the interpolation are varied as well, yielding an additional contribution to the total uncertainty.

4.3.1 Structure of power corrections

An important feature of the EFT setup described in the previous section is that the factorized cross section in SCET$_+$ differs from the ones in SCET$_\text{I}$ and SCET$_\text{II}$ only by a subset of the power corrections it receives relative to the full QCD result, so

$$\frac{\mathrm{d}\sigma_\text{I}}{\mathrm{d}Q\,\mathrm{d}Y\,\mathrm{d}q_T\,\mathrm{d}\mathcal{T}} = \frac{\mathrm{d}\sigma_+}{\mathrm{d}Q\,\mathrm{d}Y\,\mathrm{d}q_T\,\mathrm{d}\mathcal{T}}\left[1 + \mathcal{O}\!\left(\frac{q_T^2}{\mathcal{T}Q}\right)\right],$$
$$\frac{\mathrm{d}\sigma_\text{II}}{\mathrm{d}Q\,\mathrm{d}Y\,\mathrm{d}q_T\,\mathrm{d}\mathcal{T}} = \frac{\mathrm{d}\sigma_+}{\mathrm{d}Q\,\mathrm{d}Y\,\mathrm{d}q_T\,\mathrm{d}\mathcal{T}}\left[1 + \mathcal{O}\!\left(\frac{\mathcal{T}^2}{q_T^2}\right)\right]. \tag{4.45}$$

This is illustrated in fig. 4.5, and follows from comparing eq. (4.37) to eq. (4.5) and eq. (4.18), respectively. Crucially, eq. (4.45) also holds when the cross sections are evaluated at a common (not necessarily fixed-order) scale. For example, both σ_I and σ_+ share a logarithmic singularity with respect to $\mathcal{T}/Q$,
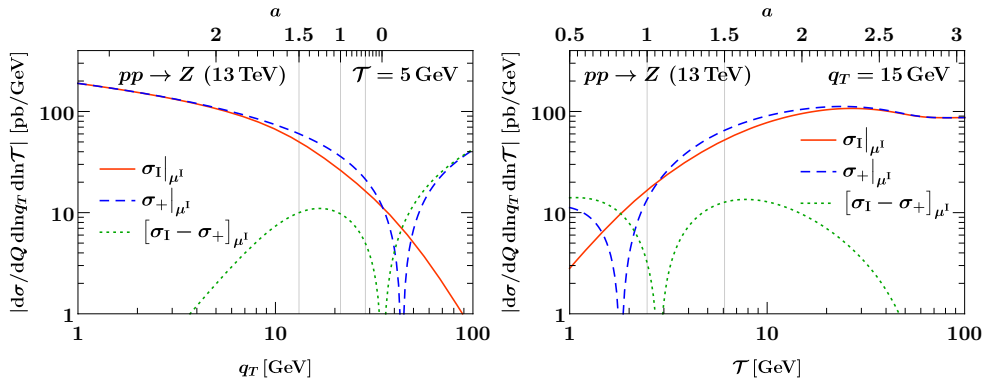
Figure 4.6 Singular/nonsingular comparison between $\mathrm{SCET_I}$ and $\mathrm{SCET_+}$ at NNLL (only resumming logs of $\mathcal{T}$) as a function of q_T for fixed $\mathcal{T} = 5\,\mathrm{GeV}$ (left) and as a function of $\mathcal{T}$ for fixed $q_T = 15\,\mathrm{GeV}$ (right). The solid red lines show the full $\mathrm{SCET_I}$ result including resummation. The dashed blue lines show the corresponding $\mathrm{SCET_+}$ singular limit with *only* $\mathrm{SCET_I}$ resummation. The dotted green lines show their difference, corresponding to the power corrections indicated in eq. (4.45). The thin vertical lines indicate the choice of transition points (a_1, a_2, a_3) with respect to the regime parameter a (upper horizontal axis), which will be discussed in sec. 4.3.3.

which can be resummed by running between the scales of the hard, soft, and (refactorized) beam functions. In $\mathrm{SCET_+}$, this amounts to setting the μ^+ scales to be equal to their μ^{I} counterparts as

$$\mu_B^+ = \mu_{\mathscr{S}}^+ = \mu_B^{\mathrm{I}}, \qquad \nu_B^+ = \nu_{\mathscr{S}}^+ = \mu_{\mathrm{FO}} \qquad \text{and} \qquad \mu_S^+ = \mu_S^{\mathrm{I}}, \qquad (4.46)$$

such that any large logarithms inside the (refactorized) beam function in eq. (4.38) are treated at fixed-order. The notation $\mathrm{d}\sigma_+\big|_{\mu^{\mathrm{I}}}$ is used to indicate that $\mathrm{d}\sigma_+$ is evaluated at scales that satisfy eq. (4.46). A natural way to judge the size of the power corrections in eq. (4.45) is then to compare $\mathrm{d}\sigma_+\big|_{\mu^{\mathrm{I}}}$ to $\mathrm{d}\sigma_{\mathrm{I}}\big|_{\mu^{\mathrm{I}}}$, with the choices for μ^{I} as given in eq. (4.10). This comparison is shown in fig. 4.6 for representative choices of fixed $\mathcal{T}$ and q_T at NNLL. The power-like behavior of the difference $\big[\mathrm{d}\sigma_{\mathrm{I}} - \mathrm{d}\sigma_+\big]_{\mu^{\mathrm{I}}}$ (dotted green) as either $q_T \to 0$ for fixed $\mathcal{T}$ (left panel) or $\mathcal{T} \to \infty$ for fixed q_T (right panel) can clearly be read off. This also provides a nontrivial check on the implementation of σ_{I} and σ_+. This comparison in fig. 4.6 is analogous to the usual procedure of comparing the full-theory result for a cross section with its singular EFT limit at a common scale μ_{FO}. Here, $\mathrm{SCET_I}$ takes on the role of the full theory, while $\mathrm{SCET_+}$ provides the singular limit, and the comparison is performed at
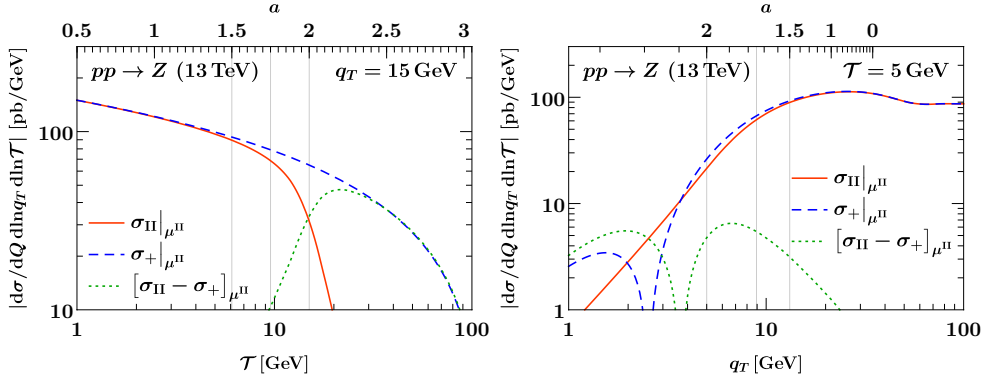
Figure 4.7 Singular/nonsingular comparison between SCET$_\text{II}$ and SCET$_+$ at NNLL (only resumming logs of b_T) as a function of $\mathcal{T}$ for fixed $q_T = 15\,\text{GeV}$ (left) and as a function of q_T for fixed $\mathcal{T} = 5\,\text{GeV}$ (right). The solid red lines show the full SCET$_\text{II}$ result including resummation. The dashed blue lines show the corresponding SCET$_+$ singular limit with *only* SCET$_\text{II}$ resummation. The dotted green lines show their difference, corresponding to the power corrections indicated in eq. (4.45). The thin vertical lines indicate the choice of transition points (a_4, a_5, a_6) with respect to the regime parameter a (upper horizontal axis), which will be discussed in sec. 4.3.3.

common scales μ^I.

Similarly, both σ_II and σ_+ have a common singular structure as $q_T/Q \to 0$. In this case, resumming the shared logarithmic terms requires running between the hard, beam, and (refactorized) soft function. In SCET$_+$, this amounts to setting the μ^+ scales to be equal to their μ^II counterparts as

$$\mu_{\mathscr{S}}^+ = \mu_S^+ = \mu_S^\text{II} \qquad \text{and} \qquad \nu_{\mathscr{S}}^+ = \nu_S^\text{II}, \tag{4.47}$$

which treats the large logarithms in the refactorized double-differential soft function in eq. (4.39) at fixed-order. This choice of scales is denoted by $\mathrm{d}\sigma_+\big|_{\mu^\text{II}}$, with scale setting in b_T space and the inverse Fourier transform understood as described in sec. 4.2.3. The explicit choices for the various μ^II are given in eq. (4.27). In fig. 4.7, a comparison between $\mathrm{d}\sigma_+\big|_{\mu^\text{II}}$ and $\mathrm{d}\sigma^\text{II}\big|_{\mu^\text{II}}$ is shown at NNLL as a function of $\mathcal{T}$ at fixed q_T (left) and vice versa (right). Even when evaluated at its intrinsic scales, $\mathrm{d}\sigma_\text{II}\big|_{\mu^\text{II}}$ (solid red) still exhibits an unresummed singularity as $\mathcal{T}/q_T \ll 1$, which, as expected, is captured by $\mathrm{d}\sigma_+\big|_{\mu^\text{II}}$ (dashed blue) up to power corrections (dotted green). This check is highly nontrivial as it involves an additional Fourier transform on both sides of the comparison.
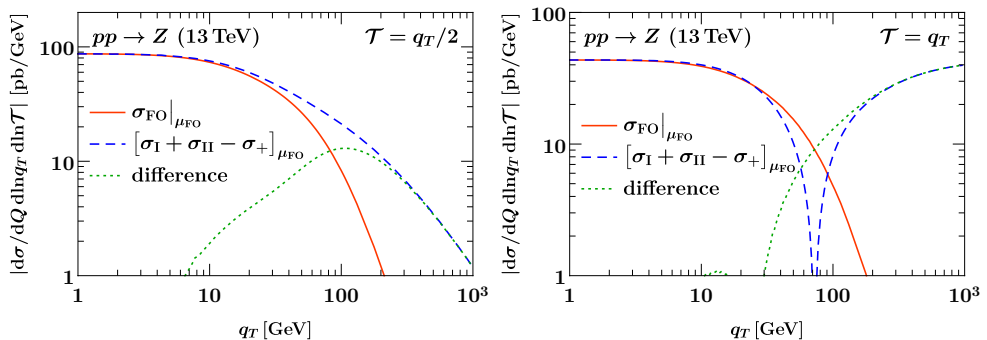
Figure 4.8 Singular/nonsingular comparison between the matched SCET descriptions and QCD at fixed $\mathcal{O}(\alpha_s)$ as a function of q_T for $\mathcal{T} = q_T/2$ (left) and $\mathcal{T} = q_T$ (right). The solid red line shows the fixed-order QCD double spectrum, the dashed blue line the matched SCET result in eq. (4.48), and the dotted green line the difference.

As a final important consequence of fig. 4.5, the complete infrared structure of the double-differential spectrum for any hierarchy between q_T and $\mathcal{T}$ adhering to both $q_T \ll Q$ and $\mathcal{T} \ll Q$ is obtained by adding the SCET$_\mathrm{I}$ and SCET$_\mathrm{II}$ cross sections and removing the overlap between the two by subtracting the SCET$_+$ cross section as

$$\frac{\mathrm{d}\sigma}{\mathrm{d}Q\,\mathrm{d}Y\,\mathrm{d}q_T\,\mathrm{d}\mathcal{T}} = \left[\frac{\mathrm{d}\sigma_\mathrm{I}}{\mathrm{d}Q\,\mathrm{d}Y\,\mathrm{d}q_T\,\mathrm{d}\mathcal{T}} + \frac{\mathrm{d}\sigma_\mathrm{II}}{\mathrm{d}Q\,\mathrm{d}Y\,\mathrm{d}q_T\,\mathrm{d}\mathcal{T}} - \frac{\mathrm{d}\sigma_+}{\mathrm{d}Q\,\mathrm{d}Y\,\mathrm{d}q_T\,\mathrm{d}\mathcal{T}} \right]$$
$$\times \left[1 + \mathcal{O}\Big(\frac{q_T^2}{Q^2}, \frac{\mathcal{T}}{Q}\Big) \right]. \tag{4.48}$$

In fig. 4.8, a numerical check of this relation at fixed $\mathcal{O}(\alpha_s)$ is depicted, which requires setting all scales equal to a common μ_FO. The comparison is plotted as a function of q_T along lines of fixed $\mathcal{T}/q_T = 1/2$ (left) and $\mathcal{T}/q_T = 1$ (right). Excellent agreement is found between the full result (solid red) and the first line on the right-hand side of eq. (4.48) (dashed blue), as evident from the power-like behavior of their difference (dotted green) as $q_T, \mathcal{T} \to 0$.

This singular/nonsingular comparison is qualitatively different from the structure of power corrections in either SCET$_\mathrm{I}$ or SCET$_\mathrm{II}$ alone, which were already verified in fig. 4.2 and fig. 4.3. Because SCET$_\mathrm{I}$ and SCET$_\mathrm{II}$ both involve an additional expansion about a specific hierarchy between q_T and $\mathcal{T}$, they incur power corrections of $\mathcal{O}(\mathcal{T}^2/q_T^2)$ and $\mathcal{O}(q_T^2/(Q\mathcal{T}))$, respectively. Accordingly, they only recover the singular limit of full QCD when approaching it along specific lines in the $(q_T, \mathcal{T})$ plane. This is different from fig. 4.8, where the combined expression in eq. (4.48) (dashed blue) describes the singular limit

$q_T, \mathcal{T} \to 0$ along an arbitrary line of approach, with the ratio $q_T/\mathcal{T}$ effectively controlling the "admixture" of power corrections of $\mathcal{O}(q_T^2/Q^2)$ and $\mathcal{O}(\mathcal{T}/Q)$, respectively. Other fixed ratios of q_T and $\mathcal{T}$ have been verified to also correctly describe the singular behavior of full QCD.

4.3.2 Matching equation

The structure of power corrections discussed in the previous section, together with the all-order resummation shared between SCET$_+$ and SCET$_\text{I}$ or SCET$_\text{II}$, suggests the following matching formula to describe all regions of the double-differential spectrum:

$$\mathrm{d}\sigma^{\mathrm{match}} = \mathrm{d}\sigma_+\big|_{\mu^+} + \big[\mathrm{d}\sigma_\mathrm{I} - \mathrm{d}\sigma_+\big]_{\mu^\mathrm{I}} + \big[\mathrm{d}\sigma_\mathrm{II} - \mathrm{d}\sigma_+\big]_{\mu^\mathrm{II}}$$
$$+ \big[\mathrm{d}\sigma_\mathrm{FO} - \mathrm{d}\sigma_\mathrm{I} - \mathrm{d}\sigma_\mathrm{II} + \mathrm{d}\sigma_+\big]_{\mu_\mathrm{FO}}. \qquad (4.49)$$

The only ingredient in this matching formula that has not yet been discussed is $\mathrm{d}\sigma_+\big|_{\mu^+}$, for which all ingredients in the SCET$_+$ factorization are evaluated at the SCET$_+$ scales μ^+, such that the full RGE of SCET$_+$ is in effect. When the power corrections in eq. (4.37) are small, i.e. the parametric assumptions of SCET$_+$ are satisfied, the μ^+ scales are given by the canonical scales from eq. (4.43). As for μ^II, these scales are set in b_T space, followed by an inverse Fourier transform. Upon approaching the SCET$_\text{I}$ region, the resummation inside the refactorization of the beam function in eq. (4.38) must be turned off, which imposes the conditions

$$\left.\begin{aligned} \mu_B^+(q_T, \mathcal{T}, b_T) &\longrightarrow \mu_B^\mathrm{I}(\mathcal{T}) \\ \mu_{\mathscr{S}}^+(q_T, \mathcal{T}, b_T) &\longrightarrow \mu_B^\mathrm{I}(\mathcal{T}) \\ \nu_{\mathscr{S}}^+(q_T, \mathcal{T}, b_T) &\longrightarrow \nu_B^+(q_T, \mathcal{T}, b_T) \end{aligned}\right\} \quad \text{for} \quad q_T \longrightarrow \sqrt{Q\mathcal{T}}, \qquad (4.50)$$

on the scales μ^+. Since the soft functions in the SCET$_+$ and SCET$_\text{I}$ regimes are identical, the soft scale is required to adhere to the condition

$$\mu_S^+(q_T, \mathcal{T}, b_T) \longrightarrow \mu_S^\mathrm{I}(\mathcal{T}) \quad \text{for} \quad q_T \longrightarrow \sqrt{Q\mathcal{T}}. \qquad (4.51)$$

These relations are required to hold for every value of b_T.

Similarly, upon approaching the SCET$_\text{II}$ region, the scales inside the refactorized soft function eq. (4.39) must become equal, leading to the conditions

$$\left.\begin{aligned} \mu_S^+(q_T, \mathcal{T}, b_T) &\longrightarrow \mu_S^\mathrm{II}(q_T, b_T) \\ \mu_{\mathscr{S}}^+(q_T, \mathcal{T}, b_T) &\longrightarrow \mu_S^\mathrm{II}(q_T, b_T) \\ \nu_{\mathscr{S}}^+(q_T, \mathcal{T}, b_T) &\longrightarrow \nu_S^\mathrm{II}(q_T, b_T) \end{aligned}\right\} \quad \text{for} \quad q_T \longrightarrow \mathcal{T}. \qquad (4.52)$$

Furthermore, the scales of the common beam function in $\mathrm{SCET_{II}}$ and $\mathrm{SCET_+}$ can be identified by

$$\left.\begin{aligned} \mu_B^+(q_T, \mathcal{T}, b_T) &\longrightarrow \mu_B^{\mathrm{II}}(q_T, b_T) \\ \nu_B^+(q_T, \mathcal{T}, b_T) &\longrightarrow \nu_B^{\mathrm{II}}(q_T, b_T) \end{aligned}\right\} \quad \text{for} \quad q_T \longrightarrow \mathcal{T}. \tag{4.53}$$

Some of the above requirements for the behavior of the scales at the boundaries are already satisfied by the canonical $\mathrm{SCET_+}$ scales, e.g. the canonical soft scales in $\mathrm{SCET_+}$ and $\mathrm{SCET_I}$ are simply equal. The canonical collinear-soft rapidity scale, given by

$$\nu_{\mathscr{S}}^+(q_T, \mathcal{T}, b_T) = \frac{(b_0/b_T)^2}{\mathcal{T}} \quad \text{for} \quad \mathcal{T} \ll q_T \ll \sqrt{Q\mathcal{T}}, \tag{4.54}$$

is the most demanding canonical $\mathrm{SCET_+}$ scale as it does not coincide with the corresponding scale on either boundary.

It is instructive to explicitly consider the behavior of eq. (4.49) on the $\mathrm{SCET_I}$ and $\mathrm{SCET_{II}}$ phase-space boundaries, as well as in the fixed-order region. By construction, for any choice of μ^+ scales satisfying eqs. (4.50) and (4.51) it automatically follows that

$$\mathrm{d}\sigma_+\big|_{\mu^+} \longrightarrow \mathrm{d}\sigma_+\big|_{\mu^{\mathrm{I}}} \quad \text{for} \quad q_T \longrightarrow \sqrt{Q\mathcal{T}}. \tag{4.55}$$

From this, the matched cross section can be seen to reduce to

$$\begin{aligned} \mathrm{d}\sigma^{\mathrm{match}} \longrightarrow {}& \mathrm{d}\sigma_{\mathrm{I}}\big|_{\mu^{\mathrm{I}}} + \big[\mathrm{d}\sigma_{\mathrm{FO}} - \mathrm{d}\sigma_{\mathrm{I}}\big]_{\mu_{\mathrm{FO}}} + \big[\mathrm{d}\sigma_{\mathrm{II}} - \mathrm{d}\sigma_+\big]_{\mu^{\mathrm{II}}} \\ & - \big[\mathrm{d}\sigma_{\mathrm{II}} - \mathrm{d}\sigma_+\big]_{\mu_{\mathrm{FO}}} \quad \text{for} \quad q_T \longrightarrow \sqrt{Q\mathcal{T}}. \end{aligned} \tag{4.56}$$

This mostly coincides with the result in eq. (4.8) of matching $\mathrm{d}\sigma_{\mathrm{I}}$ to the fixed-order result $\mathrm{d}\sigma_{\mathrm{FO}}$, and is guaranteed to capture all large logarithms of $\mathcal{T}/Q$ captured by the $\mathrm{SCET_I}$ RGE. It improves over eq. (4.8) by also resumming logarithms of q_T/Q in the power corrections of $\mathcal{O}(\mathcal{T}^2/q_T^2)$, encoded in $\big[\sigma_{\mathrm{II}} - \sigma_+\big]_{\mu^{\mathrm{II}}}$. This is not a numerically large effect and cannot be exploited to achieve the resummation of $\mathcal{T}$ at next-to-leading power, as it is only a subset of all power corrections.

Similarly, eqs. (4.52) and (4.53) imply that

$$\mathrm{d}\sigma_+\big|_{\mu^+} \longrightarrow \mathrm{d}\sigma_+\big|_{\mu^{\mathrm{II}}} \quad \text{for} \quad q_T \longrightarrow \mathcal{T}, \tag{4.57}$$

and consequently

$$\begin{aligned} \mathrm{d}\sigma^{\mathrm{match}} \longrightarrow {}& \mathrm{d}\sigma_{\mathrm{II}}\big|_{\mu^{\mathrm{II}}} + \big[\mathrm{d}\sigma_{\mathrm{FO}} - \mathrm{d}\sigma_{\mathrm{II}}\big]_{\mu_{\mathrm{FO}}} + \big[\mathrm{d}\sigma_{\mathrm{I}} - \mathrm{d}\sigma_+\big]_{\mu^{\mathrm{I}}} \\ & - \big[\mathrm{d}\sigma_{\mathrm{I}} - \mathrm{d}\sigma_+\big]_{\mu_{\mathrm{FO}}} \quad \text{for} \quad q_T \longrightarrow \mathcal{T}. \end{aligned} \tag{4.58}$$

Scale	SCET$_\mathrm{I}$	SCET$_+$	SCET$_\mathrm{II}$
μ_H	Q	Q	Q
μ_B	$\sqrt{\mathcal{T}Q}$	b_0/b_T	b_0/b_T
ν_B		Q	Q
$\mu_\mathscr{S}$		b_0/b_T	
$\nu_\mathscr{S}$		$(b_0/b_T)^2/\mathcal{T}$	
μ_S	$\mathcal{T}$	$\mathcal{T}$	b_0/b_T
ν_S			b_0/b_T

Table 4.1 Summary of canonical scales in SCET$_\mathrm{I}$, SCET$_+$, and SCET$_\mathrm{II}$ as given in eqs. (4.7), (4.22) and (4.43). For SCET$_+$ and SCET$_\mathrm{II}$, the canonical scales are given in b_T space.

This mostly coincides with the result in eq. (4.25) of matching $\mathrm{d}\sigma_\mathrm{II}$ to the fixed-order result $\mathrm{d}\sigma_\mathrm{FO}$, and thus captures all large logarithms of q_T/Q captured by the SCET$_\mathrm{II}$ RGE. In addition, it resums logarithms of $\mathcal{T}/Q$ in the $\mathcal{O}(q_T^2/(\mathcal{T}Q))$ power corrections encoded in $[\mathrm{d}\sigma_\mathrm{I} - \mathrm{d}\sigma_+]_{\mu^\mathrm{I}}$.

Finally, in the fixed-order region, all μ^+, μ^I, and μ^II scales become equal to μ_FO. Thus as desired, the matched prediction reduces to the fixed-order result

$$\mathrm{d}\sigma^\mathrm{match} \longrightarrow \mathrm{d}\sigma_\mathrm{FO}\big|_{\mu_\mathrm{FO}} \qquad \text{for} \qquad q_T, \mathcal{T} \longrightarrow Q. \tag{4.59}$$

4.3.3 Profile scales

The central SCET$_+$ scales are obtained using a regime parameter that selects the appropriate combination of scales from the boundary theories in each region of phase space, and selects a third, independent choice in the SCET$_+$ "bulk" when necessary. The profile functions that handle the transition to fixed-order can conveniently be reused from SCET$_\mathrm{I}$ and SCET$_\mathrm{II}$.

The canonical scales for SCET$_\mathrm{I}$, SCET$_\mathrm{II}$, SCET$_+$ are summarized in table 4.1. At these scales, the arguments of the logarithms in the ingredients of the factorized cross section are of order one, i.e. all large logarithms are resummed by RG evolution. In order to facilitate the interpolation between the canonical scales in different regimes, the regime parameter is defined as

$$a = 3 - \frac{|\ln(\mathcal{T}/Q)|}{|\ln(q_T/Q)|}. \tag{4.60}$$

Its definition is carefully chosen such that $a = 1$ when the SCET$_\mathrm{I}$ parametric relation $q_T = \sqrt{\mathcal{T}Q}$ is satisfied exactly, and $a = 2$ on the SCET$_\mathrm{II}$ boundary of phase space, where $q_T = \mathcal{T}$. As illustrated in the left panel of fig. 4.9, the
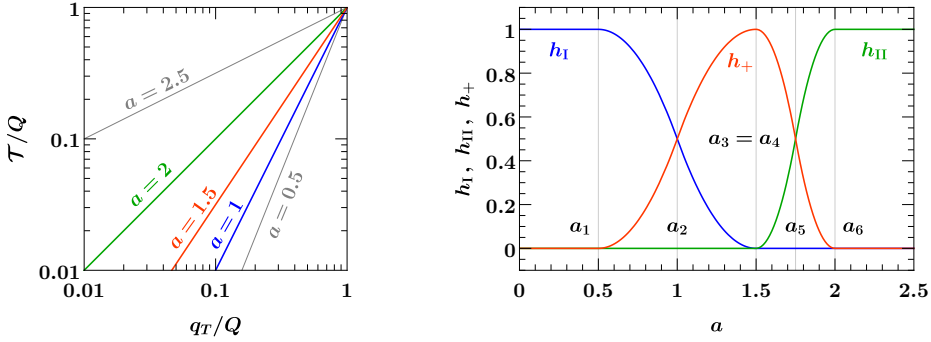
Figure 4.9 Left: Illustration of the regime parameter a that governs the matching between EFTs. For $a = 1$ the SCET$_\text{I}$ parametric relation $q_T = \sqrt{Q\mathcal{T}}$ is satisfied exactly, whereas the SCET$_\text{II}$ parametric relation $q_T = \mathcal{T}$ yields $a = 2$. Right: Helper functions used to interpolate between scales on the boundaries (SCET$_\text{I}$, SCET$_\text{II}$) and in the bulk (SCET$_+$). The helper functions have continuous derivatives and always sum to one. The individual helper functions are exactly equal to unity in their respective canonical regions.

canonical SCET$_+$ region lies at intermediate $a \sim 1.5$. The requirements on the SCET$_+$ scales were given in eqs. (4.50) and (4.51) for the transition to SCET$_\text{I}$, and in eqs. (4.52) and (4.53) for the transition to SCET$_\text{II}$. To satisfy each of these requirements, weighted products of scales on the boundary and in the bulk are taken. Schematically, this is given by

$$\mu^+ = \left[\mu^\text{I}\right]^{h_\text{I}(a)} \left[\mu^+_\text{bulk}\right]^{h_+(a)} \left[\mu^\text{II}\right]^{h_\text{II}(a)}. \tag{4.61}$$

The weights in the exponents are given by helper functions that depend on the regime parameter a, as illustrated in the right panel of fig. 4.9. They satisfy

$$h_\text{I}(a) + h_+(a) + h_\text{II}(a) = 1\,, \tag{4.62}$$

for any a and are given explicitly in eq. (4.66) below. The helper functions ensure that the appropriate scales are used in each region, e.g. $h_\text{II}(a)$ is equal to unity in the vicinity of $a = 2$ and vanishes for $a < 1.5$, with a smooth transition in between. The explicit form of eq. (4.61) for the soft and collinear-soft scales is given by

$$\begin{aligned}
\mu^+_\mathscr{S} &= \left[\mu^\text{I}_B\right]^{h_\text{I}(a)} \left[\mu^+_{\mathscr{S},\text{bulk}}\right]^{h_+(a)} \left[\mu^\text{II}_S\right]^{h_\text{II}(a)}, \\
\nu^+_\mathscr{S} &= \left[\nu\right]^{h_\text{I}(a)} \quad \left[\nu^+_{\mathscr{S},\text{bulk}}\right]^{h_+(a)} \left[\nu^\text{II}_S\right]^{h_\text{II}(a)}, \\
\mu^+_S &= \left[\mu^\text{I}_S\right]^{h_\text{I}(a)} \left[\mu^+_{S,\text{bulk}}\right]^{h_+(a)} \left[\mu^\text{II}_S\right]^{h_\text{II}(a)}.
\end{aligned} \tag{4.63}$$

As mentioned before, the most nontrivial of these cases is $\nu_{\mathscr{S}}$, which must be equal to the overall scale ν in the SCET_{I} region in order to turn off the rapidity resummation there, has a distinct canonical value in the SCET_+ bulk, and must asymptote to yet another value on the SCET_{II} boundary. The scale μ_S^+ also requires a distinct treatment in the bulk to ensure that the hierarchy $\mu_S^+ < \mu_{\mathscr{S}}^+$ inside the refactorized soft function, as implied by the SCET_+ power counting, is not upset by variations (see next section). The central choices for the above scales in the bulk are taken to be

$$\mu_{\mathscr{S},\text{bulk}}^+ = \mu_{\text{FO}}\, f_{\text{run}}^{\text{II}}\left(\frac{q_T}{Q}, \frac{b_0}{b^*(b_T)\,Q}\right),$$

$$\nu_{\mathscr{S},\text{bulk}}^+ = \mu_{\text{FO}}\, \frac{\left[f_{\text{run}}^{\text{II}}\left(\frac{q_T}{Q}, \frac{b_0}{b^*(b_T)Q}\right)\right]^2}{f_{\text{run}}^{\text{I}}\left(\frac{\mathcal{T}}{Q}\right)},$$

$$\mu_{S,\text{bulk}}^+ = \mu_{\text{FO}}\, f_{\text{run}}^{\text{I}}\left(\frac{\mathcal{T}}{Q}\right). \tag{4.64}$$

The profile function $f_{\text{run}}^{\text{I}}$ was introduced for the transition between SCET_{I} and fixed-order QCD in eq. (4.11), and the hybrid profile function $f_{\text{run}}^{\text{II}}$ for the transition between SCET_{II} and QCD in eq. (4.28). The nonperturbative $b^*(b_T)$ prescription was defined in eq. (4.30). These functions turn off the resummation of logarithms involving q_T (b_T) and $\mathcal{T}$ respectively as the fixed-order regime is approached, and also ensure that scales are frozen in the nonperturbative regime to avoid the Landau pole. Away from the nonperturbative region, the above bulk scales all assume their canonical values for $q_T, \mathcal{T} \ll Q$ as given in table 4.1, and asymptote to μ_{FO} when simultaneously taking $q_T, \mathcal{T} \to Q$. The beam function scales in the bulk can simply be associated with their SCET_{II} counterparts and only require a transition towards the SCET_{I} boundary. They are therefore given by

$$\mu_B^+ = \left[\mu_B^{\text{I}}\right]^{h_{\text{I}}(a)} \left[\mu_B^{\text{II}}\right]^{h_+(a)+h_{\text{II}}(a)},$$

$$\nu_B^+ = \left[\nu\right]^{h_{\text{I}}(a)} \left[\nu_B^{\text{II}}\right]^{h_+(a)+h_{\text{II}}(a)}. \tag{4.65}$$

For the numerical implementation, the helper functions $h_{\text{I},\text{II},+}$ are chosen as

$$h_{\text{I}}(a) \equiv \begin{cases} 1 & a < a_1\,, \\ 1 - c_{123}(a) & a_1 \le a < a_2\,, \\ c_{312}(a) & a_2 \le a < a_3\,, \\ 0 & a_3 \le a\,, \end{cases} \qquad h_{\text{II}}(a) \equiv \begin{cases} 0 & a < a_4\,, \\ c_{456}(a) & a_4 \le a < a_5\,, \\ 1 - c_{645}(a) & a_5 \le a < a_6\,, \\ 1 & a_6 \le a\,, \end{cases}$$

$$h_+(a) \equiv 1 - h_{\text{I}}(a) - h_{\text{II}}(a)\,, \tag{4.66}$$

where the polynomials governing the interpolation between zero and one are given by

$$c_{ijk}(a) = \frac{(a - a_i)^2}{(a_i - a_j)(a_i - a_k)} \, . \tag{4.67}$$

The transition points $a_{1,\dots,6}$ determine the transition between the different regions, as can be seen from the helper functions in fig. 4.9.

For values $a_3 \leq a < a_4$, the exact canonical SCET_+ scales are selected, implying that the resummation of logarithms of both q_T and $\mathcal{T}$ is fully turned on. For lower values $a_1 \leq a < a_3$, the additional q_T resummation is smoothly turned off and for $a < a_1$, the SCET_I scales are used so that only logarithms of $\mathcal{T}$ are resummed. Conversely, for higher values of the regime parameter $a_4 \leq a < a_6$, the resummation of $\mathcal{T}$ logarithms is smoothly turned off. At values $a_6 \leq a$, the SCET_II scales are selected by the helper functions, and the additional resummation of logarithms of $\mathcal{T}$ is completely turned off.

In practice, the transition points

$$(a_1, a_2, a_3, a_4, a_5, a_6) = (0.5,\ 1.0,\ 1.5,\ 1.5,\ 1.75,\ 2.0) \, , \tag{4.68}$$

are chosen. This choice ensures that for $a \geq a_6 = 2$, the SCET_II resummation is fully recovered and that the kinematic edge at $q_T \sim \mathcal{T}$ is faithfully described by preserving the $\mathcal{O}(1)$ cancellation between $\sigma_+\big|_{\mu^\text{II}}$ and the SCET_II nonsingular contribution visible at $a \sim 2$ in the left panel of fig. 4.7. In figs. 4.6 and 4.7, corresponding values of a are indicated on the horizontal axis at the top of the panels.

On the other hand, the power corrections from SCET_I are smaller and tend to set in at values of a lower than the naively expected $a = 1$, which can be seen in fig. 4.6. For example, an $\mathcal{O}(1)$ cancellation between $\sigma_+\big|_{\mu^\text{I}}$ and the SCET_I nonsingular is only in effect around $a \sim 0.5$ in the right panel of fig. 4.6, leaving more room for slowly turning off the SCET_+ resummation down towards $a_1 = 0.5$.

The physical reason behind this is the fact that the SCET_I nonsingular encodes the suppression of collinear recoil beyond the naive phase-space boundary at $a \sim 1$ (corresponding to $q_T \sim \sqrt{Q\mathcal{T}}$) that is washed out by the PDFs, unlike the sharp kinematic edge at $q_T \sim \mathcal{T}$ encoded in the SCET_II nonsingular.

For simplicity, the choice $a_3 = a_4$ is made for the central prediction, so that the canonical SCET_+ region gets reduced to a single point at $a = 1.5$. The transition points a_2 and a_5 are fixed as the midpoints between a_1 and a_3 and a_4 and a_6 respectively. Variations of the transition points, including independent variations of a_3 and a_4, are considered as part of the uncertainty estimates described in the next section.

4.3.4 Perturbative uncertainties

Perturbative uncertainties are assessed by varying the scales that enter the matched prediction in eq. (4.49). Following the same approach as for SCET_I and SCET_II on their own (see secs. 4.2.2 and 4.2.3), a similar distinction between resummation uncertainties and a fixed-order uncertainty is made. The fixed-order uncertainty Δ_FO is again estimated by varying μ_FO up and down by a factor of two, i.e. by setting $\mu_\text{FO} = \{Q/2, 2Q\}$. Since all scales (in any piece of the matching formula) include an overall factor of μ_FO, the ratios between the various scales remain unchanged and the same logarithms are resummed. The fixed-order uncertainty Δ_FO is then taken to be the maximum deviation from the central cross section.

Several sources of resummation uncertainties entering the matched prediction in eq. (4.49) are considered. To probe the tower of logarithms of $\mathcal{T}/Q$ predicted by the SCET_I RGE, variations of μ_B^I and μ_S^I parametrized by α and β as in eq. (4.12) are taken into account. This directly affects the resummed power corrections $\left[\mathrm{d}\sigma_\text{I} - \mathrm{d}\sigma_+\right]_{\mu_\text{I}}$ captured by SCET_I. In addition to this, $\mathrm{d}\sigma_+\big|_{\mu_+}$ inherits the SCET_I variations near the corresponding boundary since there h_I is large and the SCET_+ scales in eqs. (4.63) and (4.65) strongly depend on the SCET_I scales. The setup developed in this chapter thus ensures that in (or near) the SCET_I region, variations probing resummed logarithms of $\mathcal{T}/Q$ are properly treated as correlated between the SCET_+ cross section and the SCET_I matching correction. When referring to the matched prediction in eq. (4.49), Δ_I is taken to be the maximum deviation of $\mathrm{d}\sigma_\text{match}$ from its central value under these correlated variations of α and β.

In complete analogy, Δ_II is defined as the maximum deviation under correlated variations of μ_II described in sec. 4.2.3. These variations act on both $\left[\mathrm{d}\sigma_\text{II} - \mathrm{d}\sigma_+\right]_{\mu_\text{II}}$ and $\mathrm{d}\sigma_+\big|_{\mu_+}$, where now the SCET_+ scales inherit variations from μ_II near the SCET_II boundary (where h_II is large). As a result, Δ_II probes an all-order set of logarithms of $(b_0/b_T)/Q$ predicted and resummed by the SCET_II RGE, and properly captures the correlated tower of logarithms in SCET_+. It should be stressed that the current setup is fully generic with respect to the method chosen to perform scale variations for the boundary theories, as any variation will automatically be inherited by SCET_+.

As a final source of uncertainty, the uncertainty inherent to the matching procedure and the choice of SCET_+ scales in the bulk is considered. To estimate this, 8 variations of the transition points (a_1, a_3, a_4, a_6) are taken into account.

These are given by

$$
\begin{aligned}
&(\uparrow,-,-,-)\,, && (-,\downarrow,-,-)\,, && (-,-,-,\downarrow)\,, && (-,\uparrow,\uparrow,-)\,, \\
&(\downarrow,-,-,-)\,, && (-,-,\uparrow,-)\,, && (-,-,-,\uparrow)\,, && (-,\downarrow,\downarrow,-)\,,
\end{aligned}
\tag{4.69}
$$

where $\uparrow$ and $\downarrow$ indicate a variation by $+0.2$ and -0.2 respectively. A dash indicates keeping the transition point fixed, and the relations $a_2 = (a_1 + a_3)/2$ and $a_5 = (a_4 + a_6)/2$ are always retained. In addition, the two variations

$$
\mu_{\mathscr{S},\mathrm{bulk}}^+ = \mu_{\mathrm{FO}} \left(\frac{q_T}{\mathcal{T}}\right)^{+\gamma/2} f_{\mathrm{run}}^{\mathrm{II}} \left(\frac{q_T}{Q}, \frac{b_0}{b^* Q}\right),
$$

$$
\mu_{S,\mathrm{bulk}}^+ = \mu_{\mathrm{FO}} \left(\frac{q_T}{\mathcal{T}}\right)^{-\gamma/2} f_{\mathrm{run}}^{\mathrm{I}} \left(\frac{\mathcal{T}}{Q}\right),
\tag{4.70}
$$

of the SCET$_+$ bulk scales are included. Here $\gamma = \{+1/6, -1/6\}$ and $\gamma = 0$ corresponds to the central scales in eq. (4.64). Similarly to the role of β in the SCET$_{\mathrm{I}}$ variations in eq. (4.12), making the strength of the γ variations depend on the ratio $q_T/\mathcal{T}$ ensures that the hierarchy $\mu_S < \mu_{\mathscr{S}}$ implied by the SCET$_+$ power counting is not upset by variations, counting $b_0/b_T \sim q_T$. The third independent bulk scale $\nu_{\mathscr{S},\mathrm{bulk}}^+$ does not require an independent variation because it only enters through rapidity logarithms of $\nu_B^+/\nu_{\mathscr{S}}^+$, which are already being probed by variations of ν_B^+ inherited from SCET$_{\mathrm{II}}$. Taking the envelope of the eight transition point variations and the two bulk scale variations, a third contribution to the resummation uncertainty is obtained, which is denoted by Δ_+. The total uncertainty assigned to the matched prediction is then given by adding all contributions in quadrature

$$
\Delta_{\mathrm{total}} = \Delta_+ \oplus \Delta_{\mathrm{I}} \oplus \Delta_{\mathrm{II}} \oplus \Delta_{\mathrm{FO}}\,.
\tag{4.71}
$$

4.3.5 Differential and cumulant scale setting

Before presenting the numerical results of the framework developed in this chapter, the issue of differential versus cumulant scale setting must be addressed. For simplicity, the case of a cross section differential only in 0-jettiness $\mathcal{T}$ will be used as an example. There are two quantities of interest in this case, namely the spectrum $\mathrm{d}\sigma/\mathrm{d}\mathcal{T}$ and the cumulative cross section $\sigma(\mathcal{T}_{\mathrm{cut}})$ with a cut on $\mathcal{T}$. The two quantities are related by

$$
\sigma(\mathcal{T}_{\mathrm{cut}}) = \int_0^{\mathcal{T}_{\mathrm{cut}}} \mathrm{d}\mathcal{T}\, \frac{\mathrm{d}\sigma}{\mathrm{d}\mathcal{T}}\,,
\tag{4.72}
$$

where the dependence on Q^2 and Y is suppressed for readability. In a resummation analysis, one can implement the resummation scales either in terms of

the differential variable $\mathcal{T}$ to directly predict the spectrum, or in terms of the cumulant variable $\mathcal{T}_{\mathrm{cut}}$ to predict the cross section integrated up to $\mathcal{T}_{\mathrm{cut}}$. The other observable then follows from eq. (4.72). Using differential scale setting (indicated by the subscript), the differential and cumulant cross section are explicitly given by

$$\frac{\mathrm{d}\sigma_{\mathrm{diff}}}{\mathrm{d}\mathcal{T}} = \frac{\mathrm{d}\sigma}{\mathrm{d}\mathcal{T}}\Big|_{\mu(\mathcal{T})},$$

$$\sigma_{\mathrm{diff}}(\mathcal{T}_{\mathrm{cut}}) = \int^{\mathcal{T}_{\mathrm{cut}}} \mathrm{d}\mathcal{T} \left[\theta(\mathcal{T} > \mathcal{T}_{\mathrm{np}}) \frac{\mathrm{d}\sigma}{\mathrm{d}\mathcal{T}}\Big|_{\mu(\mathcal{T})} + \theta(\mathcal{T} \le \mathcal{T}_{\mathrm{np}}) \frac{\mathrm{d}\sigma}{\mathrm{d}\mathcal{T}}\Big|_{\mu(\mathcal{T}_{\mathrm{np}})} \right]. \quad (4.73)$$

In the first term under the integral in the cumulant cross section, all scales μ entering the resummed and matched prediction depend on the integration variable $\mathcal{T}$. Because the described setup only reliably predicts the spectrum away from the nonperturbative region, the resummed spectrum with differential scale setting is integrated up from some small nonperturbative cutoff $\mathcal{T}_{\mathrm{np}}$ and an "underflow" contribution compensating for the missing interval is included as the second term under the integral. For the underflow contribution, i.e. for $\mathcal{T} \le \mathcal{T}_{\mathrm{np}}$, the spectrum is evaluated at fixed scales corresponding to $\mathcal{T}_{\mathrm{np}}$, such that the integral can be done analytically. The underflow contribution is Sudakov suppressed and thus typically small.

When the scales are set at the level of the cumulant, the cumulative and differential cross section are instead given by

$$\sigma_{\mathrm{cumul}}(\mathcal{T}_{\mathrm{cut}}) = \int^{\mathcal{T}_{\mathrm{cut}}} \mathrm{d}\mathcal{T} \frac{\mathrm{d}\sigma}{\mathrm{d}\mathcal{T}}\Big|_{\mu(\mathcal{T}_{\mathrm{cut}})},$$

$$\frac{\mathrm{d}\sigma_{\mathrm{cumul}}}{\mathrm{d}\mathcal{T}} = \frac{\mathrm{d}\sigma}{\mathrm{d}\mathcal{T}}\Big|_{\mu(\mathcal{T})} + \sum_i \left[\frac{\mathrm{d}}{\mathrm{d}\mu_i} \int^{\mathcal{T}} \mathrm{d}\mathcal{T}' \frac{\mathrm{d}\sigma}{\mathrm{d}\mathcal{T}'} \right]_{\mu(\mathcal{T})} \frac{\mathrm{d}\mu_i(\mathcal{T})}{\mathrm{d}\mathcal{T}}. \quad (4.74)$$

In this case, the scales in the cumulative cross section depend on $\mathcal{T}_{\mathrm{cut}}$, and not the integration variable $\mathcal{T}$, so the integral up to $\mathcal{T}_{\mathrm{cut}}$ can easily be performed analytically. The expression for the differential cross section arises from taking the derivative of the cumulant cross section, where the chain rule leads to the sum of derivatives of each of the scales μ_i in μ with respect to $\mathcal{T}$.

Cumulant scale setting ensures that for $\mathcal{T}_{\mathrm{cut}} \to Q$, the resummed and matched cumulant cross section exactly reproduces the inclusive fixed-order cross section. This follows from the generic requirement on profile scales in the fixed-order region,

$$\mu_i(\mathcal{T}_{\mathrm{cut}}) \longrightarrow \mu_{\mathrm{FO}} \qquad \text{for} \qquad \mathcal{T}_{\mathrm{cut}} \longrightarrow Q. \quad (4.75)$$

Thus for cumulant scale setting, the spectrum has the correct (fixed-order) normalization. However, the additional derivatives of the scales in eq. (4.74)

tend to produce artifacts in the spectrum if the profile functions $\mu_i(\mathcal{T})$ used to interpolate between the resummation region $\mathcal{T} \ll Q$ to the fixed-order region $\mathcal{T} \sim Q$ undergo a rapid transition. Moreover, the scale variations using cumulant scale setting tend to produce unreliable uncertainties for the spectrum.

If instead differential scale setting is used, the spectrum is free from such artifacts. However, the integral of the spectrum will not exactly recover the inclusive fixed-order cross section, and the uncertainties obtained for the cumulant by integrating the spectrum scale variations tend to accumulate and end up being much larger than they should be for the total cross section. The reason for this is that the spectrum models the differential cross (and the corresponding uncertainties) point-by-point in $\mathcal{T}$ and fails to accurately describe any long-range correlations. As in the case of the spectrum with cumulant scale setting, this mismatch purely arises from residual scale dependence, and is therefore formally beyond the working-order. It can however still be numerically significant, which is why in general the scale setting appropriate for the quantity of interest should be used, i.e. cumulant scale setting should be used when making predictions for the cumulant, and differential scale setting when the spectrum is the quantity of interest.

The issue of differential versus cumulant scale setting is well appreciated in the literature for the single-differential case, see e.g. refs. [103, 149, 172, 173]. It ultimately results from the fact that long-range correlations across the spectrum are not accounted for by the profile scales used for the differential predictions. Conversely, profile scales for the cumulant do not correctly capture the slope of the cumulant and its uncertainty. An elaborate procedure for obtaining a spectrum with differential scales that still produces the exact cross section and uncertainties was developed in ref. [173]. In the `Geneva` Monte Carlo generator, the mismatch between differential and cumulant scales is accounted for by adding explicit higher-order terms [149].

For a simultaneous measurement of q_T and $\mathcal{T}$, there are in principle four quantities of interest, namely the double-differential spectrum $\mathrm{d}\sigma/\mathrm{d}q_T\,\mathrm{d}\mathcal{T}$, the single-differential spectra $\mathrm{d}\sigma(q_T^{\mathrm{cut}})/\mathrm{d}\mathcal{T}$ and $\mathrm{d}\sigma(\mathcal{T}_{\mathrm{cut}})/\mathrm{d}q_T$ with a cut on the other variable, and the double cumulant $\sigma(q_T^{\mathrm{cut}}, \mathcal{T}_{\mathrm{cut}})$. They are all related by integration or differentiation, allowing for four different ways of setting scales in each case. All numerical results in sec. 4.4 are obtained by using the appropriate combination of differential or cumulant scale setting with respect to either q_T or $\mathcal{T}$ for each quantity. This is achieved by evaluating the resummed prediction at profile scales given by the setup described in secs. 4.2.2 and 4.2.3 as well as sec. 4.3.3, but with q_T and $\mathcal{T}$ replaced by q_T^{cut} and $\mathcal{T}_{\mathrm{cut}}$ respectively as appropriate. This guarantees that artifacts from profile functions in spectrum

observables are avoided and ensures that cumulant observables have the correct limiting behavior. For example, $\sigma(q_T^{\mathrm{cut}}, \mathcal{T}_{\mathrm{cut}})$ will by construction recover the inclusive fixed-order cross section when lifting both cuts, while $\mathrm{d}\sigma(q_T^{\mathrm{cut}})/\mathrm{d}\mathcal{T}$ and $\mathrm{d}\sigma(\mathcal{T}_{\mathrm{cut}})/\mathrm{d}q_T$ exactly recover the resummed and matched prediction for the respective inclusive spectrum at large values of the cut.

Nevertheless, it is interesting to investigate how well the different combinations of differential and cumulant scale setting fare for observables other than the one they are designed to describe. However, since this comparison between the various scale settings is not the main topic of interest in this chapter, the issue is instead discussed in more detail in app. D.

4.4 Results

The results obtained for Drell-Yan production $pp \to Z/\gamma^* \to \ell^+\ell^-$ at the LHC, with the simultaneous measurement of the transverse momentum q_T of the lepton pair and the 0-jettiness event shape $\mathcal{T}$ are presented in this section. The center-of-mass energy is taken to be $E_{\mathrm{cm}} = 13\,\mathrm{TeV}$. The invariant mass Q of the lepton pair is measured in addition and the rapidity Y is integrated over. For results obtained at the invariant mass $Q = m_Z$, the notation $pp \to Z$ is used to denote the process, while results at other invariant masses are denoted by $pp \to Z^*$. The subsequent decay and the contribution from the virtual photon are included in either case.

To obtain numerical results for the $\mathrm{SCET_I}$, $\mathrm{SCET_{II}}$, and $\mathrm{SCET_+}$ contributions, all pieces of the relevant double-differential factorized cross sections have been implemented in `SCETlib` [174] to $\mathcal{O}(\alpha_s)$ and their RGEs to NNLL accuracy. The fixed NLO contributions in full QCD are obtained from `MCFM 8.0` [175–177]. The `MMHT2014nnlo68cl` [40] NNLO PDFs with five-flavor running and $\alpha_s(m_Z) = 0.118$ are used. Since nonperturbative effects have not been included, results are presented down to $1\,\mathrm{GeV}$ in both q_T and $\mathcal{T}$.

4.4.1 Double-differential spectrum

To highlight the necessity of the simultaneous resummation of large logarithms of both q_T and $\mathcal{T}$, results for the double spectrum (the cross section double-differential in q_T and $\mathcal{T}$) are shown where only some of the logarithms are resummed. These results are shown as surface plots in fig. 4.10, where the double-differential spectrum is plotted with respect to $\log_{10} q_T$ and $\log_{10} \mathcal{T}$ for better visibility. In each case, the left rear wall of the surface plot shows the result of integrating the double-differential spectrum up to $\mathcal{T}_{\mathrm{cut}} = 100\,\mathrm{GeV}$. Similarly, the right rear wall shows the projection onto the single-differential spectrum in $\log_{10} \mathcal{T}$, with a cut at $q_T^{\mathrm{cut}} = 100\,\mathrm{GeV}$.
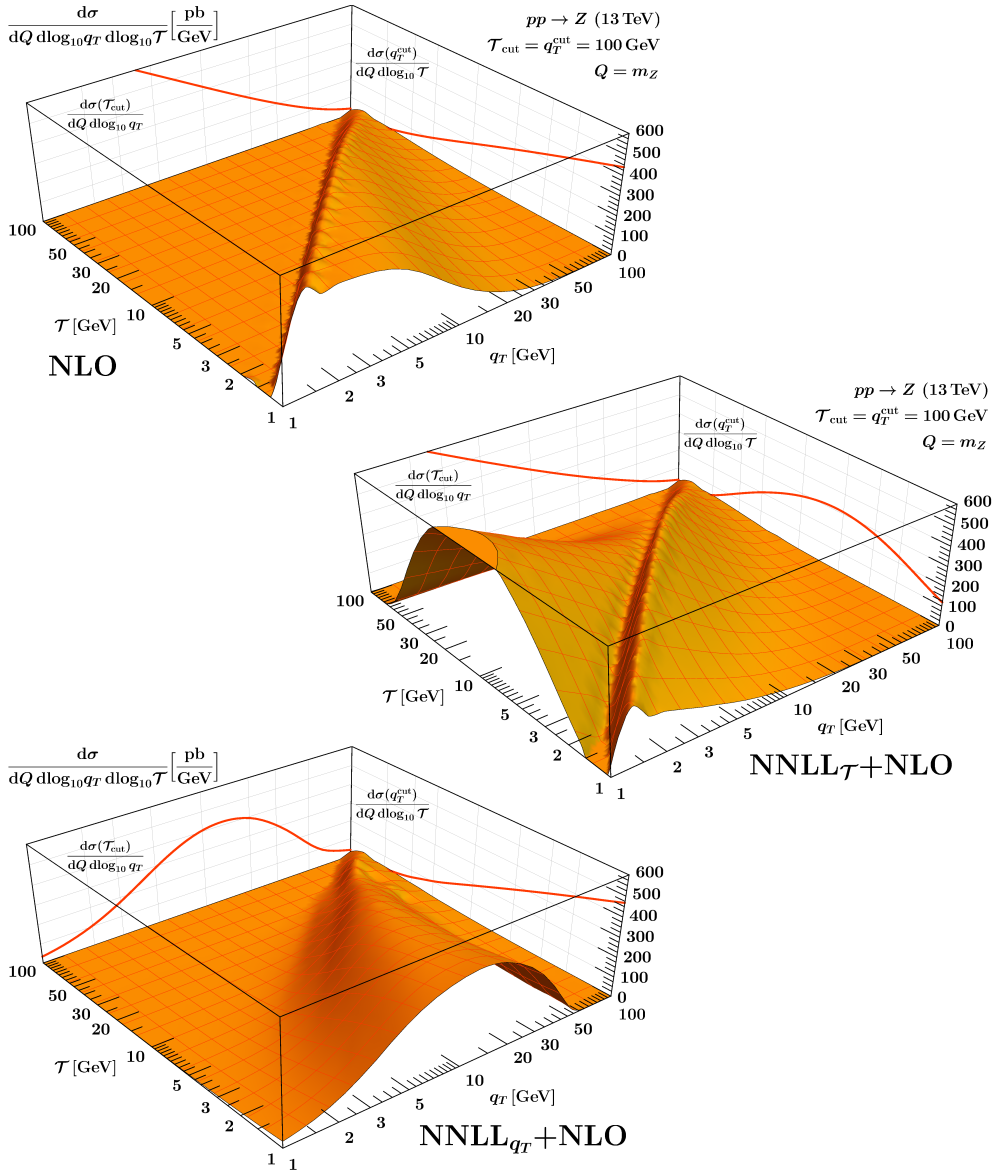
Figure 4.10 The double-differential Drell-Yan cross section at fixed NLO (top), resummed NNLL$_\mathcal{T}$+NLO (center), and NNLL$_{q_T}$+NLO (bottom). The resummed predictions are obtained by using only SCET$_\mathrm{I}$ (SCET$_\mathrm{II}$) renormalization group evolution to resum logarithms of $\mathcal{T}$ (q_T), as outlined in sec. 4.2.2 (sec. 4.2.3), and matching the result to the fixed-order cross section. For better visibility, the spectrum is shown with respect to $\log_{10} q_T$ and $\log_{10} \mathcal{T}$. On the rear walls, the results of integrating the double spectrum over either variable up to a cut at $100\,\mathrm{GeV}$ are shown.

The top left panel of fig. 4.10 shows the spectrum evaluated at fixed $\mathcal{O}(\alpha_s)$, without any resummation. The double-differential fixed-order spectrum diverges logarithmically for small $\mathcal{T}$ at any value of q_T, while its projections onto the single-differential spectra in q_T and $\mathcal{T}$ feature double-logarithmic singularities. Notably, the double-differential spectrum has a sharp kinematic edge along $q_T = \mathcal{T}$. This sharp edge is unphysical because it only reflects the kinematics of a single on-shell emission with transverse momentum k_T at rapidity η, which contributes at most $\mathcal{T} = k_T \, e^{-|\eta|} \leq k_T = q_T$. Due to the vectorial nature of q_T, however, back-to-back emissions can populate the region $\mathcal{T} > q_T$ at higher orders, and the kinematic edge will be smeared out.

Next, the cases in which only logarithms of one variable are resummed are considered, while logarithms involving the auxiliary variable are treated at fixed-order. In the middle panel of fig. 4.10, the result of resumming logarithms of $\mathcal{T}$ using the SCET$_\text{I}$ matched result in eq. (4.8) is shown. The resummation is performed at NNLL and is matched to full NLO, which is referred to as NNLL$_\mathcal{T}$+NLO. As discussed in sec. 4.2.2, this prediction is valid as long as the parametric relation $\mathcal{T} \ll q_T \sim \sqrt{Q\mathcal{T}}$ is satisfied. This corresponds to the SCET$_\text{I}$ phase-space boundary (blue) in fig. 4.1, running from the region of small $\mathcal{T}$ and intermediate q_T towards the fixed-order region where $q_T \sim \mathcal{T} \sim Q$. It is clear that away from its region of validity, the NNLL$_\mathcal{T}$+NLO result contains unresummed large logarithms of q_T because at any point in $\mathcal{T}$ the prediction diverges for very small q_T. The power corrections of $\mathcal{O}(\mathcal{T}^2/q_T^2)$ grow large when approaching the diagonal $\mathcal{T} = q_T$ (the green line in fig. 4.1) and encode the phase space boundary at $q_T \sim \mathcal{T}$. Since this boundary is treated at fixed-order, it leads to the same sharp kinematic edge along the diagonal that was also present in the fixed-order spectrum without any resummation. The projections onto the rear walls highlight that only $\mathcal{T}$ is resummed. The single-differential q_T spectrum still diverges as $q_T \to 0$, while the $\mathcal{T}$ spectrum features a physical Sudakov peak.

In the bottom panel of fig. 4.10, the result of resumming logarithms of (the variable conjugate to) q_T to NNLL and matching to fixed NLO, using the SCET$_\text{II}$ matched result in eq. (4.25) is shown. This order is denoted by NNLL$_{q_T}$+NLO. The result is valid for $\mathcal{T} \sim q_T \ll \sqrt{Q\mathcal{T}}$, i.e. around the SCET$_\text{II}$ phase-space boundary (green) in fig. 4.1, where the onset of a Sudakov peak from the q_T resummation and a smooth kinematic suppression towards $\mathcal{T} \gg q_T$ can be seen. However, the NNLL$_{q_T}$+NLO result diverges for smaller values of $\mathcal{T}$. This is due to unresummed large logarithms of $\mathcal{T}$ in both the factorized cross section in SCET$_\text{II}$ and terms of $\mathcal{O}(q_T^2/(Q\mathcal{T}))$ that are treated at fixed-order as part of the matching correction. In this case, the single-differential projections show a Sudakov peak in q_T, but a logarithmic divergence at small $\mathcal{T}$.
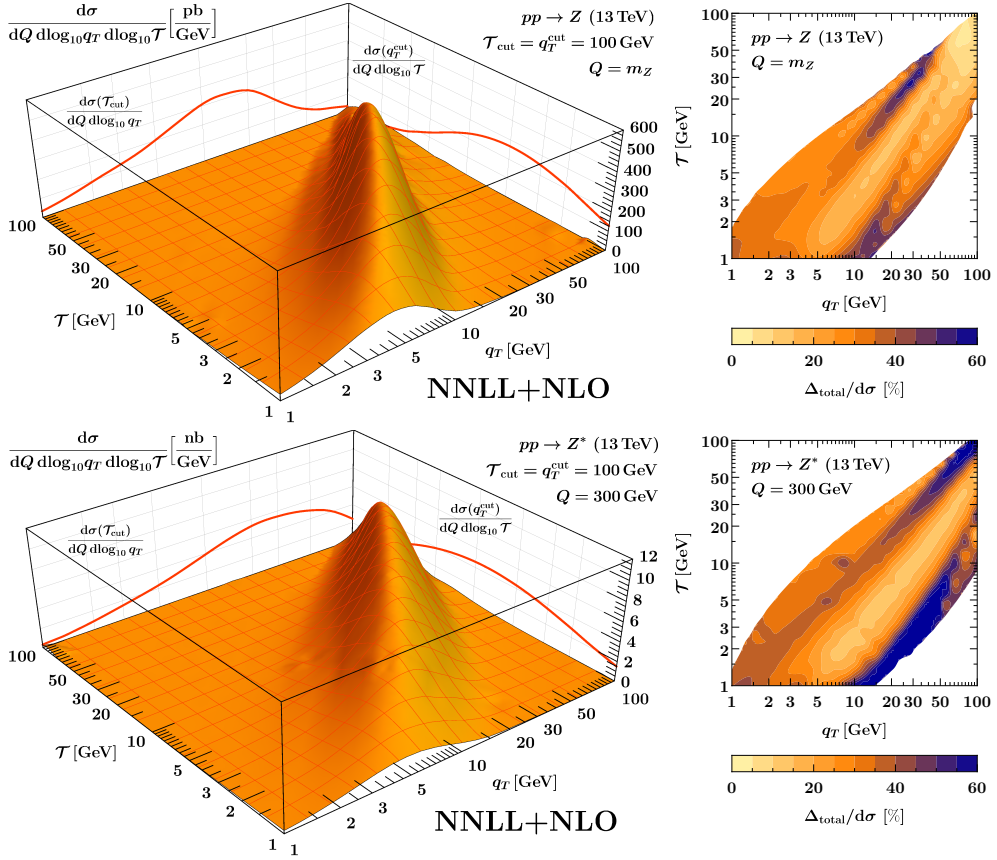
Figure 4.11 The double-differential Drell-Yan cross section at NNLL+NLO, at $Q = m_Z$ (top) and $Q = 300\,\mathrm{GeV}$ (bottom), with respect to $\log_{10} q_T$ and $\log_{10} \mathcal{T}$. The contour plots indicate total perturbative uncertainties relative to the cross section, i.e. $\Delta_{\mathrm{total}} = \Delta_+ \oplus \Delta_{\mathrm{I}} \oplus \Delta_{\mathrm{II}} \oplus \Delta_{\mathrm{FO}}$.

The final results for the Drell-Yan double spectrum as given by the fully matched prediction in eq. (4.49) are shown in fig. 4.11. Here, all resummed contributions are evaluated at NNLL and matched to fixed NLO. This achieves the complete resummation of all large logarithms in the double spectrum, so this order is simply referred to as NNLL+NLO. The top row of plots is for $Q = m_Z$, i.e. for Drell-Yan production at the Z pole. In the bottom row, the invariant mass $Q = 300\,\mathrm{GeV}$ is considered as a representative phase-space point at higher production energies. The matched and fully resummed double spectrum features a two-dimensional Sudakov peak that is situated between the two parametric phase-space boundaries as indicated in fig. 4.1. It is smoothly
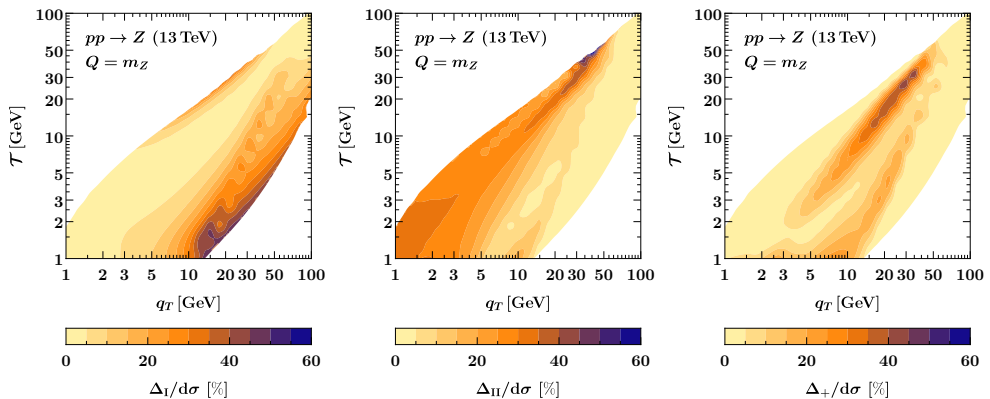
Figure 4.12 Breakdown of resummation uncertainties contributing to the relative uncertainty in the top right panel of fig. 4.11, showing (from left to right) Δ_{I}, Δ_{II}, and Δ_{+}. As in fig. 4.11, regions where the cross section is small are left blank.

suppressed beyond these boundaries, and shifts towards higher values of q_T and $\mathcal{T}$ for $Q = 300\,\mathrm{GeV}$, as expected. Integrating the double spectrum over either variable also results in a physical Sudakov peak, as can be seen from the projections onto the rear walls. Up to small differences in scale setting discussed in sec. 4.3.5, the left and right rear walls agree with the result of integrating the $\mathrm{NNLL}_{q_T}+\mathrm{NLO}$ and $\mathrm{NNLL}_{\mathcal{T}}+\mathrm{NLO}$ results in fig. 4.10 over $\mathcal{T}$ and q_T, respectively. The contour plots in fig. 4.11 show the total perturbative uncertainties Δ_{total} as percent deviations from the central result for the double spectrum. As described in sec. 4.3.4, Δ_{total} combines the estimates of all sources of resummation uncertainty in the prediction. The contour plots are left blank in the region where $\mathrm{d}\sigma/(\mathrm{d}Q\,\mathrm{d}\log_{10} q_T\,\mathrm{d}\log_{10}\mathcal{T})$ is less than 3% of its peak height.

In fig. 4.12, the uncertainty for the Drell-Yan double-differential spectrum at $Q = m_Z$ is broken down into its contributions from the $\mathrm{SCET_I}$, $\mathrm{SCET_{II}}$ and $\mathrm{SCET_+}$ resummation uncertainties. As expected, the $\mathrm{SCET_I}$ resummation uncertainty dominates in the $\mathrm{SCET_I}$ region of phase space, and similarly for $\mathrm{SCET_{II}}$. The $\mathrm{SCET_+}$ resummation uncertainty is largest along the phase-space boundaries, indicating that it is mostly sensitive to variations of the transition points, i.e. the points where the intrinsic $\mathrm{SCET_+}$ resummation is turned off in the matched prediction.
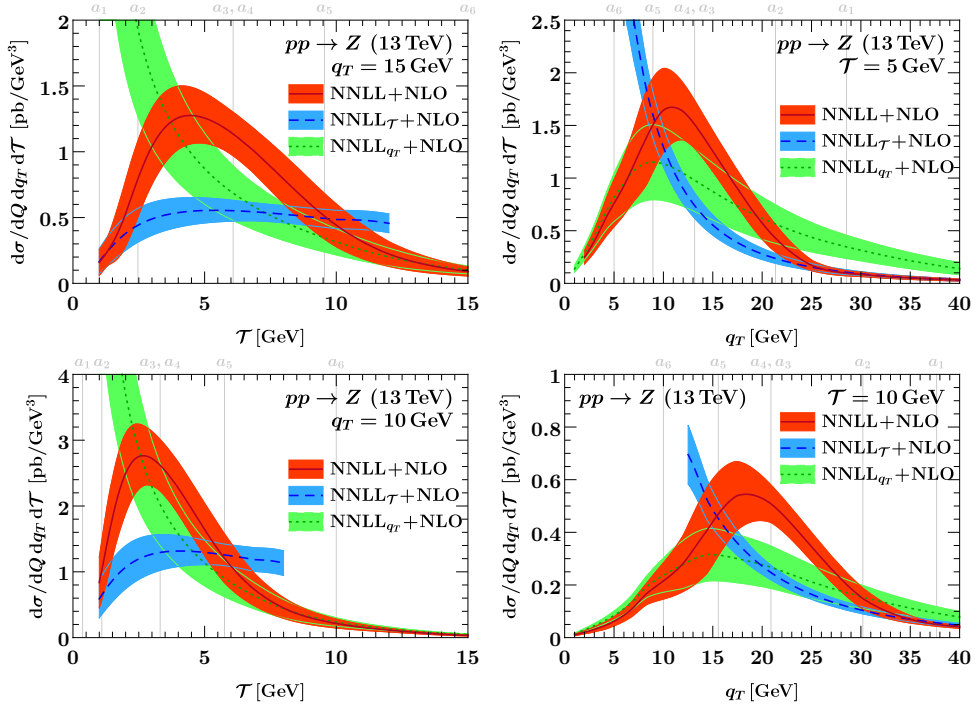
Figure 4.13 The double-differential Drell-Yan cross section for fixed q_T, as a function of $\mathcal{T}$ (left) and for fixed $\mathcal{T}$, as a function of q_T (right). The solid red curves are slices of the surface plots shown in the top left panel in fig. 4.11, up to Jacobians. The blue dashed (green dotted) curves correspond to the middle (bottom) panel of fig. 4.10. The thin vertical lines indicate the transition points a_i described in sec. 4.3.3. The SCET$_{\mathrm{I}}$ prediction (dashed blue) has an unphysical edge at $\mathcal{T} = q_T$, see fig. 4.10, and is not shown beyond $\mathcal{T} = 0.8\,q_T$ to avoid distraction.

4.4.2 Comparison with boundary theories

To further highlight the differences between the fully double-differential resummation and the single-differential resummation at either NNLL$_{q_T}$ or NNLL$_{\mathcal{T}}$, slices of the surface plots are considered in fig. 4.13, keeping q_T (left) or $\mathcal{T}$ (right) fixed. The solid red curve corresponds to the matched and fully resummed cross section in eq. (4.49), with the uncertainty band given by the total perturbative uncertainty Δ_{total} as given in eq. (4.71). The matched SCET$_{\mathrm{I}}$ (dashed blue) and SCET$_{\mathrm{II}}$ (dotted green) predictions correspond to the middle and bottom panel of fig. 4.10, respectively. Their uncertainty bands are given by $\Delta_{\mathrm{total}}^{\mathrm{I}}$ and $\Delta_{\mathrm{total}}^{\mathrm{II}}$, defined in eqs. (4.15) and (4.34), which only probe
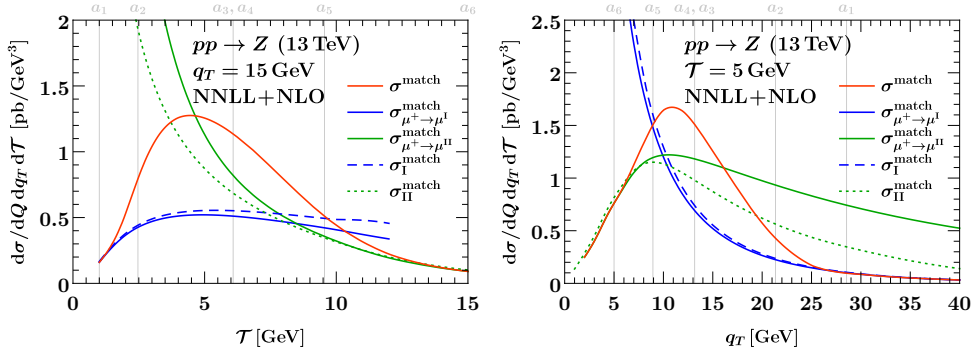
Figure 4.14 Slices of the double-differential Drell-Yan cross section at $q_T = 15\,\mathrm{GeV}$ (left) and $\mathcal{T} = 5\,\mathrm{GeV}$ (right). The solid red, dashed blue, and dotted green curves are identical to the central results in fig. 4.13. The solid blue and green curves depict the SCET_I and $\mathrm{SCET}_\mathrm{II}$ limits of the fully resummed result, given in eqs. (4.56) and (4.58). The thin vertical lines indicate the transition points a_i described in sec. 4.3.3.

a subset of higher-order terms as predicted by the respective RGE. The SCET_I prediction features an unphysical sharp edge at $\mathcal{T} = q_T$, which is also visible in the middle panel of fig. 4.10, and for this reason is cut off at $\mathcal{T} = 0.8\,q_T$. All panels in fig. 4.13 show that the final prediction smoothly interpolates between the SCET_I and $\mathrm{SCET}_\mathrm{II}$ boundary theories, both for the central values and for the uncertainties. Specifically, the matched prediction tends towards SCET_I for small values of $\mathcal{T}$ and large values of q_T and towards $\mathrm{SCET}_\mathrm{II}$ for large values of $\mathcal{T}$ and small values of q_T. The plots on the left show that $\mathrm{SCET}_\mathrm{II}$ only captures logarithms of $\mathcal{T}$ at fixed-order, leading to a diverging spectrum as $\mathcal{T} \to 0$, while the complete NNLL result features a physical Sudakov peak. Conversely, the SCET_I result diverges as $q_T \to 0$, but is rendered physical by the additional q_T resummation at NNLL.

The fully resummed prediction does not exactly agree with either boundary theory, even beyond the final transition points a_1 and a_6 where the intrinsic SCET_+ resummation is turned off completely. The reason for this is that even in these limits, the matched cross section in eq. (4.49) improves over the matched SCET_I and $\mathrm{SCET}_\mathrm{II}$ cross sections in eqs. (4.8) and (4.25) by an additional resummation of power-suppressed terms, as can be seen from eqs. (4.56) and (4.58). To assess the size of this effect, both single-differential resummations (dashed blue and dotted green) are again compared to the matched prediction (solid red) in fig. 4.14. For reference, the cases where σ_+ in the matched prediction is evaluated at μ^I (solid blue) or μ^II (solid green) directly
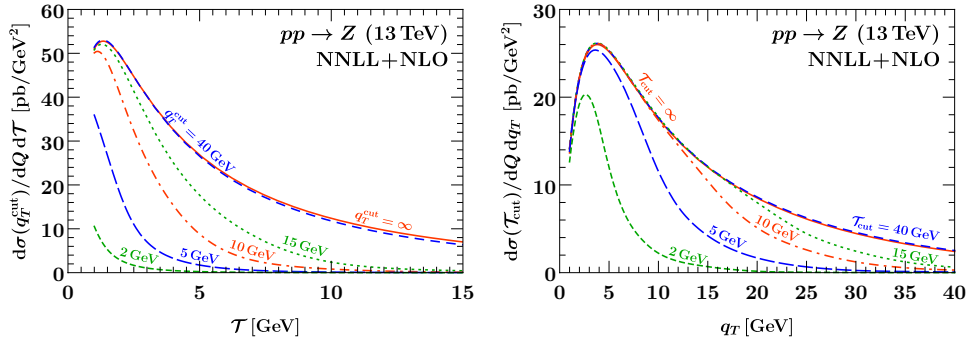
Figure 4.15 The single-differential $\mathcal{T}$ (left) and q_T (right) spectrum with a cut on the other variable at NNLL+NLO. The different curves represent different values of the cut. The solid red lines correspond to the inclusive single-differential spectrum obtained by lifting the cut.

are included. From for example the right panel, it can be verified that for q_T larger than the right-most vertical line (where $a < a_1$), the difference between the solid blue and the dashed blue curves indeed amounts to a small power-suppressed set of higher-order terms, while the best prediction (solid red) recovers the solid blue curve as it must. Similarly, for q_T lower than the left-most vertical line (where $a > a_6$), the difference between the solid green and dashed green curves can be seen to be a small correction, reflecting the size of power-suppressed higher-order terms predicted by the $\mathrm{SCET_I}$ RGE in this region. In this region, the solid red prediction recovers the solid green curve exactly. The asymptotic limits are interchanged in the left panel, where $a < a_1$ towards the left and $a > a_6$ towards the very right of the plot.

4.4.3 Single-differential spectra with cuts

In addition to the cross section differential in both q_T and $\mathcal{T}$, the setup developed in this chapter can also be used to predict the fully matched and resummed double cumulant cross section and the single-differential q_T (or $\mathcal{T}$) spectrum with a cut on the other variable. Some results for these observables were already discussed in sec. 4.3.5 from a more technical point of view. In fig. 4.15, some more detailed results for the single-differential spectra with an additional cut are shown, where the left panel shows $\mathrm{d}\sigma(q_T^{\mathrm{cut}})/\mathrm{d}\mathcal{T}$ as a function of $\mathcal{T}$ for various values of q_T^{cut}, and the right panel shows $\mathrm{d}\sigma(\mathcal{T}_{\mathrm{cut}})/\mathrm{d}q_T$ as a function of q_T for various values of $\mathcal{T}_{\mathrm{cut}}$. By increasing the value of the cut, they can be seen to approach the inclusive single-differential spectra (solid red), with which they must agree when sending $q_T^{\mathrm{cut}} \to \infty$ or $\mathcal{T}_{\mathrm{cut}} \to \infty$, respec-

tively. This agreement occurs by construction because cumulant scale setting is used for this prediction as discussed in sec. 4.3.5. From these plots it can be seen that cuts on the other variable shape either spectrum in a nontrivial way. Tight cuts $\lesssim 10\,\mathrm{GeV}$ push the peak to lower values and suppress the tail, where the q_T spectrum is somewhat more resilient to cuts on $\mathcal{T}$ than vice versa. Intermediate cuts $\sim 10 - 15\,\mathrm{GeV}$ do not change the peak in a substantial way and mostly lead to a suppression in the tail, while the effect of cuts $\gtrsim 40\,\mathrm{GeV}$ is almost negligible in the q_T and $\mathcal{T}$ ranges of interest.

4.4.4 Conclusions

The cross sections of color-singlet production processes at hadron colliders, such as Drell-Yan, that are subject to the simultaneous measurement of q_T and $\mathcal{T}$, involve Sudakov logarithms of both $\mathcal{T}/Q$ and q_T/Q. In this chapter, the simultaneous resummation of both kinds of logarithms has been achieved at NNLL accuracy, and was matched to fixed-order results at NLO. The setup explored in this chapter accomplishes this by employing $\mathrm{SCET_I}$ and $\mathrm{SCET_{II}}$ to describe the regions $\mathcal{T} \ll q_T \sim \sqrt{\mathcal{T}Q}$ and $\mathcal{T} \sim q_T \ll \sqrt{\mathcal{T}Q}$, respectively, and $\mathrm{SCET_+}$ to describe the bulk of phase space in between these boundaries [108].

The framework developed in this chapter allows for the matching of several factorized cross sections, corresponding to different regions of phase space, to one another through a Venn-diagram method that avoids double counting. It includes the appropriate profile scales for the various ingredients in the factorization formulas that respect all relevant canonical scaling relations and at the same time smoothly interpolate between the different regions of phase space. In addition, selected variations of these scales are used to estimate perturbative uncertainties in the resulting cross sections. Determining the profile scales is significantly more involved than in the usual single-differential case, and is further complicated by the requirement to choose scales in impact parameter (b_T) space for $\mathrm{SCET_{II}}$ and $\mathrm{SCET_+}$.

The presented setup of the profile scales is flexible in the sense that scale variations are inherited from the single-differential resummation of $\mathcal{T}$ and q_T and other procedures for estimating uncertainties in the individual resummations can be incorporated. The profile scales facilitate the transition between $\mathrm{SCET_I}$, $\mathrm{SCET_+}$ and $\mathrm{SCET_{II}}$ according to the introduced regime parameter a, designed such that $a = 1$ for $\mathrm{SCET_I}$ and $a = 2$ for $\mathrm{SCET_{II}}$. The precise transition points in a were chosen by comparing the various singular and nonsingular contributions, and are varied as part of the uncertainty estimate.

Finally, a new hybrid (depending on both q_T and b_T) scale choice for q_T resummation is included that allows the resummation to strictly take place in

b_T space, while turning the resummation on and off according to the target q_T value. It was shown that the simultaneous resummation of $\mathcal{T}$ and q_T using this setup yields the correct resummed single-differential cross sections after integrating over either $\mathcal{T}$ or q_T. This requires choosing scales at the level of the differential or integrated (cumulative) cross section as appropriate.

While the predictions obtained here are of some direct phenomenological interest, as $\mathcal{T}$ has been measured in bins of q_T [147], the presented analysis is also an important step towards precise *and* differential predictions for LHC cross sections in general. Specifically, the Monte Carlo event generator `Geneva` [148,149] is based on resummed predictions at NNLL′ accuracy for the cross section differential in $\mathcal{T}$, and would benefit from the simultaneous resummation of q_T. Indeed, the NNLL results clearly indicate that only resumming the logarithms of either $\mathcal{T}$ or q_T gives a poor description of the double-differential cross section. The methods displayed in this chapter apply at any order and for any color-singlet production process, allowing for a straightforward extension once the relevant perturbative ingredients become available.

<div style="text-align: right; font-size: 3em;">5</div>

Transverse momentum resummation at threshold

The momenta of the partons that initiate the hard scattering process in hadron collisions are fractions of the momenta of the colliding protons from which they are extracted. As the PDFs fall off steeply for larger momentum fractions, the probability of producing heavy particles is dominated by the scenario in which the extracted partons lose very little of their momentum before entering the hard process. This implies that the initial-state radiation tends to be soft and these processes naturally occur near the partonic threshold. The partonic cross section of such processes contains logarithms that grow large near this threshold such that their resummation is important in order to obtain reliable predictions. In addition, in cross sections differential in the transverse momentum of the heavy particle, logarithms of the ratio of this transverse momentum and the invariant mass of the particle occur as well. If the transverse momentum is parametrically smaller than the invariant mass, these logarithms must be resummed in addition to the threshold logarithms. This joint resummation has been studied extensively and a framework that achieves NLL accuracy was developed in refs. [125] and [124][1]. This setup performs the resummation of threshold logarithms in Mellin space, while the logarithms involving the transverse momentum are resummed in impact parameter space. The success of this framework is evident from the number of cases to which it was applied, including prompt-photon [178], electroweak [126], Higgs boson [127], heavy-quark [179], slepton pair [180] and gaugino pair [181] production.

In the current chapter, a novel method that achieves the joint resummation of threshold and transverse momentum logarithms at NNLL and beyond[2] is developed. In sec. 5.1, the relevant kinematic regimes are identified and factorization theorems valid to all orders in the strong coupling constant are

---

[1]After the completion of the article that this chapter represents (ref. [1]), the setup from refs. [125] and [124] was extended to NNLL accuracy in refs. [128] and [129].

[2]In fact, all the ingredients required for N^3LL accuracy are currently available.

discussed. The various consistency relations that hold between these different regimes are addressed and checked in sec. 5.2, after which the combination of the distinct regions and the resummation are discussed in sec. 5.3. This chapter is largely based on the work presented in ref. [1].

5.1 Factorization

Heavy color-singlet production processes, such as Higgs production or the production of supersymmetric particles, naturally occur near the partonic threshold $1 - z \ll 1$, where the partonic threshold parameter z is given by

$$z = z_a z_b = \frac{Q^2}{\xi_a \xi_b E_{\mathrm{cm}}^2} = \frac{Q^2}{\hat{s}} \, . \tag{5.1}$$

Here Q^2 denotes the invariant mass of the produced heavy particle and $\hat{s} = \xi_a \xi_b E_{\mathrm{cm}}^2$ is the partonic center-of-mass energy. The partons are extracted from the protons with momentum fractions $\xi_{a,b}$ and emit initial-state radiation, reducing their momentum fractions to $x_{a,b}$, before initiating the hard process. The ratio of these momentum fractions is then given by $z_{a,b} = x_{a,b}/\xi_{a,b}$.

To achieve a framework that allows for the joint resummation beyond NLL, a relative power counting between $1 - z$ and the transverse momentum $q_T \gg \Lambda_{\mathrm{QCD}}$ of the heavy particle must be assumed. Three distinct regimes, corresponding to different hierarchies of these parameters, are identified as

1. Transverse momentum regime: $\Lambda_{\mathrm{QCD}}/Q \ll q_T/Q \ll 1 - z \sim 1 \, ,$
2. Intermediate regime: $\Lambda_{\mathrm{QCD}}/Q \ll q_T/Q \ll 1 - z \ll 1 \, ,$
3. Threshold regime: $\Lambda_{\mathrm{QCD}}/Q \ll q_T/Q \sim 1 - z \ll 1 \, . \tag{5.2}$

Hierarchies in which the transverse momentum of the heavy particle is parametrically larger than $1 - z$ are kinematically suppressed. The reason for this is that the total momentum of the initial-state radiation is constrained by the strong bound on $1 - z$. In particular this means that the combined transverse momentum of the initial-state radiation must adhere to this bound and, since it must recoil against the initial-state radiation, so must the transverse momentum of the heavy particle. The same kinematic regimes and the resulting factorization theorems described in this chapter were independently identified in position space in ref. [182].

The factorization theorems for the transverse momentum and threshold regime are simply more differential versions of the standard transverse momentum and threshold resummation. The intermediate regime requires the use of SCET_+, which contains additional collinear-soft degrees of freedom as was discussed in both sec. 3.10 and sec. 4.2.4.

5.1.1 Transverse momentum regime

The transverse momentum regime is characterized by the parametric hierarchy $\Lambda_{\text{QCD}} \ll q_T \ll (1-z)Q \sim Q$. The parametric size of the energy of the incoming protons is $p^0 \sim Q$, while their virtuality scales like $p^+p^- \sim \Lambda_{\text{QCD}}^2$, uniquely fixing the scaling of the n^μ-collinear and $\bar{n}^\mu$-collinear modes. As this regime does not suffer from any threshold restrictions, the scaling of the isotropic soft radiation is set by the measurement of the total transverse momentum. Furthermore, the lack of any threshold restriction on the energy of the real radiation allows for additional collinear splittings within the proton that can contribute to the q_T measurement. The scaling of the modes in this regime is then given by

$$
\begin{aligned}
n\text{-collinear:} \quad p_n^\mu &\sim
\begin{cases}
\left(\dfrac{\Lambda_{\text{QCD}}^2}{Q}, Q, \Lambda_{\text{QCD}} \right), \\[2ex]
\left(\dfrac{q_T^2}{Q}, Q, q_T \right),
\end{cases} \\[3ex]
\bar{n}\text{-collinear:} \quad p_{\bar{n}}^\mu &\sim
\begin{cases}
\left(Q, \dfrac{\Lambda_{\text{QCD}}^2}{Q}, \Lambda_{\text{QCD}} \right), \\[2ex]
\left(Q, \dfrac{q_T^2}{Q}, q_T \right),
\end{cases} \\[3ex]
\text{soft:} \quad p_s^\mu &\sim \left(q_T, q_T, q_T \right),
\end{aligned}
\tag{5.3}
$$

and is shown schematically in fig. 5.1. The n- and $\bar{n}$-collinear modes with $p^2 \sim \Lambda_{\text{QCD}}^2$ correspond to the collinear PDF, which is matched onto the transverse-momentum-dependent (TMD) beam function. For this reason, these modes were left implicit in the SCET$_{\text{II}}$ regime in sec. 4.2.3. Here they are listed explicitly to make the connection to the threshold regime (described in sec. 5.1.2) more clear. The set of modes in eq. (5.3) leads to the transverse momentum factorization of the cross section given by

$$
\begin{aligned}
\frac{\mathrm{d}\sigma_1}{\mathrm{d}Q^2 \, \mathrm{d}q_T} = H_{ij}(Q, \mu) \int \mathrm{d}x_a \int \mathrm{d}^2\vec{k}_a \, B_i(x_a E_{\text{cm}}, \vec{k}_a, \mu, \nu) \\
\times \int \mathrm{d}x_b \int \mathrm{d}^2\vec{k}_b \, B_j(x_b E_{\text{cm}}, \vec{k}_b, \mu, \nu) \\
\times \int \mathrm{d}^2\vec{k}_s \, S_{ij}(\vec{k}_s, \mu, \nu) \, \delta(\tau - x_a x_b) \, \delta\big(q_T - |\vec{k}_a + \vec{k}_b + \vec{k}_s|\big), \quad
\end{aligned}
\tag{5.4}
$$

which holds to all orders in the strong coupling constant. Here the hadronic threshold variable has been defined as

$$
\tau \equiv Q^2/E_{\text{cm}}^2 = x_a x_b.
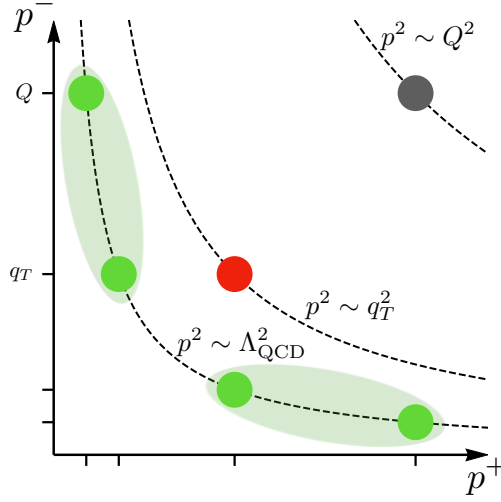\tag{5.5}
$$
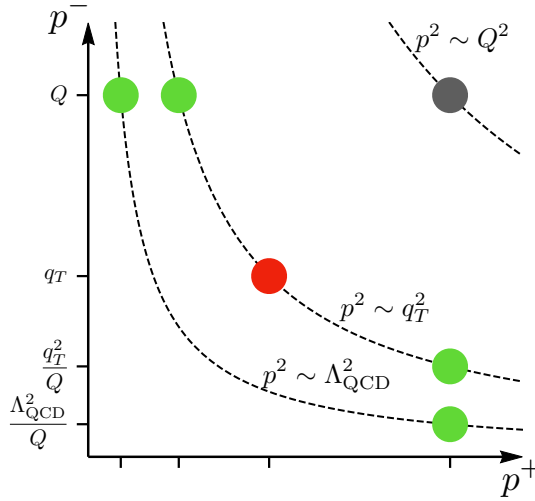
Figure 5.1 The power counting of collinear (green) and soft (red) modes for the transverse momentum regime. The scaling of the hard modes (gray) is shown for reference. The dashed lines show the various invariant-mass hyperbolas.

The transverse momentum factorization yields the full cross section up to power corrections of the form

$$\frac{\mathrm{d}\sigma}{\mathrm{d}Q^2\,\mathrm{d}q_T} = \frac{\mathrm{d}\sigma_1}{\mathrm{d}Q^2\,\mathrm{d}q_T}\left[1 + \mathcal{O}\left(\frac{q_T^2}{Q^2}\right)\right]. \tag{5.6}$$

The hard function $H_{ij}(Q, \mu)$ encodes the short-distance scattering of the partons and depends on the partonic channel, denoted by i and j. Since color-singlet production is considered here, the implicit sum over $\{i, j\}$ is restricted to the channels $\{q, \bar{q}\}$, $\{\bar{q}, q\}$ and $\{g, g\}$. The TMD beam functions $B_i(\omega, \vec{k}_T, \mu, \nu)$ are the same as those encountered in sec. 4.2.3 and are matched onto the PDFs [49,99,105,157–160] through eq. (4.20). The threshold logarithms of $1-z$ reside in the diagonal matching coefficients $\mathcal{I}_{ii}$, but are small due to the parametric hierarchy of this region. The TMD soft function $S_{ij}(\vec{k}_T, \mu, \nu)$ encodes the contribution of soft radiation to the measurement of the total transverse momentum[3]. Explicit expressions for these perturbative ingredients up to one loop can be found in app. B.

---

[3]The TMD beam and soft function are often combined into one object [158–160]. This is inconvenient here because the intermediate regime involves the TMD soft function with collinear-soft functions instead of the standard TMD beam functions. Though they are related, see eq. (5.21), they differ in the rapidity logarithms, see eq. (5.34).

Figure 5.2 The power counting of collinear (green) and soft (red) modes for the threshold regime. The scaling of the hard modes (gray) is shown for reference. The dashed lines show the various invariant-mass hyperbolas and the nonperturbative modes that are not factorized are grouped together.

5.1.2 Threshold regime

The threshold regime is characterized by the parametric hierarchy $\Lambda_{\text{QCD}} \ll q_T \sim (1 - z)Q \ll Q$. The energy of the real radiation is now set to be of the order of $(1 - z)Q$, so that the scaling of the modes representing collinear splittings within the protons is now bounded by the threshold parameter. Both collinear modes in each sector are nonperturbative and combine into (threshold) PDFs. The soft radiation still contributes to the transverse momentum measurement, but is also restricted by the threshold parameter. The modes in the threshold regime are shown in fig. 5.2 and their scaling is given by

$$
n\text{-collinear:} \quad p_n^\mu \sim \begin{cases} \left(\dfrac{\Lambda_{\text{QCD}}^2}{Q}, Q, \Lambda_{\text{QCD}} \right), \\[2ex] \left(\dfrac{\Lambda_{\text{QCD}}^2}{(1-z)Q}, (1-z)Q, \Lambda_{\text{QCD}} \right) \sim \left(\dfrac{\Lambda_{\text{QCD}}^2}{q_T}, q_T, \Lambda_{\text{QCD}} \right), \end{cases}
$$

$$
\bar{n}\text{-collinear:} \quad p_{\bar n}^\mu \sim \begin{cases} \left(Q, \dfrac{\Lambda_{\text{QCD}}^2}{Q}, \Lambda_{\text{QCD}} \right), \\[2ex] \left((1-z)Q, \dfrac{\Lambda_{\text{QCD}}^2}{(1-z)Q}, \Lambda_{\text{QCD}} \right) \sim \left(q_T, \dfrac{\Lambda_{\text{QCD}}^2}{q_T}, \Lambda_{\text{QCD}} \right), \end{cases}
$$

$$
\text{soft:} \quad p_s^\mu \sim \left(q_T, q_T, q_T \right) \sim \left((1-z)Q, (1-z)Q, (1-z)Q \right). \tag{5.7}
$$

The threshold factorization of the cross section that these modes lead to is given by

$$\frac{\mathrm{d}\sigma_3}{\mathrm{d}Q^2\,\mathrm{d}q_T} = H_{ij}(Q,\mu) \int \frac{\mathrm{d}\xi_a}{\xi_a}\, f_i^{\mathrm{thr}}(\xi_a,\mu) \int \frac{\mathrm{d}\xi_b}{\xi_b}\, f_j^{\mathrm{thr}}(\xi_b,\mu) \tag{5.8}$$

$$\times \int \mathrm{d}(2k_s^0) \int \mathrm{d}^2\vec{k}_s\, S_{ij}(2k_s^0, \vec{k}_s, \mu)\, \delta\Big(1 - \frac{\tau}{\xi_a\xi_b} - \frac{2k_s^0}{Q}\Big)\, \delta\big(q_T - |\vec{k}_s|\big),$$

which is valid for all orders in α_s and reproduces the full cross section up to power corrections given by

$$\frac{\mathrm{d}\sigma}{\mathrm{d}Q^2\,\mathrm{d}q_T} = \frac{\mathrm{d}\sigma_3}{\mathrm{d}Q^2\,\mathrm{d}q_T}\Big[1 + \mathcal{O}(1-z)\Big]. \tag{5.9}$$

The threshold PDFs $f_i^{\mathrm{thr}}(\xi,\mu)$ encode the extraction of a parton i from a proton in the threshold limit $\xi \to 1$. The k_s^0 in eq. (5.8) is the energy of the soft radiation that arises from the threshold restriction

$$Q^2 = (\xi_a E_{\mathrm{cm}} - k_s^-)(\xi_b E_{\mathrm{cm}} - k_s^+) = \hat{s} - Q\big(k_s^- e^{-Y} + k_s^+ e^Y\big) + \mathcal{O}\big((1-z)^2 Q^2\big)$$

$$= Q^2\Big(\frac{\tau}{\xi_a\xi_b} + \frac{k_s^- e^{-Y}}{Q} + \frac{k_s^+ e^Y}{Q} + \mathcal{O}\big((1-z)^2\big)\Big). \tag{5.10}$$

At hadronic threshold, where $1 - \tau = 1 - Q^2/E_{\mathrm{cm}}^2 \ll 1$, the rapidity scales as $Y \sim \mathcal{O}(1-z)$ and can be dropped. This implies that only the energy of the soft radiation, $k_s^- + k_s^+ = 2k_s^0$, is probed. The rapidity Y can also be eliminated at partonic threshold, as will be shown in sec. 5.1.4.

The fact that the soft radiation contributes to q_T, but is also restricted by the threshold parameter leads to the more differential soft function in eq. (5.8). Using the approach in ref. [183], this new soft function can be obtained explicitly at one loop as[4]

$$S_{ij}(2k^0, \vec{k}_T, \mu) = \frac{\alpha_s C_i}{\pi^2} \frac{\mathrm{d}}{\mathrm{d}(2k^0)} \frac{\mathrm{d}}{\mathrm{d}k_T^2} \Big\{ \theta(k^0)\,\theta(k_T)\Big[2\ln^2\Big(\frac{2k^0}{\mu}\Big) - \frac{\pi^2}{12} \tag{5.11}$$

$$+ \theta(k^0 - k_T)\Big(2a^2 - 4a\ln\Big(\frac{2k^0}{k_T}\Big) + 2\mathrm{Li}_2(-e^{-2a})\Big)\Big]\Big\},$$

where $a = \mathrm{arccosh}(k_0/k_T)$ and C_i is equal to C_F for the quark-antiquark channels and equal to C_A for gluonic channels. This soft function is directly related to the fully-differential soft function of ref. [184]. The projection from k^+ and k^- onto $2k^0$ does not affect the renormalization, but is responsible for the complicated finite terms above. To distinguish it from the double-differential soft function appearing in eq. (4.17), it will be referred to as the projected fully-differential soft function.

---

[4]Azimuthal symmetry implies $\delta(\vec{k}_T - \dots) = \delta(k_T^2 - \dots)/\pi$, allowing for the elimination of vector quantities.

5.1.3 Intermediate regime

The intermediate regime is described by the parametric hierarchy $\Lambda_{\mathrm{QCD}} \ll q_T \ll (1-z)Q \ll Q$. The threshold restriction determines the scaling of the collinear modes, which can no longer contribute to the q_T measurement. The soft radiation does contribute to this measurement, but is not restricted by the threshold condition. There are additional collinear-soft modes in this regime whose scaling is uniquely fixed by their sensitivity to both the transverse momentum measurement and the threshold restriction [108]. A schematic representation of the modes in this regime is shown in fig. 5.3. The explicit scaling of the various degrees of freedom is given by

$$
\begin{aligned}
n\text{-collinear:} \quad p_n^\mu \sim &\begin{cases} \left(\dfrac{\Lambda_{\mathrm{QCD}}^2}{Q}, Q, \Lambda_{\mathrm{QCD}} \right), \\[2ex] \left(\dfrac{\Lambda_{\mathrm{QCD}}^2}{(1-z)Q}, (1-z)Q, \Lambda_{\mathrm{QCD}} \right), \end{cases} \\[4ex]
\bar{n}\text{-collinear:} \quad p_{\bar{n}}^\mu \sim &\begin{cases} \left(Q, \dfrac{\Lambda_{\mathrm{QCD}}^2}{Q}, \Lambda_{\mathrm{QCD}} \right), \\[2ex] \left((1-z)Q, \dfrac{\Lambda_{\mathrm{QCD}}^2}{(1-z)Q}, \Lambda_{\mathrm{QCD}} \right), \end{cases} \\[4ex]
n\text{-collinear-soft:} \quad p_{ns}^\mu \sim &\left(\dfrac{q_T^2}{(1-z)Q}, (1-z)Q, q_T \right), \\[2ex]
\bar{n}\text{-collinear-soft:} \quad p_{\bar{n}s}^\mu \sim &\left((1-z)Q, \dfrac{q_T^2}{(1-z)Q}, q_T \right), \\[2ex]
\text{soft:} \quad p_s^\mu \sim &\left(q_T, q_T, q_T \right).
\end{aligned}
\tag{5.12}
$$

The factorization, valid to all orders in α_s, that these modes lead to is given by

$$
\begin{aligned}
\frac{\mathrm{d}\sigma_2}{\mathrm{d}Q^2 \, \mathrm{d}q_T} = {}& H_{ij}(Q,\mu) \int \frac{\mathrm{d}\xi_a}{\xi_a} f_i^{\mathrm{thr}}(\xi_a,\mu) \int \frac{\mathrm{d}\xi_b}{\xi_b} f_j^{\mathrm{thr}}(\xi_b,\mu) \int \mathrm{d}^2 \vec{k}_s \, S_{ij}(\vec{k}_s,\mu,\nu) \\
&\times \int \mathrm{d}\ell_a^- \int \mathrm{d}^2 \vec{\ell}_a \, \hat{\mathscr{S}}_i(\ell_a^-, \vec{\ell}_a, \mu, \nu) \int \mathrm{d}\ell_b^+ \int \mathrm{d}^2 \vec{\ell}_b \, \hat{\mathscr{S}}_j(\ell_b^+, \vec{\ell}_b, \mu, \nu) \\
&\times \delta \left(1 - \frac{\tau}{\xi_a \xi_b} - \frac{\ell_a^-}{Q} - \frac{\ell_b^+}{Q} \right) \delta \left(q_T - |\vec{\ell}_a + \vec{\ell}_b + \vec{k}_s| \right).
\end{aligned}
\tag{5.13}
$$

It yields the full cross section up to power corrections of the form

$$
\frac{\mathrm{d}\sigma}{\mathrm{d}Q^2 \, \mathrm{d}q_T} = \frac{\mathrm{d}\sigma_2}{\mathrm{d}Q^2 \, \mathrm{d}q_T} \left[1 + \mathcal{O}\left(1 - z, \frac{q_T^2}{(1-z)^2 Q^2} \right) \right].
\tag{5.14}
$$
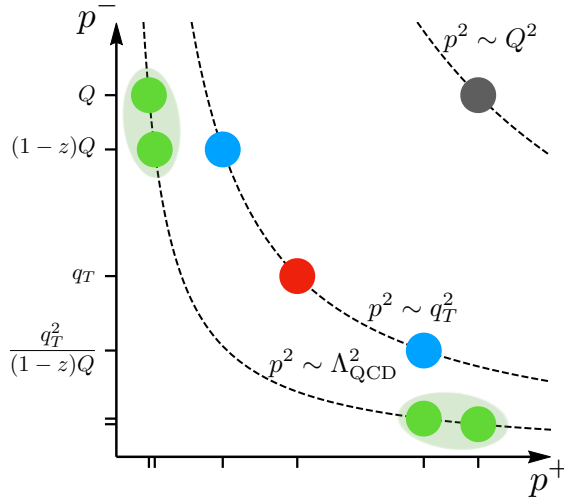
Figure 5.3 The power counting of collinear (green), collinear-soft (blue) and soft (red) modes for the intermediate regime. The scaling of the hard modes (gray) is shown for reference. The dashed lines show the various invariant-mass hyperbolas and the nonperturbative modes that are not factorized are grouped together.

This intermediate regime involves more expansions than both regimes discussed in the previous sections, but it allows for the independent resummation of q_T and threshold logarithms, whereas the threshold parameter was constrained to be of a specific size for the previously addressed regimes. The matching onto the effective theory and the decoupling of the modes follows from refs. [107] and [108]. An essential step in proving the factorization involves the cancellation of Glauber gluons, which was shown in ref. [125] using the methods developed in refs. [185], [118] and [119]. The convolution structure of the factorization theorem arises due to momentum conservation, which yields

$$Q^2 = (\xi_a E_{\mathrm{cm}} - \ell_a^-)(\xi_b E_{\mathrm{cm}} - \ell_b^+) = \hat{s} - Q(\ell_a^- e^{-Y} + \ell_b^+ e^Y) + \mathcal{O}((1-z)^2 Q^2)$$

$$= Q^2 \left(\frac{\tau}{\xi_a \xi_b} + \frac{\ell_a^- e^{-Y}}{Q} + \frac{\ell_b^+ e^Y}{Q} + \mathcal{O}((1-z)^2) \right). \tag{5.15}$$

At hadronic threshold, Y is again power suppressed and drops out. The issue of eliminating Y at partonic threshold is addressed in sec. 5.1.4.

The new ingredient in eq. (5.13) is the hatted collinear-soft function that encodes the contribution of collinear-soft radiation to the measurement of q_T. At first sight, this hatted collinear-soft function appears identical to the ones employed in the case of the joint resummation of transverse momentum and

0-jettiness in sec. 4.2.4 and calculated in ref. [108]. They involve the other light-cone component, but the calculation is symmetric under $\ell^- \leftrightarrow \ell^+$. However, the zero-bin that accounts for the overlap with other modes differs between the two. In ref. [108], the zero-bin vanished in pure dimensional regularization, converting all IR divergences into UV divergences. Here, the zero-bin that accounts for the overlap with collinear radiation with energy $(1-z)Q$ plays a similar role, but there is also a non-trivial zero-bin from the overlap with soft radiation, which can be taken into account through[5]

$$\hat{\mathscr{S}}_i(\ell^\pm, \vec{\ell}_T, \mu, \nu) = \int \mathrm{d}^2 \vec{\ell}\,'_T \, \mathscr{S}_i(\ell^\pm, \vec{\ell}_T - \vec{\ell}\,'_T, \mu, \nu) \, S_{\bar{i}i}^{-1}(\vec{\ell}\,'_T, \mu, \nu) , \qquad (5.16)$$

where $S_{\bar{i}i}^{-1}$ is the inverse of the TMD soft function. The hatted n-collinear-soft function on the left-hand side involves the $\bar{n}$-collinear momentum component. The n-collinear-soft function (from eq. (4.36)) that appears on the right-hand side ordinarily involves the n-collinear momentum component, but is here evaluated using the $\bar{n}$-collinear momentum component instead. Here the rapidity regulator $|\ell^+ - \ell^-|^{-\eta}$ has been left unexpanded. This distinction is irrelevant for the soft function, where k^+ and k^- are of the same parametric size. By consistency of the various factorization theorems, the same must be true for all other ingredients as well. If the regulator were to be expanded as $|\ell^+ - \ell^-|^{-\eta} \to |\ell^-|^{-\eta}$, the zero-bin would be scaleless. However, the regulator then explicitly breaks the $\ell^- \leftrightarrow \ell^+$ symmetry, so that the hatted collinear-soft function is still not the same as the one from ref. [108], given in eq. (B.38). The explicit expression of the hatted collinear-soft function, obtained in this way at one loop, is given in eq. (B.40).

5.1.4 Partonic threshold

At hadronic threshold, the rapidity Y drops out of the threshold restriction in eq. (5.10) since it scales as $Y \sim \mathcal{O}(1-z)$. At partonic threshold, this is no longer true and in principle a soft function differential in k^-, k^+ and $\vec{k}_T$ is required. However, since the soft function consists of Wilson lines that are boost-invariant (invariant under the RPI-III transformation from eq. (3.117)), the dependence on $e^{\pm Y}$ can be removed by a convenient boost so that

$$S_{ij}(k^- e^Y, k^+ e^{-Y}, \vec{k}_T, \mu) = S_{ij}(k^-, k^+, \vec{k}_T, \mu) . \qquad (5.17)$$

---

[5]The relation between zero-bins and inverse soft functions can be found in refs. [186, 187]. Intuitively, this can be seen by Fourier-transforming eq. (5.16) to b_T-space, effectively turning the convolution into a multiplication, so that the soft function (representing the soft overlap, i.e. the zero-bin) is divided out of the collinear-soft function.

This implies that Y can be eliminated from eq. (5.10) at partonic threshold as well, and the soft function only depends on $\vec{k}_T$ and the combination $2k^0 = k^- + k^+$.

This argument does not immediately carry over to the case of the hatted collinear-soft functions in the intermediate regime because their rapidity regulator explicitly breaks boost invariance. Performing a similar boost for the hatted collinear-soft functions leads to

$$\hat{\mathscr{S}}_i(\ell_a^- e^Y, \vec{\ell}_a, \mu, \nu) = e^{-Y} \hat{\mathscr{S}}_i(\ell_a^-, \vec{\ell}_a, \mu, \nu e^Y),$$
$$\hat{\mathscr{S}}_j(\ell_b^+ e^{-Y}, \vec{\ell}_b, \mu, \nu) = e^{Y} \hat{\mathscr{S}}_j(\ell_b^+, \vec{\ell}_b, \mu, \nu e^{-Y}). \quad (5.18)$$

Since these hatted collinear-soft functions appear together, the $e^{\pm Y}$ in front of both functions will mutually cancel. The same factors appearing in their arguments in combination with the rapidity scale may be eliminated using their rapidity evolution as

$$\hat{\mathscr{S}}_i(\ell_a^-, \vec{\ell}_a, \mu, \nu e^Y) = \int \mathrm{d}^2\vec{\ell}'_a \, V^i_{\hat{\mathscr{S}}}(\vec{\ell}_a - \vec{\ell}'_a, \mu, \nu, \nu e^Y) \, \hat{\mathscr{S}}_i(\ell_a^-, \vec{\ell}'_a, \mu, \nu),$$
$$\hat{\mathscr{S}}_j(\ell_b^+, \vec{\ell}_b, \mu, \nu e^{-Y}) = \int \mathrm{d}^2\vec{\ell}'_b \, V^j_{\hat{\mathscr{S}}}(\vec{\ell}_b - \vec{\ell}'_b, \mu, \nu, \nu e^{-Y}) \, \hat{\mathscr{S}}_j(\ell_b^+, \vec{\ell}'_b, \mu, \nu). \quad (5.19)$$

In the final result, the evolution kernels cancel against one another as

$$\int \mathrm{d}^2\vec{\ell}_a \int \mathrm{d}^2\vec{\ell}_b \, \delta\big(q_T - |\vec{\ell}_a + \vec{\ell}_b + \vec{k}_s|\big) \quad (5.20)$$
$$\times V^i_{\hat{\mathscr{S}}}(\vec{\ell}_a - \vec{\ell}'_a, \mu, \nu, \nu e^Y) \, V^j_{\hat{\mathscr{S}}}(\vec{\ell}_b - \vec{\ell}'_b, \mu, \nu, \nu e^{-Y}) = \delta\big(q_T - |\vec{\ell}'_a + \vec{\ell}'_b + \vec{k}_s|\big),$$

for the partonic channels under consideration. These manipulations are similar to those performed in eq. (4.40) and lead to the conclusion that Y may also be dropped from eq. (5.15) at partonic threshold.

5.2 Consistency relations

The factorization of the cross section in the intermediate regime involves an additional expansion with respect to both the transverse momentum factorization and the threshold factorization. When these factorizations of the boundary regions are considered in the hierarchy of the bulk region, they should agree with the SCET$_+$ factorization. This leads to consistency relations between the perturbative ingredients of the three factorization theorems.

Since the factorized cross sections should be independent of the arbitrary scales μ and ν, the dependences of the various functions on these scales must mutually cancel. This leads to an additional consistency relation for each factorization formula, linking the anomalous dimensions of the ingredients to one another.

5.2.1 Consistency between regimes

When the factorization of the transverse momentum regime in eq. (5.4) is considered in the threshold limit $1 - z \ll 1$, it should match onto the factorization theorem for the intermediate regime in eq. (5.13). Inspecting the fixed-order content in both formulas then leads to a consistency relation given by

$$\mathcal{I}_{ij}(\omega_{a,b}, \vec{k}_T, z_{a,b}, \mu, \nu) = \delta_{ij} \, Q \hat{\mathscr{S}}_i \big((1 - z_{a,b}) Q, \vec{k}_T, \mu, \nu \big) \\ \times \big[1 + \mathcal{O}(1 - z_{a,b}) \big] \,, \tag{5.21}$$

where $\mathcal{I}_{ij}$ is the matching coefficient of the TMD beam function defined through eq. (4.20), $z_{a,b} = x_{a,b}/\xi_{a,b}$ as before and $\omega_{a,b} = x_{a,b} E_{\text{cm}}$. By comparing the expressions for the TMD matching coefficients and the hatted collinear-soft function at one loop, given in eq. (B.40), eq. (5.21) is indeed found to be satisfied.

The threshold factorization in eq. (5.8) must, in an analogous way, match onto the intermediate regime. This then implies another consistency relation, given by

$$S_{ij}(2k^0, \vec{k}_T, \mu) = \int \mathrm{d}\ell_a^- \int \mathrm{d}^2\vec{\ell}_a \, \hat{\mathscr{S}}_i(\ell_a^-, \vec{\ell}_a, \mu, \nu) \int \mathrm{d}\ell_b^+ \int \mathrm{d}^2\vec{\ell}_b \, \hat{\mathscr{S}}_j(\ell_b^+, \vec{\ell}_b, \mu, \nu) \\ \times \int \mathrm{d}^2\vec{k}_s \, S_{ij}(\vec{k}_s, \mu, \nu) \, \delta(2k^0 - \ell_a^- - \ell_b^+) \\ \times \delta\big(\vec{k}_T - |\vec{\ell}_a + \vec{\ell}_b + \vec{k}_s|\big) \left[1 + \mathcal{O}\Big(\frac{k_T^2}{(k^0)^2} \Big) \right] \,, \tag{5.22}$$

where $2k^0 = (1 - z)Q$. Since the projected fully-differential soft function on the left-hand side does not involve any rapidity divergences, all of them must cancel between the hatted collinear-soft functions and the TMD soft function on the right-hand side. At one loop, this consistency relation reduces to

$$S_{ij}^{(1)}(2k^0, \vec{k}_T, \mu) = 2\hat{\mathscr{S}}_i^{(1)}(2k^0, \vec{k}_T, \mu, \nu) + \delta(2k^0) \, S_{ij}^{(1)}(\vec{k}_T, \mu, \nu) \,, \tag{5.23}$$

up to corrections of order $k_T^2/(k^0)^2$. To check this relation explicitly, the projected fully-differential soft function from eq. (5.11) has to be expanded as

$$S_{ij}(2k^0, \vec{k}_T, \mu) = \frac{\alpha_s C_i}{\pi^2} \bigg[-\mathcal{L}_1(k_T^2, \mu^2) \, \delta(2k^0) + 2\mathcal{L}_0(2k^0, \mu) \, \mathcal{L}_0(k_T^2, \mu^2) \\ - \frac{\pi^2}{12} \delta(2k^0) \, \delta(k_T^2) \bigg] \left[1 + \mathcal{O}\Big(\frac{k_T^2}{(k^0)^2} \Big) \right] \,. \tag{5.24}$$

Using the expressions for the TMD soft function and the hatted collinear-soft function from eq. (B.29) and eq. (B.40) respectively, the consistency relation between the threshold regime and the intermediate regime is explicitly found to be satisfied at 1-loop accuracy.

5.2.2 Consistency within regimes

Since the cross section is an observable quantity, it must be independent of the scales μ and ν. This requirement can be translated into consistency relations for the anomalous dimensions of the various ingredients occurring in a factorization theorem. Since the rapidity RGE of each ingredient involves the same anomalous dimension multiplied by a numerical prefactor, only the independence of the factorizations on the scale μ provides non-trivial consistency relations. The RGEs and anomalous dimensions of all the ingredients occurring in the various regimes are gathered in app. C.

Consistency of the transverse momentum factorization in eq. (5.4) implies the relation

$$\gamma_H^i(Q^2,\mu) + \tilde{\gamma}_B^i(\omega_a,\mu,\nu) + \tilde{\gamma}_B^i(\omega_b,\mu,\nu) + \tilde{\gamma}_S^i(\mu,\nu) = 0 \,, \qquad (5.25)$$

where $\gamma_H^i(Q^2,\mu)$ is the anomalous dimension of the relevant hard function, equal to the squared absolute value of the anomalous dimension of the corresponding hard matching coefficient, given in app. C.1. This relation can be verified using the relation $Q^2 = \omega_a \omega_b$. The tildes on the anomalous dimensions corresponding to the TMD beam and TMD soft functions serve to distinguish them from those corresponding to the inclusive beam and soft functions.

For the threshold factorization in eq. (5.8), the various anomalous dimensions are required to satisfy

$$\gamma_H^i(Q^2,\mu)\,\delta(2k^0) + \frac{2}{Q}\gamma_f^i\Big(\frac{Q-2k^0}{Q},\mu\Big) + \hat{\gamma}_S^i(2k^0,\mu) = 0 \,. \qquad (5.26)$$

This implies that the anomalous dimension $\hat{\gamma}_S^i$ of the projected fully-differential soft function is equal to that of the threshold soft function in ref. [188]. A relation between the non-cusp anomalous dimension of the projected fully-differential soft function and the beam thrust soft function can also be obtained. The consistency relation for deep inelastic scattering in the threshold limit [189] is given by

$$\gamma_H^i(\alpha_s) + \gamma_J^i(\alpha_s) + \gamma_f^i(\alpha_s) = \gamma_H^i(\alpha_s) + \gamma_B^i(\alpha_s) + \gamma_f^i(\alpha_s) = 0 \,, \qquad (5.27)$$

where the fact that the non-cusp anomalous dimension of the jet function is equal to that of the virtuality-dependent beam function has been used [100]. Using this, the consistency of the threshold factorization in eq. (5.26) leads to

$$\gamma_f^i(\alpha_s) - \gamma_B^i(\alpha_s) + \hat{\gamma}_S^i(\alpha_s) = 0\,. \tag{5.28}$$

The relation in eq. (5.27) can also be used to rewrite the non-cusp anomalous dimensions in the consistency relation of the beam thrust factorization for Drell-Yan [99] as

$$\gamma_H^i(\alpha_s) + 2\gamma_B^i(\alpha_s) + \gamma_S^i(\alpha_s) = \gamma_B^i(\alpha_s) - \gamma_f^i(\alpha_s) + \gamma_S^i(\alpha_s) = 0\,. \tag{5.29}$$

Comparing these then leads to the all-order relation

$$\hat{\gamma}_S^i(\alpha_s) = -\gamma_S^i(\alpha_s)\,. \tag{5.30}$$

The consistency relation for the factorization in the intermediate regime from eq. (5.13) reads

$$\left(\gamma_H^i(Q^2,\mu) + \tilde{\gamma}_S^i(\mu,\nu)\right)\delta(1-\xi) + 2\gamma_f^i(\xi,\mu) + 2Q\,\hat{\gamma}_{\mathscr{S}}^i\!\left(\frac{(1-\xi)Q}{\nu},\mu\right) = 0\,. \tag{5.31}$$

This can be used to determine the non-cusp anomalous dimension of the hatted collinear-soft function through

$$\hat{\gamma}_{\mathscr{S}}^i(\alpha_s) = -\frac{1}{2}\left(\gamma_H^i(\alpha_s) + 2\gamma_f^i(\alpha_s) + \tilde{\gamma}_S^i(\alpha_s)\right), \tag{5.32}$$

which vanishes up to 2-loop order. Alternatively, the zero-bin in eq. (5.16) and consistency of the SCET$_+$ factorization in eq. (4.36) [108] imply that

$$\begin{aligned}\hat{\gamma}_{\mathscr{S}}^i(\alpha_s) &= -\frac{1}{2}\left(\gamma_H^i(\alpha_s) + 2\tilde{\gamma}_B^i(\alpha_s) + \gamma_S^i(\alpha_s)\right) - \tilde{\gamma}_S^i(\alpha_s) \\ &= -\frac{1}{2}\left(\tilde{\gamma}_S^i(\alpha_s) + \gamma_S^i(\alpha_s)\right), \end{aligned} \tag{5.33}$$

where the second line follows from the consistency of the SCET$_{\text{II}}$ factorization in eq. (4.17). This relation has been verified up to two loops.

5.3 Resummation

The natural scales that minimize the logarithms in each of the perturbative ingredients can be read off directly from the anomalous dimensions in app. C.1 and are given in momentum space by

$$\begin{aligned}\mu_H &\sim Q\,, & \mu_B &\sim q_T\,, & \mu_{\hat{\mathscr{S}}} &\sim q_T\,, & \mu_S &\sim q_T\,, \\ & & \nu_B &\sim \omega \sim Q\,, & \nu_{\hat{\mathscr{S}}} &\sim (1-z)Q\,, & \nu_S &\sim q_T\,. \end{aligned} \tag{5.34}$$

The simultaneous resummation of logarithms of q_T/Q and $1-z$ is achieved by evaluating each ingredient at its natural scale, where it contains no large logarithms, and evolving them to a common μ and ν scale. The orders at which the various ingredients are required in order to obtain resummed results at some desired accuracy are summarized in table 3.1. The evolution function that relates a function at some scale μ_0 to the same function at a different scale μ is obtained by solving the μ-RGE of said function. For multiplicatively renormalized functions, i.e. the hard function, the TMD beam function and the TMD soft function, the evolution function was given in eq. (3.195). For the other functions, renormalized through a convolution structure, the evolution function can be found in eq. (3.200).

The evolution functions that relate the perturbative functions at different rapidity scales ν_0 and ν can be obtained in a similar way through the ν-RGEs. It is most convenient to perform the resummation of logarithms involving q_T in impact parameter space [94, 95, 157, 164], as discussed in sec. 4.2.3. The Fourier transform will turn all the convolutions in $\vec{q}_T$ occurring in the factorization formulas and the RGEs into multiplications. For the scales in eq. (5.34), this would simply entail replacing $q_T \to b_0/b_T$.

5.3.1 Combining regimes

To obtain a cross section that describes the joint resummation of q_T and threshold throughout all three regimes described in the previous sections, the various factorization formulas have to be matched to one another. Because of the consistency relation between the transverse momentum regime and the intermediate regime, given in eq. (5.21), choosing the rapidity beam scale as

$$\nu_B \sim (1-z)Q\,,\tag{5.35}$$

smoothly interpolates between these regimes. Schematically, this can be written as

$$\frac{\mathrm{d}\sigma_{1+2}}{\mathrm{d}Q^2\,\mathrm{d}q_T} = \frac{\mathrm{d}\sigma_1}{\mathrm{d}Q^2\,\mathrm{d}q_T}\bigg|_{\nu_B\,\sim\,(1-z)Q}.\tag{5.36}$$

In ref. [190], it was noted that such a scale choice removes the large logarithms in the anomalous dimension of the TMD beam function matching coefficient. The factorization analysis performed in this chapter establishes that this indeed sums all threshold logarithms in the intermediate regime.

Matching the transverse momentum, threshold and intermediate regime can

be done in an additive way through

$$\frac{d\sigma_{1+2+3}}{dQ^2\,dq_T} = \frac{d\sigma_2}{dQ^2\,dq_T} + \left(\frac{d\sigma_1}{dQ^2\,dq_T} - \frac{d\sigma_2}{dQ^2\,dq_T}\bigg|_{\nu_{\mathscr{J}}=\nu_B}\right)$$
$$+ \left(\frac{d\sigma_3}{dQ^2\,dq_T} - \frac{d\sigma_2}{dQ^2\,dq_T}\bigg|_{\nu_{\mathscr{J}}=\nu_S}\right), \qquad (5.37)$$

in complete analogy to the matching of the various EFT regimes in the previous chapter in eq. (4.49). Here the subscripts $\nu_{\mathscr{J}}=\nu_B$ and $\nu_{\mathscr{J}}=\nu_S$ indicate that the additional threshold resummation and transverse momentum resummation are turned off respectively. The intermediate regime plays a crucial role by accounting for the overlap between both boundary regimes. To smoothly turn off the resummation when approaching either of these boundary regimes, profiles functions [103, 154] akin to those developed in sec. 4.3.3 are required. Finally, the fixed-order region can also be included in the matched cross section in complete analogy to eq. (4.49) to yield the total cross section

$$\frac{d\sigma}{dQ^2\,dq_T} = \frac{d\sigma_{1+2+3}}{dQ^2\,dq_T} + \left[\frac{d\sigma_{\rm FO}}{dQ^2\,dq_T} - \frac{d\sigma_{1+2+3}}{dQ^2\,dq_T}\right]_{\mu_{\rm FO}}. \qquad (5.38)$$

When profile scales are employed at the level of the cumulant, this additive matching ensures that the inclusive cross section with threshold resummation is recovered upon integration over q_T.

5.3.2 Conclusions

The framework developed in this chapter allows for the simultaneous resummation of threshold and transverse momentum logarithms in heavy color-singlet production processes. The setup resums all the logarithms directly in momentum space. Using SCET, three kinematic regimes characterized by distinct hierarchies were identified. The three regimes have their own degrees of freedom and each leads to a different all-order factorization theorem. These factorizations can be used to obtain resummed predictions by evaluating the various ingredients at their natural scales, minimizing their logarithms, and evolving them to a common scale.
The consistency of each factorization theorem was checked explicitly, as was the consistency between the intermediate region and the boundary regions. All the ingredients necessary for resummation at NNLL accuracy are gathered in apps. B and C, but the discussed setup is not limited to this resummation order. In fact, all ingredients for N^3LL resummation can be obtained from the literature. The required 4-loop cusp anomalous dimension was given in

ref. [191] and the 4-loop beta-function can be found in refs. [192, 193]. Results for the relevant 2-loop hard functions and their corresponding non-cusp anomalous dimensions were obtained in refs. [189, 194–199]. The 2-loop TMD beam and soft functions were calculated in refs. [200–206] and the 2-loop projected fully-differential soft function can be extracted from ref. [207]. The remaining non-cusp anomalous dimensions that are required at N^3LL (and the 2-loop hatted collinear-soft function) can be obtained from refs. [198, 208–211] or through consistency relations.

To describe the full phase space, the three factorizations have to be matched to one another and to the full fixed-order QCD result. Two of the three regimes are related through a particular scale choice and all three can be matched through an additive procedure similar to the one employed in chap. 4.

It should be noted that the same approach can be used to describe heavy particle production in the presence of a veto on jets with $q_T^{\text{jet}} > q_T^{\text{cut}}$, where instead of transverse momentum logarithms, the cross section contains logarithms of q_T^{cut}/Q. The convolutions in q_T are then replaced by multiplications where each ingredient depends on q_T^{cut}, but the framework is otherwise the same.

6

Generalized threshold factorization

Existing factorization theorems for color-singlet production processes near kinematic threshold at hadron colliders are obtained in the limit in which the momentum fractions x_a and x_b of both incoming partons approach $x_{a,b} \to 1$. In this chapter, the more general situation, in which only one of the momentum fractions is restricted, is considered. In sec. 6.1, a novel factorization formula, describing this forward threshold configuration in which $x_a \to 1$ while x_b is left unconstrained, is derived. By combining this with an analogous factorization of the opposite limit and accounting for the overlap between the two, a generalized threshold factorization is obtained. The resulting approximation of the cross section of this factorization is checked extensively against available exact results in sec. 6.2. In sec. 6.3 some first applications are described. These include the approximation of the exact partonic rapidity spectrum and a comparison to the soft threshold expansion at higher powers. This chapter proceeds largely along the lines of ref. [3].

6.1 Factorization

The production of some color-singlet final state L in combination with hadronic radiation X in proton-proton collisions is schematically given by

$$p(P_a^\mu) + p(P_b^\mu) \to L(q^\mu) + X(P_X^\mu), \tag{6.1}$$

where the definition of the momenta of the various ingredients has been made explicit. In this chapter, these types of processes are considered at hadronic center-of-mass energies $E_{\rm cm}^2 = (P_a + P_b)^2$. The final state L is characterized by its total invariant mass $Q = \sqrt{q^2}$, rapidity Y, and transverse momentum $q_T \equiv |\vec{q}_T|$. The invariant mass and rapidity are related to the momentum fractions x_a and x_b through eq. (2.39) and the cross section differential in

these momentum fractions can be parametrized as [118, 119, 185]

$$\frac{\mathrm{d}\sigma}{\mathrm{d}x_a\,\mathrm{d}x_b} = \int\frac{\mathrm{d}z_a}{z_a}\int\frac{\mathrm{d}z_b}{z_b}\,\hat{\sigma}_{ij}(z_a, z_b, \mu)\, f_i\Big(\frac{x_a}{z_a}, \mu\Big)\, f_j\Big(\frac{x_b}{z_b}, \mu\Big). \qquad (6.2)$$

Here $\hat{\sigma}_{ij}(z_a, z_b, \mu)$ denotes the partonic cross section, $f_{i,j}(x, \mu)$ are the standard PDFs, and a sum over the partonic indices i and j is left implicit.

6.1.1 Motivation

In the soft threshold limit $\tau = Q^2/E_{\mathrm{cm}}^2 \to 1$, explored in a more differential setting in sec. 5.1.2, the cross section from eq. (6.2) is known to factorize as [212–217]

$$\frac{\mathrm{d}\sigma}{\mathrm{d}x_a\,\mathrm{d}x_b} = H_{ij}(Q, \mu)\int\mathrm{d}k^-\int\mathrm{d}k^+\, S_{ij}^{\mathrm{thr}}(k^-, k^+, \mu)$$
$$\times f_i^{\mathrm{thr}}\Big[x_a\Big(1 + \frac{k^-}{Qe^Y}\Big), \mu\Big] f_j^{\mathrm{thr}}\Big[x_b\Big(1 + \frac{k^+}{Qe^{-Y}}\Big), \mu\Big], \qquad (6.3)$$

up to power corrections of $\mathcal{O}(1 - \tau)$. In this limit, the partons extracted from the protons directly initiate the hard interaction, described by the hard function $H_{ij}(Q, \mu)$. Any additional hadronic radiation is forced to be soft and is encoded in the threshold soft function $S_{ij}^{\mathrm{thr}}(k^-, k^+, \mu)$. Only the hard Born processes, e.g. $q\bar{q} \to \gamma^*$ or $gg \to H$, contribute in the limit $\tau \to 1$ and are included in the hard function. Any nondiagonal partonic channels such as $qg \to Lq$ vanish in the soft threshold limit. The threshold PDF $f_i^{\mathrm{thr}}(x, \mu)$ was already introduced in eq. (5.8) and describes the extraction of a parton i from the proton in the limit $x \to 1$.

At the partonic level, the soft threshold limit is given by $z \equiv z_a z_b \to 1$ and implies that both $z_{a,b} \to 1$. By using the fact that the threshold PDF is related to the usual PDF through

$$f_i^{\mathrm{thr}}\big(x(1 + 1 - z), \mu\big) = \frac{1}{z}f_i\Big(\frac{x}{z}, \mu\Big), \qquad (6.4)$$

at leading power in $1 - z$, the threshold factorization of the partonic cross section is found to be

$$\hat{\sigma}_{ij}(z_a, z_b, \mu) = H_{ij}(Q, \mu)\,\hat{S}_{ij}^{\mathrm{thr}}(z_a, z_b, \mu). \qquad (6.5)$$

Here, the threshold soft function at partonic threshold is defined as

$$\hat{S}_{ij}^{\mathrm{thr}}(z_a, z_b, \mu) \equiv Q^2\, S_{ij}^{\mathrm{thr}}\big(Qe^Y(1 - z_a), Qe^{-Y}(1 - z_b), \mu\big). \qquad (6.6)$$

Since $z = \tau/(\xi_a\xi_b)$, and the PDFs fall off steeply for larger values of the momentum fractions $\xi_{a,b}$, logarithms of $1-z$ can dominate the PDF integral even for typical values of $\tau \sim 10^{-4}$ at the LHC. Because of this, the soft threshold factorization has been used extensively in the literature. It allows for the all-order resummation of large logarithms of $1-z$, as studied in for example refs. [188, 195, 212–233]. The resummation at next-to-leading power (NLP) in $1-z$ has also received recent interest [234–236].

Because of the dominance of the threshold logarithms, the inclusive partonic cross section at fixed-order can be approximated by successively adding higher-power terms in $1-z$, as was done for Drell-Yan and gluon-fusion Higgs production at N^{3}LO in refs. [237–244].

6.1.2 Forward threshold factorization

Before aiming for a factorization theorem for the cross section differential in the momentum fractions x_a and x_b, it will prove convenient to first consider measuring the lightcone momenta $q^\pm$ of the produced color-singlet state directly. Working in the hadronic center-of-mass frame, these momentum components are fixed by

$$q^+ q^- = Q^2 + q_T^2 \qquad \text{and} \qquad Y = \frac{1}{2}\ln\left(\frac{q^-}{q^+}\right), \tag{6.7}$$

and corresponding momentum fractions can be defined as

$$x_\mp = \frac{q^\mp}{P_{a,b}^\mp} = \frac{\sqrt{Q^2 + q_T^2}}{E_{\text{cm}}} e^{\pm Y}, \tag{6.8}$$

where the momenta of the incoming protons $P_a^- = P_b^+ = E_{\text{cm}}$ have been plugged in. These momentum fractions manifestly obey $x_- \geq x_a$ and $x_+ \geq x_b$, so that the conditions $x_a \to 1$ and $x_b \to 1$ imply $x_- \to 1$ and $x_+ \to 1$ respectively. The generalized threshold limit that is considered here is given by

$$\lambda_{\text{QCD}}^2 \ll \lambda^2 \sim 1 - x_- \ll 1 \qquad \text{for generic } x_+, \tag{6.9}$$

where $\lambda_{\text{QCD}} \equiv \Lambda_{\text{QCD}}/Q$. In this limit, the emissions in X are found to have momenta[1]

$$p_X^\mu \sim \left(q^+, P_a^- - q^-, \vec{p}_{X\perp}\right) \sim \left(q^+, \lambda^2 q^-, \lambda\sqrt{q^+ q^-}\right), \tag{6.10}$$

which corresponds to a collinear scaling in the $\bar{n}$-direction. Physically this

---

[1]Since the total X contains the beam remnant in addition to these emissions, the notation p_X^μ is used here instead of P_X^μ.
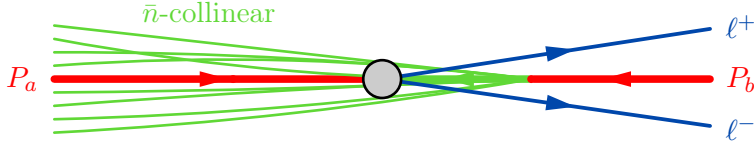
Figure 6.1 Illustration of Drell-Yan at large rapidities.

entails that, at large q^- (or, equivalently, large Y), the hadronic final state that recoils against the produced color-singlet L becomes collimated with the incoming beam, as shown in fig. 6.1. This situation implies a factorization theorem for the cross section differential in x_- and x_+, given by

$$\frac{\mathrm{d}\sigma}{\mathrm{d}x_- \, \mathrm{d}x_+} = H_{ij}(q^+q^-, \mu) \int \mathrm{d}t \, f_i^{\mathrm{thr}} \Big[x_- \Big(1 + \frac{t}{q^+q^-} \Big), \mu \Big] B_j(t, x_+, \mu), \quad (6.11)$$

which holds to leading power in $1 - x_-$. The derivation of this factorization formula will be described below. In this factorization, $B_i(t, x, \mu)$ represents the inclusive beam function [99, 100], defined in eq. (3.182), that is also present in the exclusive factorization formula for N-jettiness [99, 109]. The hard function $H_{ij}(Q, \mu)$ is the same as in eq. (6.3)

The measurement of the transverse momentum q_T can be considered in addition to that of x_- and x_+. From eq. (6.10) it follows that in general $q_T \sim p_{X\perp} \sim \lambda Q$, so that the dependence on q_T is entirely described by the $\bar{n}$-collinear modes. The factorization from eq. (6.11) then takes the slightly altered form

$$\frac{\mathrm{d}\sigma}{\mathrm{d}x_- \, \mathrm{d}x_+ \, \mathrm{d}\vec{q}_T} = H_{ij}(q^+q^-, \mu) \int \mathrm{d}t \, f_i^{\mathrm{thr}} \Big[x_- \Big(1 + \frac{t}{q^+q^-} \Big), \mu \Big] B_j(t, x_+, \vec{q}_T, \mu),$$
$$(6.12)$$

which holds up to corrections of $\mathcal{O}(\lambda^2 \sim 1 - x_-)$. This factorization involves the double-differential beam function [110, 150] that already occurred in eq. (4.4) for the joint resummation of 0-jettiness and q_T. Its matching onto the PDFs was given in eq. (4.6) and explicit expressions of the matching coefficients can be found in app. B.2.

From the scaling $\lambda_{\mathrm{QCD}} \ll \lambda$, adopted in eq. (6.9), the relation $\lambda_{\mathrm{QCD}} \sim \lambda^2$ may be considered without loss of generality. This relation can be understood by realizing that λ_{QCD} denotes the scale of the PDFs, which is in general allowed

Mode	Lab frame	Leptonic frame ($Y = 0$)
$p_{\bar{n}}$	$\left(q^+, \lambda^2 q^-, \lambda\sqrt{q^- q^+}\right)$	$Q\left(1, \lambda^2, \lambda\right)$
$P_{\bar{n}}$	$\left(q^+, \dfrac{\Lambda_{\text{QCD}}^2}{q^+}, \Lambda_{\text{QCD}}\right)$	$Q\left(1, \lambda_{\text{QCD}}^2, \lambda_{\text{QCD}}\right)$
P_n	$\left(\dfrac{\Lambda_{\text{QCD}}^2}{q^-}, q^-, \Lambda_{\text{QCD}}\right)$	$Q\left(\lambda_{\text{QCD}}^2, 1, \lambda_{\text{QCD}}\right)$
P_s	$\left(\dfrac{1}{\lambda^2}\dfrac{\Lambda_{\text{QCD}}^2}{q^-}, \lambda^2 q^-, \Lambda_{\text{QCD}}\right)$	$Q\left(\dfrac{\lambda_{\text{QCD}}^2}{\lambda^2}, \lambda^2, \lambda_{\text{QCD}}\right)$
P_{us}	$\left(\dfrac{\Lambda_{\text{QCD}}^2}{q^-}, \dfrac{\Lambda_{\text{QCD}}^2}{q^+}, \dfrac{\Lambda_{\text{QCD}}^2}{\sqrt{q^+ q^-}}\right)$	$Q\left(\lambda_{\text{QCD}}^2, \lambda_{\text{QCD}}^2, \lambda_{\text{QCD}}^2\right)$
P_G	$\left(\dfrac{\Lambda_{\text{QCD}}^2}{q^-}, \dfrac{\Lambda_{\text{QCD}}^2}{q^+}, \Lambda_{\text{QCD}}\right)$	$Q\left(\lambda_{\text{QCD}}^2, \lambda_{\text{QCD}}^2, \lambda_{\text{QCD}}\right)$

Table 6.1 Relevant modes in the limit $\lambda_{\text{QCD}} \sim \lambda^2 \sim 1 - x^- \ll 1$ in the lab (hadronic center-of-mass) frame and the leptonic frame, where $Y = 0$.

to be as large as λ^2 and does not necessarily have to be nonperturbative. If this scale does happen to be nonperturbative, then the physics below λ_{QCD} is simply described by the PDF evolution. Since λ^2 is allowed to be as small as λ_{QCD}, it may be nonperturbative as well. The only relevant issue is that $\lambda \gg \lambda_{\text{QCD}}$ is perturbative. In order to derive the factorization formula in eq. (6.12) (and by extension also the one in eq. (6.11)), the relevant degrees of freedom have to be identified. These modes are summarized in table 6.1 and will be described in more detail in what follows.

The hadronic final state X is described by $\bar{n}$-collinear modes, denoted by $p_{\bar{n}}$. Their minus component follows from momentum conservation, but their plus component is unconstrained, leading to the scaling given in eq. (6.10). As $p_{\bar{n}}^2 \sim \lambda^2 q^+ q^- \sim \lambda^2 Q^2 \gg \Lambda_{\text{QCD}}^2$, these modes describe the perturbative QCD final state X.

The partons inside the incoming protons are described by the modes P_n and $P_{\bar{n}}$. Since these modes are nonperturbative, their momenta are constrained via $P_n^2 \sim P_{\bar{n}}^2 \sim \Lambda_{\text{QCD}}^2$. Furthermore, for their momentum fractions to be of the required size to initiate the hard interaction, their components must scale as $P_n^- \sim q^-$ and $P_{\bar{n}}^+ \sim x_b E_{\text{cm}} \sim q^+$.

The interactions between the $p_{\bar{n}}$ and P_n modes are described by soft modes, which must then necessarily adhere to $p_s^- \sim p_{\bar{n}}^- \sim \lambda^2 Q$ and $p_{s\perp} \sim P_{n\perp} \sim$

Λ_{QCD}. Hence, they have a SCET$_{\text{I}}$-like relation with respect to the $p_{\bar{n}}$ modes and a SCET$_{\text{II}}$-like relation with respect to the P_n modes. The interactions with these soft modes decouple at the level of the Lagrangian via the BPS field redefinitions (see sec. 3.6.2) and are moved into soft Wilson lines. In the scenario in which $\lambda_{\text{QCD}} \sim \lambda$, the soft modes become degenerate with the $p_{\bar{n}}$ and P_n modes.

The power counting of the modes and the relations between them are easiest in the leptonic frame, in which the color-singlet final state has a total rapidity $Y = 0$. This frame is obtained by boosting $q^{\pm} \to \sqrt{q^+ q^-} \sim Q$. In this frame, the $p_{\bar{n}}$ modes are genuinely $\bar{n}$-collinear and the scaling of the soft modes is homogeneous. In the lab frame, the q^+ and q^- have to be kept track of separately, since the generalized threshold limit involves a large q^-, but a generic q^+. The resulting $p_{\bar{n}}$ modes in the lab frame do not appear to be $\bar{n}$-collinear because $q^+ \sim \lambda^2 q^-$ is in principle allowed. They are, however, collinear relative to the soft modes, which are boosted in the n-collinear direction in the lab frame and effectively become n-collinear-soft modes [107, 108].

Finally, there are additional ultrasoft modes p_{us} and Glauber modes p_G, which describe the possible interactions between P_n and $P_{\bar{n}}$. The requirement that the latter are kept on shell by these interactions means that $p_{us}^- \sim P_{\bar{n}}^-$ and $p_{us}^+ \sim P_n^+$. As the ultrasoft modes themselves are required to be on-shell modes as well, they are uniquely fixed by this. The effects of the Glauber modes and ultrasoft modes cancel, so they are not considered here any further. This follows from the collinear factorization theorem [118, 119, 185], since the measurement considered here is still inclusive over all perpendicular momenta at the scale $\lambda_{\text{QCD}} Q$.

There are no interactions between the various modes in the leading-power SCET Lagrangian, so that the cross section factorizes into separate matrix elements, each describing a single sector [99]. The $p_{\bar{n}}$ and $P_{\bar{n}}$ modes combine into the beam function and the P_n and p_s modes into the threshold PDF, as discussed in refs. [245, 246].

The arguments of the functions in the factorization follow from overall momentum conservation, which (at leading power in λ) must hold for label and residual momenta separately. The label momenta carried by the P_n and $P_{\bar{n}}$ modes are given by $\omega_n \sim \omega_{\bar{n}} \sim Q$. The residual momenta of the collinear and soft modes are $k_{\bar{n}\perp} \sim \lambda Q$ and $k_{\bar{n}} \sim k_s \sim \lambda^2 Q$. Overall momentum conservation is then enforced through the delta functions

$$\delta(\omega_{\bar{n}} - q^+) \, \delta(\omega_n - q^-) \, \delta(\vec{k}_{\bar{n}\perp} + \vec{q}_T) \, \delta(k_s^- - k_{\bar{n}}^-) \,. \tag{6.13}$$

The first three delta functions lead to the $x_{\pm}$ and $\vec{q}_T$ arguments of the thresh-

old PDF and beam function. The analogous $\delta(k_s^+ - k_{\bar{n}}^+)$ has disappeared by absorbing the $k_{\bar{n}}$-dependence into $\omega_{\bar{n}}$ [99].

By combining the P_n and p_s modes, the threshold PDF depends on $(\omega_n + k_s^-)/P_a^- = x_-(1 + k_s^-/q^-)$. In this case, the momentum $k_s^- \sim \lambda^2 Q$ of the p_s modes has to be taken into account because it is much larger than the typical residual momentum $k_n^- \sim \Lambda_{\mathrm{QCD}}^2 Q$ of the P_n modes that is absorbed into ω_n. The fourth delta function finally leads to the convolution in $t = q^+ k_{\bar{n}}^-$.

6.1.3 Kinematic endpoint factorization

The additional dependence on q_T enables a change of variables back to the original momentum fractions x_a and x_b, directly corresponding to the experimentally accessible variables Q and Y. By expanding in the small parameter $\lambda \sim \sqrt{1 - x_-} \sim q_T/Q$, the argument of the threshold PDF reads

$$x_- \left(1 + \frac{t}{q^+ q^-}\right) = x_a \left(1 + \frac{q_T^2}{2Q^2} + \frac{t}{Q^2}\right), \tag{6.14}$$

at leading power in λ. There is no Jacobian, so that the factorization from eq. (6.12) simply takes the form

$$\frac{\mathrm{d}\sigma}{\mathrm{d}x_a\, \mathrm{d}x_b\, \mathrm{d}\vec{q}_T} = H_{ij}(Q,\mu) \int \mathrm{d}t\, f_i^{\mathrm{thr}}\left[x_a\left(1 + \frac{q_T^2}{2Q^2} + \frac{t}{Q^2}\right),\mu\right] B_j(t, x_b, \vec{q}_T, \mu), \tag{6.15}$$

up to power corrections of $\mathcal{O}(1 - x_a)$. The additional q_T measurement, which was crucial in enabling the translation back to $x_{a,b}$, can now be integrated over to obtain the inclusive rapidity spectrum

$$\frac{\mathrm{d}\sigma}{\mathrm{d}x_a\, \mathrm{d}x_b} = H_{ij}(Q,\mu) \int \mathrm{d}\hat{t}\, f_i^{\mathrm{thr}}\left[x_a\left(1 + \frac{\hat{t}}{Q^2}\right),\mu\right] \hat{B}_j(\hat{t}, x_b, \mu), \tag{6.16}$$

which holds up to power corrections of $\mathcal{O}(1 - x_a)$, but is valid for generic x_b. Here the shift $t \to \hat{t} \equiv t + q_T^2/2$ has been made. The modified inclusive (virtuality-dependent) beam function is defined as

$$\hat{B}_i(\hat{t}, x, \mu) \equiv \int \mathrm{d}^2\vec{k}_T\, B_i\left(\hat{t} - \frac{k_T^2}{2}, x, \vec{k}_T, \mu\right), \tag{6.17}$$

which is a projection of the double-differential beam function that absorbs the shift $t \to \hat{t}$. It obeys the same RGE as the inclusive beam function $B_i(t, x, \mu)$, but has different constant terms. The matching of the modified inclusive beam function onto the PDFs is given by

$$\hat{B}_i(\hat{t}, x, \mu) \equiv \sum_j \int_x^1 \frac{\mathrm{d}z}{z}\, \hat{\mathcal{I}}_{ij}(\hat{t}, z, \mu)\, f_j\left(\frac{x}{z}, \mu\right) \left[1 + \mathcal{O}\left(\frac{\Lambda_{\mathrm{QCD}}^2}{\hat{t}}\right)\right], \tag{6.18}$$

and is completely analogous to eq. (3.182). Explicit expressions for the matching coefficients are gathered in app. B.2.

Because the factorization in eq. (6.16) is valid for any x_b, it must also contain the soft threshold factorization from eq. (6.3) as $x_b \to 1$. This implies that, at leading power in $1 - x_b$, the modified inclusive beam function obeys[2]

$$\hat{B}_j(\omega k^-, x_b, \mu) = \int \frac{\mathrm{d}k^+}{\omega} \, S_{ij}^{\mathrm{thr}}(k^-, k^+, \mu) \, f_j^{\mathrm{thr}}\Big[x_b\Big(1 + \frac{k^+}{\omega}\Big)\Big] . \qquad (6.19)$$

An identical relation holds for the double-differential beam function. These relations have been checked explicitly through $\mathcal{O}(\alpha_s^2)$.

By adding the result in eq. (6.16) and the analogous result in the opposite limit ($x_b \to 1$ for generic x_a) and subtracting their overlap, which is precisely given by the soft threshold limit, the generalized threshold factorization is obtained as

$$\frac{\mathrm{d}\sigma}{\mathrm{d}x_a \, \mathrm{d}x_b} = H_{ij} \left[f_i^{\mathrm{thr}} \otimes \hat{B}_j + \hat{B}_i \otimes f_j^{\mathrm{thr}} + S_{ij}^{\mathrm{thr}} \otimes f_i^{\mathrm{thr}} f_j^{\mathrm{thr}} \right], \qquad (6.20)$$

where all arguments have been omitted for clarity and $\otimes$ indicates the relevant convolution structures. The corresponding partonic generalized threshold factorization is given by

$$\hat{\sigma}(z_a, z_b) = H_{k\ell} \left[\delta_{ki} \hat{\mathcal{I}}'_{\ell j}(z_a, z_b) + \hat{\mathcal{I}}'_{ki}(z_b, z_a) \, \delta_{\ell j} - \delta_{ki} \, \delta_{\ell j} \, \hat{S}_{ij}^{\mathrm{thr}}(z_a, z_b) \right], \quad (6.21)$$

where the primed matching coefficients

$$\hat{\mathcal{I}}'_{ij}(z_a, z_b) \equiv Q^2 \, \hat{\mathcal{I}}_{ij}\big(Q^2(1 - z_a), z_b\big) , \qquad (6.22)$$

have been defined for convenience.

6.2 Validation

The exact rapidity spectra are known to NLO for Higgs production through gluon fusion [247] and to NNLO for Drell-Yan [248, 249], allowing for a direct comparison of the factorization formula in eq. (6.16) to these exact results. The validation for the NLO results is carried out analytically, while the comparison at NNLO is performed numerically. For simplicity, all scales will be set to $\mu = Q$ in this section, and the scale-dependence of various functions will be left implicit.

---

[2] The indices carried by the soft function actually indicate a color channel, not individual flavors. The absence of i on the left-hand side is therefore merely a consequence of the convention in which the soft function carries two indices.

6.2.1 Analytic validation at NLO

The partonic equivalent of the kinematic endpoint factorization from eq. (6.18) is given by

$$\hat{\sigma}_{ij}(z_a, z_b) = H_{ik}(Q, \mu) \, \hat{\mathcal{I}}'_{kj}(z_a, z_b, \mu) \,, \tag{6.23}$$

at leading power in $1 - z_a$. This result can be compared at NLO against the exact Drell-Yan partonic rapidity spectrum from refs. [248] by expanding the latter in the limit $z_a \to 1$. These results are expressed in terms of the partonic variables z and y, which are related to $z_{a,b}$ through

$$z = z_a z_b \qquad \text{and} \qquad y = \frac{z_b(1 - z_a^2)}{(1 - z_a z_b)(z_a + z_b)} \,. \tag{6.24}$$

The Jacobian between the two parametrizations is then given by

$$\frac{\mathrm{d}z \, \mathrm{d}y}{\mathrm{d}z_a \, \mathrm{d}z_b} = \frac{2[1 - y(1-z)][1 - (1-y)(1-z)]}{1 - z^2} \,, \tag{6.25}$$

and the integration limits $0 \leq z_{a,b} \leq 1$ correspond to $0 \leq z \leq 1$ and $0 \leq y \leq 1$. In order to be able to compare the NLO results for $pp \to \gamma^*$ predicted by eq. (6.23) against the exact partonic results from ref. [248], the plus distributions in z and y have to be translated to distributions in z_a and z_b at leading power.

Plus distributions are defined through their integral over integration regions that include the singularity, and the fact that they reduce to their argument in the bulk, i.e. in regions away from the singularity. The relations between the plus distributions in the bulk can be obtained by directly plugging in eq. (6.24). The boundary terms can be determined by comparing the integrals over the region given by $x_a \leq z_a(z, y) \leq 1$ and $x_b \leq z_b(z, y) \leq 1$ for generic x_a and x_b. This integration region is indicated by the gray box in the (z_a, z_b)-plane in fig. 6.2 and can be expressed in terms of z and y as

$$\begin{aligned}
&\theta\big[z_a(z,y) \geq x_a\big] \, \theta\big[z_b(z,y) \geq x_b\big] \\
&= \theta\big[x_a x_b \leq z < \min\{x_a, x_b\}\big] \, \theta\big[y_{\text{low}}(z) \leq y \leq y_{\text{high}}(z)\big] + \theta\big[\max\{x_a, x_b\} \leq z\big] \\
&\quad + \theta\big[x_b \leq z < x_a\big] \, \theta\big[y \leq y_{\text{high}}(z)\big] + \theta\big[x_a \leq z < x_b\big] \, \theta\big[y_{\text{low}}(z) \leq y\big] \,. \tag{6.26}
\end{aligned}$$

The integration bounds in y are given by

$$y_{\text{high}}(z) = \frac{z(1 - x_a^2)}{(1 - z)(x_a^2 + z)} \qquad \text{and} \qquad y_{\text{low}}(z) = \frac{x_b^2 - z^2}{(1 - z)(z + x_b^2)} \,, \tag{6.27}$$
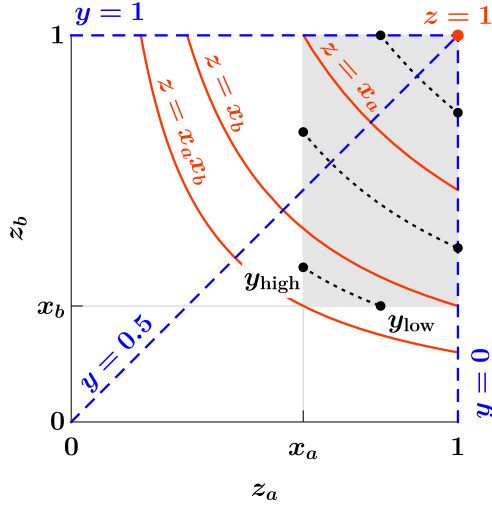
Figure 6.2 The (z_a, z_b)-plane as parametrized by (z, y). The relevant integration region $x_a \leq z_a \leq 1$ and $x_b \leq z_b \leq 1$ (for $x_a > x_b$) is indicated by the gray area. The red lines indicate the integration boundaries on z, the dotted black lines represent integration paths over y for fixed z. Lines of constant y are given as dashed blue lines.

and are indicated in fig. 6.2. Relations between the two parametrizations can be derived by integrating distributions in terms of z and y over the region given in eq. (6.26), expanding the result to leading power in $1-x_a$, and comparing to the corresponding integral over the same region in terms of z_a and z_b. The identities between distributions that are required at NLO are collected in table 6.2. The final entry in table 6.2 contains the most intricate structure. Integrating this structure over the gray shaded area in fig. 6.2 yields

$$
\int_0^1 dz \int_0^1 dy \, \theta\big[z_a(z,y) - x_a\big] \, \theta\big[z_b(z,y) - x_b\big] \, \mathcal{L}_0(z) \left(\mathcal{L}_0(y) + \mathcal{L}_0(1-y)\right)
$$
$$
= \int_{x_a x_b}^{\min\{x_a, x_b\}} dz \, \frac{g_a(z) + g_b(z)}{1 - z} + \theta[x_a - x_b] \int_{x_b}^{x_a} dz \, \frac{g_a(z)}{1 - z}
$$
$$
+ \theta[x_b - x_a] \int_{x_a}^{x_b} dz \, \frac{g_b(z)}{1 - z}, \tag{6.28}
$$

where the functions

$$
g_a(z) \equiv \ln\left(\frac{y_{\text{high}}(z)}{1 - y_{\text{high}}(z)}\right) \qquad \text{and} \qquad g_b(z) \equiv \ln\left(\frac{1 - y_{\text{low}}(z)}{y_{\text{low}}(z)}\right), \tag{6.29}
$$

have been introduced for convenience. By defining the functions $G_a(z)$ and

$\mathrm{d}z\,\mathrm{d}y\,\times\,\mathrm{LHS}$	$=\mathrm{d}z_a\mathrm{d}z_b\,\times\,\mathrm{RHS}$
$f(z)\,\delta(y)$	$f(z_b)\,\delta(1-z_a)$
$r(z)\,\mathcal{L}_0(y)$	$r(z_b)\left[\ln\!\left(\frac{2z_b}{1-z_b^2}\right)\delta(1-z_a)+\mathcal{L}_0(1-z_a)\right]+\mathcal{O}(1)$
$f(z)\,\delta(1-y)$	$f(z_a)\,\delta(1-z_b)$
$r(z)\,\mathcal{L}_0(1-y)$	$\mathcal{O}(1)$
$r(z)\,\mathcal{O}(y^0(1-y)^0)$	$\mathcal{O}(1)$
$\mathcal{L}_0(1-z)$	$\frac{\pi^2}{6}\delta(1-z_a)\,\delta(1-z_b)-\mathcal{L}_1(1-z_a)\,\delta(1-z_b)$
$\times[\mathcal{L}_0(y)+\mathcal{L}_0(1-y)]$	$+\mathcal{L}_0(1-z_a)\,\mathcal{L}_0(1-z_b)-\delta(1-z_a)\,\mathcal{L}_1(1-z_b)$
	$+\delta(1-z_a)\,\frac{1}{1-z_b}\ln\!\left(\frac{2z_b}{1+z_b}\right)+\mathcal{O}(1)$

Table 6.2 Translation identities of distributional structure between the (z,y) and (z_a, z_b) parametrizations. Here $f(z)$ is an arbitrary (potentially distribution-valued) function and $r(z) = \mathcal{O}((1-z)^0)$ has at most an integrable singularity as $z \to 1$. When indicated, the relations receive power corrections in $1 - z_a$ starting at $\mathcal{O}(1) \equiv \mathcal{O}((1-z_a)^0)$.

$G_b(z)$ such that

$$\frac{\mathrm{d}G_a(z)}{\mathrm{d}z} = \frac{g_a(z)}{1-z} \qquad \text{and} \qquad \frac{\mathrm{d}G_b(z)}{\mathrm{d}z} = \frac{g_b(z)}{1-z}, \tag{6.30}$$

the integral in eq. (6.28) is found to be equal to

$$\int_0^1 \mathrm{d}z \int_0^1 \mathrm{d}y\, \theta\big[z_a(z,y)-x_a\big]\,\theta\big[z_b(z,y)-x_b\big]\,\mathcal{L}_0(z)\,(\mathcal{L}_0(y)+\mathcal{L}_0(1-y))$$
$$= G_a(x_a) + G_b(x_b) - G_a(x_a x_b) - G_b(x_a x_b). \tag{6.31}$$

A possible primitive for $G_{a,b}(z)$ is given by

$$G_{a,b}(z) = -\ln(1-z)\ln(-z+i0) - \mathrm{Li}_2\!\left(\frac{1-z}{1+x_{a,b}}\right)$$

$$- \mathrm{Li}_2\!\left(\frac{1-z}{1-x_{a,b}} - i0\right) - \mathrm{Li}_2(z), \tag{6.32}$$

where the imaginary parts cancel between the different terms. Comparing the integral given in eq. (6.31) against the exact distribution in the bulk then gives

rise to the explicit distributional identity

$$\frac{\mathrm{d}z\,\mathrm{d}y}{\mathrm{d}z_a\,\mathrm{d}z_b}\mathcal{L}_0(z)\left(\mathcal{L}_0(y)+\mathcal{L}_0(1-y)\right)$$
$$=\left[\frac{\pi^2}{6}\delta(1-z_a)\,\delta(1-z_b)-\mathcal{L}_1(1-z_a)\,\delta(1-z_b)+\mathcal{L}_0(1-z_a)\,\mathcal{L}_0(1-z_b)\right.$$
$$-\,\delta(1-z_a)\,\mathcal{L}_1(1-z_b)+\delta(1-z_a)\frac{1}{1-z_b}\ln\left(\frac{2z_b}{1+z_b}\right)$$
$$\left.+\,\delta(1-z_b)\frac{1}{1-z_a}\ln\left(\frac{2z_a}{1+z_a}\right)+\frac{1}{(1+z_a)(1+z_b)}\right]. \tag{6.33}$$

The result given in the last line of table 6.2 is then obtained by expanding the right-hand side to leading power in $1-z_a$. The result in eq. (6.33) relates plus distributions of some function $y(z_a,z_b)$ to simpler plus distributions of $1-z_a$ and $1-z_b$, plus regular terms. Additional boundary terms are then generated by moving the regular terms out of the plus distributions. In this sense, it is the two-dimensional analog of typical distributional identities such as

$$\left[\frac{1+z^2}{1-z}\right]_+=2\mathcal{L}_0(1-z)+\frac{3}{2}\delta(1-z)-(1+z). \tag{6.34}$$

After expanding the exact partonic cross sections from ref. [248] to leading power in $1-z_a$ using the results in table 6.2, they can be compared against the NLO predictions from the partonic factorization formula in eq. (6.23). The hard function for producing a virtual photon can be found up to one loop in app. B.1. Since the hadronic cross section is differential in $\mathrm{d}x_a\,\mathrm{d}x_b$ instead of $\mathrm{d}Q\,\mathrm{d}Y$, this hard function should be multiplied by the Jacobian $E_{\mathrm{cm}}^2/(2Q)$, effectively changing

$$\frac{\mathrm{d}\sigma_B^q}{\mathrm{d}Q}\longrightarrow\sigma_B^{\gamma,q}\,Q_q^2\equiv\frac{4\pi\alpha_{\mathrm{em}}^2}{3N_cQ^2}\,Q_q^2. \tag{6.35}$$

Here the Drell-Yan process has been restricted to $q\bar{q}\to\gamma^*\to\ell^+\ell^-$ and the quark charge Q_q has been factored out explicitly. Because the RGE of the double-differential beam function in eq. (C.9) does not involve $\vec{k}_T$, the modified inclusive beam function must satisfy the same RGE. From consistency with the DGLAP equation in eq. (C.10), the RGE for the modified matching coefficient is then found to be

$$\mu\frac{\mathrm{d}}{\mathrm{d}\mu}\hat{\mathcal{I}}_{ij}(\hat{t},z,\mu)=\sum_k\int\mathrm{d}\hat{t}'\int\frac{\mathrm{d}z'}{z'}\,\hat{\mathcal{I}}_{ik}(\hat{t}-\hat{t}',\frac{z}{z'},\mu)$$
$$\times\left[\delta_{kj}\,\delta(1-z')\,\gamma_B^i(\hat{t}',\mu)-2\,\delta(\hat{t}')P_{kj}(\alpha_s,z')\right]. \tag{6.36}$$

Solving this equation order-by-order in perturbation theory then yields the matching coefficients of the modified inclusive beam function up to the coefficients of the $\delta(t)$, which are not predicted by the RGE and have to be calculated explicitly from eq. (6.17). Apart from these boundary terms, the matching coefficients of the modified inclusive beam function have the same structure as the matching coefficients of the inclusive beam function. Results for the modified matching coefficients can be found in app. B.2.

Defining the perturbative expansion of the partonic cross section as

$$\hat{\sigma}_{ij}(z_a, z_b) = \sum_{n=0}^{\infty} \left(\frac{\alpha_s}{4\pi}\right)^n \hat{\sigma}_{ij}^{(n)}(z_a, z_b),$$

(6.37)

and plugging the results for the hard function (adjusted by eq. (6.35)) and the modified inclusive beam function into eq. (6.23) up to $\mathcal{O}(\alpha_s)$ yields the results

$$\hat{\sigma}_{ij}^{(0)}(z_a, z_b) = \sigma_B^{\gamma,q} Q_q^2 \left(\delta_{iq}\delta_{\bar{q}j} + \delta_{i\bar{q}}\delta_{qj}\right) \delta(1 - z_a)\delta(1 - z_b),$$

$$\hat{\sigma}_{q\bar{q}}^{(1)}(z_a, z_b) = \sigma_B^{\gamma,q} Q_q^2 \left[\Gamma_0^q \mathcal{L}_1(1 - z_a)\,\delta(1 - z_b)\right.$$

$$+ \mathcal{L}_0(1 - z_a)\left(-\frac{\gamma_{B,0}^q}{2}\,\delta(1 - z_b) + P_{qq}^{(0)}(z_b)\right)$$

$$\left. + \delta(1 - z_a)\left(\delta(1 - z_b)\left(\frac{\pi^2}{2}\Gamma_0^q + 2C_{q\bar{q},1}^V\right) + \hat{I}_{qq}^{(1)}(z_b)\right)\right],$$

$$\hat{\sigma}_{qg}^{(1)}(z_a, z_b) = \sigma_B^{\gamma,q} Q_q^2 \left[\mathcal{L}_0(1 - z_a)P_{qg}^{(0)}(z_b) + \delta(1 - z_a)\,\hat{I}_{qg}^{(1)}(z_b)\right].$$

(6.38)

The results for $q \leftrightarrow \bar{q}$ are identical and the gq and $g\bar{q}$ channels are power-suppressed. The partonic cross section determined here is related to the parametrization used in ref. [248] via

$$\hat{\sigma}_{ij}(z_a, z_b) = \frac{\mathrm{d}z\,\mathrm{d}y}{\mathrm{d}z_a\,\mathrm{d}z_b}\frac{\sigma_B^{\gamma,q}}{2z}\,\hat{\sigma}_{ij}^{\text{ref. [248]}}(z, y).$$

(6.39)

When this difference is taken into account, and the results from ref. [248] are expanded to leading power in $1 - z_a$, exact agreement with the partonic cross sections in eq. (6.38) is found.

The rapidity distributions for gluon-fusion Higgs production $pp \to H$ at NLO were obtained in ref. [247]. In this case, the difference in parametrizations is found to be

$$\hat{\sigma}_{ij}(z_a, z_b) = \frac{\mathrm{d}z\,\mathrm{d}y}{\mathrm{d}z_a\,\mathrm{d}z_b}\frac{\sigma_B^{ggH}}{z}\left[\frac{\mathrm{d}\hat{\sigma}_{ij}}{\mathrm{d}y}\right]^{\text{ref. [247]}}.$$

(6.40)
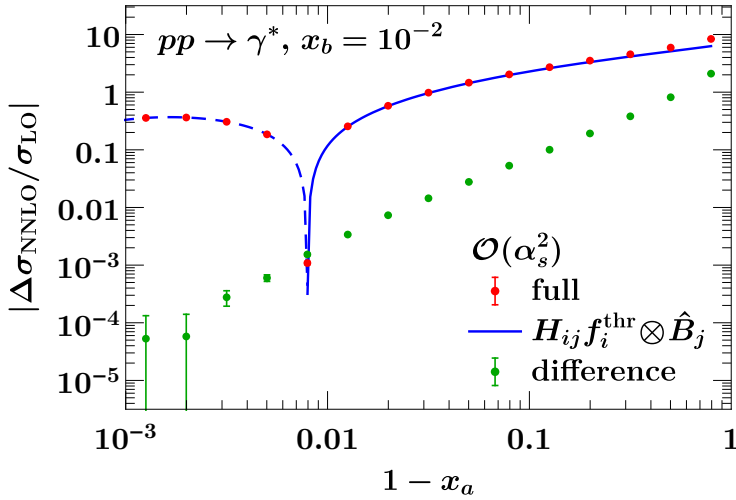
Figure 6.3 Comparison of the $\mathcal{O}(\alpha_s^2)$ contribution to $pp \to \gamma^*$ predicted by the endpoint factorization in eq. (6.16) (blue) against the full result from `Vrap` (red). Dashing in the blue line indicates negative results. The difference is shown in green and the error bars indicate integration uncertainties.

The distributions with arguments $y(1 - y)$ that appear in ref. [247] can be translated through

$$\delta\big(y(1 - y)\big) = \delta(y) + \delta(1 - y)\,,$$
$$\mathcal{L}_0\big(y(1 - y)\big) = \mathcal{L}_0(y) + \mathcal{L}_0(1 - y)\,, \tag{6.41}$$

which follow from comparing full integrals and applying partional fractioning. The results from ref. [247] may then be expanded to leading power through the identities in table 6.2. Comparing these against the results obtained from eq. (6.23) by plugging in the relevant perturbative ingredients given in app. B to $\mathcal{O}(\alpha_s)$, exact agreement between the two is found for all channels.

6.2.2 Numerical validation for Drell-Yan at NNLO

To numerically validate the factorization formula for the inclusive rapidity spectrum from eq. (6.16) for Drell-Yan at NNLO, the hard function and matching coefficients of the modified inclusive beam function are implemented up to 2-loop accuracy in `SCETlib` [174]. The results are compared against `Vrap` [249], considering $pp \to \gamma^*$, keeping $\alpha_s = 0.118$ fixed, and using flat PDFs $f_i^{\mathrm{thr}}(x) = f_i(x) = \theta(1-x)$ for simplicity. This effectively amounts to taking cumulant integrals of the partonic cross section, meaning that plus distributions $\mathcal{L}_n(1-z_a)$ contribute $\ln^n(1 - x_a)$, delta functions $\delta(1 - z_a)$ integrate to unity and power

corrections of $\mathcal{O}((1 - z_a)^0)$ turn into $\mathcal{O}(1 - x_a)$. In fig. 6.3, the numerical comparison of the $\mathcal{O}(\alpha_s^2)$ contribution for Drell-Yan is shown as a function of $1 - x_a$, while $x_b = 10^{-2}$ is kept fixed. Excellent agreement between the endpoint factorization (blue) from eq. (6.16) and the full cross section (red) from ref. [249] is found in the singular limit $x_a \to 1$, with the difference (green) vanishing like a power. Although fig. 6.3 involves only a single representative value of x_b, other values have been checked as well and show a similar agreement. Furthermore, the agreement in the singular limit is also found to hold for $pp \to Z/\gamma^*$ on the resonance.

Analogous numerical comparisons have been performed for each individual channel as well. Here the $ij = q\bar{q}$ channel includes all topologies in which i and j are part of the same quark line. The leading-power limit then corresponds directly to the qqV matching coefficient of the modified inclusive beam function in eq. (B.27). This channel also includes contributions from topologies $q\bar{q} \to g \to q\bar{q}V$. The qq' channel includes all remaining quark-initiated processes, which (at leading power) corresponds to the combination of the qqS and $q\bar{q}V$ matching coefficients in eq. (B.27). The results are shown in fig. 6.4. Each partonic channel shows excellent agreement between the prediction from eq. (6.16) and the singular limit of the full result from ref. [249]. The systematic deviation in the $q\bar{q}$ channel around $1 - x_a \sim 10^{-4}$ is also found at NLO, for which exact agreement was found analytically in sec. 6.2.1. These deviations can thus be attributed to a systematic effect in the PDF integrations in `Vrap`.

6.3 Applications

A way to determine the quality of the generalized threshold approximation is to compare its deviation from the exact cross section against the deviation that the traditional soft threshold approximation exhibits. This study is performed in sec. 6.3.1, where the generalized threshold approximation is found to agree better with the exact cross section for Drell-Yan than the soft threshold approximation at both NLO and NNLO. The main reason for this is the fact that the partonic cross section involved in the former contains terms of higher powers in $1 - z_a$ and $1 - z_b$ than the partonic cross section involved in the latter. Furthermore, higher powers in the generalized expansion are found to approach the full result faster than higher powers in the soft expansion.
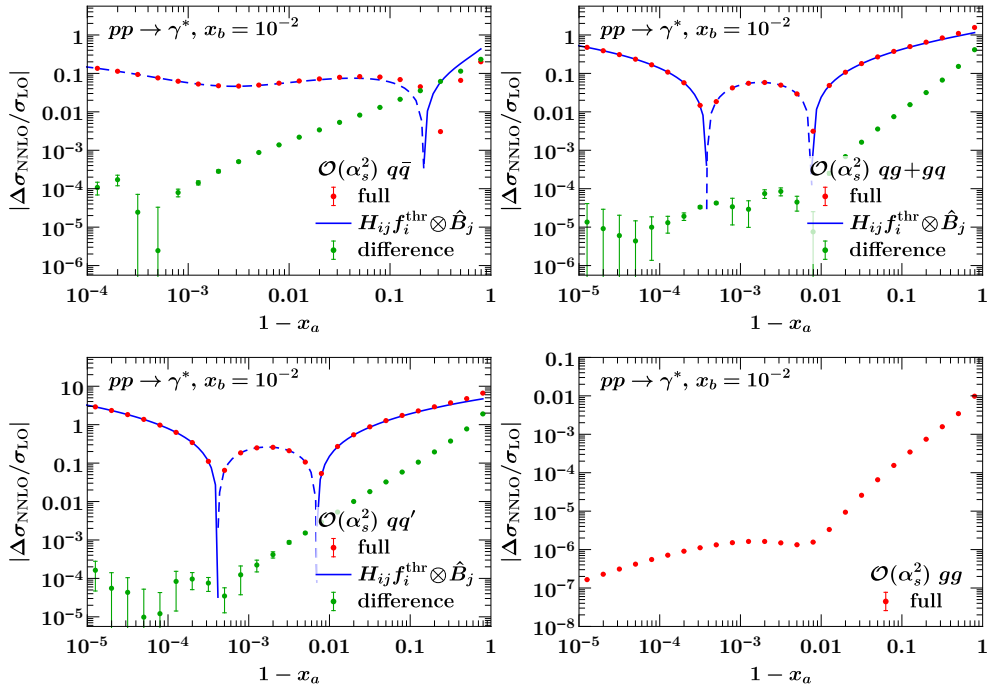
Figure 6.4 Breakdown of fig. 6.3 into partonic channels. The $\mathcal{O}(\alpha_s^2)$ contributions predicted by eq. (6.16) (red) and the full result from Vrap (blue) in the limit $x_a \to 1$ are shown. Their difference is shown in green and the dashes in the blue line indicate a negative result. The gg channel is power suppressed, so its full result by itself vanishes like a power.

6.3.1 Generalized threshold approximation

The performance of the generalized threshold factorization in eq. (6.20) can be determined by investigating how well it approaches the full fixed-order result in comparison to the soft threshold factorization from eq. (6.3). The full NNLO rapidity spectrum is computed using Vrap[3] [249], while eq. (6.20) is implemented using SCETlib [174]. The MMHT2014nnlo68cl [40] NNLO PDFs with $\alpha_s(m_Z) = 0.118$ are used and $n_f = 5$ active flavors are considered. The results for the $\mathcal{O}(\alpha_s)$ and $\mathcal{O}(\alpha_s^2)$ contributions to the Drell-Yan rapidity spectrum are shown in the first and second row in fig. 6.5 respectively. These results have been separated into quark channels ($q\bar{q} + qq'$) and channels involving at least one gluon ($qg + gq + gg$). The $\mathcal{O}(\alpha_s)$ results for Higgs production are shown

---

[3]The current public version Vrap 0.9 assumes $f_q(x) = f_{\bar{q}}(x)$ for $q = s, c, b$, which is in conflict with most recent PDF determinations. For the numerical results presented in this section, it has been manually modified to allow for possible sea quark asymmetries.

Figure 6.5 The $\mathcal{O}(\alpha_s)$ (top row) and $\mathcal{O}(\alpha_s^2)$ (middle row) contributions to the Drell-Yan cross section and the $\mathcal{O}(\alpha_s)$ (bottom row) contributions to the Higgs cross section. Shown are the full result (solid red), the generalized threshold approximation (dashed blue) and the soft threshold approximation (dotted gray). The results in the left and right columns are obtained at $\mu = Q$ and $\mu = Q/2$ respectively. All of the results are normalized to the tree-level cross section σ_{LO}.

on the third row in fig. 6.5. For Drell-Yan, the generalized threshold limit
(blue) is found to approximate the full result (red) well for all channels and
all Y. It performs significantly better than the soft threshold approximation
(gray), which provides a much less accurate approximation in the $q\bar{q}$ channel
and none for the other channels. For $gg \to H$, the generalized threshold ex-
pansion also performs superior to the soft one, although it is still $\mathcal{O}(20\%)$ off.
This is consistent with the expectation that for gluon-induced processes, hard
central radiation plays a larger role than for Drell-Yan.

6.3.2 Exact partonic cross sections at NLO

Since the generalized threshold factorization in eq. (6.21) contains the full
singularity structure in both $1 - z_a$ and $1 - z_b$, it is possible to determine the
exact partonic cross sections in terms of z_a and z_b. The power corrections to
eq. (6.21) can be obtained by evaluating

$$\text{p.c.} = \hat{\sigma}(z_a, z_b) - \left[H_{ik}\, \hat{\mathcal{I}}'_{kj}(z_a, z_b) + H_{kj}\, \hat{\mathcal{I}}'_{ki}(z_b, z_a) - H_{ij}\, \hat{S}^{\text{thr}}_{ij}(z_a, z_b) \right]_{\text{bulk}}, \tag{6.42}$$

where the terms in square brackets are to be evaluated in the bulk $z_{a,b} < 1$,
where delta functions vanish and plus distributions reduce to their arguments.
The first two terms in square brackets, representing expansions in $1 - z_a$ and
$1 - z_b$ respectively, are obtained by plugging in the relevant perturbative in-
gredients from app. B. The final term may be obtained from either of these
by performing an additional expansion in the opposite limit. The results from
refs. [248] and [247], written in terms of $z_{a,b}$, are used for the full cross section
$\hat{\sigma}(z_a, z_b)$. Adding the power corrections determined in this way to the general-
ized threshold factorization in eq. (6.21) then leads to the exact cross sections
in terms of z_a and z_b.

Using the perturbative expansion in eq. (6.37) and defining $\bar{z}_a \equiv 1 - z_a$ and $\bar{z}_b \equiv 1 - z_b$, the NLO coefficient for the $q\bar{q}$ channel in $pp \to \gamma^*$ is found to be

$$
\frac{\hat{\sigma}_{q\bar{q}}^{(1)}(z_a, z_b, Q, \mu)}{\sigma_B^{\gamma, q} Q_q^2 C_F} = \delta(\bar{z}_a)\delta(\bar{z}_b)(2\pi^2 - 16) + 4\mathcal{L}_1(\bar{z}_a)\delta(\bar{z}_b) + 4\mathcal{L}_0(\bar{z}_a)\mathcal{L}_0(\bar{z}_b)
$$

$$
+ 4\delta(\bar{z}_a)\mathcal{L}_1(\bar{z}_b) + \left\{ -2(1+z_b)\mathcal{L}_0(\bar{z}_a) \right.
$$

$$
+ \delta(\bar{z}_a)\left[2\bar{z}_b - 4(1+z_b)\ln\bar{z}_b - \frac{2(1+z_b^2)\ln z_b}{\bar{z}_b} + \frac{4}{\bar{z}_b}\ln\left(\frac{2z_b}{1+z_b}\right) \right.
$$

$$
\left. + 2(1+z_b)\ln\left(\frac{1-z_b^2}{2z_b}\right) \right] - 4\ln\left(\frac{\mu}{Q}\right)\delta(\bar{z}_a)\left[2\mathcal{L}_0(\bar{z}_b) + \frac{3}{2}\delta(\bar{z}_b) - (1+z_b) \right]
$$

$$
\left. + \frac{2(z_a^2 + z_b^2)[(1+z_a)^2 + z_a z_b(3 + 2z_a + z_a z_b)]}{(1+z_a)(1+z_b)(z_a + z_b)^2} + (z_a \leftrightarrow z_b) \right\}, \qquad (6.43)
$$

where $(a \leftrightarrow b)$ indicates that the expression in curly brackets is to be repeated with collinear directions a and b interchanged. The qg channel for Drell-Yan is given by

$$
\frac{\hat{\sigma}_{qg}^{(1)}(z_a, z_b, Q, \mu)}{\sigma_B^{\gamma, q} Q_q^2 T_F} = 2(z_b^2 + \bar{z}_b^2)\mathcal{L}_0(\bar{z}_a) + \delta(\bar{z}_a)\left[2(z_b^2 + \bar{z}_b^2)\ln\left(\frac{2\bar{z}_b}{1+z_b}\right) + 4z_b\bar{z}_b \right]
$$

$$
- 4\ln\left(\frac{\mu}{Q}\right)\delta(\bar{z}_a)(z_b^2 + \bar{z}_b^2) + \frac{1}{(1+z_a)(z_a + z_b)^3}\left[-4z_a^5 z_b^3 \right.
$$

$$
- 4z_a^4 z_b^2(-1 + z_b + 2z_b^2) + 2z_a^3(1 + 4z_b^2 + 2z_b^3 - 4z_b^4 - 4z_b^5)
$$

$$
+ 2z_a^2 z_b(1 + 4z_b + 8z_b^2 - 8z_b^3 - 4z_b^4) + 2z_a z_b^2(1 + 4z_b - 2z_b^2 - 4z_b^3)
$$

$$
\left. - 2z_b^3(1 - 2z_b + 2z_b^2) \right]. \qquad (6.44)
$$

The gq channel simply follows from $\hat{\sigma}_{gq}^{(1)}(z_a, z_b, Q, \mu) = \hat{\sigma}_{qg}^{(1)}(z_a, z_b, Q, \mu)$ and results for $q \leftrightarrow \bar{q}$ are identical.

The partonic cross section for gluon-fusion Higgs production can be parametrized as

$$
\hat{\sigma}_{ij}(z_a, z_b, m_t, m_H, \mu) = \sigma_B^{ggH} \alpha_s^2 |C_t(m_t, \mu)|^2 \sum_{n=0}^{\infty} \left(\frac{\alpha_s}{4\pi}\right)^n \hat{\eta}_{ij}^{(n)}(z_a, z_b, m_H, \mu),
$$

$$
(6.45)
$$

where the Born cross section σ_B^{ggH} and the Wilson coefficients $C_t(m_t, \mu)$ and $C_{gg}(m_H, \mu)$, resulting from integrating out the top-quark and matching onto SCET respectively, are given in app. B.1.

The NLO coefficient of the gg channel in terms of z_a and z_b is then found to be

$$
\frac{\hat{\eta}_{gg}^{(1)}(z_a, z_b, m_H, \mu)}{C_A} = 2\pi^2 \delta(\bar{z}_a)\delta(\bar{z}_b) + 4\mathcal{L}_1(\bar{z}_a)\delta(\bar{z}_b) + 4\delta(\bar{z}_a)\mathcal{L}_1(\bar{z}_b)
$$

$$
+ 4\mathcal{L}_0(\bar{z}_a)\mathcal{L}_0(\bar{z}_b) + \left\{ 4\mathcal{L}_0(\bar{z}_a)\left[\frac{1}{z_b} - 2 + z_b - z_b^2 \right] + 4\delta(\bar{z}_a)\frac{1}{\bar{z}_b}\left[\frac{\ln(2\bar{z}_b)}{z_b} \right.\right.
$$

$$
- 3\ln \bar{z}_b + 2\ln\left(\frac{1+z_b}{2} \right) - \frac{\ln(1+z_b)}{z_b} - z_b(3 - 2z_b + z_b^2)\ln\left(\frac{1+z_b}{2\bar{z}_b} \right) \Bigg]
$$

$$
- 4\ln\left(\frac{\mu}{m_H} \right)\delta(\bar{z}_a)\left[2\mathcal{L}_0(\bar{z}_b)\frac{(1-z_b+z_b^2)^2}{z_b} \right]
$$

$$
+ \frac{4z_b}{z_a(1+z_a)(1+z_b)(z_a+z_b)^4}\Big[2z_b^2 + z_b^3 + 3z_a^6 z_b^4 + 2z_a^5 z_b^3(5 + 5z_b + 2z_b^2)
$$

$$
+ z_a^4 z_b^2(16 + 17z_b + 12z_b^2 + 6z_b^3 + 2z_b^4)
$$

$$
+ z_a^3 z_b(5 + 22z_b + 12z_b^2 + 8z_b^3 + 8z_b^4 + 2z_b^5)
$$

$$
+ z_a^2(3 + 2z_b^2 + 7z_b^3 + 2z_b^4 + 4z_b^5 + 2z_b^6)
$$

$$
+ z_a z_b(4 + z_b + z_b^2 + z_b^3 + z_b^5) \Big] + (z_a \leftrightarrow z_b) \Bigg\}. \tag{6.46}
$$

The qg and gq channels are related by $\hat{\eta}_{qg}^{(1)}(z_a, z_b, m_H, \mu) = \hat{\eta}_{gq}^{(1)}(z_b, z_a, m_H, \mu)$ and the latter is given by

$$
\frac{\hat{\eta}_{gq}^{(1)}(z_a, z_b, m_H, \mu)}{C_F} = 2\mathcal{L}_0(\bar{z}_a)\frac{2 - 2z_b + z_b^2}{z_b}
$$

$$
+ 2\delta(\bar{z}_a)\left[z_b + \frac{2 - 2z_b + z_b^2}{z_b}\left(\ln\left(\frac{2\bar{z}_b}{1+z_b} \right) - 2\ln\left(\frac{\mu}{m_H} \right) \right) \right]
$$

$$
+ \frac{2}{(1+z_a)z_b(z_a+z_b)^3}\Big[z_a^3(2 - 2z_b + z_b^2) + z_a^2(4 - 2z_b - 4z_b^2 + 7z_b^3 - 2z_b^5)
$$

$$
+ z_a z_b(4 - 4z_b + 4z_b^2 + z_b^3 - 2z_b^4) - z_b^2(-2 + 2z_b - 2z_b^2 + z_b^3) \Big]. \tag{6.47}
$$

The $q\bar{q}$ channel is fully regular and reads

$$
\frac{\hat{\eta}_{q\bar{q}}^{(1)}(z_a, z_b, m_H, \mu)}{C_F} = \frac{N_c^2 - 1}{N_c}\frac{4(1 + z_a z_b)(z_a^4 z_b^2 + z_a^2 z_b^4 - 4z_a^2 z_b^2 + z_a^2 + z_b^2)}{(z_a + z_b)^4}, \tag{6.48}
$$

where N_c denotes the number of colors.

The NLO Drell-Yan cross sections agree with the results in refs. [214, 250, 251] and the NLO Higgs production cross sections are in full agreement with
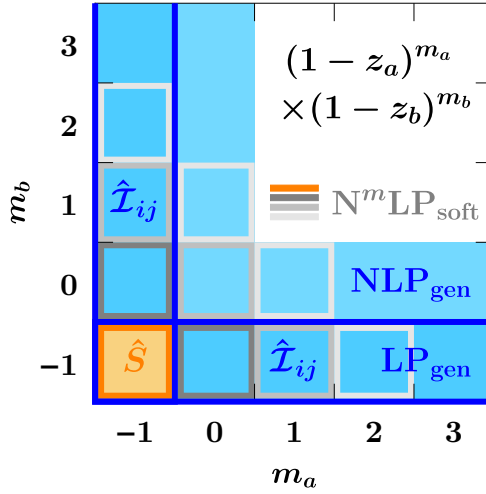
Figure 6.6 Schematic comparison between the first few $N^m LP_{\text{soft}}$ and $N^m LP_{\text{gen}}$ of the inclusive cross section. The columns and rows denote the powers m_a and m_b of $1 - z_a$ and $1 - z_b$ that are included at various orders in the expansion. The lower left box represents the LP_{soft}, while the first row and column make up the LP_{gen}.

ref. [248]. The exact cross sections obtained in this section have also been compared numerically against the rapidity spectra obtained from `Vrap 0.9` [249] for Drell-Yan and from `Sushi 1.7.0` [252, 253] for Higgs production, finding excellent agreement. As the (z, y)-parametrization is used in `Vrap 0.9`, this effectively confirms the distributional identities given in table 6.2.

6.3.3 Subleading powers

The total partonic cross section may be expressed as a series in the powers of both $1 - z_a$ and $1 - z_b$, schematically

$$\hat{\sigma}_{ij}(z_a, z_b) = \sum_{m_a, m_b} \hat{\sigma}_{ij}^{(m_a, m_b)}(z_a, z_b), \tag{6.49}$$

where each coefficient function scales as $\hat{\sigma}_{ij}^{(m_a, m_b)}(z_a, z_b) \sim (1 - z_a)^{m_a}(1 - z_b)^{m_b}$. The leading-power soft approximation eq. (6.3) corresponds to all terms with $m_a = m_b = -1$. Higher powers in this expansion, denoted by $N^m LP_{\text{soft}}$, are obtained by considering all terms with $m_a + m_b + 2 \leq m$. The leading power of the generalized threshold approximation eq. (6.21) captures all terms with $\min\{m_a, m_b\} = -1$. Higher powers in this expansion, denoted by $N^m LP_{\text{gen}}$, correspond to terms with $\min\{m_a, m_b\} = m - 1$. The relation between the soft
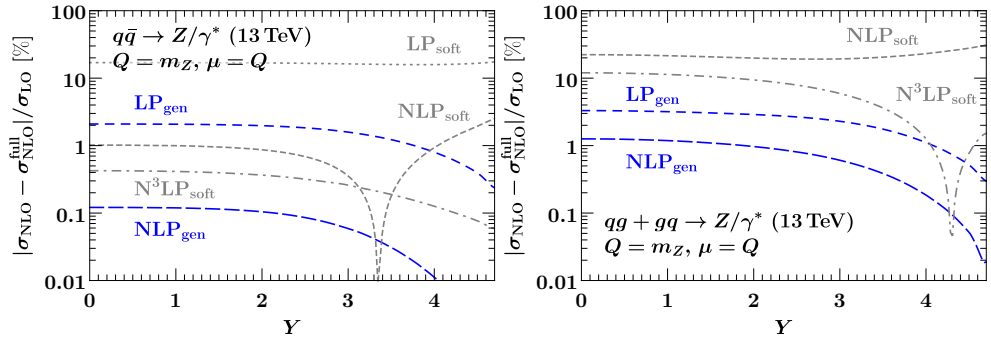
Figure 6.7 Deviations of the generalized (dashed blue) and soft (gray) threshold expansions from the full NLO result for Drell-Yan. The left-hand plot shows the result for the $q\bar{q}$ channel and the right-hand plot corresponds to the $qg + gq$ channel. The deviations are given as a percentage of the LO result.

and generalized threshold power expansions is illustrated in fig. 6.6. The deviations of the various powers of the soft (gray) and generalized (blue) threshold expansions from the full result are shown in fig. 6.7 for the various channels in Drell-Yan. For the $q\bar{q}$ channel, an order-of-magnitude improvement when going from LP_{gen} to NLP_{gen} is found, which should be contrasted with the relatively small improvement between NLP_{soft} and $\text{N}^3\text{LP}_{\text{soft}}$. For the $qg + gq$ channel, where the LP_{soft} vanishes, the LP_{gen} already performs better than even the $\text{N}^3\text{LP}_{\text{soft}}$ result for most values of Y. Results at different scales are found to exhibit a similar behavior.

The fact that the generalized threshold approximation performs better than the soft one was to be expected. The reason for this is that the performed expansion of the partonic cross section in both z_a and z_b is valid near all edges of the partonic phase space, i.e. for $z_a \to 1$ and arbitrary z_b and vice versa, whereas the soft threshold expansion is valid only near a single point on the edge, where both $z_a \to 1$ and $z_b \to 1$. It can in fact be seen from fig. 6.6 that each order in the generalized threshold expansion fully contains two orders of the soft expansion. The LP_{gen} result, for example, contains the entire NLP_{soft} constribution. However, since the RGE of the beam function does not predict its dependence on x, this cannot be used to perform a resummation at NLP_{soft}.

6.3.4 Conclusions

In this chapter, a novel factorization formula that describes the kinematic endpoint (the limit of large rapidities) was derived. It describes all kinematic

limits in x_a and x_b or, equivalently, in Q and Y, including in particular the limit $|Y| \to Y_{\mathrm{max}}$ at generic Q. Unlike the hadronic threshold limit $Q \to E_{\mathrm{cm}}$, this limit is directly accessible at the LHC.

Traditional soft threshold factorization theorems only involve the Born partonic subprocess, e.g. $q\bar{q}$ annihilation for Drell-Yan, while other partonic channels are typically treated as power corrections at fixed-order. The factorization obtained in eq. (6.16) also captures the non-diagonal collinear splittings in the unconstrained direction at leading power.

The partonic cross section described by this new factorization theorem has been checked against the exact results for all channels of the relevant processes (Drell-Yan and Higgs) to the highest available accuracy. Agreement within a few percent is found for generic values of the rapidity, while the results at larger rapidities agree increasingly well.

This new endpoint factorization enables the resummation of large logarithmic corrections that arise when one PDF is probed at large x_a (with the extracted parton as the "projectile"), while capturing the full dynamics of the struck "target" at small or intermediate x_b. Although only color-singlet processes have been considered in this chapter, the same methods may be used to generalize soft threshold factorizations for other processes as well.

7

Exploring the benefit of joint resummation

The simultaneous resummation of two different measurements has been considered for many specific cases, including the ones described in previous chapters. In this chapter, the benefit of such joint resummations is investigated in a case study, focussing on the collection of e^+e^- event shapes called angularities. In addition to the advantage that the combined resummation of two different observables provides, the added benefit of the simultaneous resummation of more observables is considered as well. The method used to quantify the improvement that resummed distributions provide is described in sec. 7.1. The required resummed results are obtained either from parton shower Monte Carlo event generators or through an analytical method. The analytic resummation of an arbitrary number of angularities at NLL accuracy is described in sec. 7.2. Results for the added benefit of the joint resummation of multiple angularities are shown in sec. 7.3. The methods and results covered in this chapter closely follow the contents of ref. [4].

7.1 Setup and method

To study the added benefit of simultaneously resumming multiple variables, the amount of information that a certain resummed cross section contains about a cross section involving a different variable has to be determined. The specific example used to study this is described in sec. 7.1.1. The degree to which cross sections involving a certain number of resummed variables are able to reproduce cross sections differential in a different variable has to be quantified. The method that is used for this employs a reweighing procedure, which is described in sec. 7.1.2.

7.1.1 Motivation

Although chaps. 4 and 5 describe the simultaneous resummation of two kine-matic variables, one could in principle consider the simultaneous resummation of ever more observables, which might lead to increasingly precise predictions for differential cross sections. All of these observables ultimately correspond to measurements that are performed on the same final state, so that some de-gree of correlation between the measured observables is to be expected. These kinematic correlations might then diminish the added benefit of resumming an increasing number of variables. The current chapter explores this concept by considering the simultaneous resummation of a number of variables and investigating to what degree this can be used to improve the prediction of a cross section differential in a different variable.

For concreteness, the process of $e^+e^- \to$ dijets is considered, upon which the measurements of a certain number of event shapes, known as angularities [254], are performed. Angularities are defined as

$$e_\alpha = \frac{2}{Q} \sum_i E_i \left[\sin\left(\frac{\theta_i}{2}\right) \right]^\alpha , \tag{7.1}$$

where Q is the center-of-mass energy and the sum runs over all final-state particles i with energy E_i and angle θ_i with respect to a chosen axis. By altering the parameter α, various distinct angularities are obtained, which include variables closely related to thrust [255] and (total) broadening [256,257] for $\alpha = 2$ and $\alpha = 1$ respectively. All outgoing particles are considered to be part of either of the two final-state (hemisphere) jets and the angularity in eq. (7.1) is obtained by adding the angularities corresponding to both jets. For each of these, the sum in eq. (7.1) is restricted to the particles contained in the corresponding jet and the angle θ_i is measured with respect to the Winner-Take-All axis [258, 259] of that jet. This axis is by construction insensitive to the recoil of soft radiation.

Since distributions involving angularities tend to be peaked around small values of e_α, the more natural variable $\ell_\alpha \equiv \log_{10} e_\alpha$ is used throughout this chapter as well. The term "angularity" will be used for both e_α and ℓ_α.

7.1.2 Optimal reweighing procedure

Cross sections are obtained by integrating the squared amplitude of a process over the phase space of the final state. The squared amplitude effectively as-signs a weight to each point in phase space, related to the probability of the process under consideration leading to the final state represented by that point.

If no such weight is provided, i.e. if the squared amplitude is absent, the phase space is called flat. In flat phase space, there are no preferred points so that, up to four-momentum conservation, each point is assigned an equal probability. Hence, by measuring observables using flat phase space, no information about the probability of the process enters in determining the differential cross section. The procedure that is employed to assess the degree to which resummed cross sections are able to reproduce cross sections differential in a different variable is based on reweighing the results from flat phase space by the resummed results. To perform this procedure in general, a resummed cross section differential in n angularities ℓ_{α_i}, with $i \in I = \{i_1, \ldots, i_n\}$, is required. The cross section differential in ℓ_{α_j}, with $j \notin I$, is then obtained by reweighing the cross section differential in all $n+1$ angularities originating from flat phase space with the resummed cross section, i.e.

$$\frac{\mathrm{d}\sigma_{\mathrm{reweigh}}}{\mathrm{d}\ell_{\alpha_j}} = \int \prod_{i \in I} [\mathrm{d}\ell_{\alpha_i}] \frac{\mathrm{d}\sigma_{\mathrm{flat}}}{\mathrm{d}\ell_{\alpha_j} \prod_{i \in I}[\mathrm{d}\ell_{\alpha_i}]} \times \frac{\mathrm{d}\sigma_{\mathrm{resum}}}{\prod_{i \in I}[\mathrm{d}\ell_{\alpha_i}]} \bigg/ \frac{\mathrm{d}\sigma_{\mathrm{flat}}}{\prod_{i \in I}[\mathrm{d}\ell_{\alpha_i}]} . \tag{7.2}$$

The resummed cross sections differential in n angularities are obtained through either analytical resummation, described in detail in sec. 7.2, or via Monte Carlo parton showers.

The flat k-body phase space is generated by using `Rambo` [260] "on diet" [261]. A slight modification is included that improves the sampling in the collinear and soft regions. Specifically, a transformation is performed that distributes the first random number of "Algorithm 1" in ref. [261] logarithmically. To compensate for this, the weight of the event is adjusted by the Jacobian of this transformation. This then ensures that the phase space is sampled sufficiently to also obtain reliable predictions for small values of the angularities. The generated momenta $p_1^\mu, \ldots, p_k^\mu$ are then clustered into two hemisphere jets by the exclusive k_T [262] algorithm with the Winner-Take-All recombination scheme [258, 259, 263] using the `FastJet` package [264]. This involves determining the distance measure

$$d_{ij} = 2 \min\{E_i^2, E_j^2\}\left(1 - \cos(\theta_{ij})\right), \tag{7.3}$$

for all pairs of particles with momenta p_i^μ and p_j^μ. The particles i and j that give rise to the smallest d_{ij} are then clustered into a single, new momentum $p_{(ij)}^\mu$ according to

$$E_{(ij)} = E_i + E_j,$$
$$\frac{\vec{p}_{(ij)}}{|\vec{p}_{(ij)}|} = \begin{cases} \vec{p}_i/|\vec{p}_i| & \text{if} \quad E_i > E_f, \\ \vec{p}_j/|\vec{p}_j| & \text{if} \quad E_f > E_i. \end{cases} \tag{7.4}$$

The complete algorithm of determining distance measures and clustering momenta is then iterated until only two momenta are left, representing the two hemisphere jets. By determining which original momenta were clustered into the same momentum, each particle can be assigned to either of the two jets, after which the angularities of interest can be calculated.

The various distributions occurring in eq. (7.2) are constructed in 16 equally spaced bins of each angularity ℓ_{α_i} on the interval $[-4, 0]$ and the integration is approximated by a sum over bins. It has been verified that the chosen binning does not alter the conclusions in sec. 7.3.3.

The deviation of the reweighed distribution in eq. (7.2) from the corresponding resummed result obtained from a direct calculation can be translated into a goodness-of-fit measure by

$$\chi^2_{\alpha_j} = \int \mathrm{d}\ell_{\alpha_j} \left| \frac{\mathrm{d}\sigma_{\mathrm{reweigh}}}{\mathrm{d}\ell_{\alpha_j}} - \frac{\mathrm{d}\sigma_{\mathrm{resum}}}{\mathrm{d}\ell_{\alpha_j}} \right|^2 . \tag{7.5}$$

The optimal set I_n^{opt} of n angularities that, averaged over all α_j in a chosen set, approaches the single-differential cross section $\mathrm{d}\sigma/\mathrm{d}\ell_{\alpha_j}$ best when reweighing can be found by considering the global goodness-of-fit variable

$$\chi^2 = \frac{1}{N - n} \sum_{j \notin I} \chi^2_{\alpha_j} , \tag{7.6}$$

where N represents the number of angularities that are summed over and n the number of angularities used to reweigh with.

7.2 Analytic resummation of n angularities

The analytic resummation of n angularities is carried out through factorization formulas obtained using SCET. The various kinematic regions in phase space and the relevant degrees of freedom for each region are determined in sec. 7.2.1 by making use of Lund planes. The factorization formulas for each region are presented in sec. 7.2.2 and the resummation is carried out in sec. 7.2.3. The procedure used to match the resummed cross sections of the various regions in phase space to one another is described in sec. 7.2.5. This method is based on the power corrections, addressed in sec. 7.2.4, that each factorization receives.

7.2.1 Phase space regions and degrees of freedom

In the collinear limit, the probability $W_{ij}(z, \theta)$ of a particle j emitting a particle i can be characterized in terms of the momentum fraction z of the radiated
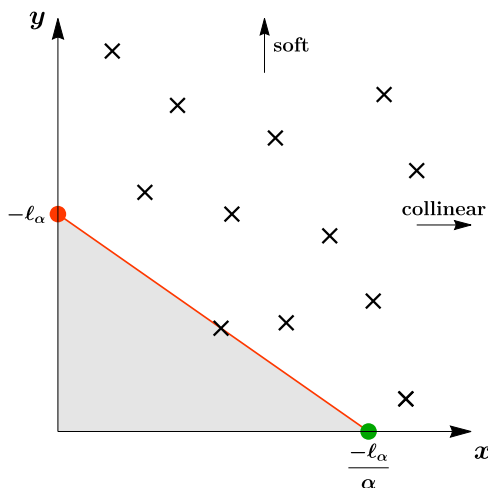
Figure 7.1 Illustration of the Lund plane with $x = \log_{10}(1/\theta)$ and $y = \log_{10}(1/z)$. The crosses represent emissions and the red line the measurement of an angularity ℓ_α, set by the dominant emission. There can be no emissions in the shaded area, while emissions above this region only contribute at higher orders. The green and orange dot denote the collinear and soft mode respectively.

particle and its angle θ with respect to particle i as

$$\frac{\mathrm{d}W_{ij}(z,\theta)}{\mathrm{d}\theta\,\mathrm{d}z} = \frac{\alpha_s}{\pi}\frac{P_{ij}^{(0)}(z)}{\theta}\,. \tag{7.7}$$

At LL accuracy, the splitting functions given in app. B.2 are proportional to $\sim 1/z$, so that these emissions are distributed uniformly in $x \equiv \log_{10}(1/\theta)$ and $y \equiv \log_{10}(1/z)$. The Lund plane [265] spanned by these variables is shown in fig. 7.1, where the crosses indicate various emissions. The angularity arising from a single emission with small z and θ can we written as

$$\ell_\alpha = -y - \alpha x\,, \tag{7.8}$$

where the identifications[1] $2E_i/Q \to z_i$ and $\theta_i/2 \to \theta$ are made with respect to the definition in eq. (7.1). This then corresponds to a straight line in the Lund plane with slope $-\alpha$. Due to the uniform distribution of emissions in the (logarithmically spaced) Lund plane, a single emission will dominate the measurement at LL accuracy, as indicated by the red line in fig. 7.1. All emissions above and to the right of this line are more soft, more collinear,

---

[1]The factor of $1/2$ is purely for convenience and does not affect the leading logarithms.

or both and only enter beyond LL accuracy. There are no emissions below the line, otherwise one of these would have been the dominant emission. The shaded area under the line corresponds to the Sudakov factor describing the no-emission probability and can be used to calculate the cumulative cross section at LL through

$$\sigma(e_\alpha^{\mathrm{cut}}) = \int_0^{e_\alpha^{\mathrm{cut}}} \mathrm{d}e_\alpha \, \frac{\mathrm{d}\sigma}{\mathrm{d}e_\alpha} = \sigma_B^q \, \exp\!\Big(-\frac{4\alpha_s C_F}{\pi} \times [\text{gray area}] \times \ln^2 10\Big), \quad (7.9)$$

where σ_B^q is the Born cross section. The boundary of the shaded area in fig. 7.1 is fixed by the points at which it crosses both axes. The cross section can thus be obtained from these points, which correspond to degrees of freedom in SCET. For the measurement of a single angularity, these are ultrasoft and collinear modes, represented by the orange and green dot respectively. Each collinear direction gives rise to a distinct collinear mode, so for the process $e^+e^- \to$ dijets currently under consideration, there are two collinear modes. The scaling of these modes is given by

$$\begin{aligned} n\text{-collinear:} \quad & p_n^\mu \sim Q\big(e_\alpha^{2/\alpha}, 1, e_\alpha^{1/\alpha}\big), \\ \bar{n}\text{-collinear:} \quad & p_{\bar{n}}^\mu \sim Q\big(1, e_\alpha^{2/\alpha}, e_\alpha^{1/\alpha}\big), \\ \text{ultrasoft:} \quad & p_{us}^\mu \sim Q\big(e_\alpha, e_\alpha, e_\alpha\big). \end{aligned} \quad (7.10)$$

When the simultaneous measurement of two angularities ℓ_{α_1} and ℓ_{α_2} is considered, the straight lines describing the variables in the Lund plane have to cross one another at some point to ensure that the cross section involves both measurements. Assuming the hierarchy $\alpha_1 > \alpha_2$ for definiteness, three distinct cases can be distinguished, as shown in fig. 7.2. The boundaries of these three regions of phase space for the simultaneous measurement of two angularities are found to be given by

$$\begin{aligned} \text{Regime 1:} \quad & -\ell_{\alpha_2} < -\ell_{\alpha_1} \quad \text{and} \quad \frac{-\ell_{\alpha_1}}{\alpha_1} = \frac{-\ell_{\alpha_2}}{\alpha_2}, \\ \text{Regime 2:} \quad & -\ell_{\alpha_2} < -\ell_{\alpha_1} \quad \text{and} \quad \frac{-\ell_{\alpha_1}}{\alpha_1} < \frac{-\ell_{\alpha_2}}{\alpha_2}, \\ \text{Regime 3:} \quad & -\ell_{\alpha_2} = -\ell_{\alpha_1} \quad \text{and} \quad \frac{-\ell_{\alpha_1}}{\alpha_1} < \frac{-\ell_{\alpha_2}}{\alpha_2}, \end{aligned} \quad (7.11)$$

which agree with the regions of phase space identified in refs. [108, 132, 133]. In all three cases, there are soft (orange) and collinear (green) degrees of freedom. The intermediate regime 2 additionally contains a collinear-soft mode (blue), described in more detail in sec. 3.10, which contributes to both measurements
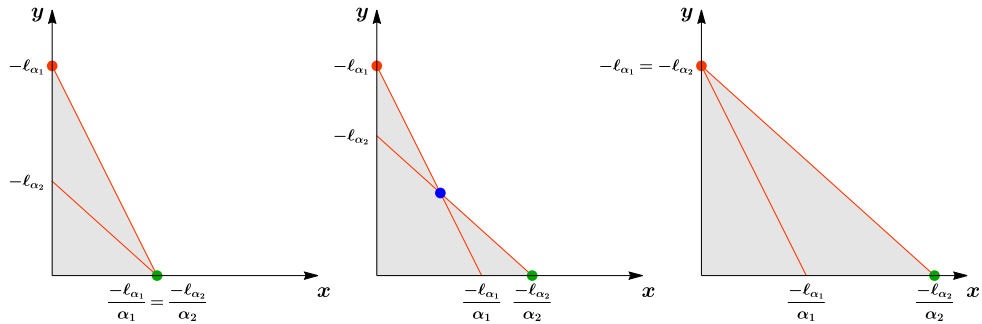
Figure 7.2 The measurement of two angularities ℓ_{α_1} and ℓ_{α_2} represented in the Lund plane. Each panel describes a distinct region of phase space. The left and right panels involve only collinear (green) and soft (orange) modes, while the center panel contains an additional collinear-soft (blue) mode. Emissions in the shaded region are vetoed.

since it corresponds to the intersection of the lines representing those measurements.

This method of finding all relevant regions of phase space through the use of Lund planes can be generalized to the simultaneous measurement of an arbitrary number of angularities. There is only one additional subtlety that has to be taken into account when more than two angularities are considered, which is illustrated in fig. 7.3 for three angularities with parameters $\alpha_1 > \alpha_2 > \alpha_3$. If the line corresponding to ℓ_{α_3} were to be placed above the position indicated by the dotted line, the angularity ℓ_{α_2} would no longer be connected to the boundary of the region in which emissions are forbidden and hence not affect the cross section. The point at which the dotted line crosses the y-axis is given by

$$C_{\alpha_3}^{\alpha_1\alpha_2} = \frac{1}{\alpha_1 - \alpha_2}\Big[(\alpha_2 - \alpha_3)\ell_{\alpha_1} - (\alpha_1 - \alpha_3)\ell_{\alpha_2}\Big]. \tag{7.12}$$

The phase space of a cross section involving an arbitrary number n of angularities can be divided into various regions, as listed explicitly in eq. (7.11) for $n = 2$. The region that involves the largest amount of angularities is the one for which the edge of the forbidden (gray) region in the Lund plane involves every line corresponding to an individual angularity. For $n = 2$, this corresponds to the central panel in fig. 7.2 and for $n = 3$, this situation is depicted in fig. 7.3. This region will be denoted by $R_n(\alpha_1, \ldots, \alpha_n)$, and its boundary
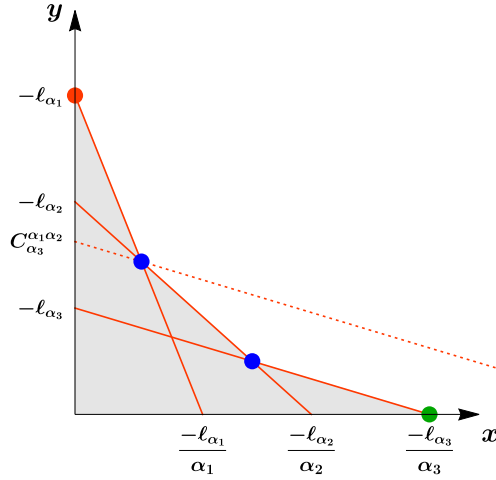
Figure 7.3 The Lund plane describing the region of phase space for the simultaneous measurement of three angularities that involves all angularities. The various modes are denoted by the green (collinear), orange (soft) and blue (collinear-soft) dots. The dotted line serves to indicate the point $C_{\alpha_3}^{\alpha_1\alpha_2}$, which shows up in the boundary conditions of the regions of phase space.

conditions in phase space are given by

$$
\begin{aligned}
y\text{-conditions:} &\quad -\ell_{\alpha_1} > -\ell_{\alpha_2}\,, \quad C_{\alpha_3}^{\alpha_1\alpha_2} > -\ell_{\alpha_3}\,, \quad \ldots\,, \quad C_{\alpha_n}^{\alpha_{n-2}\alpha_{n-1}} > -\ell_{\alpha_n}\,, \\
x\text{-conditions:} &\quad -\frac{\ell_{\alpha_n}}{\alpha_n} > -\frac{\ell_{\alpha_{n-1}}}{\alpha_{n-1}}\,, \quad \ldots\,, \quad -\frac{\ell_{\alpha_2}}{\alpha_2} > -\frac{\ell_{\alpha_1}}{\alpha_1}\,.
\end{aligned}
\tag{7.13}
$$

The first line contains the set of $n-1$ conditions that the points at which each line in the Lund plane crosses the y-axis should adhere to. The $n-1$ conditions on the second line ensure the correct hierarchy of the points at which these lines cross the x-axis. As these conditions consist solely of inequalities, this region in n-dimensional phase space is itself n-dimensional and will be referred the as the "bulk".

Regions that involve fewer angularities can be obtained by raising or lowering the point at which an angularity crosses either axis in the Lund plane, such that two modes (the colored dots) merge. This can be seen explicitly in fig. 7.2 by starting from the central panel and raising $-\ell_{\alpha_2}$ until it reaches $-\ell_{\alpha_2} = -\ell_{\alpha_1}$ in the right panel, sliding the mode indicated by the blue dot up to the orange dot in the process.

In full generality, the boundaries of a region in phase space involving a subset of angularities $\ell_{\beta_1}, \ldots, \ell_{\beta_m}$ with $m \leq n$ and $\{\beta_1, \ldots, \beta_m\} \subset \{\alpha_1, \ldots, \alpha_n\}$ are

found to be described by the conditions[2]

y-conditions: $\quad -\ell_{\beta_1} > -\ell_{\beta_2}\,, \quad C_{\beta_3}^{\beta_1\beta_2} > -\ell_{\beta_3}\,, \quad \ldots\,, \quad C_{\beta_m}^{\beta_{m-2}\beta_{m-1}} > -\ell_{\beta_m}\,,$

x-conditions: $\quad -\dfrac{\ell_{\beta_m}}{\beta_m} > -\dfrac{\ell_{\beta_{m-1}}}{\beta_{m-1}}\,, \quad \ldots\,, \quad -\dfrac{\ell_{\beta_2}}{\beta_2} > -\dfrac{\ell_{\beta_1}}{\beta_1}\,,$

B-conditions: $\quad -\ell_{\beta_1} = -\ell_{\alpha_i} \qquad$ for every α_i with $\alpha_i > \beta_1\,,$

$$C_{\alpha_i}^{\beta_j\beta_{j+1}} = -\ell_{\alpha_i} \qquad \text{for every } \alpha_i \text{ with } \beta_j > \alpha_i > \beta_{j+1}\,,$$

$$-\frac{\ell_{\beta_m}}{\beta_m} = -\frac{\ell_{\alpha_i}}{\alpha_i} \qquad \text{for every } \alpha_i \text{ with } \beta_m > \alpha_i\,, \tag{7.14}$$

where the B-conditions (boundary-conditions) contain all restrictions on the angularities that are only connected to the boundary of the shaded area in the Lund plane through a single point, i.e. the angularities not involved in the region. As any such regime is characterized by $n - m$ equalities, it represents an m-dimensional region in the n-dimensional phase space, denoted by $R_m(\beta_1, \ldots, \beta_m)$. By considering all possible combinations of angularities, it then follows that there are $\binom{n}{n-m}$ different regions of dimension m in the phase space of n angularities.

7.2.2 Factorization

The relevant degrees of freedom for the bulk regime for $n = 2$ angularities are depicted by the colored dots in the central panel of fig. 7.2. The orange dot represents the ultrasoft mode, the green dot the n- and $\bar{n}$-collinear modes, and the blue dot corresponds to the n- and $\bar{n}$-collinear-soft modes that contribute to the measurement of both angularities. The factorization formula for this regime was derived using SCET in refs. [108, 133] and is given by

$$\frac{\mathrm{d}^2\sigma^{R_2(\alpha_1,\alpha_2)}}{\mathrm{d}(Q^{\alpha_1}e_{\alpha_1})\,\mathrm{d}(Q^{\alpha_2}e_{\alpha_2})} = H_{q\bar{q}}(Q,\mu)\,S_{q\bar{q}}(Q^{\alpha_1}e_{\alpha_1},\mu) \underset{\alpha_1}{\otimes} \left[\mathscr{S}(Q^{\alpha_1}e_{\alpha_1},Q^{\alpha_2}e_{\alpha_2},\mu)\right]^2$$

$$\underset{\alpha_2}{\otimes} \left[J(Q^{\alpha_2}e_{\alpha_2},\mu)\right]^2\,, \tag{7.15}$$

where a sum over the relevant relevant combinations of quark and antiquark flavors is understood and the squares of the collinear-soft function and jet function are defined as

$$\left[\mathscr{S}(Q^{\alpha_1}e_{\alpha_1},Q^{\alpha_2}e_{\alpha_2},\mu)\right]^2 \equiv \mathscr{S}_q(Q^{\alpha_1}e_{\alpha_1},Q^{\alpha_2}e_{\alpha_2},\mu) \underset{\alpha_1,\alpha_2}{\otimes} \mathscr{S}_{\bar{q}}(Q^{\alpha_1}e_{\alpha_1},Q^{\alpha_2}e_{\alpha_2},\mu)\,,$$

$$\left[J(Q^{\alpha}e_{\alpha},\mu)\right]^2 \equiv J_q(Q^{\alpha}e_{\alpha},\mu) \underset{\alpha}{\otimes} J_{\bar{q}}(Q^{\alpha}e_{\alpha},\mu)\,. \tag{7.16}$$

---

[2]Note that although the convention $\beta_1 > \ldots > \beta_m$ is still used, subsequent β_i and β_{i+1} do not necessarily correspond to consecutive α_j.

Convolutions between two functions f and g are indicated by

$$f(Q^\alpha e_\alpha) \underset{\alpha}{\otimes} g(Q^\alpha e_\alpha) \equiv \int \mathrm{d}(Q^\alpha e'_\alpha) \, f(Q^\alpha e_\alpha - Q^\alpha e'_\alpha) \, g(Q^\alpha e'_\alpha) , \qquad (7.17)$$

where f and g may depend on additional arguments. Convolutions in multiple variables are indicated by the corresponding subscripts.

The hard function $H_{q\bar{q}}(Q, \mu)$ in eq. (7.15) includes the Born cross section σ_B^q and describes any virtual corrections. The jet function $J_q(Q^\alpha e_\alpha, \mu)$ describes collinear radiation and the contributions of soft and collinear-soft radiation to the measured angularities are taken into account by the soft function $S_{q\bar{q}}(Q^\alpha e_\alpha, \mu)$ and collinear-soft function $\mathscr{S}_q(Q^{\alpha_1} e_{\alpha_1}, Q^{\alpha_2} e_{\alpha_2}, \mu)$ respectively. At NLL accuracy, only tree-level expressions are required for the perturbative functions. The hard function reduces to the Born cross section at tree-level and the other functions are simply products of delta functions of their arguments.

The region of phase space represented by the left panel of fig. 7.2 can be reached from the region $R_2(\alpha_1, \alpha_2)$ by raising $-\ell_{\alpha_1}/\alpha_1$ or lowering $-\ell_{\alpha_2}/\alpha_2$ until the two are equal, matching the collinear-soft modes to the collinear modes in the process. The factorization formula of this region then no longer contains any collinear-soft functions, but instead involves jet functions depending on both angularities. The explicit factorization then reads

$$\frac{\mathrm{d}^2 \sigma^{R_1(\alpha_1)}}{\mathrm{d}(Q^{\alpha_1} e_{\alpha_1}) \, \mathrm{d}(Q^{\alpha_2} e_{\alpha_2})} = H_{q\bar{q}}(Q, \mu) \, S_{q\bar{q}}(Q^{\alpha_1} e_{\alpha_1}, \mu) \underset{\alpha_1}{\otimes} \left[J(Q^{\alpha_1} e_{\alpha_1}, Q^{\alpha_2} e_{\alpha_2}, \mu) \right]^2 .$$
$$(7.18)$$

In this regime, soft radiation does not contribute to the measurement e_{α_2} and the factorization formula is simply a more differential version of the factorization formula for the measurement of a single angularity e_{α_1}.

Analogously, to obtain the factorization formula describing the region of phase space depicted in the right panel in fig. 7.2, the soft and collinear-soft functions merge into a more differential soft function to yield

$$\frac{\mathrm{d}^2 \sigma^{R_1(\alpha_2)}}{\mathrm{d}(Q^{\alpha_1} e_{\alpha_1}) \, \mathrm{d}(Q^{\alpha_2} e_{\alpha_2})} = H_{q\bar{q}}(Q, \mu) \, S_{q\bar{q}}(Q^{\alpha_1} e_{\alpha_1}, Q^{\alpha_2} e_{\alpha_2}, \mu) \underset{\alpha_2}{\otimes} \left[J(Q^{\alpha_2} e_{\alpha_2}, \mu) \right]^2 .$$
$$(7.19)$$

This is then a more differential version of the factorization theorem for the single-differential cross section in e_{α_2}. As the regions $R_1(\alpha_1)$ and $R_1(\alpha_2)$, described by the factorizations in eqs. (7.18) and (7.19) respectively, are both connected to the region $R_2(\alpha_1, \alpha_2)$, the former are known as "daughter regions" with respect to the latter. The region $R_2(\alpha_1, \alpha_2)$ is then referred to as

a "parent region" with respect to both $R_1(\alpha_1)$ and $R_1(\alpha_2)$. The factorization in eq. (7.15), valid in the region $R_2(\alpha_1, \alpha_2)$, involves an additional expansion with respect to the factorizations of both daughter regions, but may be used to simultaneously resum logarithms of both angularities.

The RGEs and anomalous dimensions of the perturbative functions appearing in the factorizations are given in app. C.1. Making use of these, the μ-independence of the cross section leads to a consistency requirement on the anomalous dimensions. For the factorization formula in eq. (7.15) this condition given by

$$
\begin{aligned}
0 = {}& 2\gamma_{q\bar{q}}(Q^2, \mu)\, \delta(Q^{\alpha_1} e_{\alpha_1})\, \delta(Q^{\alpha_2} e_{\alpha_2}) + 2\gamma_J^q(Q^{\alpha_2} e_{\alpha_2}, \mu)\, \delta(Q^{\alpha_1} e_{\alpha_1}) \\
&+ 2\bar{\gamma}_{\mathscr{S}}^q(Q^{\alpha_1} e_{\alpha_1}, Q^{\alpha_2} e_{\alpha_2}, \mu) + \bar{\gamma}_S^q(Q^{\alpha_1} e_{\alpha_1}, \mu)\, \delta(Q^{\alpha_2} e_{\alpha_2}) \,,
\end{aligned}
\tag{7.20}
$$

where the bars on the soft and collinear-soft anomalous dimensions serve to distinguish them from other soft and collinear-soft anomalous dimensions appearing throughout this thesis. By plugging in the explicit anomalous dimensions, this consistency relation is indeed found to be satisfied.

For the measurement of n angularities, the factorization formula for the cross section describing the bulk region $R_n(\alpha_1, \ldots, \alpha_n)$ follows from the modes appearing in the corresponding Lund plane. Specifically, there is a single soft mode, a single collinear mode (for each of the two collinear directions) and there are $n - 1$ collinear-soft modes (per collinear direction), leading to the general factorization formula

$$
\begin{aligned}
\frac{\mathrm{d}^n \sigma^{R_n(\alpha_1, \ldots, \alpha_n)}}{\mathrm{d}(Q^{\alpha_1} e_{\alpha_1}) \ldots \mathrm{d}(Q^{\alpha_n} e_{\alpha_n})} = {}& H(Q, \mu)\, S(Q^{\alpha_1} e_{\alpha_1}, \mu) \\
& \underset{\alpha_1}{\otimes} \left[\mathscr{S}(Q^{\alpha_1} e_{\alpha_1}, Q^{\alpha_2} e_{\alpha_2}, \mu) \right]^2 \underset{\alpha_2}{\otimes} \ldots \underset{\alpha_k}{\otimes} \left[\mathscr{S}(Q^{\alpha_k} e_{\alpha_k}, Q^{\alpha_{k+1}} e_{\alpha_{k+1}}, \mu) \right]^2 \underset{\alpha_{k+1}}{\otimes} \ldots \\
& \underset{\alpha_{n-1}}{\otimes} \left[\mathscr{S}(Q^{\alpha_{n-1}} e_{\alpha_{n-1}}, Q^{\alpha_n} e_{\alpha_n}, \mu) \right]^2 \underset{\alpha_n}{\otimes} \left[J(Q^{\alpha_n} e_{\alpha_n}, \mu) \right]^2 \,,
\end{aligned}
\tag{7.21}
$$

where the subscripts q and $\bar{q}$ have been left implicit. When taking derivatives of this expression with respect to μ, the anomalous dimensions of all intermediate collinear-soft functions effectively combine into a single collinear-soft anomalous dimension involving the angularities e_{α_1} and e_{α_n}, leading to the conclusion that this factorization formula also obeys the corresponding consistency relation. Factorization formulas corresponding to regions that involve fewer angularities are again obtained by merging two degrees of freedom, i.e. merging two functions into a single, more differential function.
Since at NLL accuracy all perturbative functions are delta functions, the more-differential functions that arise due to the merging of modes do not give rise

to any different results for the cross section. This then implies that (at least at NLL) the cross section for a specific kinematic region of interest does not depend on the total set of angularities that are measured, but instead only on the subset of angularities that occur in said region.

7.2.3 Resummation

The large logarithms in a factorization formula such as eq. (7.21) may be resummed by evaluating each ingredient at its natural scale (where its logarithms are minimized) and then evolving them to a common scale. RGEs that involve a convolution may be solved in a conjugate space such as Laplace space. Plugging the solutions in the factorized cross section in eq. (7.21) and performing the inverse Laplace transform then yields the resummed cross section in momentum space. The resummation is performed at the level of the cumulative cross section, which is obtained by the analog of the first equality in eq. (7.9) for n angularities. The cumulative cross section is then found to be

$$
\sigma_{R_n(\alpha_1,\ldots,\alpha_n)} = \sigma_B^q \frac{\exp\left[K_H + K_S^0(\alpha_1) + 2K_J - \gamma_E\left(2\eta_J + \eta_S^{n-1}(\alpha_n)\right)\right]}{\Gamma\left[1 + 2\eta_J + \eta_S^{n-1}(\alpha_n)\right]}
$$
$$
\times \left(\frac{Q}{\mu_H}\right)^{\eta_H} \left(\frac{Qe_{\alpha_1}}{\mu_S}\right)^{\eta_S^0(\alpha_1)} \left(\frac{Qe_{\alpha_n}^{1/\alpha_n}}{\mu_J}\right)^{2\alpha_n\eta_J}
$$
$$
\times \prod_{i=1}^{n-1} \left\{ \frac{\exp\left[K_S^i(\alpha_{i+1}) - K_S^i(\alpha_i) - \gamma_E\,\eta_S^{i-1,i}(\alpha_i)\right]}{\Gamma\left[1 + \eta_S^{i-1,i}(\alpha_i)\right]} \right.
$$
$$
\left. \times \left(e_{\alpha_i}^{\alpha_{i+1}-1} e_{\alpha_{i+1}}^{1-\alpha_i}\left(\frac{Q}{\mu_{i,i+1}}\right)^{\alpha_{i+1}-\alpha_i}\right)^{\frac{2\eta_\Gamma(\mu_{i,i+1},\mu)}{(\alpha_i-1)(1-\alpha_{i+1})}} \right\}. \quad (7.22)
$$

The various functions that appear are defined in terms of the evolution kernels that can be found in app. C.2 as

$$
K_S^i(\alpha_j) \equiv -\frac{4}{\alpha_j - 1} K_\Gamma^q(\mu_{i,i+1}, \mu), \qquad\qquad \eta_S^i(\alpha_j) \equiv \frac{4}{\alpha_j - 1} \eta_\Gamma^q(\mu_{i,i+1}, \mu),
$$
$$
K_J \equiv \frac{2\alpha_n}{\alpha_n - 1} K_\Gamma^q(\mu_J, \mu) + K_{\gamma_J^q}(\mu_J, \mu), \qquad \eta_J \equiv \frac{2}{1 - \alpha_n} \eta_\Gamma^q(\mu_J, \mu),
$$
$$
K_H \equiv -4K_\Gamma^q(\mu_H, \mu) + K_{\gamma_H^q}(\mu_H, \mu), \qquad \eta_H \equiv 4\eta_\Gamma^q(\mu_H, \mu). \quad (7.23)
$$

Furthermore, the notation

$$
\eta_S^{i-1}(\alpha_i) - \eta_S^i(\alpha_i) = \frac{4}{\alpha_i - 1} \int_{\alpha_s(\mu_{i-1,i})}^{\alpha_s(\mu_{i,i+1})} \frac{\mathrm{d}\alpha_s'}{\beta(\alpha_s')}\, \Gamma_{\mathrm{cusp}}^q(\alpha_s') \equiv \eta_S^{i-1,i}(\alpha_i), \quad (7.24)
$$

Region $R_n(\alpha_1, \ldots, \alpha_n)$	Boundary conditions $B_n(\alpha_1, \ldots, \alpha_n)$
$R_3(\alpha_1, \alpha_2, \alpha_3)$	-
$R_2(\alpha_1, \alpha_2)$	$e_{\alpha_3} = e_{\alpha_2}^{\alpha_3/\alpha_2}$
$R_2(\alpha_1, \alpha_3)$	$e_{\alpha_2} = (e_{\alpha_1}^{\alpha_3-\alpha_2}/e_{\alpha_3}^{\alpha_2-\alpha_1})^{1/(\alpha_3-\alpha_1)}$
$R_2(\alpha_2, \alpha_3)$	$e_{\alpha_1} = e_{\alpha_2}$
$R_1(\alpha_1)$	$e_{\alpha_2} = e_{\alpha_1}^{\alpha_2/\alpha_1}$ and $e_{\alpha_3} = e_{\alpha_1}^{\alpha_3/\alpha_1}$
$R_1(\alpha_2)$	$e_{\alpha_1} = e_{\alpha_2}$ and $e_{\alpha_3} = e_{\alpha_2}^{\alpha_3/\alpha_2}$
$R_1(\alpha_3)$	$e_{\alpha_1} = e_{\alpha_3}$ and $e_{\alpha_2} = e_{\alpha_3}$

Table 7.1 The boundary conditions of the various regions in the three-angularity phase space with $\alpha_1 > \alpha_2 > \alpha_3$.

has been introduced. The natural scales of the functions at which the large logarithms are minimized depend on the (sub)set of angularities relevant to the region under consideration. Denoting this set of angularities by $\beta_1, \ldots, \beta_m$, the various scales are given by

$$\mu_H = Q\,, \qquad\qquad \mu_S \equiv \mu_{0,1} = Q e_{\beta_1}\,,$$

$$\mu_J = Q e_{\beta_m}^{1/\beta_m}\,, \qquad \mu_{\mathscr{S}}(\beta_i, \beta_{i+1}) \equiv \mu_{i,i+1} = Q \left(\frac{e_{\beta_i}^{1-\beta_{i+1}}}{e_{\beta_{i+1}}^{1-\beta_i}} \right)^{\frac{1}{\beta_i - \beta_{i+1}}}\,, \qquad (7.25)$$

where each angularity e_α should be understood to represent the cumulative variable e_α^{cut}.

7.2.4 Power corrections

The power corrections to each factorization formula can be determined by considering the ratio of scales involved in the functions that are merged into a more differential function when transitioning towards a lower-dimensional (daughter) region in phase space. The measurement of three angularities will be used as an example to display this procedure. The various regions of phase space and their B-conditions, i.e. the equalities in eq. (7.14), can be found in table 7.1 for $\alpha_1 > \alpha_2 > \alpha_3$. In general, the power corrections of a factorization formula valid in an n-dimensional region $R_n(\alpha_1, \ldots, \alpha_n)$ towards an $(n-1)$-dimensional daughter region $R_{n-1}(\alpha_1, \ldots, \alpha_i, \alpha_{i+1}, \ldots, \alpha_n)$ are denoted by $P_n(\alpha_1, \ldots, \alpha_n; \alpha_i)$. The argument after the semicolon indicates the angularity that appears in the parent region, but not in the daughter region. Using

this notation, the power corrections from the one-dimensional regions towards the fixed-order region are given by [133]

$$P_1(\alpha_i; \alpha_i) = e_{\alpha_i}^{\min[2/\alpha_i, 1]}. \tag{7.26}$$

The power corrections of a factorization formula representing a two-dimensional parent region towards the neighboring one-dimensional daughter regions are given by

$$P_2(\alpha_i, \alpha_j; \alpha_j) = \left(\frac{\mu_{\mathscr{S}}(\alpha_i, \alpha_j)}{\mu_J(\alpha_i)} \right)^{\#},$$

$$P_2(\alpha_i, \alpha_j; \alpha_i) = \left(\frac{\mu_{\mathscr{S}}(\alpha_i, \alpha_j)}{\mu_S(\alpha_j)} \right)^{\#}. \tag{7.27}$$

The different powers # may be fixed by demanding that each power correction should reduce to the power corrections of the one-dimensional region at the corresponding boundary, i.e.

$$\left[P_2(\alpha_i, \alpha_j; \alpha_j) \right]_{B_1(\alpha_j)} \stackrel{!}{=} P_1(\alpha_j; \alpha_j),$$

$$\left[P_2(\alpha_i, \alpha_j; \alpha_i) \right]_{B_1(\alpha_i)} \stackrel{!}{=} P_1(\alpha_i; \alpha_i), \tag{7.28}$$

where the boundary conditions B_1 can be found in table 7.1. By plugging in the various scales, the complete set of power corrections (indicated by the absence of the semicolon) of the factorization formula representing a two-dimensional region is then found to be

$$P_2(\alpha_i, \alpha_j) = \left\{ \left(\frac{e_{\alpha_j}}{e_{\alpha_i}^{\alpha_j/\alpha_i}} \right)^{\frac{\alpha_i \min[2/\alpha_j, 1]}{\alpha_i - \alpha_j}}, \left(\frac{e_{\alpha_i}}{e_{\alpha_j}} \right)^{\frac{\alpha_i \min[2/\alpha_i, 1]}{\alpha_i - \alpha_j}} \right\}. \tag{7.29}$$

The power corrections from the three-dimensional region towards any of its daughter regions can be found in an analogous way. By demanding that these power corrections reduce to those of any of the daughter regions at the corresponding boundaries, the complete set of power corrections of the three-dimensional region is

$$P_3(\alpha_i, \alpha_j, \alpha_k) = \left\{ \left(\frac{e_{\alpha_k}}{e_{\alpha_j}^{\alpha_k/\alpha_j}} \right)^{\frac{\alpha_j \min[2/\alpha_k, 1]}{\alpha_j - \alpha_k}}, \left(\frac{e_{\alpha_i}^{\alpha_j - \alpha_k} e_{\alpha_k}^{\alpha_i - \alpha_j}}{e_{\alpha_j}^{\alpha_i - \alpha_k}} \right)^{\frac{\alpha_j \min[2/\alpha_j, 1]}{(\alpha_j - \alpha_i)(\alpha_j - \alpha_k)}}, \right.$$

$$\left. \left(\frac{e_{\alpha_i}}{e_{\alpha_j}} \right)^{\frac{\alpha_i \min[2/\alpha_i, 1]}{\alpha_i - \alpha_j}} \right\}. \tag{7.30}$$

This procedure can be generalized to the case of regions involving n angularities. There are three different types of power corrections that need to be considered, all of them already present for $n = 3$. They are given by

$$P_n(\alpha_1, \ldots, \alpha_n; \alpha_n) = \left(\frac{e_{\alpha_n}}{e_{\alpha_{n-1}}^{\alpha_n/\alpha_{n-1}}} \right)^{E_n(\alpha_1, \ldots, \alpha_n; \alpha_n)},$$

$$P_n(\alpha_1, \ldots, \alpha_n; \alpha_i) = \left(\frac{e_{\alpha_{i-1}}^{\alpha_i - \alpha_{i+1}} e_{\alpha_{i+1}}^{\alpha_{i-1} - \alpha_i}}{e_{\alpha_i}^{\alpha_{i-1} - \alpha_{i+1}}} \right)^{E_n(\alpha_1, \ldots, \alpha_n; \alpha_i)} \quad \text{for} \quad 2 \leq i \leq n - 1,$$

$$P_n(\alpha_1, \ldots, \alpha_n; \alpha_1) = \left(\frac{e_{\alpha_1}}{e_{\alpha_2}} \right)^{E_n(\alpha_1, \ldots, \alpha_n; \alpha_1)}. \tag{7.31}$$

The powers E can then be found by requiring

$$\left[P_n(\alpha_1, \ldots, \alpha_n; \alpha_1) \right]_{B_{n-1}(\alpha_1, \ldots, \alpha_{n-1})} \overset{!}{=} P_{n-1}(\alpha_1, \ldots, \alpha_{n-1}; \alpha_1),$$

$$\left[P_n(\alpha_1, \ldots, \alpha_n; \alpha_i) \right]_{B_{n-1}(\alpha_2, \ldots, \alpha_n)} \overset{!}{=} P_{n-1}(\alpha_2, \ldots, \alpha_n; \alpha_i), \tag{7.32}$$

for $2 \leq i \leq n - 1$.

7.2.5 Matching phase space regions

The different regions in phase space that are found by using the Lund planes are each described by different (cumulative) cross sections. In order to obtain a combined prediction valid throughout phase space, these regions need to be matched to each another. For any given point in n-dimensional phase space, the combined cumulative cross section is defined as a linear combination of all possible regions that occur in phase space as

$$\sigma(e_{\alpha_1}, \ldots, e_{\alpha_n}) = \sum_{R_m} a_m(\beta_1, \ldots, \beta_m) \, \sigma^{R_m(\beta_1, \ldots, \beta_m)}, \tag{7.33}$$

where again $\beta_1, \ldots, \beta_m$ is any subset of the full set of angularities $\alpha_1, \ldots, \alpha_n$. The dependence of the transition variables a_m and the cross sections σ^{R_m} on the full set of angularities has been suppressed. The sum runs over all regions R_m with $n \geq m \geq 0$ and the set of transition variables is normalized as

$$\sum_{R_m} a_m(\beta_1, \ldots, \beta_m) = 1, \tag{7.34}$$

at every point in phase space spanned by the n angularities under consideration. In principle, this includes the matching to the fixed-order region R_0, but this matching is not performed here for simplicity, so that $a_0 = 0$. Following the approach in ref. [266], the specific admixture of transition variables

$a_m(\beta_1, \ldots, \beta_m)$ at a given point in phase space is determined by the size of the power corrections to the factorization formula valid at that point. The transitions between the different regions are realized through a transition function defined as

$$
f_{\text{trans}}(x_i, x_f, x) = \begin{cases} 0 & \text{if } x > x_i\,, \\ \sum_{j=0}^{5} c_j(x_i, x_f)\, x^j & \text{if } x_i \geq x > x_f\,, \\ 1 & \text{if } x_f \geq x\,, \end{cases} \tag{7.35}
$$

which smoothly interpolates between 0 and 1. The coefficients c_j are determined by demanding the continuity of f_{trans} and its first and second derivative at both transition points x_i and x_f. The explicit expressions obtained in this way are given by

$$
c_0(x_i, x_f) = -\frac{10x_f^2 x_i^3 - 5x_f x_i^4 + x_i^5}{(x_f - x_i)^5}\,, \qquad c_3(x_i, x_f) = \frac{10(x_f^2 + 4x_f x_i + x_i^2)}{(x_f - x_i)^5}\,,
$$

$$
c_1(x_i, x_f) = \frac{30x_f^2 x_i^2}{(x_f - x_i)^5}\,, \qquad\qquad c_4(x_i, x_f) = -\frac{15(x_f + x_i)}{(x_f - x_i)^5}\,,
$$

$$
c_2(x_i, x_f) = -\frac{30(x_f^2 x_i + x_f x_i^2)}{(x_f - x_i)^5}\,, \qquad c_5(x_i, x_f) = \frac{6}{(x_f - x_i)^5}\,. \tag{7.36}
$$

The values of the transition variables $a_m(\beta_1, \ldots, \beta_m)$ at a given point p in the n-dimensional space spanned by $\ell_{\alpha_1}, \ldots, \ell_{\alpha_n}$ are determined iteratively. First, all transition variables are set to 0. The region in which point p lies is then determined through the conditions given in eq. (7.14). If it lies outside of all regions, all coefficients are kept at zero. If p lies inside a certain region $R_m(\beta_1, \ldots, \beta_m)$ involving m angularities, the following procedure is followed

- The set of daughter regions involving $m - 1$ angularities, obtained by removing any single angularity from $R_m(\beta_1, \ldots, \beta_m)$, is determined.

- The shortest Euclidean distance in the space spanned by $\ell_{\alpha_1}, \ldots, \ell_{\alpha_n}$ from the point p towards each daughter region is determined using the method of Lagrange multipliers [267]. These distances are translated to a number between 0 and 1 through eq. (7.35), where the initial and final points x_i and x_f correspond to the distances where the power corrections are 10% and 50% respectively. The result of this procedure is denoted by $\tilde{a}_m(\beta_1, \ldots, \beta_m; \beta_j)$, where the angularity after the semicolon again indicates the angularity that is involved in the parent region, but not in the daughter region.

- The coefficient of the region $R_m(\beta_1, \ldots, \beta_m)$ is defined through

$$a_m(\beta_1, \ldots, \beta_m) = 1 - \max_j \left[\tilde{a}_m(\beta_1, \ldots, \beta_m; \beta_j) \right], \qquad (7.37)$$

and a preliminary weight $b_{m-1}(\gamma_1, \ldots, \gamma_{m-1}; \beta_i)$ is assigned to each of the m daughter regions $R_{m-1}(\gamma_1, \ldots, \gamma_{m-1})$. The β_i after the semi-colon in this case indicates the angularity that should be added to the set $\{\gamma_1, \ldots, \gamma_{m-1}\} \subset \{\beta_1, \ldots, \beta_m\}$ to recover the set of angularities $\{\beta_1, \ldots, \beta_m\}$ on which the parent region depends. These preliminary weights are given by

$$b_{m-1}(\gamma_1, \ldots, \gamma_{m-1}; \beta_i) = \frac{\tilde{a}_m(\beta_1, \ldots, \beta_m; \beta_i) \left[1 - a_m(\beta_1, \ldots, \beta_m) \right]}{\sum_j \left[\tilde{a}_m(\beta_1, \ldots, \beta_m; \beta_j) \right]} .$$
$$(7.38)$$

- For each of the daughter regions R_{m-1}, the steps above are repeated in order to determine the transition variables a_{m-1}. The only notable difference is that the right-hand side of eq. (7.37) is to be multiplied by a factor $0 \leq \tilde{x} \leq 1$, given by the sum of all the preliminary weights that the region under consideration might have inherited from all of its parent regions. For a region $R_{m-1}(\gamma_1, \ldots, \gamma_{m-1})$ this factor is then given by

$$\tilde{x} = \sum_i b_{m-1}(\gamma_1, \ldots, \gamma_{m-1}; \beta_i) . \qquad (7.39)$$

This procedure is repeated until all regions from R_m down to R_2 have been considered. The transition variables of the regions $R_1(\beta_i)$ are then given by the sum of all preliminary weights

$$a_1(\beta_i) = \sum_j b_1(\beta_i; \beta_j) , \qquad (7.40)$$

they might have inherited from any of their parent regions. After all transition variables have been determined, the cumulative distribution can be obtained through eq. (7.33). Due to the finite bin size, the cumulative distribution turns out to slightly decrease towards the fixed-order region in a small number of bins. To ensure these binning effects do not lead to negative spectra upon differentiation, any such bins are set equal to the average of their neighboring bins.
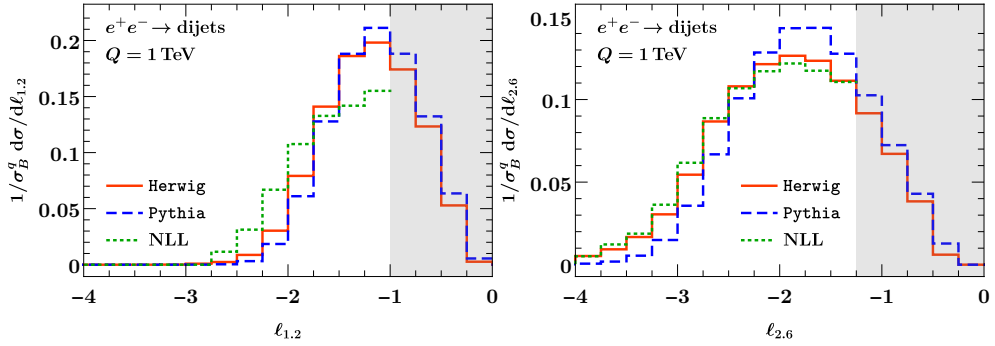
Figure 7.4 The `Herwig` (solid red), `Pythia` (dashed blue) and analytical NLL (dotted green) predictions for the $\ell_{1.2}$ (left panel) and $\ell_{2.6}$ (right panel) distributions. The fixed-order region has been grayed out and the analytical results have been normalized to the fraction of the area of the `Herwig` results that lies to the left of that region.

7.3 Results

The results of the reweighing procedure described in sec. 7.1.2 for both analytically and numerically obtained resummed cross sections are presented in this section. Comparisons of reweighed cross sections with directly computed cross sections are gathered in sec. 7.3.1. The results for the goodness-of-fit parameter, which serve to assess the benefit of increasingly differential resummed cross sections, are shown in sec. 7.3.2. Most numerical results are obtained from `Herwig 7.1.4`, for leading-order $e^+e^- \to$ dijets (excluding bottom and top quark jets) at a center-of-mass energy $Q = 1$ TeV. The final-state parton shower is turned on, but the hadronization and initial-state QED radiation are switched off. For comparison, corresponding results from `Pythia 8.240` are used as well. Unless indicated otherwise, 4-body phase space is used in the reweighing procedure and the set of angularities $\alpha_i = 0.2 \times s$ with $s = 1, 2, \ldots, 15$ is considered. The differential cross sections obtained from `Herwig`, `Pythia` and flat k-body phase space are acquired through the generation of 10^7 events. In the implementation of the analytical results, the value of α_s is kept constant below 2 GeV in order to avoid the Landau pole.

7.3.1 Reweighed results

The single-differential angularity distributions obtained by using either `Herwig`, `Pythia` or the analytic method described in sec. 7.2 are compared in fig. 7.4 for two representative angularities $\ell_{1.2}$ (left panel) and $\ell_{2.6}$ (right panel). The
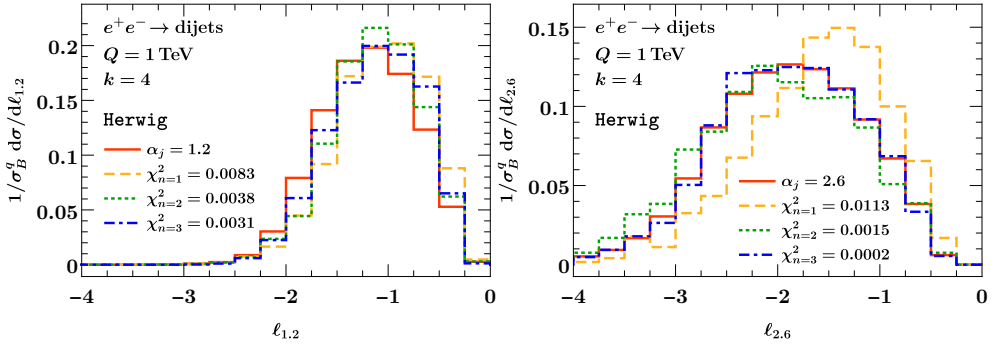
Figure 7.5 Two examples of the reweighing procedure using `Herwig` for $\ell_{1.2}$ (left panel) and $\ell_{2.6}$ (right panel). The dashed yellow, dotted green and dash-dotted blue curves depict the results for reweighing with $n = 1$, $n = 2$ and $n = 3$ angularities respectively. The red curve shows the distribution directly obtained from `Herwig`.

results for `Herwig` and `Pythia` are in good agreement with one another. The analytical result agrees very well with the numerical results for the angularity $\ell_{2.6}$, but shows some deviations for $\ell_{1.2}$. The reason for this is that the re-summation region in phase space is very narrow in the latter case compared to the former, so that the limited number of bins leads to larger numerical discrepancies.

The reweighing procedure is performed using the optimal set I_n^{opt} of angularities that minimizes the global goodness-of-fit variable in eq. (7.6). The results for reweighing with $n = 1, 2$ and 3 angularities are shown in fig. 7.5 by the dashed yellow, dotted green and dash-dotted blue curves respectively. The optimal sets of angularities are given by $I_1^{\text{opt}} = \{0.8\}$, $I_2^{\text{opt}} = \{0.2, 1.8\}$ and $I_3^{\text{opt}} = \{0.2, 1.4, 2.8\}$. The resulting global goodness-of-fit χ_n^2 is indicated for each number of angularities n used to reweigh with. The solid red curves represent the single-differential resummed result directly obtained from `Herwig`. The left panel depicts the results for $\alpha_j = 1.2$ and the right panel shows the results for $\alpha_j = 2.6$. For $\alpha_j = 1.2$, reweighing with an increasing number of angularities does not provide a significant improvement. For $\alpha_j = 2.6$, however, the improvement from reweighing with two angularities over reweighing with a single angularity is substantial.

The corresponding set of plots obtained by the analytic resummation is shown in fig. 7.6. The optimal sets I_n^{opt} as determined by `Herwig` are used and the total set of considered angularities is restricted to $\alpha_i = 0.2 \times s$ with $s = 6, 7, \ldots, 15$. This restriction is imposed because angularities with lower parameters α_i tend
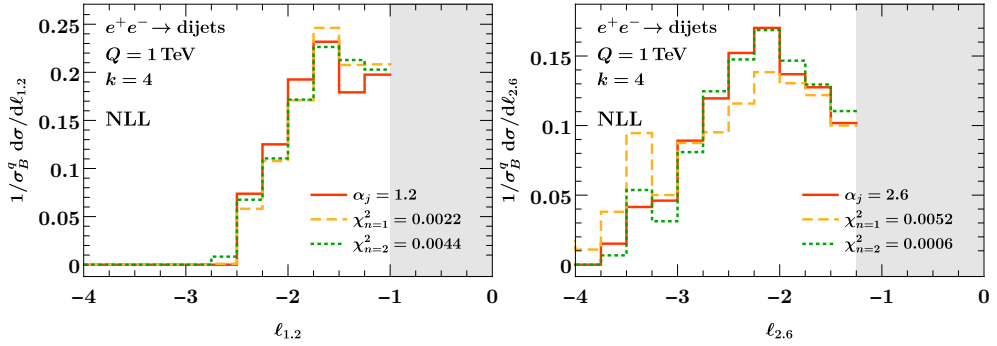
Figure 7.6 Two examples of the reweighing procedure using analytic predictions for $\ell_{1.2}$ (left panel) and $\ell_{2.6}$ (right panel). The dashed yellow and dotted green curves depict the results for reweighing with $n = 1$ and $n = 2$ angularities respectively. The red curve shows the distribution directly obtained by projecting down from the three-angularity cross section. The fixed-order region is grayed out.

to peak closer to (or even in) the fixed-order region, which is not included in the analytical results. Considering a restricted set of angularities then ensures that a sufficient number of bins are populated also for lower values of α_i.

All distributions that enter in these plots are obtained from projecting the resummed result differential in three angularities with angularity exponents $\{\alpha_j, 1.4, 2.8\}$ down to cross sections involving either one or two angularities. For example, the resummed cross section that is used in the reweighing procedure leading to the dotted green line in the left panel in fig. 7.6 is obtained through the projection

$$\frac{\mathrm{d}\sigma_{\mathrm{resum}}}{\mathrm{d}\ell_{\alpha_{1.4}} \, \mathrm{d}\ell_{\alpha_{2.8}}} = \int \mathrm{d}\ell_{\alpha_j} \, \frac{\mathrm{d}\sigma_{\mathrm{resum}}}{\mathrm{d}\ell_{\alpha_j} \, \mathrm{d}\ell_{\alpha_{1.4}} \, \mathrm{d}\ell_{\alpha_{2.8}}} \, . \tag{7.41}$$

These projections turn out to deviate somewhat from the corresponding resummed cross section obtained from a direct analytic calculation, i.e. without any projection. This discrepancy is expected to be largely due to binning issues. As described in sec. 7.2.1, the number of distinct kinematic regions in phase space increases dramatically when cross sections differential in more angularities are considered. The result of the differential cross section in (the center of) each bin is obtained by determining the cumulative cross section on the edges of the bin[3] and taking a numerical derivative. Due to the rela-

---

[3]The use of cumulative cross sections is required to, at least theoretically, enable the recovery of the inclusive cross section [103, 172, 173]. This issue is discussed in more detail in sec. 4.3.5.
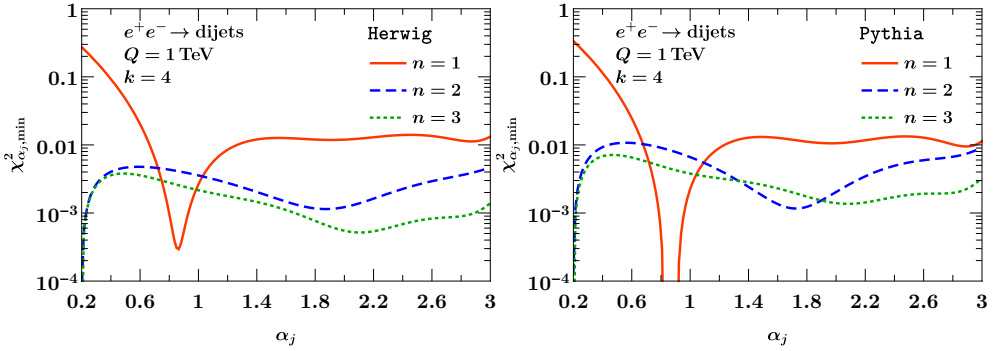
Figure 7.7 The goodness-of-fit $\chi^2_{\alpha_j}$ from the reweighing procedure with $n = 1$ (solid red), $n = 2$ (dashed blue) and $n = 3$ (dotted green) angularities. In each case, the optimal set I_n^{opt} of angularities is used. The left panel shows the results from `Herwig` and the right panel the analogous results from `Pythia`.

tively small number of bins and the increasing number of kinematic regions, situations in which the edges and the center of a bin lie in different kinematic regions might occur. In these cases, the prediction of the spectrum (at the center of the bin) is determined from input provided by cumulative distributions obtained from factorization formulas that are not valid at that point. As this is a binning issue, the effect is expected to diminish when a larger number of bins is considered. In order to be able to focus solely on the differences that arise due to reweighing with a different number of angularities, the projected distributions are used for the analytic results. The results in fig. 7.6 obtained in this manner then show a similar behavior to those in fig. 7.5. For $\ell_{\alpha_{1.2}}$ (left panel), the improvement from reweighing with one angularity to reweighing with two angularities is not significant. For $\ell_{\alpha_{2.6}}$ (right panel), this improvement, reflected by the global goodness-of-fit χ^2, is about an order of magnitude. The result for reweighing with $n = 4$ angularities is not shown since the severity of the aforementioned binning issue increases for cross sections involving more angularities, causing the results for $n = 4$ to be unreliable.

7.3.2 Optimal reweighing improvement

To determine the maximal degree to which the resummation of n angularities can be used to approximate cross sections differential in a single angularity, the optimal set I_n^{opt} of angularities that minimizes the global χ^2 from eq. (7.6) is used. Up to $n = 3$ angularities, all possible sets I are considered in order to find the global minimum, denoted by $\chi^2_{\min}$. For $n = 4$ and $n = 5$ angularities, this minimum is found by starting from the optimal set I_{n-1}^{opt} for $n - 1$
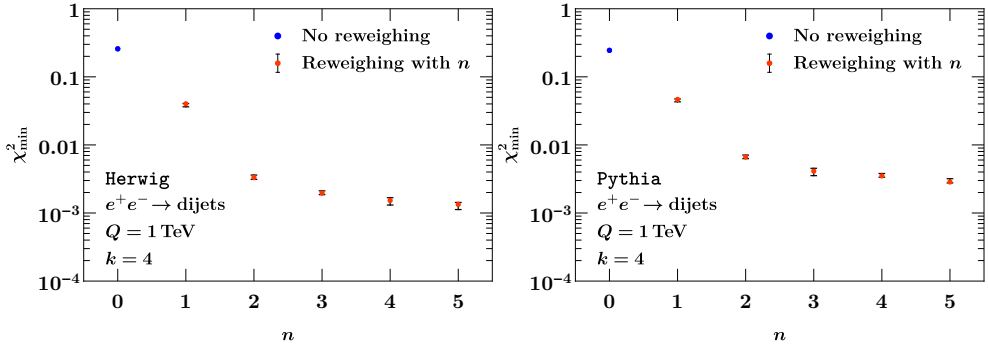
Figure 7.8 The global minimum $\chi^2_{\min}$ for reweighing with $n = 1, \ldots, 5$ angularities using `Herwig` (left panel) and `Pythia` (right panel). The value of χ^2 at $n = 0$ (blue dot) shows the result from pure flat phase space, without any reweighing.

angularities and iteratively determining the angularity whose addition to I^{opt}_{n-1} leads to a minimum in χ^2. This last method has been verified by applying it to $n = 3$, for which it yields results that are very close to the global minimum. The value of the global minimum $\chi^2_{\min}$ is rather sensitive to statistical fluctuations, owing to the finite size of the Monte Carlo samples distributed over 16^{n+1} bins. Furthermore, it is not expected to follow a Gaussian distribution. To obtain an estimate of the statistical uncertainty, the reweighing procedure is performed with 11 replicas of the 10^6 events. The median of the 11 values of $\chi^2_{\min}$ obtained in this way is taken as the central prediction and the spread of the 7 most central results as the statistical uncertainty, roughly corresponding to one standard deviation.

The individual $\chi^2_{\alpha_j}$ from eq. (7.5) that are determined by reweighing with the optimal set I^{opt}_n of angularities are called $\chi^2_{\alpha_j,\min}$. Fig. 7.7 shows the improvement obtained for cross sections differential in a single angularity ℓ_{α_j} through reweighing with the optimal set of $n = 1, 2, 3$ angularities using either `Herwig` (left) or `Pythia` (right). The results for the goodness-of-fit $\chi^2_{\alpha_j,\min}$ shown here correspond to the median of the results of all 11 replicas. Reweighing with $n = 1$ angularity using `Pythia` leads to the same optimal set $I^{\mathrm{opt}}_1 = \{0.8\}$ for each of the 11 replicas, so that $\chi^2_{0.8,\min}$ vanishes. Since the optimal angularity for `Herwig` is not the same in each of the 11 replicas, this behavior is absent in the left plot. For $n = 2$ and $n = 3$, however, $\chi^2_{0.2,\min}$ vanishes since $\alpha_i = 0.2$ is always part of the optimal sets I^{opt}_2 and I^{opt}_3. Reweighing with $n = 2$ angularities is found to perform substantially better than reweigh-
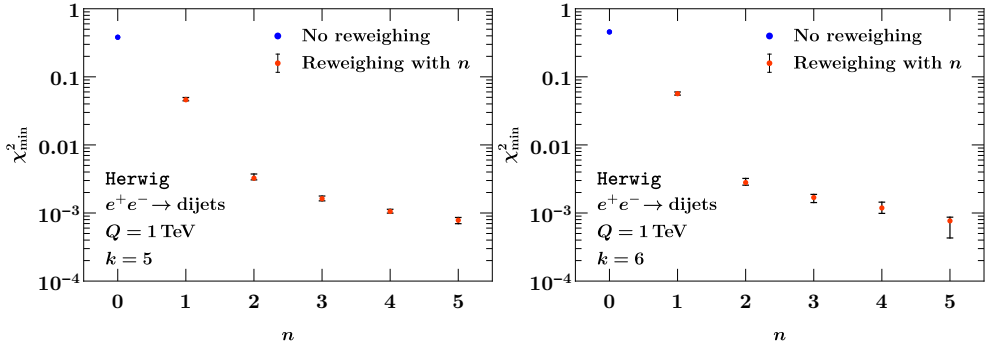
Figure 7.9 The global minimum $\chi^2_{\min}$ for reweighing with $n = 1, \ldots, 5$ angularities from 5-body (left) and 6-body (right) phase space using `Herwig`. The value of χ^2 at $n = 0$ (blue dot) shows the result from pure flat phase space, without any reweighing.

ing with only a single angularity for all target angularities ℓ_{α_j} except those very close to angularities occurring in the optimal set I_1^{opt}. For $n = 3$, there is a non-negligible, but less significant, improvement over $n = 2$.

In fig. 7.8, the global minimum goodness-of-fit $\chi^2_{\min}$ is shown for $n = 1, \ldots, 5$. The left and right panels again contain results obtained using `Herwig` and `Pythia` respectively. The result at $n = 0$ (the blue dot) represents the description of angularity distributions by predictions without any reweighing, i.e. from pure flat phase space, and provides a reference value for the reweighed results. The median values are shown as red dots and the black error bars correspond roughly to one standard deviation, obtained using the procedure described above. Reweighing with two angularities is found to improve substantially over reweighing with a single angularity, while reweighing with three angularities improves only slightly over reweighing with two angularities. The benefit of reweighing with $n = 4$ or $n = 5$ angularities becomes increasingly smaller. The left and right panel in fig. 7.9 show analogous results for $\chi^2_{\min}$, obtained by using 5- and 6-body flat phase space respectively. While the qualitative behavior is largely the same, there are some numerical differences. Specifically, the larger number of particles worsens the sampling of the collinear and soft regions of phase space relevant for angularities and hence increases the statistical fluctuations, reflected by the larger uncertainties. The qualitative behavior of the displayed results has been verified to be similar for different center-of-mass energies $Q = 200$ GeV and $Q = 4$ TeV.

7.3.3 Conclusions

In this chapter, the benefits and limitations of joint resummation have been addressed, using as an example the simultaneous resummation of n angularities in e^+e^- collisions. Specifically, the degree to which resummed cross sections differential in n angularities can be used to reproduce cross sections differential in a single, different angularity, was investigated. This was done through a procedure in which a flat phase-space generator is reweighed by the resummed cross section involving n angularities, which is then compared against the direct result for various single-differential cross sections.

The resummed cross sections are obtained from both Monte Carlo parton showers (`Herwig` and `Pythia`) and through the analytic method developed in sec. 7.2. Although a framework for the simultaneous resummation of two angularities was already described in refs. [108, 132, 133], identifying all the phase space regimes and relevant modes, and smoothly connecting them through the estimation of power corrections significantly increases the complexity of the method for three or more angularities.

An order-of-magnitude improvement was found when reweighing by distributions involving two angularities over reweighing with a single-angularity distribution, demonstrating the benefit of joint resummation. Reweighing with an increasing number of angularities yields some further improvement, albeit with an increasingly diminishing effect. Augmenting Monte Carlo parton showers by analytic resummation at NLL is probably not very beneficial due to the sizable perturbative uncertainty at this order. Matching the NLL results to a fixed-order calculation, or performing the resummation at NNLL would likely improve this. The presented setup can in principle also be extended to hadronic collisions with final-state jets. In that case, gluon jets also have to be considered and non-global logarithms [140] will arise from soft radiation that simultaneously contributes to the angularities (measured on the jets) and the out-of-jet region.

8

Conclusions

As the accuracy of measurements at particle colliders such as the LHC increases, ever more exclusive final states can be considered. To match the demand of current experiments, precise predictions of increasingly differential cross sections are required. When multiple observables that constrain QCD radiation are measured on a particular final state, logarithms of the ratios of their corresponding scales occur in the cross section. When these scales are widely separated, the logarithms grow large and require resummation.

The research described in this thesis is aimed at both improving the resummation accuracy of some existing frameworks, as well as developing new methods for the simultaneous resummation of multiple types of logarithms. The considered measurements are sensitive to infrared (soft and collinear) radiation that arises in the context of QCD, which was addressed in chap. 2. By using SCET (discussed in chap. 3), factorization formulas that separate the various energy scales may be obtained. Through the renormalization group evolution of the ingredients in such a factorization, the large logarithms of the ratios of said scales may be resummed.

The simultaneous resummation of logarithms involving the transverse momentum q_T and logarithms involving beam thrust $\mathcal{T}$ was performed at NNLL accuracy and matched to the NLO fixed-order result in chap. 4. The matching of the various regions of phase space, each described by a different factorization theorem, was carried out through the use of profile scales that smoothly interpolate between them, by introducing a regime parameter. Furthermore, a new hybrid scale choice was used in order to perform the resummation of logarithms of q_T in impact parameter space, while transitioning towards the fixed-order region as a function of the value of q_T instead of its Fourier-conjugate. The resummed double-differential cross section was shown to reproduce both single-differential cross sections upon integration over the other variable. Since $\mathcal{T}$ has been measured in bins of q_T, the results obtained in this chapter are of some direct phenomenological interest. Furthermore, the presented results clearly

show that resumming only logarithms involving either q_T or $\mathcal{T}$ provides a poor description of the double-differential cross section. The Monte Carlo generator Geneva uses $\mathcal{T}$ as its jet resolution parameter and would benefit from the additional resummation of logarithms of q_T.

In chap. 5, a setup for the joint resummation of transverse momentum and threshold logarithms in heavy color-singlet production was developed. The method is not limited to any order and currently all ingredients are available for resummation at N^{3}LL accuracy. The factorization theorems valid in the various regions of phase space were matched to each other and to the fixed-order result through the additive procedure also employed in chap. 4. The described method may be of some importance to Higgs production or the possible production of supersymmetric particles, but can also be used to describe heavy-particle production in the presence of a veto on jets.

A novel factorization formula for processes occurring near the kinematic threshold was derived in chap. 6. In contrast with the traditional soft threshold factorizations, this new factorization also holds in the limit of large rapidities for generic invariant masses, which is directly accessible at the LHC. It describes the complete soft and collinear singular structure and includes the nondiagonal partonic channels. This generalized threshold factorization was checked against all currently available results and was found to improve over the soft threshold factorization. It may be used to improve a number of theoretical predictions and to resum the large logarithms that occur when one of the PDFs is probed at large Bjorken-x.

In chap. 7, a framework was developed that allows for the simultaneous resummation of an arbitrary number of e^+e^- event shapes, known as angularities, at NLL accuracy. By reweighing a flat phase space generator by these resummed results, or those obtained from Herwig or Pythia, the degree to which cross sections differential in a single, different angularity can be predicted was studied. Reweighing with resummed cross sections involving two angularities was found to improve by an order of magnitude over reweighing with a single-differential resummed cross section. This highlights the added benefit of joint resummations, such as the ones presented in chaps. 4 and 5. Reweighing with resummed cross sections involving three or more angularities was found to provide only a small additional improvement. Although the benefit of including the analytic resummation at NLL accuracy in Monte Carlo parton showers is likely to be small, the corresponding NNLL resummation of n angularities might lead to increasingly precise parton showers. This is important for Machine Learning

techniques applied to the field of jet substructure, which often rely on samples from these Monte Carlo parton showers.

The research presented in this thesis involves the development of precise *and* multi-differential cross section predictions. As the Standard Model is tested with an ever-increasing accuracy, such predictions are vital in the current search for the faintest hints of new physics from beyond the Standard Model that might hide within the experimental data.

A

Plus distributions and Fourier transforms

The plus distribution $[f(x)]_+^{x_0} \equiv [\theta(x)f(x)]_+^{x_0}$ of a function $f(x)$, which is less singular than $1/x^2$ for $x \to 0$, is defined to be equal to its argument for $x \neq 0$ and to integrate to zero on the interval between 0 and its boundary condition. Adopting the notation and conventions from ref. [154], these defining conditions read

$$\left[f(x)\right]_+^{x_0} = f(x) \quad \text{if} \quad x \neq 0 \qquad \text{and} \qquad \int_0^{x_0} \mathrm{d}x \left[f(x)\right]_+^{x_0} = 0 \,. \qquad \text{(A.1)}$$

The definition of the plus distribution can then be written as

$$\left[f(x)\right]_+^{x_0} \equiv \lim_{\epsilon \to 0} \left[\theta(x - \epsilon) \, f(x) + \delta(x - \epsilon) \int_{x_0}^{x} \mathrm{d}x' \, f(x') \right]. \qquad \text{(A.2)}$$

Plus distributions with different boundary conditions x_0 and x_1 are related through

$$\left[f(x)\right]_+^{x_0} = \left[f(x)\right]_+^{x_1} + \delta(x) \int_{x_0}^{x_1} \mathrm{d}x' \, f(x') \,. \qquad \text{(A.3)}$$

For the specific choice $x_0 = 1$, the superscript is left implicit. Integrating the plus distribution against a test function $g(x)$ gives

$$\int_{-\infty}^{x_{\max}} \mathrm{d}x \left[f(x)\right]_+^{x_0} g(x) = \int_0^{x_{\max}} \mathrm{d}x \, f(x) \left(g(x) - g(0)\right) + g(0) \int_{x_0}^{x_{\max}} \mathrm{d}x \, f(x) \,, \qquad \text{(A.4)}$$

from which it follows that the integral over the plus distribution is given by

$$\int_{-\infty}^{x_{\max}} \mathrm{d}x \left[f(x)\right]_+^{x_0} = \int_{x_0}^{x_{\max}} \mathrm{d}x \, f(x) \,. \qquad \text{(A.5)}$$

The plus distributions that occur most often are defined as

$$\mathcal{L}_n(x) \equiv \left[\frac{\ln^n(x)}{x}\right]_+ \qquad \text{and} \qquad \mathcal{L}^a(x) \equiv \left[\frac{1}{x^{1-a}}\right]_+, \qquad (A.6)$$

for $a > -1$ and integer $n \geq 0$. The $\mathcal{L}_n(x)$ appear in the useful expansion

$$\frac{\theta(x)}{x^{1+\epsilon}} = -\frac{1}{\epsilon}\,\delta(x) + \mathcal{L}_0(x) - \epsilon\,\mathcal{L}_1(x) + \mathcal{O}(\epsilon^2)\,. \qquad (A.7)$$

The two plus distributions in eq. (A.6) are related through

$$\mathcal{L}_n(x) = \frac{\mathrm{d}^n}{\mathrm{d}a^n}\mathcal{L}^a(x)\Big|_{a=0}\,. \qquad (A.8)$$

Their arguments may be rescaled by a constant $\lambda > 0$ through the relations

$$\lambda\mathcal{L}_n(\lambda x) = \sum_{k=0}^n \binom{n}{k}\ln^k(\lambda)\,\mathcal{L}_{n-k}(x) + \frac{\ln^{n+1}(\lambda)}{n+1}\,\delta(x)\,,$$

$$\lambda\mathcal{L}^a(\lambda x) = \lambda^a(x) + \frac{\lambda^a - 1}{a}\,\delta(x)\,. \qquad (A.9)$$

The convolution between two $\mathcal{L}^a(x)$ is given by

$$\int \mathrm{d}x'\,\mathcal{L}^a(x - x')\,\mathcal{L}^b(x') = \left(\mathcal{L}^{a+b}(x) + \frac{\delta(x)}{a+b}\right)V(a,b)$$

$$+ \left(\frac{1}{a} + \frac{1}{b}\right)\mathcal{L}^{a+b}(x) - \frac{1}{b}\,\mathcal{L}^a(x) - \frac{1}{a}\mathcal{L}^b(x)\,, \quad (A.10)$$

where

$$V(a,b) \equiv \frac{\Gamma(a)\Gamma(b)}{\Gamma(a+b)} - \frac{1}{a} - \frac{1}{b}\,. \qquad (A.11)$$

The convolutions between an $\mathcal{L}^a(x)$ and an $\mathcal{L}_n(x)$ or between two $\mathcal{L}_n(x)$ can be obtained by taking derivatives according to eq. (A.3). The explicit results can be found in ref. [154] and are not repeated here.

The particular two-dimensional plus distribution, originally defined in ref. [108], that is required in some intermediate steps is given by

$$\mathcal{L}_\Delta(x_1, x_2) \equiv \lim_{\epsilon \to 0} \frac{\mathrm{d}}{\mathrm{d}x_1} \frac{\mathrm{d}}{\mathrm{d}x_2} \left[\theta(x_2 - x_1^2)\,\theta(x_1 - \epsilon)\ln x_1\,(\ln x_2 - \ln x_1)\right.$$

$$\left. + \frac{1}{4}\,\theta(x_1^2 - x_2)\,\theta(x_2 - \epsilon^2)\ln^2 x_2\right]. \qquad (A.12)$$

For distributions with dimensionful arguments in one spatial dimension, the shorthands

$$\mathcal{L}_n(k, \mu) \equiv \frac{1}{\mu} \mathcal{L}_n\left(\frac{k}{\mu}\right) \qquad \text{and} \qquad \mathcal{L}^a(k, \mu) \equiv \frac{1}{\mu} \mathcal{L}^a\left(\frac{k}{\mu}\right), \tag{A.13}$$

are employed. Furthermore, a useful distribution occurring in evolution functions can be defined as

$$\mathcal{V}_a(x) \equiv \frac{e^{-\gamma_E a}}{\Gamma(1+a)} \left(a\mathcal{L}^a(x) + \delta(x)\right). \tag{A.14}$$

For dimensionful arguments, the definition

$$\mathcal{V}_a(k, \mu) \equiv \frac{1}{\mu} \mathcal{V}_a\left(\frac{k}{\mu}\right), \tag{A.15}$$

is used in accordance with eq. (A.13). For identical μ, these obey the useful group property

$$\int d\ell \, \mathcal{V}_a(k - \ell, \mu) \, \mathcal{V}_b(\ell, \mu) = \mathcal{V}_{a+b}(k, \mu). \tag{A.16}$$

Distributions with different arguments μ are related through

$$\mathcal{V}_a(k, \mu) = \left(\frac{\mu'}{\mu}\right)^a \mathcal{V}_a(k, \mu'). \tag{A.17}$$

For the plus distributions in two spatial dimensions, the conventions of ref. [163] are adopted. Defining $k_T^2 \equiv |\vec{k}_T|^2 \geq 0$, the two-dimensional delta function and plus distributions are given by

$$\delta(\vec{k}_T) = \frac{1}{\pi} \delta(k_T^2),$$

$$\mathcal{L}_n(\vec{k}_T, \mu) = \frac{1}{\pi\mu^2} \left[\frac{\mu^2}{k_T^2} \ln^n\left(\frac{k_T^2}{\mu^2}\right)\right]_+^{\mu} \equiv \frac{1}{\pi\mu^2} \mathcal{L}_n\left(\frac{k_T^2}{\mu^2}\right),$$

$$\mathcal{L}^a(\vec{k}_T, \mu) = \frac{1}{\pi\mu^2} \left[\left(\frac{k_T^2}{\mu^2}\right)^{a-1}\right]_+^{\mu} \equiv \frac{1}{\pi\mu^2} \mathcal{L}^a\left(\frac{k_T^2}{\mu^2}\right). \tag{A.18}$$

The Fourier transformation, connecting an n-dimensional momentum p to its position-space conjugate x, is defined as

$$f(p) = \int \frac{d^n x}{(2\pi)^n} e^{+ip \cdot x} \, \tilde{f}(x) \qquad \text{and} \qquad \tilde{f}(x) = \int d^n p \, e^{-ip \cdot x} \, \tilde{f}(x). \tag{A.19}$$

For functions depending on the two-dimensional momentum $\vec{k}_T$ (or its conjugate $\vec{b}_T$), that exhibit azimuthal symmetry, i.e. $f(\vec{k}_T) = f(k_T)$, this simplifies to

$$f(k_T) = \frac{1}{2\pi} \int_0^\infty \mathrm{d}b_T\, b_T\, J_0(b_T k_T)\, \tilde{f}(b_T)\,,$$

$$\tilde{f}(b_T) = 2\pi \int_0^\infty \mathrm{d}k_T\, k_T\, J_0(b_T k_T)\, f(k_T)\,, \qquad (A.20)$$

where $J_0(x)$ signifies the 0th-order Bessel function of the first kind. Azimuthally symmetric functions g, differential in $\vec{k}_T$, obey

$$\frac{\mathrm{d}g}{\mathrm{d}\vec{k}_T} = \frac{1}{2\pi k_T} \frac{\mathrm{d}g}{\mathrm{d}k_T} \qquad \text{and} \qquad \tilde{g}(\vec{b}_T) = \tilde{g}(b_T)\,, \qquad (A.21)$$

where the lack of any argument for $\mathrm{d}g/\mathrm{d}\vec{k}_T$ is conventional. The Fourier transforms of the various $\mathcal{L}_n(\vec{k}_T, \mu)$ may be found in ref. [163]. The transforms of the distributions required for this thesis are explicitly given by

$$\int \mathrm{d}^2\vec{k}_T\, e^{-i\vec{k}_T \cdot \vec{b}_T}\, \delta(\vec{k}_T) = 1\,,$$

$$\int \mathrm{d}^2\vec{k}_T\, e^{-i\vec{k}_T \cdot \vec{b}_T}\, \mathcal{L}_0(\vec{k}_T, \mu) = -L_b\,,$$

$$\int \mathrm{d}^2\vec{k}_T\, e^{-i\vec{k}_T \cdot \vec{b}_T}\, \mathcal{L}_1(\vec{k}_T, \mu) = \frac{1}{2}L_b^2\,,$$

$$(A.22)$$

where

$$L_b \equiv \ln\left(\frac{b_T^2 \mu^2}{b_0^2}\right) \qquad \text{with} \qquad b_0 \equiv 2e^{-\gamma_E} \approx 1.12291\ldots\,. \qquad (A.23)$$

Perturbative functions

The various perturbative functions appearing throughout the factorization theorems in this thesis are summarized here. Different functions of the same type are denoted by the same symbol but can be distinguished through their arguments. For example, the inclusive soft function and the TMD soft function are denoted by $S_{ij}(k, \mu)$ and $S_{ij}(\vec{k}_T, \mu, \nu)$ respectively. In cases where the arguments of two different functions are equal, or where confusion may arise, different symbols will be used. For example, the modified beam function from chap. 6 is written with a hat. Fourier-transformed functions are denoted by a tilde, e.g. $\tilde{S}_{ij}(b_T, \mu, \nu)$ represents the TMD soft function in impact parameter space.

B.1 Hard functions

The Wilson coefficient matching the quark current in QCD onto SCET was computed to $\mathcal{O}(\alpha_s)$ in refs. [93,268] and given in eq. (3.162). The hard function involved in Drell-Yan cross sections differential in the invariant mass Q is then given by [99]

$$H_{ij}(Q, \mu) = \sum_q \frac{\mathrm{d}\sigma_B^q}{\mathrm{d}Q} \left(\delta_{iq}\delta_{j\bar{q}} + \delta_{i\bar{q}}\delta_{jq} \right) |C_{q\bar{q}}(Q^2, \mu)|^2, \qquad \text{(B.1)}$$

where the sum runs over $q = \{u, d, c, s, b\}$ and the squared matching coefficient is explicitly given by

$$|C_{q\bar{q}}(Q^2, \mu)|^2 = 1 + \frac{\alpha_s C_F}{2\pi} \left[-\ln^2\left(\frac{Q^2}{\mu^2}\right) + 3\ln\left(\frac{Q^2}{\mu^2}\right) - 8 + \frac{7\pi^2}{6} \right]. \qquad \text{(B.2)}$$

up to corrections of $\mathcal{O}(\alpha_s^2)$. The differential Born cross section for $q\bar{q} \to Z/\gamma^* \to \ell^+\ell^-$ is given by

$$\frac{\mathrm{d}\sigma_B^q}{\mathrm{d}Q} = \frac{8\pi\alpha_{\mathrm{em}}^2}{3N_c E_{\mathrm{cm}}^2 Q} \left[Q_q^2 + \frac{(v_q^2 + a_q^2)(v_\ell^2 + a_\ell^2) - 2Q_q v_q v_\ell (1 - m_Z^2/Q^2)}{(1 - m_Z^2/Q^2)^2 + m_Z^2 \Gamma_Z^2/Q^4} \right], \qquad \text{(B.3)}$$

where α_{em} is the fine-structure constant, N_c is the number of colors, Q_q is the quark charge in units of $|e|$, $v_{\ell,q}$ and $a_{\ell,q}$ are the standard vector and axial couplings of the leptons and quarks, and m_Z and Γ_Z are the mass and width of the Z boson. If $q\bar{q} \to \gamma^*$ is considered, only the first term in square brackets contributes.

The hard function for gluon-fusion Higgs production in the limit $m_H^2 \ll 4m_t^2$ is given by

$$H_{ij}(m_t, m_H, \mu) = \sigma_B^{ggH} \left|\alpha_s \, C_t(m_t, \mu)\right|^2 \delta_{ig}\delta_{jg} \left|C_{gg}(m_H, \mu)\right|^2, \tag{B.4}$$

and can be distinguished from the hard function for Drell-Yan through its arguments. The Born cross section is given by

$$\sigma_B^{ggH} = \frac{1}{72\pi v^2(N_c^2 - 1)}, \tag{B.5}$$

where $v^2 = 1/(\sqrt{2}G_F) \approx 246.22\,\text{GeV}$ is the Higgs vacuum expectation value. The Wilson coefficient $C_t(m_t, \mu)$ results from integrating out the top quark in a contact interaction suppressed by v [269–272] and is given by

$$C_t(m_t, \mu) = 1 + \frac{\alpha_s}{4\pi}\left[5C_A - 3C_F\right] + \mathcal{O}(\alpha_s^2). \tag{B.6}$$

The Wilson coefficient C_{gg} is obtained by matching the composite gluon operator onto SCET, leading to [195, 196, 273]

$$C_{gg}(m_H, \mu) = 1 + \frac{\alpha_s C_A}{2\pi}\left[-\ln\left(\frac{m_H^2}{\mu^2}\right) + \frac{7\pi^2}{6}\right] + \mathcal{O}(\alpha_s^2). \tag{B.7}$$

B.2 Beam functions

The virtuality-dependent beam function, also known as inclusive beam function, is matched onto the PDFs through

$$B_i(t, x, \mu) = \sum_j \int_x^1 \frac{dz}{z}\, \mathcal{I}_{ij}(t, z, \mu)\, f_j\left(\frac{x}{z}, \mu\right)\left[1 + \mathcal{O}\left(\frac{\Lambda_{\text{QCD}}^2}{t}\right)\right]. \tag{B.8}$$

The matching coefficients up to $\mathcal{O}(\alpha_s)$ are given by [99, 100, 274]

$$\mathcal{I}_{ij}(t, z, \mu) = \delta_{ij}\,\delta(t)\,\delta(1-z) + \frac{\alpha_s}{4\pi}\left[\delta_{ij}\,\Gamma_0^i\,\mathcal{L}_1(t, \mu^2)\,\delta(1-z)\right.$$
$$\left. + \mathcal{L}_0(t, \mu^2)\,\tilde{P}_{ij}^{(0)}(z) + \delta(t)\,I_{ij}^{(1)}(z)\right], \tag{B.9}$$

where the short-hand notation

$$\tilde{P}_{ij}^{(0)}(z) \equiv P_{ij}^{(0)}(z) - \delta_{ij}\,\delta(1-z)\frac{\gamma_{B,0}^i}{2}\,, \tag{B.10}$$

has been introduced. The coefficients Γ_0^i and $\gamma_{B,0}^i$ of the cusp and non-cusp anomalous dimensions are listed in app. C.2 and the $P_{ij}^{(0)}(z)$ are defined by

$$P_{qq}^{(0)}(z) = 2C_F\,\theta(z)P_{qq}(z)\,, \qquad P_{gq}^{(0)}(z) = 2C_F\,\theta(z)P_{gq}(z)\,, \tag{B.11}$$
$$P_{qg}^{(0)}(z) = 2T_F\,\theta(z)P_{qg}(z)\,, \qquad P_{gg}^{(0)}(z) = 2C_A\,\theta(z)P_{gg}(z) + \beta_0\,\delta(1-z)\,.$$

The Altarelli-Parisi splitting functions are given by

$$P_{qq}(z) = \mathcal{L}_0(1-z)(1+z^2) + \frac{3}{2}\delta(1-z)\,,$$
$$P_{gq}(z) = \frac{1+(1-z)^2}{z}\,,$$
$$P_{qg}(z) = \left((1-z)^2 + z^2\right),$$
$$P_{gg}(z) = 2\mathcal{L}_0(1-z)\frac{(1-z+z^2)^2}{z}\,. \tag{B.12}$$

The finite terms in eq. (B.9) are explicitly given by

$$I_{qq}^{(1)}(z) = 2C_F\left[\mathcal{L}_1(1-z)(1+z^2) - \frac{\pi^2}{6}\delta(1-z) + \left(1-z - \frac{1+z^2}{1-z}\ln(z)\right)\right],$$
$$I_{gq}^{(1)}(z) = 2C_F\left[P_{gq}(z)\ln\left(\frac{1-z}{z}\right) + z\right],$$
$$I_{qg}^{(1)}(z) = 2T_F\left[P_{qg}(z)\left(\ln\left(\frac{1-z}{z}\right) - 1\right) + 1\right], \tag{B.13}$$
$$I_{gg}^{(1)}(z) = 2C_A\left[\mathcal{L}_1(1-z)\frac{2(1-z+z^2)^2}{z} - \frac{\pi^2}{6}\delta(1-z) - P_{gg}(z)\ln(z)\right],$$

where any step-functions forcing $1 \geq z$ and $z \geq 0$ have been left implicit. The 1-loop matching coefficients [205, 275] for the TMD beam function, whose analogous matching onto the PDFs was given in eq. (4.20), are given by

$$\mathcal{I}_{ij}(\omega, \vec{k}_T, z, \mu, \nu) = \delta_{ij}\,\delta(1-z)\,\delta(\vec{k}_T)$$
$$+ \frac{\alpha_s}{4\pi}\left[-\delta_{ij}\left(\Gamma_0^i\ln\left(\frac{\nu}{\omega}\right) + \frac{\gamma_{B,0}^i}{2}\right)\delta(1-z)\,\mathcal{L}_0(\vec{k}_T, \mu)\right.$$
$$\left. + P_{ij}^{(0)}(z)\,\mathcal{L}_0(\vec{k}_T, \mu) + \delta(\vec{k}_T)\,\tilde{I}_{ij}^{(1)}(z)\right], \tag{B.14}$$

where the finite terms include a tilde to distinguish them from those appearing in eq. (B.13). As they do not depend on k_T, their expressions in momentum space and impact parameter space are equal, so this tilde cannot be confused with the Fourier transform. The matching coefficients of the TMD beam function in position space read

$$
\tilde{\mathcal{I}}_{ij}(\omega, b_T, z, \mu, \nu) = \delta_{ij}\,\delta(1-z) + \frac{\alpha_s}{4\pi}\left[\delta_{ij}\left(\Gamma_0^i \ln\left(\frac{\nu}{\omega}\right) + \frac{\gamma_{B,0}^i}{2}\right)\delta(1-z)\,L_b\right.
$$
$$
\left. - P_{ij}^{(0)}(z)\,L_b + \tilde{I}_{ij}^{(1)}(z)\right]. \tag{B.15}
$$

The finite terms are in this case given by

$$
\begin{aligned}
\tilde{I}_{qq}^{(1)}(z) &= 2C_F\,(1-z)\,, & \tilde{I}_{gq}^{(1)}(z) &= 2C_F\,z\,, \\
\tilde{I}_{qg}^{(1)}(z) &= 4T_F\,z(1-z)\,, & \tilde{I}_{gg}^{(1)}(z) &= 0\,,
\end{aligned} \tag{B.16}
$$

where again any $\theta(1-z)$ and $\theta(z)$ have been omitted.

The matching equation for the double-differential beam function was given in eq. (4.6). It is convenient to decompose its matching coefficients as

$$
\mathcal{I}_{ij}(t, z, \vec{k}_T, \mu) = \delta(\vec{k}_T)\,\mathcal{I}_{ij}(t, z, \mu) + \Delta\mathcal{I}_{ij}(t, z, \vec{k}_T, \mu)\,. \tag{B.17}
$$

The $\Delta\mathcal{I}_{ij}$ piece can be interpreted as a correction over the limit $t \ll k_T^2$, where recoil from collinear radiation is power suppressed and the double-differential beam function becomes proportional to $\delta(\vec{k}_T)$. By construction, it vanishes when integrated over $\vec{k}_T$. At 1-loop accuracy, it can be extracted from the full calculation of $\mathcal{I}_{ij}(t, z, \vec{k}_T, \mu)$ [150, 276] and has the compact form

$$
\Delta\mathcal{I}_{ij}(t, z, \vec{k}_T, \mu) = \frac{\alpha_s}{4\pi}\Delta I_{ij}^{(1)}(t, z, \vec{k}_T) + \mathcal{O}(\alpha_s^2)\,,
$$
$$
\Delta I_{ij}^{(1)}(t, z, \vec{k}_T) = \mathcal{L}_0(t, \mu^2)\,\tilde{P}_{ij}^{(0)}(z)\left[\frac{1}{\pi}\,\delta\left(k_T^2 - \frac{1-z}{z}t\right) - \delta(\vec{k}_T)\right]\,, \tag{B.18}
$$

where the plus prescription on the second line may be dropped freely as the term in square brackets vanishes for $t \to 0$. Accumulating over the transverse plane up to $q_T^{\mathrm{cut}} > 0$ leads to the result

$$
\int \mathrm{d}^2\vec{k}_T\,\theta\big[q_T^{\mathrm{cut}} - |\vec{k}_T|\big]\,\Delta I_{ij}^{(1)}(t, z, \vec{k}_T) = -\mathcal{L}_0(t, \mu^2)\,\tilde{P}_{ij}^{(0)}(z)\,\theta\left[(q_T^{\mathrm{cut}})^2 < \frac{1-z}{z}t\right]\,. \tag{B.19}
$$

The modified inclusive (virtuality-dependent) beam function was defined in eq. (6.17) as a projection of the double-differential beam function. This projection implies that the matching coefficients are related through

$$\hat{\mathcal{I}}_{ij}(t, z, \mu) = \int d^2\vec{k}_T \, \mathcal{I}_{ij}\Big(t - \frac{k_T^2}{2}, z, \vec{k}_T, \mu\Big)\,.$$ (B.20)

By defining the perturbative expansion of the matching coefficients as

$$\hat{\mathcal{I}}_{ij}(t, z, \mu) = \sum_{n=0}^{\infty} \Big(\frac{\alpha_s}{4\pi}\Big)^n \hat{\mathcal{I}}_{ij}^{(n)}(t, z, \mu)\,,$$ (B.21)

and solving the RGE from eq. (6.36) order-by-order in α_s, the tree-level and 1-loop matching coefficients are found to be

$$\hat{\mathcal{I}}_{ij}^{(0)}(t, z, \mu) = \delta_{ij}\, \delta(t)\, \delta(1-z)\,,$$

$$\hat{\mathcal{I}}_{ij}^{(1)}(t, z, \mu) = \mathcal{L}_1(t, \mu^2)\, \delta_{ij}\, \Gamma_0^i\, \delta(1-z)$$

$$+ \mathcal{L}_0(t, \mu^2)\Big[P_{ij}^{(0)}(z) - \frac{\gamma_{B0}^i}{2}\, \delta_{ij}\, \delta(1-z)\Big] + \delta(t)\, \hat{I}_{ij}^{(1)}(z)\,.$$ (B.22)

The 2-loop expression is given by

$$\hat{\mathcal{I}}_{ij}^{(2)}(t, z, \mu) = \mathcal{L}_3(t, \mu^2)\, \delta_{ij}\, \frac{(\Gamma_0^i)^2}{2}\, \delta(1-z)$$

$$+ \mathcal{L}_2(t, \mu^2)\, \frac{\Gamma_0^i}{2}\Big[-\Big(\beta_0 + \frac{3}{2}\gamma_{B0}^i\Big)\delta_{ij}\, \delta(1-z) + 3P_{ij}^{(0)}(z)\Big]$$

$$+ \mathcal{L}_1(t, \mu^2)\Big[\Big(-\frac{\pi^2}{6}(\Gamma_0^i)^2 + \frac{\beta_0}{2}\gamma_{B0}^i + \frac{(\gamma_{B0}^i)^2}{4} + \Gamma_1^i\Big)\delta_{ij}\, \delta(1-z)$$

$$- \big(\beta_0 + \gamma_{B0}^i\big)P_{ij}^{(0)}(z) + \big(P_{ik}^{(0)} \otimes P_{kj}^{(0)}\big)(z) + \Gamma_0^i\hat{I}_{ij}^{(1)}(z)\Big]$$

$$+ \mathcal{L}_0(t, \mu^2)\Big[\Big(\zeta_3(\Gamma_0^i)^2 + \frac{\pi^2}{12}\Gamma_0^i\, \gamma_{B0}^i - \frac{\gamma_{B1}^i}{2}\Big)\delta_{ij}\, \delta(1-z)$$

$$+ P_{ij}^{(1)}(z) - \frac{\pi^2}{6}\Gamma_0^i\, P_{ij}^{(0)}(z) - \Big(\beta_0 + \frac{\gamma_{B0}^i}{2}\Big)\hat{I}_{ij}^{(1)}(z)$$

$$+ \big(\hat{I}_{ik}^{(1)} \otimes P_{kj}^{(0)}\big)(z)\Big]$$

$$+ \delta(t)\, \hat{I}_{ij}^{(2)}(z)\,,$$ (B.23)

and the 3-loop matching coefficient reads

$$
\begin{aligned}
\hat{\mathcal{I}}_{ij}^{(3)}(t,z,\mu) = {}& \mathcal{L}_5(t,\mu^2)\,\delta_{ij}\,\frac{(\Gamma_0^i)^3}{8}\,\delta(1-z) \\
& + \mathcal{L}_4(t,\mu^2)\,\frac{5}{8}(\Gamma_0^i)^2\left[-\left(\frac{2}{3}\beta_0 + \frac{\gamma_{B0}^i}{2}\right)\delta_{ij}\delta(1-z) + P_{ij}^{(0)}(z)\right] \\
& + \mathcal{L}_3(t,\mu^2)\,\Gamma_0^i\left[\left(-\frac{\pi^2}{6}(\Gamma_0^i)^2 + \frac{\beta_0^2}{3} + \frac{5}{6}\beta_0\,\gamma_{B0}^i\right.\right. \\
& \qquad\qquad + \frac{(\gamma_{B0}^i)^2}{4} + \Gamma_1^i\Big)\delta_{ij}\delta(1-z) - \left(\frac{5}{3}\beta_0 + \gamma_{B0}^i\right)P_{ij}^{(0)}(z) \\
& \qquad\qquad + \left(P_{ik}^{(0)} \otimes P_{kj}^{(0)}\right)(z) + \frac{\Gamma_0^i}{2}\,\hat{I}_{ij}^{(1)}(z)\bigg] \\
& + \cdots + \delta(t)\,\hat{I}_{ij}^{(3)}(z)\,,
\end{aligned}
\tag{B.24}
$$

where the notation $(g\otimes h)(z) \equiv \int_z^1 \mathrm{d}z'/z'\, g(z')\, h(z/z')$ is used to indicate Mellin convolutions of two functions in z, which are evaluated analytically using the `MT` package [277]. The dots in the 3-loop result indicate terms proportional to $\mathcal{L}_{0,1,2}(t,\mu^2)$. Including these terms is straightforward, but they have been omitted for the sake of readability. The boundary terms $\hat{I}_{ij}^{(n)}(z)$ are not predicted by the RGE, but instead have to be calculated directly from eq. (B.20). At one loop, the relation

$$
\hat{\mathcal{I}}_{ij}^{(1)}(t,z,\mu) = \mathcal{I}_{ij}^{(1)}(t,z,\mu) + \delta(t)\,P_{ij}^{(0)}(z)\ln\frac{2z}{1+z}\,,
\tag{B.25}
$$

holds for all partonic channels. The explicit expressions for the 1-loop finite terms are given by

$$
\begin{aligned}
\hat{I}_{qq}^{(1)}(z) = {}& 2C_F\,\theta(z)\Big[\mathcal{L}_1(1-z)(1+z^2) - \frac{\pi^2}{6}\delta(1-z) + \theta(1-z)(1-z) \\
& \qquad\qquad + P_{qq}(z)\ln\frac{2}{1+z}\Big]\,, \\
\hat{I}_{qg}^{(1)}(z) = {}& 2T_F\,\theta(z)\Big[P_{qg}(z)\ln\frac{2(1-z)}{1+z} + \theta(1-z)\,2z(1-z)\Big]\,, \\
\tilde{I}_{gg}^{(1)}(z) = {}& 2C_A\,\theta(z)\Big[\mathcal{L}_1(1-z)\frac{2(1-z+z^2)^2}{z} - \frac{\pi^2}{6}\delta(1-z) + P_{gg}(z)\ln\frac{2}{1+z}\Big]\,, \\
\hat{I}_{gq}^{(1)}(z) = {}& 2C_F\,\theta(z)\Big[P_{gq}(z)\ln\frac{2(1-z)}{1+z} + \theta(1-z)\,z\Big]\,.
\end{aligned}
\tag{B.26}
$$

The 2-loop quark finite terms are conveniently decomposed by their flavor

structure as

$$\hat{I}^{(2)}_{q_iq_j}(z) = \hat{I}^{(2)}_{\bar{q}_i\bar{q}_j}(z) = \delta_{ij}\,\hat{I}^{(2)}_{qqV}(z) + \hat{I}^{(2)}_{qqS}(z)\,,$$

$$\hat{I}^{(2)}_{q_i\bar{q}_j}(z) = \hat{I}^{(2)}_{\bar{q}_iq_j}(z) = \delta_{ij}\,\hat{I}^{(2)}_{q\bar{q}V}(z) + \hat{I}^{(2)}_{qqS}(z)\,,$$

$$\hat{I}^{(2)}_{q_ig}(z) = \hat{I}^{(2)}_{\bar{q}_ig}(z) = \hat{I}^{(2)}_{qg}(z)\,, \tag{B.27}$$

as was done for the inclusive beam function in refs. [101, 102]. The explicit expressions for the finite terms of the 2-loop matching coefficients may be found in ref. [3].

B.3 Soft functions

The (beam) thrust soft function, also known as the inclusive soft function, is given up to $\mathcal{O}(\alpha_s)$ by [99, 278, 279]

$$S_{ij}(k,\mu) = \delta(k) + \frac{\alpha_s C_i}{2\pi}\left[-8\mathcal{L}_1(k,\mu) + \frac{\pi^2}{6}\delta(k)\right], \tag{B.28}$$

where C_i is equal to either C_F or C_A for $i = q, \bar{q}$ or $i = g$ respectively. The TMD soft function in momentum space, up to $\mathcal{O}(\alpha_s)$, is given by [105]

$$S_{ij}(\vec{k}_T,\mu,\nu) = \delta(\vec{k}_T) + \frac{\alpha_s C_i}{2\pi}\left[-2\mathcal{L}_1(\vec{k}_T,\mu) + 4\mathcal{L}_0(\vec{k}_T,\mu)\ln\left(\frac{\nu}{\mu}\right) - \frac{\pi^2}{6}\delta(\vec{k}_T)\right]. \tag{B.29}$$

In impact parameter space, the TMD soft function reads

$$\tilde{S}_{ij}(b_T,\mu,\nu) = 1 + \frac{\alpha_s C_i}{2\pi}\left[-L_b^2 - 4L_b\ln\left(\frac{\nu}{\mu}\right) - \frac{\pi^2}{6}\right], \tag{B.30}$$

with L_b given in eq. (A.23).

The projected fully-differential soft function was given in eq. (5.11) and is repeated here for completeness

$$S_{ij}(2k^0,\vec{k}_T,\mu) = \frac{\alpha_s C_i}{\pi^2}\frac{\mathrm{d}}{\mathrm{d}(2k^0)}\frac{\mathrm{d}}{\mathrm{d}k_T^2}\left\{\theta(k^0)\,\theta(k_T)\left[2\ln^2\left(\frac{2k^0}{\mu}\right) - \frac{\pi^2}{12}\right.\right. \tag{B.31}$$

$$\left.\left. + \theta(k^0 - k_T)\left(2a^2 - 4a\ln\left(\frac{2k^0}{k_T}\right) + 2\mathrm{Li}_2(-e^{-2a})\right)\right]\right\},$$

where $a = \mathrm{arccosh}(k_0/k_T)$. The projection from the fully-differential soft function from ref. [184] onto $2k^0$ leads to the complicated finite terms.

The double-differential soft function [108] can conveniently be decomposed into a term involving the TMD soft function and a correction term as

$$S_{ij}(k, \vec{k}_T, \mu, \nu) = \delta(k)\, S_{ij}(\vec{k}_T, \mu, \nu) + \Delta S_{ij}(k, \vec{k}_T, \mu, \nu)\,. \tag{B.32}$$

The correction is in this case over the limit $k \gg \vec{k}_T$, where the contribution of soft radiation to the $\mathcal{T} = k$ measurement becomes power suppressed. At one loop, the correction term is given by

$$\Delta S_{ij}(k, \vec{k}_T, \mu, \nu) = \frac{\alpha_s}{4\pi} \Delta S_{ij}^{(1)}(k, \vec{k}_T) + \mathcal{O}(\alpha_s^2)\,,$$

$$\Delta S_{ij}^{(1)}(k, \vec{k}_T) = 4C_i \left[\frac{2}{\pi\mu^3}\, \mathcal{L}_\Delta\left(\frac{k}{\mu}, \frac{k_T^2}{\mu^2}\right) - \delta(k)\, \mathcal{L}_1(\vec{k}_T, \mu) \right]\,, \tag{B.33}$$

where $\mathcal{L}_\Delta$ was defined in eq. (A.12). The second line is not yet manifestly independent of μ, but can be simplified by noting that

$$\mathcal{L}_\Delta(x_1, x_2) - \delta(x_1)\mathcal{L}_1(x_2) = \frac{\mathrm{d}}{\mathrm{d}x_1}\frac{\mathrm{d}}{\mathrm{d}x_2}\theta(x_2 - x_1^2)\left[-\frac{1}{2}\ln^2\left(\frac{x_1^2}{x_2}\right)\right]\,. \tag{B.34}$$

This can be shown by writing all three distributions in terms of $\theta(x_1 - \epsilon)$ and $\theta(x_2 - \epsilon^2)$ for infinitesimal ϵ, collecting terms, and noting that the result is finite as $\epsilon \to 0$. The required double-cumulant of $\Delta S_{ij}^{(1)}$ for $\mathcal{T}_\mathrm{cut} > 0$ and $q_T^\mathrm{cut} > 0$ can be read off from eq. (B.34) and is equal to

$$\int^{\mathcal{T}_\mathrm{cut}}\mathrm{d}k \int^{q_T^\mathrm{cut} > |\vec{k}_T|}\mathrm{d}^2\vec{k}_T\, \Delta S_{ij}^{(1)}(k, \vec{k}_T) = 4C_F\, \theta(q_T^\mathrm{cut} - \mathcal{T}_\mathrm{cut})\left[-2\ln^2\left(\frac{\mathcal{T}_\mathrm{cut}}{q_T^\mathrm{cut}}\right)\right]\,. \tag{B.35}$$

Using eq. (B.34) and integrating by parts also yields the cumulant up to $\mathcal{T}_\mathrm{cut} > 0$ in position space as

$$\int^{\mathcal{T}_\mathrm{cut}}\mathrm{d}k\, \Delta \tilde{S}_{ij}^{(1)}(k, b_T) = 4C_F\left[\frac{1}{4}x^2\, {}_3F_4\left(1, 1, 1; 2, 2, 2, 2; -\frac{x^2}{4}\right) - 2\ln^2\left(\frac{xe^{\gamma_E}}{2}\right)\right]\,, \tag{B.36}$$

where $x \equiv b_T \mathcal{T}_\mathrm{cut}$ and ${}_iF_j(x_1, \ldots, x_i; y_1, \ldots, y_j; z)$ is the generalized hypergeometric function. Finally, the spectrum of $\Delta \tilde{S}_{ij}^{(1)}$ at $\mathcal{T} > 0$ in position space is given by

$$\Delta \tilde{S}_{ij}^{(1)}(\mathcal{T}, b_T) = 4C_F\, \frac{1}{\mathcal{T}}\left[\frac{1}{2}x^2\, {}_2F_3\left(1, 1; 2, 2, 2; -\frac{x^2}{4}\right) - 4\ln\left(\frac{xe^{\gamma_E}}{2}\right)\right]\,, \quad (\text{B.37})$$

where now $x \equiv b_T \mathcal{T}$.

B.4 Collinear-soft functions

The collinear-soft function appearing in eq. (4.36) is given at one loop by [108]

$$\mathscr{S}_i(k, \vec{k}_T, \mu, \nu) = \delta(k)\delta(\vec{k}_T) + \frac{\alpha_s C_i}{4\pi} \left[4\mathcal{L}_0(k, \mu)\,\mathcal{L}_0(\vec{k}_T, \mu) - 4\delta(k)\,\mathcal{L}_1(\vec{k}_T, \mu) \right.$$
$$\left. + 4\delta(k)\,\mathcal{L}_0(\vec{k}_T, \mu)\ln\left(\frac{\nu}{\mu}\right) - \frac{\pi^2}{3}\delta(k)\delta(\vec{k}_T) \right].$$
$$(B.38)$$

The position-space equivalent is given by

$$\tilde{\mathscr{S}}_i(k, b_T, \mu, \nu) = \delta(k) + \frac{\alpha_s C_i}{4\pi} \left[-4L_b\,\mathcal{L}_0(k, \mu) - 2L_b^2\,\delta(k) \right.$$
$$\left. - 4L_b\ln\left(\frac{\nu}{\mu}\right)\delta(k) - \frac{\pi^2}{3}\delta(k) \right].$$
$$(B.39)$$

The 1-loop expression for the hatted collinear-soft function from eq. (5.13) is given by

$$\hat{\mathscr{S}}_i(k, \vec{k}_T, \mu, \nu) = \delta(k)\delta(\vec{k}_T) + \frac{\alpha_s C_i}{4\pi} \left[4\mathcal{L}_0(k, \mu)\,\mathcal{L}_0(\vec{k}_T, \mu) \right.$$
$$\left. - 4\delta(k)\,\mathcal{L}_0(\vec{k}_T, \mu)\ln\left(\frac{\nu}{\mu}\right) \right].$$
$$(B.40)$$

Renormalization group evolution

In app. C.1, the renormalization group equations and anomalous dimensions of the various perturbative functions that appear in factorization theorems throughout this thesis are gathered. The ingredients required for resummation, including the beta function, cusp anomalous dimension and the relevant non-cusp anomalous dimensions, are given in app. C.2.

C.1 Renormalization group equations

The RGE for the Drell-Yan matching coefficient is given by

$$\mu \frac{\mathrm{d}}{\mathrm{d}\mu} C_{q\bar{q}}(Q^2, \mu) = \gamma_{q\bar{q}}(Q^2, \mu)\, C_{q\bar{q}}(Q^2, \mu)\,,$$

$$\gamma_{q\bar{q}}(Q^2, \mu) = \Gamma^q_{\mathrm{cusp}}(\alpha_s) \ln\!\Big(\frac{-Q^2}{\mu^2}\Big) + \gamma^q_C(\alpha_s)\,. \tag{C.1}$$

For the gluon-fusion Higgs production matching coefficient, the RGE instead reads

$$\mu \frac{\mathrm{d}}{\mathrm{d}\mu} C_{gg}(m_H, \mu) = \gamma_{gg}(m_H, \mu)\, C_{gg}(m_H, \mu)\,,$$

$$\gamma_{gg}(m_H, \mu) = \Gamma^g_{\mathrm{cusp}}(\alpha_s) \ln\!\Big(\frac{-m_H^2}{\mu^2}\Big) + \gamma^g_C(\alpha_s) - \gamma_t(\alpha_s) - \frac{\beta(\alpha_s)}{\alpha_s}\,. \tag{C.2}$$

The RGE of the inclusive beam function is given by

$$\mu \frac{\mathrm{d}}{\mathrm{d}\mu} B_i(t, x, \mu) = \int \mathrm{d}t'\, \gamma^i_B(t - t', \mu)\, B_i(t', x, \mu)\,,$$

$$\gamma^i_B(t, \mu) = -2\Gamma^i_{\mathrm{cusp}}(\alpha_s)\, \mathcal{L}_0(t, \mu^2) + \gamma^i_B(\alpha_s)\, \delta(t)\,. \tag{C.3}$$

The TMD beam function adheres to the μ-RGE

$$\mu \frac{\mathrm{d}}{\mathrm{d}\mu} B_i(\omega, \vec{k}_T, \mu, \nu) = \tilde{\gamma}_B^i(\omega, \mu, \nu) \, B_i(\omega, \vec{k}_T, \mu, \nu) \,,$$

$$\tilde{\gamma}_B^i(\omega, \mu, \nu) = 2\Gamma_{\mathrm{cusp}}^i(\alpha_s) \ln\left(\frac{\nu}{\omega}\right) + \tilde{\gamma}_B^i(\alpha_s) \,, \qquad (\mathrm{C.4})$$

where the anomalous dimension can be distinguished from that of the inclusive beam function by the tilde. Since it does not depend on k_T, it is equal to its Fourier transform. The ν-RGE of the TMD beam function in position space is given by

$$\nu \frac{\mathrm{d}}{\mathrm{d}\nu} \tilde{B}_i(\omega, b_T, \mu, \nu) = -\frac{1}{2} \tilde{\gamma}_\nu^i(b_T, \mu) \, \tilde{B}_i(\omega, b_T, \mu, \nu) \,. \qquad (\mathrm{C.5})$$

The rapidity anomalous dimension reads

$$\tilde{\gamma}_\nu^i(b_T, \mu) = -4\eta_\Gamma^i(\mu_0, \mu) + \tilde{\gamma}_{\nu,\mathrm{FO}}^i(b_T, \mu_0) + \tilde{\gamma}_{\nu,\mathrm{np}}^i(b_T) \,, \qquad (\mathrm{C.6})$$

where the evolution kernel η_Γ^i was defined in eq. (3.193). The nonperturbative model $\tilde{\gamma}_{\nu,\mathrm{np}}^i(b_T)$ is set to zero throughout this thesis. The fixed-order boundary condition of the resummed rapidity anomalous dimension through NNLL reads

$$\tilde{\gamma}_{\nu,\mathrm{FO}}^i(b_T, \mu_0) = \frac{\alpha_s}{4\pi} \left[-2\Gamma_0^i L_b \right] + \frac{\alpha_s^2}{(4\pi)^2} \left[-\Gamma_0^i \beta_0 L_b^2 - 2\Gamma_1^i L_b + \gamma_{\nu,1}^i \right] \,, \qquad (\mathrm{C.7})$$

where the 1-loop coefficient $\gamma_{\nu,0}^i = 0$ has already been plugged in. For the regulator employed here, the 2-loop coefficient is given by [205]

$$\gamma_{\nu,1} = C_i \left[-C_A \left(\frac{128}{9} - 56\zeta_3 \right) - \beta_0 \frac{112}{9} \right] \,. \qquad (\mathrm{C.8})$$

The RGE of the double-differential beam function is given by

$$\mu \frac{\mathrm{d}}{\mathrm{d}\mu} B_i(t, x, \vec{k}_T, \mu) = \int \mathrm{d}t' \, \gamma_B^i(t - t', \mu) \, B_i(t', x, \vec{k}_T, \mu) \,, \qquad (\mathrm{C.9})$$

where the anomalous dimension is equal to that of the inclusive beam function in eq. (C.3).

The RGE of the parton distribution functions, better known as the DGLAP equation, is given by

$$\mu \frac{\mathrm{d}}{\mathrm{d}\mu} f_i(x, \mu) = \sum_j \int_x^1 \frac{\mathrm{d}z}{z} \, 2P_{ij}(\alpha_s, z) \, f_j\left(\frac{x}{z}, \mu\right) \,, \qquad (\mathrm{C.10})$$

where the expansion

$$P_{ij}(\alpha_s, z) = \sum_{n=0}^{\infty} \left(\frac{\alpha_s}{4\pi}\right)^{n+1} P_{ij}^{(n)}(z), \tag{C.11}$$

has been defined. For the threshold PDFs, the mixing between PDFs of different flavors is suppressed and the RGE and anomalous dimension simplify to [220]

$$\mu \frac{\mathrm{d}}{\mathrm{d}\mu} f_i^{\mathrm{thr}}(x, \mu) = \int_x^1 \mathrm{d}x' \, \gamma_f^i(x - x', \mu) \, f_i^{\mathrm{thr}}(x', \mu),$$
$$\gamma_f^i(x, \mu) = 2 P_{ii}^{\mathrm{thr}}(\alpha_s, 1 + x), \tag{C.12}$$

where now

$$P_{ii}^{\mathrm{thr}}(\alpha_s, 1) = \sum_{n=0}^{\infty} \left(\frac{\alpha_s}{4\pi}\right)^{n+1} P_{ii}^{\mathrm{thr}\,(n)}(x). \tag{C.13}$$

The coefficient that occurs in this thesis is given by

$$P_{qq}^{\mathrm{thr}\,(0)}(x) = 2 C_F \, \theta(x) P_{qq}^{\mathrm{thr}}(x),$$
$$P_{qq}^{\mathrm{thr}}(x) = 2\mathcal{L}_0(1 - x) + \frac{3}{2}\delta(1 - x). \tag{C.14}$$

The RGE of the inclusive soft function is given by

$$\mu \frac{\mathrm{d}}{\mathrm{d}\mu} S_{ij}(k, \mu) = \int \mathrm{d}k' \, \gamma_S^i(k - k', \mu) \, S_{ij}(k', \mu),$$
$$\gamma_S^i(k, \mu) = 4\Gamma_{\mathrm{cusp}}^i(\alpha_s)\mathcal{L}_0(k, \mu) + \gamma_S^i(\alpha_s)\delta(k). \tag{C.15}$$

The TMD soft function obeys the μ-RGE

$$\mu \frac{\mathrm{d}}{\mathrm{d}\mu} S_{ij}(\vec{k}_T, \mu, \nu) = \tilde{\gamma}_S^i(\mu, \nu) \, S_{ij}(\vec{k}_T, \mu, \nu),$$
$$\tilde{\gamma}_S^i(\mu, \nu) = 4\Gamma_{\mathrm{cusp}}^i(\alpha_s) \ln\left(\frac{\mu}{\nu}\right) + \tilde{\gamma}_S^i(\alpha_s), \tag{C.16}$$

where the tilde serves to distinguish between the TMD and the inclusive soft function. Its ν-RGE in position space reads

$$\nu \frac{\mathrm{d}}{\mathrm{d}\nu} \tilde{S}_{ij}(b_T, \mu, \nu) = \tilde{\gamma}_\nu(b_T, \mu) \, \tilde{S}_{ij}(b_T, \mu, \nu). \tag{C.17}$$

The RGE of the projected fully-differential soft function from eq. (5.11) is given by

$$\mu \frac{\mathrm{d}}{\mathrm{d}\mu} S_{ij}(2k^0, \vec{k}_T, \mu) = \int \mathrm{d}(2k'^0)\, \hat{\gamma}_S^i(2k^0 - 2k'^0, \mu)\, S_{ij}(2k'^0, \vec{k}_T, \mu)\,,$$

$$\hat{\gamma}_S^i(2k^0, \mu) = -4\Gamma_{\mathrm{cusp}}^i(\alpha_s)\mathcal{L}_0(2k^0, \mu) + \hat{\gamma}_S^i(\alpha_s)\,\delta(2k^0)\,. \qquad (\text{C.18})$$

The double-differential soft function is described by the RGEs

$$\mu \frac{\mathrm{d}}{\mathrm{d}\mu} S_{ij}(k, \vec{k}_T, \mu, \nu) = \tilde{\gamma}_S^i(\mu, \nu)\, S_{ij}(k, \vec{k}_T, \mu, \nu)\,,$$

$$\nu \frac{\mathrm{d}}{\mathrm{d}\nu} \tilde{S}_{ij}(k, b_T, \mu, \nu) = \tilde{\gamma}_\nu^i(b_T, \mu)\, \tilde{S}_{ij}(k, b_T, \mu, \nu)\,, \qquad (\text{C.19})$$

where the anomalous dimensions of the μ-RGE is equal to that of the TMD beam function.

The RGE of the soft function appearing in the factorizations describing the measurement of n angularities in sec. 7.2.2 is given by

$$\mu \frac{\mathrm{d}}{\mathrm{d}\mu} S_{ij}(Q^\alpha e_\alpha, \mu) = \int \mathrm{d}(Q^\alpha e'_\alpha)\, \bar{\gamma}_S^i(Q^\alpha e_\alpha - Q^\alpha e'_\alpha, \mu)\, S_{ij}(Q^\alpha e'_\alpha, \mu)\,,$$

$$\bar{\gamma}_S^i(Q^\alpha e_\alpha, \mu) = \frac{4}{\alpha - 1}\Gamma_{\mathrm{cusp}}^i(\alpha_s)\mathcal{L}_0(Q^\alpha e_\alpha, \mu^\alpha)$$

$$+ \left[\bar{\gamma}_S^i(\alpha_s) - 2\Gamma_{\mathrm{cusp}}^i(\alpha_s)\ln\!\left(\frac{Q^2}{\mu^2}\right)\right]\delta(Q^\alpha e_\alpha)\,, \qquad (\text{C.20})$$

where the bar serves to distinguish the anomalous dimension from the other soft anomalous dimensions.

The μ-RGE of the collinear-soft function appearing in sec. 4.2.4 is given by

$$\mu \frac{\mathrm{d}}{\mathrm{d}\mu} \mathscr{S}_i(k, \vec{k}_T, \mu, \nu) = \int \mathrm{d}k'\, \gamma_{\mathscr{S}}^i(k - k', \mu, \nu)\, \mathscr{S}_i(k', \vec{k}_T, \mu, \nu)\,,$$

$$\gamma_{\mathscr{S}}^i(k, \mu, \nu) = -2\Gamma_{\mathrm{cusp}}^i(\alpha_s)\mathcal{L}_0\!\left(k, \frac{\mu^2}{\nu}\right) + \gamma_{\mathscr{S}}^i(\alpha_s)\,\delta(k)\,, \qquad (\text{C.21})$$

while its ν-RGE in position space reads

$$\nu \frac{\mathrm{d}}{\mathrm{d}\nu} \tilde{\mathscr{S}}_i(k, b_T, \mu, \nu) = \frac{1}{2} \tilde{\gamma}_\nu^i(b_T, \mu)\, \tilde{\mathscr{S}}_i(k, b_T, \mu, \nu)\,. \qquad (\text{C.22})$$

The μ-RGE of the hatted collinear-soft function from sec. 5.1.3 is given by

$$\mu \frac{\mathrm{d}}{\mathrm{d}\mu} \hat{\mathscr{S}}_i(k, \vec{k}_T, \mu, \nu) = \int \mathrm{d}k'\, \hat{\gamma}_{\mathscr{S}}^i(k - k', \mu, \nu)\, \hat{\mathscr{S}}_i(k', \vec{k}_T, \mu, \nu)\,,$$

$$\hat{\gamma}_{\mathscr{S}}^i(k, \mu, \nu) = -2\Gamma_{\mathrm{cusp}}^i(\alpha_s)\mathcal{L}_0\!\left(k, \frac{\mu^2}{\nu}\right) + \hat{\gamma}_{\mathscr{S}}^i(\alpha_s)\,\delta(k)\,. \qquad (\text{C.23})$$

The ν-RGE of the hatted collinear-soft function in position space reads

$$\nu\frac{\mathrm{d}}{\mathrm{d}\nu}\tilde{\hat{\mathscr{S}}}_i(k,b_T,\mu,\nu) = -\frac{1}{2}\,\tilde{\hat{\gamma}}_\nu^i(b_T,\mu)\,\tilde{\hat{\mathscr{S}}}_i(k,b_T,\mu,\nu)\,. \tag{C.24}$$

The RGE of the collinear-soft function appearing in the factorization of the cross sections differential in multiple angularities is given by

$$\mu\frac{\mathrm{d}}{\mathrm{d}\mu}\mathscr{S}_i(Q^\alpha e_\alpha, Q^\beta e_\beta, \mu) = \int\mathrm{d}(Q^\alpha e'_\alpha)\int\mathrm{d}(Q^\beta e'_\beta)\,\mathscr{S}_i(Q^\alpha e'_\alpha, Q^\beta e'_\beta, \mu)$$
$$\times\,\bar{\gamma}^i_{\mathscr{S}}(Q^\alpha e_\alpha - Q^\alpha e'_\alpha, Q^\beta e_\beta - Q^\beta e'_\beta, \mu)\,,$$
$$\bar{\gamma}^i_{\mathscr{S}}(Q^\alpha e_\alpha, Q^\beta e_\beta, \mu) = -\frac{2}{\alpha-1}\Gamma^i_{\mathrm{cusp}}(\alpha_s)\mathcal{L}_0(Q^\alpha e_\alpha, \mu^\alpha)\,\delta(Q^\beta e_\beta)$$
$$+\frac{2}{\beta-1}\Gamma^i_{\mathrm{cusp}}(\alpha_s)\mathcal{L}_0(Q^\beta e_\beta, \mu^\beta)\,\delta(Q^\alpha e_\alpha)$$
$$+\bar{\gamma}^i_{\mathscr{S}}(\alpha_s)\,\delta(Q^\alpha e_\alpha)\,\delta(Q^\beta e_\beta)\,, \tag{C.25}$$

where the bar again serves to distinguish the anomalous dimension from other collinear-soft anomalous dimensions.

The jet function appearing in the same factorization formula is renormalized through

$$\mu\frac{\mathrm{d}}{\mathrm{d}\mu}J_i(Q^\alpha e_\alpha, \mu) = \int\mathrm{d}(Q^\alpha e'_\alpha)\,\gamma^i_J(Q^\alpha e_\alpha - Q^\alpha e'_\alpha, \mu)\,J_i(Q^\alpha e'_\alpha, \mu)\,,$$
$$\gamma^i_J(Q^\alpha e_\alpha, \mu) = -\frac{2}{\alpha-1}\Gamma^i_{\mathrm{cusp}}(\alpha_s)\mathcal{L}_0(Q^\alpha e_\alpha, \mu^\alpha) + \gamma^i_J(\alpha_s)\,\delta(Q^\alpha e_\alpha)\,. \tag{C.26}$$

C.2 Anomalous dimensions

The beta function is expanded as

$$\beta(\alpha_s) = -2\alpha_s\sum_{n=0}^\infty \beta_n\Big(\frac{\alpha_s}{4\pi}\Big)^{n+1}\,, \tag{C.27}$$

with coefficients in the $\overline{\mathrm{MS}}$ scheme, up to three loops, given by [280, 281]

$$\beta_0 = \frac{11}{3}C_A - \frac{4}{3}T_F n_f\,,$$
$$\beta_1 = \frac{34}{3}C_A^2 - \Big(\frac{20}{3}C_A + 4C_F\Big)T_F n_f\,,$$
$$\beta_2 = \frac{2857}{54}C_A^3 + \Big(C_F^2 - \frac{205}{18}C_F C_A - \frac{1415}{54}C_A^2\Big)2T_F n_f$$
$$+\Big(\frac{11}{9}C_F + \frac{79}{54}C_A\Big)4T_F^2 n_f^2\,. \tag{C.28}$$

Solving the RGE of the strong coupling constant, given in eq. (2.20), up to three loops yields the running coupling

$$\frac{1}{\alpha_s(\mu)} = \frac{X}{\alpha_s(\mu_0)} + \frac{\beta_1}{4\pi\beta_0} \ln X$$
$$+ \frac{\alpha_s(\mu_0)}{16\pi^2} \left[\frac{\beta_2}{\beta_0} \left(1 - \frac{1}{X} \right) + \frac{\beta_1^2}{\beta_0^2} \left(\frac{\ln X}{X} + \frac{1}{X} - 1 \right) \right], \quad \text{(C.29)}$$

where $X = 1 + \alpha_s(\mu_0)\beta_0 \ln(\mu/\mu_0)/(2\pi)$. The evolution kernels appearing in the solutions of the various RGEs are defined through

$$K_\Gamma^i(\mu_0, \mu) = \int_{\alpha_s(\mu_0)}^{\alpha_s(\mu)} \frac{\mathrm{d}x}{\beta(x)} \Gamma_{\text{cusp}}^i(x) \int_{\alpha_s(\mu_0)}^x \frac{\mathrm{d}y}{\beta(y)},$$

$$\eta_\Gamma^i(\mu_0, \mu) = \int_{\alpha_s(\mu_0)}^{\alpha_s(\mu)} \frac{\mathrm{d}x}{\beta(x)} \Gamma_{\text{cusp}}^i(x),$$

$$K_{\gamma_X^i}(\mu_0, \mu) = \int_{\alpha_s(\mu_0)}^{\alpha_s(\mu)} \frac{\mathrm{d}x}{\beta(x)} \gamma_X^i(x). \quad \text{(C.30)}$$

Their explicit expressions at NNLL accuracy are found to be

$$K_\Gamma^i(\mu, \mu_0) = -\frac{\Gamma_0^i}{4\beta_0^2} \left[\frac{4\pi}{\alpha_s(\mu_0)} \left(1 - \frac{1}{r} - \ln r \right) + \left(\frac{\Gamma_1^i}{\Gamma_0^i} - \frac{\beta_1}{\beta_0} \right) (1 - r + \ln r) \right.$$
$$+ \frac{\beta_1}{2\beta_0} \ln^2(r) + \frac{\alpha_s(\mu_0)}{4\pi} \left(\left(\frac{\beta_1^2}{\beta_0^2} - \frac{\beta_2}{\beta_0} \right) \left(\frac{1 - r^2}{2} + \ln r \right) \right.$$
$$+ \left(\frac{\beta_1 \Gamma_1^i}{\beta_0 \Gamma_0^i} - \frac{\beta_1^2}{\beta_0^2} \right) (1 - r + r \ln r)$$
$$\left. \left. - \left(\frac{\Gamma_2^i}{\Gamma_0^i} - \frac{\beta_1 \Gamma_1^i}{\beta_0 \Gamma_0^i} \right) \frac{(1 - r)^2}{2} \right) \right],$$

$$\eta_\Gamma^i(\mu, \mu_0) = -\frac{\Gamma_0^i}{2\beta_0} \left[\ln r + \frac{\alpha_s(\mu_0)}{4\pi} \left(\frac{\Gamma_1^i}{\Gamma_0^i} - \frac{\beta_1}{\beta_0} \right) (r - 1) \right.$$
$$\left. + \frac{\alpha_s(\mu_0)^2}{16\pi^2} \left(\frac{\Gamma_2^i}{\Gamma_0^i} - \frac{\beta_1 \Gamma_1^i}{\beta_0 \Gamma_0^i} + \frac{\beta_1^2}{\beta_0^2} - \frac{\beta_2}{\beta_0} \right) \frac{r^2 - 1}{2} \right],$$

$$K_{\gamma_X^i}(\mu, \mu_0) = -\frac{\gamma_{X,0}^i}{2\beta_0} \left[\ln r + \frac{\alpha_s(\mu_0)}{4\pi} \left(\frac{\gamma_{X,1}^i}{\gamma_{X,0}^i} - \frac{\beta_1}{\beta_0} \right) (r - 1) \right], \quad \text{(C.31)}$$

where $r = \alpha_s(\mu)/\alpha_s(\mu_0)$. The cusp and non-cusp anomalous dimensions are expanded as

$$\Gamma_{\text{cusp}}^i(\alpha_s) = \sum_{n=0}^{\infty} \Gamma_n^i \left(\frac{\alpha_s}{4\pi} \right)^{n+1} \quad \text{and} \quad \gamma_X^i(\alpha_s) = \sum_{n=0}^{\infty} \gamma_{X,n}^i \left(\frac{\alpha_s}{4\pi} \right)^{n+1}, \quad \text{(C.32)}$$

where the superscript $i = q, g$ distinguishes between quarks and gluons. The coefficients of the $\overline{\text{MS}}$ cusp anomalous dimension to three loops are [208, 282, 283]

$$\Gamma_0^i = 4C_i \,,$$

$$\Gamma_1^i = 4C_i \left[C_A \left(\frac{67}{9} - \frac{\pi^2}{3} \right) - \frac{20}{9} T_F \, n_f \right] = \frac{4}{3} C_i \left[(4 - \pi^2) C_A + 5\beta_0 \right],$$

$$\Gamma_2^i = 4C_i \left[C_A^2 \left(\frac{245}{6} - \frac{134\pi^2}{27} + \frac{11\pi^4}{45} + \frac{22\zeta_3}{3} \right) \right.$$

$$+ C_A \, T_F \, n_f \left(-\frac{418}{27} + \frac{40\pi^2}{27} - \frac{56\zeta_3}{3} \right)$$

$$\left. + C_F \, T_F \, n_f \left(-\frac{55}{3} + 16\zeta_3 \right) - \frac{16}{27} T_F^2 \, n_f^2 \right], \tag{C.33}$$

where $i = q, g$ and, as before, $C_q = C_F$ and $C_g = C_A$.

The coefficients of the non-cusp anomalous dimension of the hard matching coefficients are given by

$$\gamma_{C,0}^q = -6C_F \,,$$

$$\gamma_{C,1}^q = -C_F \left[\left(\frac{82}{9} - 52\zeta_3 \right) C_A + \left(3 - 4\pi^2 + 48\zeta_3 \right) C_F + \left(\frac{65}{9} + \pi^2 \right) \beta_0 \right],$$

$$\gamma_{C,0}^g = -2\beta_0 \,,$$

$$\gamma_{C,1}^g = C_A \left[\left(-\frac{118}{9} + 4\zeta_3 \right) C_A + \left(-\frac{38}{9} + \frac{\pi^2}{3} \right) \beta_0 \right] - 2\beta_1 \,,$$

$$\gamma_{t,n} = -2n\beta_n \,. \tag{C.34}$$

The coefficients of the non-cusp inclusive beam anomalous dimension are [100–102, 274]

$$\gamma_{B,0}^q = 6C_F \,,$$

$$\gamma_{B,1}^q = C_F \left[\left(\frac{146}{9} - 80\zeta_3 \right) C_A + (3 - 4\pi^2 + 48\zeta_3) C_F + \left(\frac{121}{9} + \frac{2\pi^2}{3} \right) \beta_0 \right],$$

$$\gamma_{B,0}^g = 2\beta_0 \,,$$

$$\gamma_{B,1}^g = C_A \left[\left(\frac{182}{9} - 32\zeta_3 \right) C_A + \left(\frac{94}{9} - \frac{2\pi^2}{3} \right) \beta_0 \right] + 2\beta_1 \,. \tag{C.35}$$

The coefficients for the TMD beam function are instead given by [205]

$$
\begin{aligned}
\tilde{\gamma}_{B,0}^{q} &= 6C_F \,, \\
\tilde{\gamma}_{B,1}^{q} &= C_F\left[(2 - 24\zeta_3)C_A + (3 - 4\pi^2 + 48\zeta_3)C_F + \left(1 + \frac{4\pi^2}{3}\right)\beta_0\right] \,, \\
\tilde{\gamma}_{B,0}^{g} &= 2\beta_0 \,, \\
\tilde{\gamma}_{B,1}^{g} &= C_A\left[(-8 + 24\zeta_3)C_A + 8\beta_0 - 22C_F\right] + 6\beta_0 C_F \,.
\end{aligned}
\tag{C.36}
$$

The coefficients of the non-cusp anomalous dimension of the soft functions are given by

$$
\begin{aligned}
\gamma_{S,0}^{i} &= \tilde{\gamma}_{S,0}^{i} = \hat{\gamma}_{S,0}^{i} = \bar{\gamma}_{S,0}^{i} = 0 \,, \\
\gamma_{S,1}^{i} &= -\tilde{\gamma}_{S,1}^{i} = -\hat{\gamma}_{S,1}^{i} = C_i\left[\left(-\frac{128}{9} + 56\zeta_3\right)C_A + \left(\frac{112}{9} - \frac{2\pi^2}{3}\right)\beta_0\right] \,.
\end{aligned}
\tag{C.37}
$$

The collinear-soft functions have non-cusp coefficients given by

$$
\begin{aligned}
\gamma_{\mathscr{S},0}^{i} &= \hat{\gamma}_{\mathscr{S},0}^{i} = \bar{\gamma}_{\mathscr{S},0}^{i} = \hat{\gamma}_{\mathscr{S},1}^{i} = 0 \,, \\
\gamma_{\mathscr{S},1}^{i} &= -\gamma_{S,1}^{i} \,,
\end{aligned}
\tag{C.38}
$$

where the last line follows from eq. (5.33). The 1-loop non-cusp anomalous dimension of the jet function in the n-angularity factorizations is given by

$$
\gamma_{J,0}^{i} = 6C_F \,.
\tag{C.39}
$$

D

Differential and cumulant scale setting

The topic of differential versus cumulant scale setting was raised in sec. 4.3.5. The main differences between the two were discussed, most notably, the failure of the integrated spectrum to recover the inclusive cross section when differential scale settings are used and the less reliable uncertainties obtained when employing cumulant scale setting. All results obtained in sec. 4.4 involve the corresponding scale setting, e.g. the prediction for a cross section differential in $\mathcal{T}$ and cumulative in q_T uses differential scale setting for the former and cumulative scale setting for the latter, so that these issues are avoided.

In this appendix, the performances of the various combinations of differential and cumulant scale settings to predict observables other than the ones they were designed to describe accurately are investigated. Of particular interest is the performance of the $(q_T, \mathcal{T})$ scale setting described in earlier sections at the level of cumulant observables. This can be done by transforming a spectrum using differential scale setting in q_T and $\mathcal{T}$ to a prediction for the cumulant up to q_T^{cut} and $\mathcal{T}_{\mathrm{cut}}$, using the analog of eq. (4.73). The only nontrivial new procedure is computing the double cumulant directly from $(q_T, \mathcal{T})$ scales, where the overlap in underflow contributions has to be taken into account by

$$
\begin{aligned}
\sigma_{\mathrm{diff,diff}}(q_T^{\mathrm{cut}}, \mathcal{T}_{\mathrm{cut}}) = \int^{q_T^{\mathrm{cut}}} \mathrm{d}q_T \int^{\mathcal{T}_{\mathrm{cut}}} \mathrm{d}\mathcal{T} \bigg[& \theta(q_T > q_T^{\mathrm{np}})\, \theta(\mathcal{T} > \mathcal{T}_{\mathrm{np}}) \frac{\mathrm{d}\sigma}{\mathrm{d}q_T\, \mathrm{d}\mathcal{T}}\Big|_{\mu(q_T, \mathcal{T})} \\
& + \theta(q_T \le q_T^{\mathrm{np}})\, \theta(\mathcal{T} > \mathcal{T}_{\mathrm{np}}) \frac{\mathrm{d}\sigma}{\mathrm{d}q_T\, \mathrm{d}\mathcal{T}}\Big|_{\mu(q_T^{\mathrm{np}}, \mathcal{T})} \\
& + \theta(q_T > q_T^{\mathrm{np}})\, \theta(\mathcal{T} \le \mathcal{T}_{\mathrm{np}}) \frac{\mathrm{d}\sigma}{\mathrm{d}q_T\, \mathrm{d}\mathcal{T}}\Big|_{\mu(q_T, \mathcal{T}_{\mathrm{np}})} \\
& - \theta(q_T \le q_T^{\mathrm{np}})\, \theta(\mathcal{T} \le \mathcal{T}_{\mathrm{np}}) \frac{\mathrm{d}\sigma}{\mathrm{d}q_T\, \mathrm{d}\mathcal{T}}\Big|_{\mu(q_T^{\mathrm{np}}, \mathcal{T}_{\mathrm{np}})} \bigg].
\end{aligned}
\tag{D.1}
$$

Since the distinction between differential and cumulant scale setting is only relevant for q_T versus q_T^{cut} but not for the underlying resummation in b_T
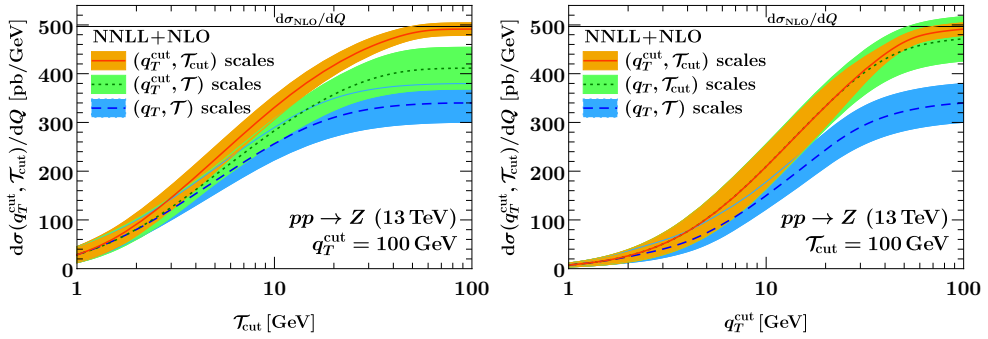
Figure D.1 The double cumulant cross section as a function of $\mathcal{T}_{\mathrm{cut}}$ for $q_T^{\mathrm{cut}} = 100\,\mathrm{GeV}$ (left) and as a function of q_T^{cut} for $\mathcal{T}_{\mathrm{cut}} = 100\,\mathrm{GeV}$ (right). The bands indicate the total perturbative uncertainty Δ_{total}, see sec. 4.3.4.

space, the dependence of the hybrid scales on b_T is suppressed. In practice, $q_T^{\mathrm{np}} = \mathcal{T}_{\mathrm{np}} = 1\,\mathrm{GeV}$ is used and the integrals in eqs. (4.73) and (D.1) are implemented as sums over logarithmically spaced bins with bin size $\Delta(\log_{10} q_T) = \Delta(\log_{10} \mathcal{T}) = 0.08$, where the spectrum is evaluated at the logarithmic midpoint of each bin. Scale variations in the integrated results are performed by integrating each instance of the spectrum separately and computing maximum deviations from the central results in the end. The final results are interpolated for clarity.

In figures D.1 to D.3, the default scale setting for various cumulant observables (solid orange) is compared against more differential scale settings (dashed blue and dotted green), i.e. choosing μ in terms of q_T rather than q_T^{cut} and/or $\mathcal{T}$ rather than $\mathcal{T}_{\mathrm{cut}}$. Fig. D.1 shows the double cumulant cross section, for which the scales are by default set in terms of q_T^{cut} and $\mathcal{T}_{\mathrm{cut}}$. The horizontal reference line indicates the inclusive fixed-order cross section. In fig. D.2 the $\mathcal{T}$ spectrum with a cut on q_T is shown. The default scales for this cross section are expressed in terms of q_T^{cut} and $\mathcal{T}$. Fig. D.3 depicts the converse q_T spectrum with a cut on $\mathcal{T}$. In both figs. D.2 and D.3, the left panel shows the dependence on the cut at a representative point along the spectrum, with the reference line indicating the resummed prediction for the inclusive (strictly single-differential) spectrum. The right panel in either figure shows the spectrum at a representative choice of the cut.

It should be noted that, in all cases, the cumulative predictions obtained using the default scale setting (solid orange) cleanly asymptote to the respective target observable (the reference line) for large values of the cut. The central double-differential prediction in the left panel of fig. D.3 slightly overshoots the
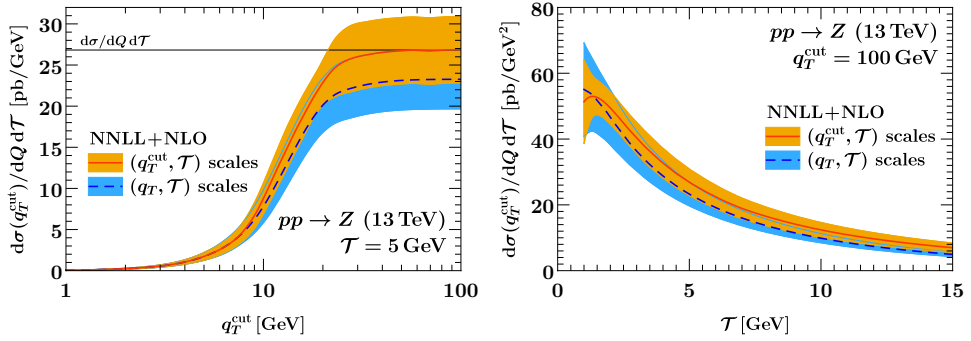
Figure D.2 The $\mathcal{T}$ spectrum with a cut on q_T as a function of q_T^{cut} at fixed $\mathcal{T} = 5\,\mathrm{GeV}$ (left) and as a function of $\mathcal{T}$ at fixed $q_T^{\mathrm{cut}} = 100\,\mathrm{GeV}$ (right). The bands indicate the total perturbative uncertainty Δ_{total}, see sec. 4.3.4. The colors correspond to different scale setting prescriptions with the solid orange line representing the default scale setting.

inclusive result beyond the phase-space boundary $\mathcal{T}_{\mathrm{cut}} \gtrsim q_T$ (where the calculation is effectively a leading-order calculation), but is within uncertainties. Furthermore, the uncertainty obtained using the default scales is smaller than any of the ones obtained from more differential scale settings. As described before, this is expected since differential scale setting cannot account for correlations between different bins of the spectrum, giving rise to a larger band in the cumulant cross sections.

Another conclusion that can be drawn is that predictions obtained using q_T or q_T^{cut} scale setting are mutually compatible. In other words, their uncertainty bands (very nearly) overlap, as long as the scale setting with respect to $\mathcal{T}$ is done the same way in both cases. This can be seen from the right panel of fig. D.1 by comparing the default $(q_T^{\mathrm{cut}}, \mathcal{T}_{\mathrm{cut}})$ scales (solid orange) and the $(q_T, \mathcal{T}_{\mathrm{cut}})$ scales (dotted green). Similarly, in fig. D.2, it can be seen that the default $(q_T^{\mathrm{cut}}, \mathcal{T})$ scales (solid orange) and the $(q_T, \mathcal{T})$ scale setting (dashed blue) roughly differ by their respective uncertainties. These relations are expected since the (unphysical) scale dependence is canceled by higher-order corrections, which the scale variations are designed to probe. For the case of q_T versus q_T^{cut} scales, the specific choice of hybrid profile scales in eq. (4.28) is the reason that differences between the two prescriptions only start to appear when turning off the resummation, such that g_{run} is nonzero. For example, for a high $\mathcal{T}_{\mathrm{cut}} = 100\,\mathrm{GeV}$, which is also a good approximation for the inclusive q_T spectrum, the two prescriptions fully agree in the canonical region $q_T^{\mathrm{cut}} \leq 20\,\mathrm{GeV}$ (see the right panel of fig. D.1). This is responsible for the good overall agreement since most of the cross section is concentrated in the canonical region.
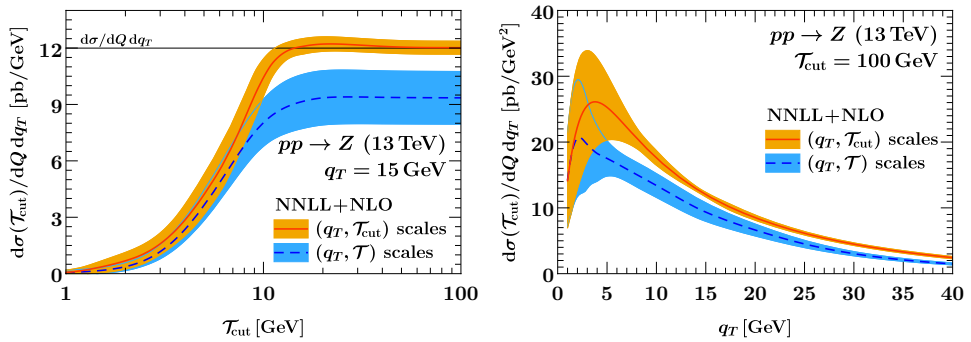
Figure D.3 The q_T spectrum with a cut on $\mathcal{T}$ as a function of $\mathcal{T}_{\mathrm{cut}}$ for $q_T = 15\,\mathrm{GeV}$ (left) and as a function of q_T for $\mathcal{T}_{\mathrm{cut}} = 100\,\mathrm{GeV}$ (right). The bands indicate the total perturbative uncertainty Δ_{total}, see sec. 4.3.4. The colors correspond to different scale setting prescriptions with the solid orange line representing the default scale setting.

The comparison of $\mathcal{T}$ versus $\mathcal{T}_{\mathrm{cut}}$ scales is much less favorable, with the former failing to reproduce the latter's inclusive limit within uncertainties in all cases. This is in line with the discrepancy reported in ref. [173] for a single-differential measurement of thrust in e^+e^- collisions at a comparable working-order (NLL′+NLO). The mismatch is most striking between the default scales (solid orange) and $(q_T, \mathcal{T})$ scales (dashed blue) in figs. D.1 and D.3, implying that more effort is required to ensure both a correct integral and the best possible prediction for the shape of the double-differential spectrum.

The conclusion of the analysis presented here is then that the mismatch mostly reduces to the question of differential versus cumulant scale setting in $\mathcal{T}$ alone, so that the methods developed for the single-differential case in refs. [149, 173] can be brought to bear here as well if desired. However, since this is a well-known issue that is merely inherited from the single-differential case, the matter is not pursued any further here.

To illustrate that the issue is indeed a correlated higher-order effect related to scale choices, a modification of the profile scales can be considered. To be specific, the canonical scale $\mu_S^{\mathrm{I}} \sim (\mu_B^{\mathrm{I}})^2/\mu_H^{\mathrm{I}} \sim \mathcal{T}$ in SCET$_{\mathrm{I}}$ can be lowered by a factor of $c = 0.5$ without parametrically violating the canonical scaling. Including a smooth interpolation to the fixed-order and nonperturbative region,
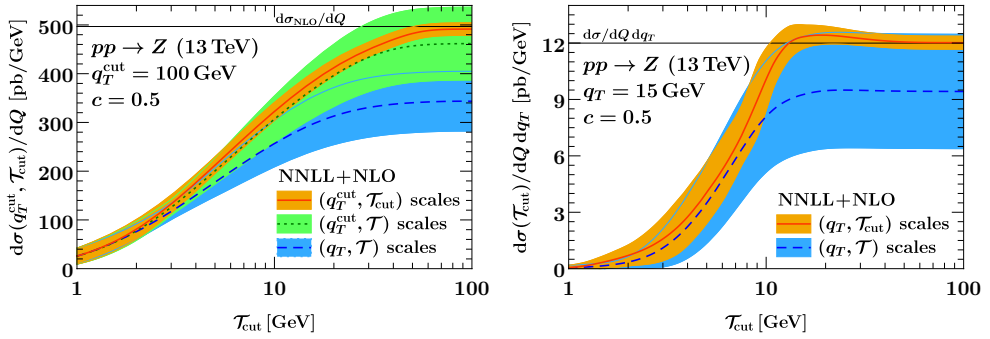
Figure D.4 Left: The double cumulant cross section as a function of $\mathcal{T}_{\mathrm{cut}}$ for $q_T^{\mathrm{cut}} = 100\,\mathrm{GeV}$ for different scale setting prescriptions, with a modified slope $c = 0.5$ of the $\mathrm{SCET}_{\mathrm{I}}$ profile scales, see eq. (D.2). Right: The q_T spectrum with a cut on $\mathcal{T}$ as a function of $\mathcal{T}_{\mathrm{cut}}$ for different scale setting prescriptions, also using modified $\mathrm{SCET}_{\mathrm{I}}$ profile scales with $c = 0.5$. The bands indicate the total perturbative uncertainty Δ_{total}, see sec. 4.3.4.

this can be achieved by replacing eq. (4.11) with

$$
f_{\mathrm{run}}^{\mathrm{I}}(c; x) = \begin{cases}
x_0\left(1 + \frac{c^2 x^2}{4 x_0^2}\right) & x \le 2x_0/c\,, \\
c\,x & 2x_0/c < x \le x_1\,, \\
c\,x + \frac{(2 - cx_2 - cx_3)(x - x_1)^2}{2(x_2 - x_1)(x_3 - x_1)} & x_1 < x \le x_2\,, \\
1 - \frac{(2 - cx_1 - cx_2)(x - x_3)^2}{2(x_3 - x_1)(x_3 - x_2)} & x_2 < x \le x_3\,, \\
1 & x_3 < x\,,
\end{cases}
\tag{D.2}
$$

and keeping the entire remaining profile setup unchanged. Setting $c = 1$ then recovers the original eq. (4.11). The results obtained using the modified profile function from eq. (D.2) are shown in fig. D.4, where the left panels of figs. D.1 and D.3 are repeated using the modified setup. For simplicity, the modified profile function is used for both differential and cumulant scale setting. It can be seen that the simple modification eq. (D.2) already substantially improves the agreement between differential and cumulant scale setting, with the result from $(q_T^{\mathrm{cut}}, \mathcal{T})$ scales (dotted green, left panel) covering the inclusive fixed-order cross section and the result from $(q_T, \mathcal{T})$ scales (dashed blue, right panel) covering the result from single-differential q_T resummation, at the price of much larger uncertainties.

In conclusion, with additional effort, for example by applying the methods used in refs. [149, 173], it would be possible to fully reconcile the best possible predictions for both the differential shape and the cumulant of the double-differential spectrum.

Summary

This thesis represents research that has been conducted in the field of elementary particle physics. Although this is a fundamental science and has little to do with the everyday life, it does address questions that appeal to the imagination of many, such as "What is everything made of?", or "What keeps everything together?". Exactly because everybody wonders about these things from time to time, this summary is aimed at a broad audience.

The goal of this summary is then to provide the reader with a small glimpse into the world of elementary particles and the modest contribution that this thesis makes to it.

The Standard Model

Although the idea that all matter is built up from tiny building blocks is thousands of years old, it was not until the nineteenth century that the first experimental evidence for this was provided. Discoveries followed one another in rapid succession and at the moment over a hundred different building blocks are known. These particles are called *atoms* and are about a million times as small as the width of a human hair.

With the discovery of the atom, the search for the most fundamental building blocks of nature seemed to have come to an end. It was therefore a big surprise when experiments conducted around the twentieth century showed that the atoms themselves consisted of even smaller particles. Every atom was found to contain a positively charged nucleus, surrounded by a cloud of negatively charged particles, called *electrons*, each with an electrical charge of -1. The atomic nucleus is in turn made up out of *protons* and *neutrons*. The proton has an electrical charge of $+1$, exactly opposite to the charge of the electron. Neutrons are, as their name suggests, neutral and do not carry any electrical charge. Since atoms as a whole are electrically neutral, they must contain an equal amount of protons and electrons. The exact number of protons (and electrons) in an atom determines the specific type of atom. For example, a helium atom contains two protons and two electrons, while an iron atom consists of twenty-six protons and electrons. The number of neutrons in an atom may vary, corresponding to different so-called isotopes.
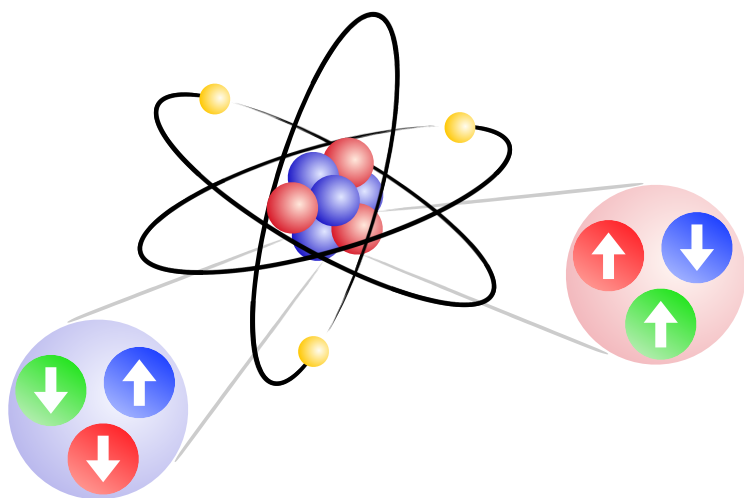
Figure 1 A schematic representation of an atom. Electrons (the yellow orbs) orbit around the nucleus, which contains protons (the red orbs) and neutrons (the blue orbs). The up- and down-quarks (the orbs with arrows pointing up or down) are visible in the enlarged pictures of the proton and neutron.

Even though the existence of only three fundamental building blocks seemed very elegant, protons and neutrons were also found to consist of smaller particles. These particles are called *up-quarks* and *down-quarks* and have an electrical charge of $+2/3$ and $-1/3$ respectively. A proton contains two up-quarks and one down-quark, while a neutron carries two down-quarks and a single up-quark. A graphical representation of an atom can be found in figure 1.

Apart from electrical charge, the quarks turn out to carry an additional type of charge: *color charge*. Despite the somewhat confusing name, this charge has nothing to do with actual color. Where electrical charge comes in two sorts (positive and negative), there are three possible color charges, denoted by *red*, *green* and *blue*. Just as the combination of a positively charged particle and a negatively charged particle is electrically neutral, three particles with a red, green and blue color charge together form a color-neutral combination (also known as *white*). The three quarks inside a proton (or inside a neutron) all have a different color, so protons (and neutrons) carry no net color charge. Only color-neutral particles such as protons and neutrons can be observed directly.

Up-quarks, down-quarks and electrons are currently believed to be fundamental particles of matter: they cannot be divided into smaller particles. There is one additional matter particle, called the *electron-neutrino*, which is not im-

portant here, but is mentioned merely for completeness. All known matter is eventually built from these four elementary particles.

The existence of the four matter particles is predicted by a theory developed around 1967 that carries the somewhat pretentious name *the Standard Model*. The Standard Model additionally predicts two exact copies of each of the four matter particles, with the only difference that these copies have a larger mass. Each of these three collections, all containing four matter particles, is called a *generation*.

Apart from the existence of matter particles, the Standard Model also describes the forces that act between these particles. There are three forces within the Standard Model: *electromagnetism*, the *strong nuclear force* and the *weak nuclear force*. The fourth and final known force, gravity, is not described by the Standard Model. Particles are only affected by a certain force if they carry a specific type of charge. For example, particles are only affected by the electromagnetic force if they are electrically charged and only by the strong nuclear force if they carry a color charge.

The forces between the matter particles are transmitted by force-carrying particles. The force carrier of the electromagnetic force is the *photon*, the particle that light is also made of. The strong nuclear force is transferred by the *gluon*. The three quarks in the proton are thus held together because they exchange gluons and in doing so exert an attractive force upon each other. The strong nuclear force has a fitting name: the force between two quarks in the proton is roughly equal to the force required to lift three male African elephants. The crucial difference between photons and gluons is the fact that photons themselves are not electrically charged, but gluons do carry a color charge. This then means that gluons also affect one another through the strong nuclear force.

The third force, the weak nuclear force, is transmitted through so-called *W*- and *Z-particles* and is responsible for the radioactive decay of some atoms. The final particle that is contained within the Standard Model is the *Higgs particle*. The Higgs particle is not a matter particle or force carrier, but provides a mechanism through which the other particles acquire their respective masses.

A schematic overview of the particle content of the Standard Model is shown in figure 2. Every particle whose existence the Standard Model predicts has been discovered in experiments. Furthermore, no elementary particle that is not predicted by the Standard Model has ever been found. Hence, the Standard Model is an enormously successful theory. Despite its successes though, it

Figure 2 The particles that are described by the Standard Model and the year of their discovery. The first three columns represent the three generations of matter particles, while the fourth column contains the force carries.

cannot be the ultimate theory of the universe. One of the many both theoretical and experimental motivations for this is the fact that gravity is not contained within the Standard Model.

The search for new particles that are not predicted by the Standard Model is one of the biggest challenges of modern-day particle physics.

Searching for particles

The method that is used to search for new particles is based on what is probably the most famous equation in physics:

$$E = m\,c^2\,. \tag{1}$$

Here E stands for energy, m for mass and c is a constant[1]. What this formula then entails, is that energy and mass can be converted into one another according to some exchange rate, which happens to be c^2. The conversion of

---

[1]To be precise, it is the speed of light, roughly equal to a billion kilometers per hour.
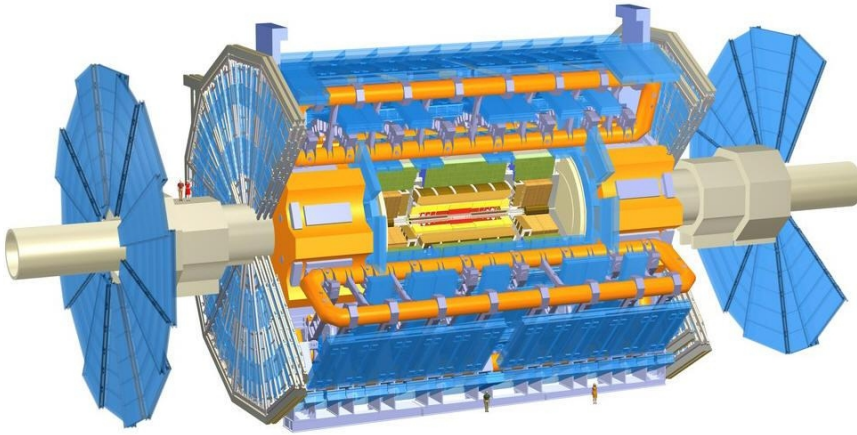
Figure 3 The ATLAS detector. The detector is 46 meters long and has a diameter of 25 meters. The protons enter the detector from both sides and collide in the middle. Around this location, multiple layers of advanced measuring equipment are installed, allowing for the detection of various kinds of particles. The displayed people show the scale of the detector.

mass into energy occurs for example in the generation of nuclear energy, or in the detonation of an atomic bomb. The exact same exchange rate applies in the other direction as well, so energy can also be converted into mass.

The current experimental setup that uses this principle is based in Geneva and is called the Large Hadron Collider (LHC). The LHC is a 27 kilometer long, circular tunnel, built about a hundred meters under the surface. In this tunnel, protons are accelerated in opposite directions until they revolve around the tunnel more than 11 000 times per second. The protons are then made to collide, allowing the quarks (and gluons) inside the protons to interact with each other. Because of the enormous amount of energy that is stored in the motion of the protons, new particles may be created in these interactions through equation (1). These might be particles from the Standard Model that are already known, but may also be new, as of yet undiscovered particles.

Many detectors are set up near the location where the protons collide (see for example figure 3), in order to be able to measure the end products of the interactions that take place. There is, however, a catch: most particles decay into different particles before reaching the detectors. From a single measured final state it is therefore impossible to determine whether a particle from the Standard Model, or a new particle was created in the original interaction.

However, by performing a great number of collisions, at the LHC about forty million per second, and counting the amount of times that a certain final state is measured, the probability of that final state to occur can be determined. This measured probability can then be compared against the prediction from the Standard Model. If the experimentally determined probability of a certain final state is found to be larger than predicted by the Standard Model, it may be concluded that particles must have been created that lead to that particular final state, but are not included in the Standard Model.

Theoretical predictions

Through the use of the Standard Model, the probability for a specific process to occur can be calculated. By adding the probabilities of all processes that lead to a certain final state, the probability of that final state can be determined. This may be compared with rolling two dice, where the final state is the total number of pips that the dice show. By throwing the two dice many times and counting how often some final state, for example 'ten pips', occurs, the probability of that final state can be determined experimentally.

To theoretically predict this probability, the probabilities of all possibilities that lead to this final state have to be added. There are three possibilities that lead to 'ten pips', namely: ⚄⚄, ⚃⚅ and ⚅⚃. The total amount of possible outcomes when throwing two dice is equal to $6 \times 6 = 36$, for each of the six possibilities of the first die, the second die can take six different values. For the case of fair dice, the probability of each possibility is the same, so the total probability of the final state 'ten pips' is equal to $3/36$, which comes down to a little over eight percent.

Individual processes in particles physics are often represented graphically by so-called *Feynman diagrams*. An example of a Feynman diagram is shown on the left-hand side in figure 4, where the particles A and B on the left represent the initial state (the particles that collide) and the particles C and D on the right the final state. By drawing and calculating all possible Feynman diagrams that give rise to the same final state (the particles C and D), the total probability of that state can be predicted.

There is, however, a complication: particles can temporarily split into two different particles, which may subsequently recombine into a single particle. This is for example the case in the Feynman diagram on the right in figure 4, which has the same final state as the left diagram. Since a particle resulting from such a splitting may itself split again, this gives rise to an infinite amount of possibilities that all lead to the same final state. As calculating infinitely
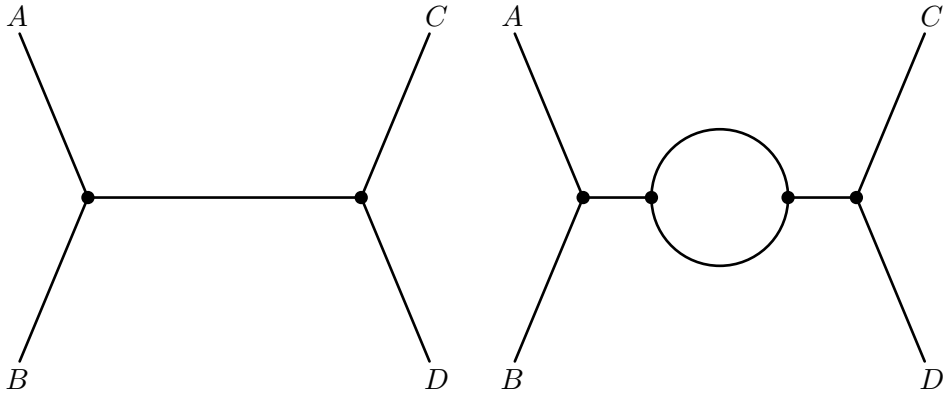
Figure 4 Two Feynman diagrams with possible scenarios in which the incoming particles A and B give rise to the final state composed of the particles C and D.

many diagrams would take a lot of time, this seems to be a problem.

The solution to this issue follows from the fact that every interaction between two particles (every black dot in the diagrams in figure 4) reduces the probability of a diagram. The exact factor by which the probability is reduced depends on the type of interactions. For example, for interactions between quarks and gluons, which are governed by the strong nuclear force, the probability of a certain scenario decreases roughly by a factor of ten for every two interactions. For these strong interactions, this reduction factor, known as a *coupling constant*, is denoted by the symbol α_s.

The infinite amount of scenarios that lead to a specific final state can then be organized according to the amount of interactions (black dots) that appear per scenario as

$$\text{Probability of final state} \; = \; c_0 \; + \; \alpha_s \times c_1 \; + \; \alpha_s^2 \times c_2 \; + \; \dots \,, \qquad (2)$$

where the dots denote the fact that the series continues to infinity. The first term on the right-hand side, c_0, represents the probability that no interaction takes place. In that case, the final state has to be equal to the initial state. The next term, $\alpha_s \times c_1$, is the combined probability of all the diagrams that contain exactly two interactions (like the left diagram in figure 4). Because of the reduction factor α_s, this term is about ten times as small as the previous term. The third term, $\alpha_s^2 \times c_2$, represents the probability of all diagrams with exactly four interactions (like the diagram on the right in figure 4). This term contains two instances of the reduction factor, hence it is about $10 \times 10 = 100$ times as small as the first term c_0.
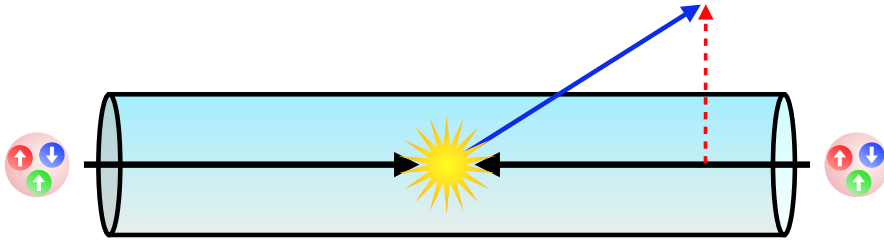
Figure 5 A collision between two incoming protons (the black arrows). The momentum of one of the produced particles is indicated by the blue arrow. The transverse momentum is the degree to which this momentum points in a direction perpendicular to the protons, indicated by the red dashed arrow.

Because every next term in equation (2) is smaller than the previous term, the series may be truncated at a given point, provided that one accepts that the prediction is no longer exact, but is an approximation instead. For example, if only the terms c_0 and $\alpha_s \times c_1$ are taken into account, the error that is made is proportional to the reduction factor of the third term, which amounts to $\alpha_s^2 \approx 1/100$. This shows the power of this method: By calculating only two terms in an infinite series, the true answer may be approximated to 1% accuracy.

Multiple measurements

Apart from the probability that a specific final state occurs, experiments are also able to measure certain properties of that state. An example of a property that can be measured is the so-called *transverse momentum*. Momentum is the amount of energy with which a particle moves in a certain direction. The term 'transverse' indicates that the momentum is measured in the direction perpendicular to the direction in which the protons at the LHC move before they collide, see figure 5.

The meaning of momentum becomes clear in an example from everyday life: There is more energy in a car moving with 50 kilometers per hour than there is in a car moving 30 kilometers per hour. The first car then has a larger momentum than the second. A fully loaded truck that drives at 50 kilometers per hour contains more energy than the car driving at 50 kilometers per hour, so the truck has an even larger momentum.

In nature, (transverse) momentum is a conserved quantity. It cannot be lost, only transferred from one particle to the next. In the scenario depicted in the diagrams in figure 4, the transverse momentum of the final state then has to be equal to the transverse momentum of the initial state. Since the momen-

tum is measured in the direction perpendicular to the incoming protons, the transverse momentum of the initial state (and therefore also the final state) has to be zero by definition. What is then the reason that nonzero transverse momenta are measured at the LHC?

Before the incoming particles are considered as the initial state, so before the diagrams in figure 4 begin, these particles can emit radiation. This radiation consists of so-called *soft* and *collinear* particles. Soft particles carry very little energy, so little in fact that they might not even be measured by the detectors. Collinear particles propagate in exactly the same direction as some other particle, so they are often also not detected as individual particles. By emitting this radiation, the incoming particles can obtain a transverse momentum that, by momentum conservation, must be equal (but opposite) to the transverse momentum of the soft and collinear radiation. The transverse momentum of the final state is then completely determined by the soft and collinear radiation, which is difficult to detect.
All measurements considered in this thesis are affected in one way or another by the soft and collinear radiation.

The energy of the soft and collinear radiation is vastly lower than the energy with which the incoming particles collide and eventually form the measured final state. Combined measurements of the probability of a certain final state and the transverse momentum are thus sensitive to processes that occur at two completely different energies.
Simultaneously considering a process occurring at a small energy E_{small} and a process occurring at a large energy E_{large}, leads to a problem in the theoretical calculation. It turns out that the coefficients $c_1, c_2, \ldots$ develop a dependence on the ratio of the energies, E_{large}/E_{small}. To be more specific, this ratio appears in every coefficient to the same power as the power of the coupling constant α_s that corresponds to that coefficient. The coefficient c_2, for example, depends on the ratio $(E_{large}/E_{small})^2$. A typical value of this ratio might be $E_{large}/E_{small} = 10$. In that case, this ratio effectively cancels the suppression from α_s in each term. The result is then that every term in equation (2) is roughly of the same size again, so that the series cannot be truncated anymore.

Effective theories, factorization and resummation

Because the issue occurs due to the attempt to describe two completely different processes simultaneously, the solution is very intuitive: try to separate the two processes and consider them individually.

The measurement of the transverse momentum is fully determined by the soft and collinear radiation and is completely insensitive to the energetic interaction between the two colliding particles. This measurement might then just as well be described by a simplified version of the Standard Model, from which everything that has to do with the energetic collision of the incoming particles is omitted. What remains after all (to this measurement) irrelevant information has been removed, is called an *effective theory*.

The principle of effective theories can be found in everyday life as well. A mason, for example, does not have to take the attractive force between atoms into account in order to build a house.

By means of an effective theory, the series in equation (2) can be split into two different series, one depending only on E_{small} and the other only depending on E_{large}. Such a division is called *factorization* since the series is split into two (independent) factors. As both of these factors now depend on only a single energy, they can be calculated individually, without the appearance of any large ratios. Both series can then be truncated after a certain amount of terms.

These factors are eventually recombined to obtain a single result. This process is known as *resummation* and effectively ensures that the ratios of E_{large}/E_{small} no longer appear in the coefficients of the series in equation (2). Instead, the total contribution of all these ratios is taken into account in a single, overarching coefficient that is calculated during the resummation process.

In general, it is not easy to prove that such a factorization is actually possible. Furthermore, the procedure depends on the exact measurement (in this case the transverse momentum) that is being done. For every variable that one would like to measure, a new factorization has to be proven.

The work described in this thesis encompasses the development of factorizations and resummations of processes in which two or more measurement are considered simultaneously. The procedure described above is significantly complicated in these situations. Every measurement might in principle correspond to a different energy, so multiple ratios of energies can occur in the coefficients of the series in (2). In that case, it has to be proven that the series can be factorized into as many factors as there are measurements. On the other hand, some of the measurements might also correspond to the same energies, so that a factorization into a smaller number of factors might be in order. One of the most important challenges when considering multiple measurements simultaneously is then to figure out which factorization has to be used in which situation.

In chapter 4, the simultaneous resummation of two measurements is carried

out, one of which is the transverse momentum. This resummation enables the calculation of predictions that are valid for all possible energies that these measurements might have with respect to each other and to the energy of the incoming, colliding particles. The final predictions are shown in three-dimensional graphs in figure 4.11. The results in this chapter represent the first predictions of the combination of the two measurements under consideration. This particular combination of measurements has been considered at experiments and may also be used to improve simulations of particle collisions made by certain computer programs.

The simultaneous factorization and resummation of two measurements is also the subject of chapter 5. Again, one of the measurements is the transverse momentum. Although the measurements in this chapter are not factorized and resummed for the first time, the developed procedure does lead to a more accurate result than the previous methods. This framework may be applied to the production of Higgs bosons, or that of hypothetical, unknown, heavy particles that are not predicted by the Standard Model.

The factorization that is derived in chapter 6 is a more general version than currently known in the literature and has many future applications. It is the first factorization that describes both the soft and the collinear behavior of a certain class of processes.

Finally, in chapter 7, the question of how many measurements can be resummed simultaneously is raised. The idea behind this question is the fact that all measurements ultimately measure some property of the same set of particles (the final state). It might then be the case that every property of the final state is known after a certain amount of measurements, so that subsequent measurements do not provide any new information. This means that additional measurements no longer give rise to new ratios of energies in the coefficients in equation (2). In that case, the resummation of these extra measurements is not required. The results of this chapter imply that the resummation of two measurements provides a large improvement over resumming only a single measurement. A reassuring conclusion, given the subjects of the other chapters in this thesis. In addition, the results show that resumming even more measurements provides an increasingly smaller improvement.

In short, the research described in this thesis is aimed at improving the precision of the predictions that the Standard Model makes. By determining the probability of these known processes with an increasing accuracy, it will hopefully become possible to discover new and unknown particles. After all, to find a needle in a haystack, one first has to know exactly what hay looks like.

Samenvatting

Dit proefschrift representeert onderzoek dat is gedaan in het veld van de elementaire deeltjesfysica. Hoewel het een fundamentele wetenschap is en weinig van doen heeft met het alledaagse leven, richt het zich wel op vragen die tot de verbeelding van velen zullen spreken, zoals "Waar is alles uit opgebouwd?", of "Wat houdt alles bij elkaar?". Juist omdat iedereen zich dit soort dingen wel eens afvraagt, is deze samenvatting gericht op een breed publiek.

Het doel van deze samenvatting is dan ook om de lezer een klein inzicht te verschaffen in de wereld van de elementaire deeltjes en de bescheiden bijdrage die dit proefschrift daaraan levert.

Het Standaardmodel

Hoewel het idee dat alle materie is opgebouwd uit kleine bouwstenen al duizenden jaren oud is, werden de eerste experimentele bewijzen hiervoor pas in de negentiende eeuw geleverd. De ontdekkingen volgden elkaar snel op en momenteel zijn er meer dan honderd verschillende soorten bouwstenen bekend. Deze deeltjes worden *atomen* genoemd en zijn ongeveer een miljoen keer zo klein als de dikte van een haar.

Met de ontdekking van het atoom leek de zoektocht naar de meest fundamentele bouwstenen van de natuur tot een einde te zijn gekomen. Het was dan ook een grote verrassing toen experimenten rond het begin van de twintigste eeuw aantoonden dat atomen zelf ook weer bestonden uit nog kleinere deeltjes. Ieder atoom bleek te bestaan uit een positief geladen kern, omringd door een wolk van negatief geladen deeltjes, genaamd *elektronen*, elk met een elektrische lading van -1. De atoomkern is op zijn beurt weer opgebouwd uit *protonen* en *neutronen*. Het proton heeft een elektrische lading van $+1$, precies tegenovergesteld aan dat van een elektron. Neutronen zijn, zoals de naam doet vermoeden, neutraal en hebben geen elektrische lading. Omdat atomen als geheel elektrisch neutraal zijn, moeten ze dus net zoveel protonen als elektronen bevatten. De precieze hoeveelheid protonen (en dus ook elektronen) in een atoom bepaalt over wat voor soort atoom het gaat. Een heliumatoom bevat bijvoorbeeld twee protonen en twee elektronen, terwijl een ijzeratoom bestaat uit zesentwintig protonen en elektronen. Het aantal neutronen in een atoom
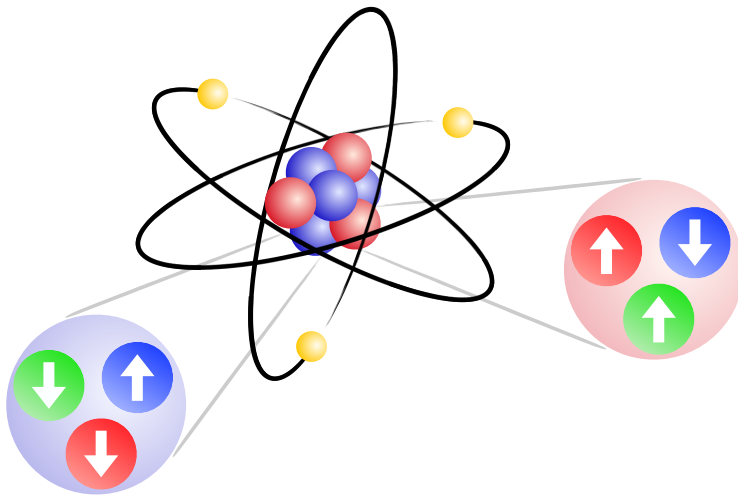
Figuur 1 Een schematische weergave van een atoom. Elektronen (de gele bollen) cirkelen rond de kern die protonen (de rode bollen) en neutronen (de blauwe bollen) bevat. The up- en down-quarks (de bollen met omhoog en omlaag wijzende pijlen) zijn zichtbaar in de vergrootte afbeeldingen van het proton en neutron.

kan variëren, wat leidt tot verschillende zogenaamde isotopen.

Ondanks dat het hebben van slechts drie fundamentele bouwstenen erg elegant was, bleken protonen en neutronen zelf ook weer te bestaan uit kleinere deeltjes. Deze deeltjes worden *up-quarks* en *down-quarks* genoemd en hebben een elektrische lading van respectievelijk $+2/3$ en $-1/3$. Een proton is opgebouwd uit twee up-quarks en een down-quark, terwijl een neutron twee down-quarks bevat, maar slechts een enkele up-quark. Een grafische weergave van een atoom is te vinden in figuur 1.

Buiten de elektrische lading blijken de quarks nog een extra soort lading te dragen: *kleurlading*. Ondanks de ietwat verwarrende naam heeft deze lading niks te maken met een daadwerkelijke kleur. Waar elektrische lading in twee verschillende vormen voorkomt (positief en negatief), zijn er drie mogelijke kleurladingen, die aangeduid worden met *rood*, *groen* en *blauw*. Net zoals een positief geladen deeltje en een negatief geladen deeltje samen neutraal zijn, vormen een rood, een groen en een blauw geladen deeltje samen een kleurneutraal geheel (ook wel *wit* genoemd). De drie quarks in een proton (of in een neutron) hebben alledrie een andere kleur, dus protonen (en neutronen) hebben netto geen kleurlading. Alleen kleur-neutrale deeltjes, zoals protonen en neutronen kunnen direct worden geobserveerd.

Voor zover bekend zijn up-quarks, down-quarks en elektronen fundamentele materiedeeltjes: ze kunnen niet meer verder worden opgedeeld in kleinere deeltjes. Er is nog één extra materiedeeltje, genaamd het *elektron-neutrino*, dat hier verder niet van belang is, maar alleen wordt genoemd voor de volledigheid. Alle bekende materie is uiteindelijk opgebouwd uit deze vier elementaire deeltjes.

Het bestaan van de vier materiedeeltjes wordt voorspeld door een theorie die werd opgesteld rond 1967 en die de ietwat hooghartige naam *het Standaardmodel* draagt. Het Standaardmodel voorspelt verder nog twee exacte kopieën van elk van de vier materiedeeltjes, met als enige verschil dat deze kopieën een grotere massa hebben. Ieder van deze drie collecties, elk bestaand uit vier materiedeeltjes, wordt een *generatie* genoemd.

Buiten het bestaan van de materiedeeltjes, beschrijft het Standaardmodel ook de krachten die tussen deze deeltjes werken. Er zijn drie krachten binnen het Standaardmodel: *elektromagnetisme*, de *sterke kernkracht* en de *zwakke kernkracht*. De vierde en laatste kracht die bekend is, de zwaartekracht, maakt geen deel uit van het Standaardmodel. Deeltjes kunnen alleen worden beïnvloed door een bepaalde kracht als ze een specifiek soort lading bezitten. Zo worden deeltjes alleen beïnvloed door de elektromagnetische kracht als ze een elektrische lading hebben en alleen door de sterke kernkracht als ze een kleurlading hebben.

De krachten tussen de materiedeeltjes worden overgebracht door krachtdragende deeltjes. De krachtdrager van de elektromagnetische kracht is het *foton*, het deeltje waar ook licht uit bestaat. De sterke kernkracht wordt overgebracht door het *gluon*. De drie quarks in het proton worden dus bij elkaar gehouden doordat ze gluonen met elkaar uitwisselen en zo een aantrekkende kracht op elkaar uitoefenen. De sterke kernkracht heeft zijn naam niet voor niets: de kracht tussen twee quarks in een proton is ongeveer gelijk aan de kracht die nodig zou zijn om drie Afrikaanse mannetjesolifanten op te tillen. Het grote verschil tussen gluonen en fotonen is het feit dat fotonen zelf geen elektrische lading dragen, maar gluonen wel een kleurlading hebben. Dit betekent dat gluonen ook kracht uitoefenen op elkaar.

De derde kracht, de zwakke kernkracht, wordt overgebracht door zogenaamde W- en Z-*deeltjes* en is verantwoordelijk voor het radioactief verval van sommige atomen. Het laatste deeltje dat deel uitmaakt van het Standaardmodel is het *Higgsdeeltje*. Het Higgsdeeltje is geen materiedeeltje en ook geen krachtdrager, maar is verantwoordelijk voor een mechanisme waardoor de andere deeltjes aan hun massa komen.

Figuur 2 De deeltjes die deel uitmaken van het Standaardmodel en het jaar van hun ontdekking. De eerste drie kolommen zijn de drie generaties materiedeeltjes en in de vierde kolom staan de krachtdragende deeltjes.

Een schematische weergave van de volledige deeltjesverzameling die het Standaardmodel bevat, is te vinden in figuur 2. Alle deeltjes die het Standaardmodel voorspelt, zijn ook daadwerkelijk aangetroffen in experimenten. Daarnaast is er geen enkel elementair deeltje gevonden dat niet door het Standaardmodel werd voorspeld. Het Standaardmodel is dus een enorm succesvolle theorie. Toch kan het niet de ultieme theorie van het universum zijn. Een van de vele zowel theoretische als experimentele motivaties hiervoor is bijvoorbeeld het feit dat de zwaartekracht niet door het Standaardmodel wordt beschreven.

De zoektocht naar nieuwe deeltjes, die niet door het Standaardmodel worden voorspeld, is een van de grootste uitdagingen van de moderne deeltjesfysica.
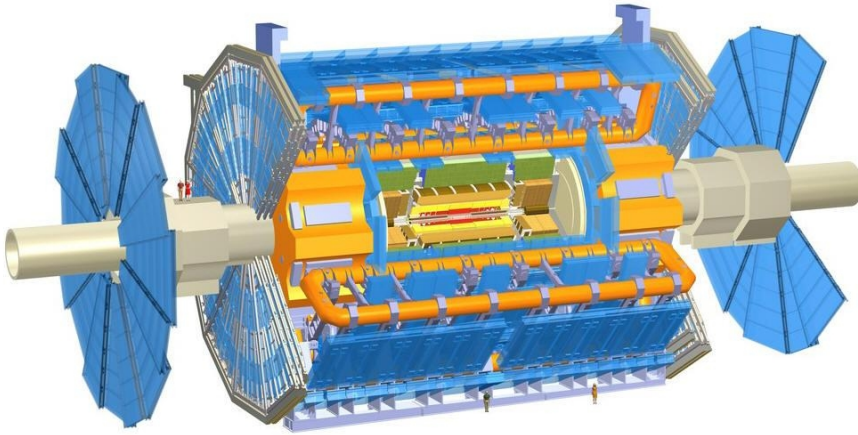
Figuur 3 De ATLAS detector. De detector is 46 meter lang en heeft een diameter van 25 meter. De protonen komen de detector binnen vanuit beide kanten en botsen in het midden. Om deze plek heen zitten meerdere lagen geavanceerde meetapparatuur, die in staat zijn om verschillende soorten deeltjes waar te nemen. De afgebeelde personen geven de schaal van de detector weer.

Zoeken naar deeltjes

De methode die men gebruikt om te zoeken naar nieuwe deeltjes is gebaseerd op de misschien wel bekendste formule uit de natuurkunde:

$$E = m\,c^2\,. \tag{1}$$

Hierin staat E voor energie, m voor massa en is c een constante waarde[1]. Wat deze formule dus zegt, is dat energie en massa in elkaar omgezet kunnen worden aan de hand van een bepaalde wisselkoers, die gelijk aan c^2 blijkt te zijn. De omzetting van massa in energie vindt bijvoorbeeld plaats bij het opwekken van kernenergie, of in de ontploffing van een atoombom. Exact dezelfde wisselkoers geldt echter ook de andere kant op, dus energie kan ook worden omgezet in massa.

De huidige experimentele opstelling die gebruik maakt van dit principe staat in Genève en heet de Large Hadron Collider (LHC). De LHC is een 27 kilometer lange, cirkelvormige tunnel, die zo'n honderd meter onder de grond ligt. In deze tunnel worden protonen eerst in tegenovergestelde richting versneld totdat ze meer dan 11 000 keer per seconde rond gaan. Vervolgens laat men de protonen tegen elkaar aan botsen, waardoor de quarks (en gluonen) in de

---

[1]Om precies te zijn, de lichtsnelheid, gelijk aan ongeveer een miljard kilometer per uur.

protonen interacties met elkaar kunnen aangaan. Vanwege de enorme hoeveelheid energie die in de beweging van de protonen zat, kunnen in deze interacties dan deeltjes ontstaan via vergelijking (1). Dit kunnen bekende deeltjes uit het Standaardmodel zijn, maar mogelijk ook nieuwe, tot nog toe onbekende deeltjes.

Bij de plek waar de protonen botsen zijn een hoop detectoren opgesteld (zie bijvoorbeeld figuur 3), zodat de eindproducten van de interacties die plaatsvinden kunnen worden gemeten. Er zit echter een addertje onder het gras: de meeste deeltjes vervallen in andere deeltjes voordat ze bij de detectoren aankomen. Het is dus onmogelijk om aan de hand van een gemeten eindtoestand met zekerheid te zeggen of er oorspronkelijk een deeltje uit het Standaardmodel, of een nieuw deeltje was gecreëerd.
Door heel veel botsingen te laten plaatsvinden, bij de LHC zo'n veertig miljoen per seconde, en het aantal keer te tellen dat een bepaalde eindtoestand wordt gemeten, kan echter wel de waarschijnlijkheid van die eindtoestand worden bepaald. Deze waarschijnlijkheid kan dan worden vergeleken met de voorspelling die het Standaardmodel doet. Indien de experimenteel gevonden waarschijnlijkheid van een specifieke eindtoestand groter is dan wat het Standaardmodel voorspelt, kan de conclusie worden getrokken dat er deeltjes moeten zijn ontstaan die ook tot die specifieke eindtoestand leiden, maar niet door het Standaardmodel worden beschreven.

Theoretische voorspellingen

Met behulp van het Standaardmodel kan de waarschijnlijkheid worden uitgerekend dat een specifiek proces voorkomt. Door alle waarschijnlijkheden van alle processen die tot een bepaalde eindtoestand leiden op te tellen, kan vervolgens de totale waarschijnlijkheid van die eindtoestand worden bepaald. Dit is te vergelijken met het gooien van twee dobbelstenen, waarbij de eindtoestand het totaal aantal ogen dat de dobbelstenen aangeven is. Door heel vaak twee dobbelstenen te gooien en te tellen hoe vaak bijvoorbeeld de eindtoestand 'tien ogen' voorkomt, kan de waarschijnlijkheid van die eindtoestand experimenteel worden bepaald.
Om deze waarschijnlijkheid theoretisch te voorspellen, moet de waarschijnlijkheid van elke mogelijkheid die tot deze eindtoestand leidt worden opgeteld. Er zijn in totaal drie mogelijkheden die tot 'tien ogen' leiden: ⚄⚄, ⚃⚅ en ⚅⚃. De totale hoeveelheid mogelijke uitkomsten bij het werpen van twee dobbelstenen is gelijk aan $6 \times 6 = 36$, voor elk van de zes mogelijkheden van de eerste dobbelsteen kan de andere dobbelsteen immers zes verschillende waar-
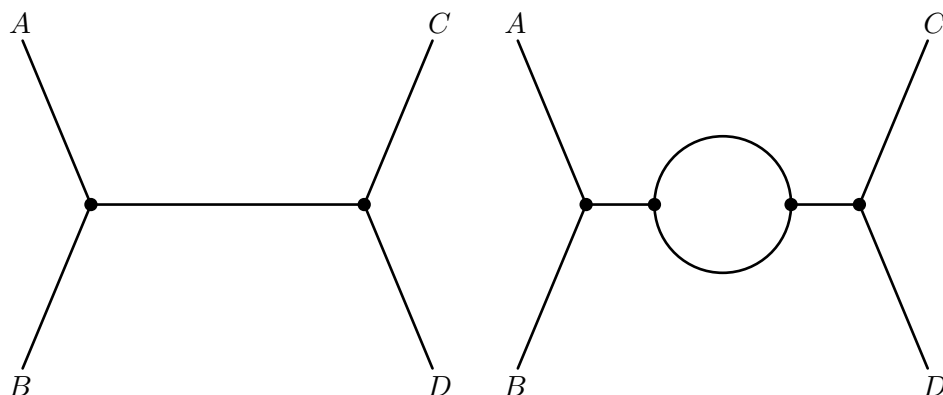
Figuur 4 Twee Feynman diagrammen met mogelijke scenarios waarop twee inkomende deeltjes A en B de eindtoestand bestaande uit deeltjes C en D kunnen vormen.

den aannemen. In het geval van eerlijke dobbelstenen is de waarschijnlijkheid van elke mogelijkheid gelijk, zodat de totale waarschijnlijkheid van de eindtoestand 'tien ogen' gelijk moet zijn aan 3/36, wat neerkomt op iets meer dan acht procent.

In de deeltjesfysica worden individuele processen vaak grafisch weergegeven in zogenaamde *Feynman diagrammen*. Een voorbeeld hiervan is weergegeven in de linkerafbeelding in figuur 4, waar de deeltjes A en B aan de linkerkant de begintoestand voorstellen (de deeltjes die botsen) en de deeltjes C en D aan de rechterkant de eindtoestand. Door alle mogelijke Feynman diagrammen die tot dezelfde eindtoestand (de deeltjes C en D) leiden te tekenen en uit te rekenen, kan dan de totale waarschijnlijkheid van die eindtoestand worden voorspeld. Er is echter een complicatie: deeltjes kunnen tijdelijk opsplitsen in twee andere deeltjes, die vervolgens weer samensmelten tot één deeltje. Dit is bijvoorbeeld het geval in het rechterdiagram in figuur 4, dat dezelfde eindtoestand heeft als het linkerdiagram. Aangezien een gesplitst deeltje zelf ook weer zou kunnen splitsen, zijn er dus oneindig veel mogelijkheden die tot dezelfde eindtoestand leiden. Omdat het uitrekenen van oneindig veel diagrammen wel erg veel tijd zou kosten, lijkt dit een probleem te zijn.

De oplossing van dit probleem zit in het feit dat elke interactie tussen twee deeltjes (elk zwart bolletje in de diagrammen in figuur 4) de waarschijnlijkheid van een diagram verkleint. De precieze factor waarmee de waarschijnlijkheid wordt verkleind hangt af van het soort interacties. Voor interacties tussen quarks en gluonen, beschreven door de sterke kernkracht, geldt bijvoorbeeld dat de waar-

schijnlijkheid van een bepaald scenario ongeveer tien keer kleiner wordt voor elke twee interacties. Deze verkleiningsfactor, ook wel *koppelingsconstante* genoemd, wordt voor de sterke kernkracht aangegeven met het symbool α_s.

De oneindige verzameling scenarios die tot een specifieke eindtoestand leiden kan vervolgens worden geordend aan de hand van de hoeveelheid interacties (zwarte bolletjes) die per scenario voorkomen als

$$\text{Waarschijnlijkheid van eindtoestand} = c_0 + \alpha_s \times c_1 + \alpha_s^2 \times c_2 + \ldots, \quad (2)$$

waar de puntjes aangeven dat de reeks zich tot in het oneindige voortzet. De eerste term aan de rechterkant, c_0, is de waarschijnlijkheid dat er geen interactie plaatsvindt. In dat geval moet de eindtoestand dus gelijk zijn aan de begintoestand. De volgende term, $\alpha_s \times c_1$, is de gezamenlijke waarschijnlijkheid van alle diagrammen met precies twee interacties (zoals het linkerdiagram in figuur 4). Vanwege de verkleiningsfactor α_s is deze term ongeveer tien keer zo klein als de voorgaande term. De derde term, $\alpha_s^2 \times c_2$, staat voor de waarschijnlijkheid van alle diagrammen met precies vier interacties (zoals het rechterdiagram in figuur 4). Deze term bevat twee verkleiningsfactoren en is dus ongeveer $10 \times 10 = 100$ keer zo klein als de eerste term c_0.

Omdat ieder volgende term in vergelijking (2) steeds kleiner is, kan de reeks op een bepaald moment worden afgekapt, mits men accepteert dat de voorspelling niet langer exact is, maar slechts een benadering. Als bijvoorbeeld alleen de termen c_0 en $\alpha_s \times c_1$ worden meegenomen, is de fout die wordt gemaakt proportioneel met de verkleiningsfactor van de derde term, ofwel $\alpha_s^2 \approx 1/100$. Dit laat de kracht van deze methode zien: Door slechts twee termen van een oneindige reeks uit te rekenen, kan het daadwerkelijke antwoord tot op 1% nauwkeurigheid worden benadert.

Meerdere metingen

Buiten de waarschijnlijkheid dat een bepaalde eindtoestand voorkomt kunnen experimenten ook eigenschappen van die eindtoestand meten. Een voorbeeld van een eigenschap die kan worden gemeten is de zogenaamde *transversale impuls*. Impuls is de hoeveelheid energie waarmee een deeltje zich in een bepaalde richting voortbeweegt. Het begrip 'transversaal' betekent dat de impuls wordt gemeten in de richting loodrecht op de richting waarin de protonen bij de LHC bewegen voordat ze tegen elkaar botsen, zie figuur 5.

De betekenis van impuls wordt duidelijker aan de hand van een voorbeeld uit het alledaagse leven: Er zit meer energie in een auto die met 50 kilometer per uur rijdt, dan in een auto die met 30 kilometer per uur rijdt. De eerste auto
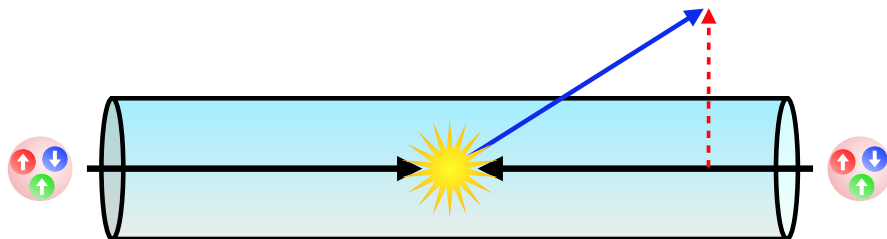
Figuur 5 Een botsing tussen twee inkomende protonen (de zwarte pijlen). De impuls van een van de geproduceerde deeltjes is weergegeven met de blauwe pijl. De transversale impuls is de mate waarin deze impuls loodrecht van de botsende protonen af wijst, weergegeven door de rode, gestippelde pijl.

heeft dan dus een grotere impuls dan de tweede. In een volgeladen vrachtwagen die met 50 kilometer per uur rijdt zit weer meer energie dan in de auto die met 50 kilometer per uur rijdt, zodat de vrachtwagen een nog grotere impuls heeft.

In de natuur is (transversale) impuls een behouden grootheid, het kan niet verloren gaan, maar alleen worden overgedragen van deeltje op deeltje. In het scenario afgebeeld in de diagrammen in figuur 4 moet de transversale impuls van de eindtoestand dus gelijk zijn aan de transversale impuls van de begintoestand. Aangezien de impuls wordt gemeten in de richting loodrecht op de inkomende protonen, zou de transversale impuls van de begintoestand (en dus ook de eindtoestand) per definitie gelijk aan nul moeten zijn. Hoe kan het dan toch zo zijn dat er een transversale impuls gemeten wordt bij de LHC?

Voordat de inkomende deeltjes als dusdanig worden beschouwd, dus voor de diagrammen in figuur 4 beginnen, kunnen deze deeltjes straling uitzenden. Deze straling bestaat uit zogenaamde *zachte* en *collineaire* deeltjes. Zachte deeltjes hebben heel weinig energie, zo weinig dat ze mogelijk niet eens gemeten worden door de detectoren. Collineaire deeltjes bewegen in exact dezelfde richting als een ander deeltje, zodat ze vaak ook niet individueel waargenomen kunnen worden door de detectoren. Door uitzending van deze straling kunnen de ingaande deeltjes dus een transversale impuls verkrijgen die vanwege impulsbehoud gelijk (maar tegengesteld) moet zijn aan de transversale impuls van de zachte en collineaire straling. De transversale impuls van de eindtoestand wordt dus eigenlijk volledig bepaald door de zachte en collineaire straling, ook al is die zelf erg lastig te meten.

Alle metingen die in dit proefschrift worden beschouwd, worden op een bepaalde manier beïnvloed door de zachte en collineaire straling.

De energie van de zachte en collineaire straling is vele malen lager dan de energie waarmee inkomende deeltjes tegen elkaar botsen en uiteindelijk de gemeten eindtoestand vormen. Gecombineerde metingen van zowel de waarschijnlijkheid van een bepaalde eindtoestand als de transversale impuls zijn dus gevoelig voor processen die plaatsvinden bij twee totaal verschillende energieën.

Het tegelijkertijd beschouwen van een proces met een kleine energie E_{klein} en een proces met een grote energie E_{groot}, levert een probleem op voor de theoretische berekening. Het blijkt dat de coefficiënten c_1, c_2, ... afhankelijk worden van de verhouding tussen de energieën, $E_{\text{groot}}/E_{\text{klein}}$. Om precies te zijn komt deze verhouding in elke coefficiënt voor tot dezelfde macht als de macht van de koppelingsconstante α_s die bij die coefficiënt hoort. Dus de coefficiënt c_2 is bijvoorbeeld afhankelijk van de verhouding $(E_{\text{groot}}/E_{\text{klein}})^2$. Een typische waarde van deze verhouding kan bijvoorbeeld $E_{\text{groot}}/E_{\text{klein}} = 10$ zijn. In dat geval doet deze verhouding in elke term dus effectief de verkleinende werking van α_s teniet. Het gevolg hiervan is dan dat iedere term in vergelijking (2) weer ongeveer even groot is, zodat de reeks niet meer afgekapt kan worden.

Effectieve theorieën, factorisatie en hersommatie

Aangezien het probleem ontstaat doordat wordt geprobeerd om twee totaal verschillende processen tegelijkertijd te beschrijven, is de oplossing eigenlijk heel intuïtief: probeer de processen los van elkaar te beschouwen.

De meting van de transversale impuls wordt volledig bepaald door de zachte en collineaire straling en is totaal ongevoelig voor de hoog-energetische interactie tussen de botsende deeltjes. Deze meting kan dus net zo goed beschreven worden met een versimpelde versie van het Standaardmodel, waaruit alles dat te maken heeft met de energieke botsing van de inkomende deeltjes weg is gelaten. Wat er overblijft nadat alle (voor deze meting) onbelangrijke zaken zijn weggehaald, wordt een *effectieve theorie* genoemd.

Het principe van effectieve theorieën is ook in het alledaagse leven terug te vinden. Een bouwvakker hoeft bijvoorbeeld geen rekening te houden met de aantrekkingskracht tussen atomen om een huis te kunnen bouwen.

Door middel van een effectieve theorie kan de reeks in vergelijking (2) worden opgesplitst in twee verschillende reeksen, één die alleen afhangt van E_{klein} en één die alleen van E_{groot} afhangt. Een dergelijke opsplitsing wordt een *factorisatie* genoemd, aangezien de reeks wordt gesplitst in twee (onafhankelijke) factoren. Aangezien allebei deze factoren nu van slechts één energie afhangen, kunnen ze allebei apart van elkaar worden uitgerekend, zonder dat er grote verhoudingen tevoorschijn komen. Beide reeksen kunnen dan dus worden afgekapt na een bepaald aantal termen.

Uiteindelijk worden deze factoren weer samengevoegd om zo één resultaat te krijgen. Dit proces wordt *hersommatie* genoemd en zorgt er effectief voor dat de verhoudingen $E_{\text{groot}}/E_{\text{klein}}$ niet langer voorkomen in de coëfficiënten van de reeks in vergelijking (2). In plaats daarvan wordt de totale bijdrage van al deze verhoudingen in één keer in rekening gebracht door een overkoepelende coëfficiënt die tijdens de hersommatie wordt berekend.

In de praktijk blijkt het lang niet altijd eenvoudig te zijn om te bewijzen dat een factorisatie daadwerkelijk mogelijk is. Daarnaast is de procedure afhankelijk van de precieze meting (in dit geval de transversale impuls) die wordt gedaan. Voor elke variabele die men zou willen meten, moet er een nieuwe factorisatie worden bewezen.

Het onderzoek beschreven in dit proefschrift omvat de ontwikkeling van factorisaties en hersommaties van processen waarin twee of meerdere metingen tegelijkertijd worden beschouwd. De hierboven beschreven procedure wordt in deze gevallen aanmerkelijk complexer. Met elke meting kan in principe een andere energie gemoeid gaan, zodat er meerdere verhoudingen van energieën kunnen voorkomen in de coëfficiënten van de reeks in vergelijking (2). In dat geval moet worden bewezen dat de reeks kan worden gefactoriseerd in evenveel factoren als er metingen zijn. Het kan echter ook zo zijn dat een aantal metingen met dezelfde energie corresponderen, zodat een factorisatie in aan kleinere hoeveelheid factoren van toepassing is. Een van de belangrijkste opgaven bij het beschouwen van meerdere metingen is dan ook om uit te zoeken welke factorisatie er wanneer gebruikt moet worden.

In hoofdstuk 4 wordt de gelijktijdige hersommatie van twee metingen uitgevoerd, waarvan er eentje de transversale impuls is. Dankzij deze hersommatie is het mogelijk om tot een voorspelling te komen die geldig is voor alle energieën die deze metingen zouden kunnen hebben ten opzichte van elkaar en de energie van de inkomende, botsende deeltjes. De uiteindelijke voorspellingen zijn weergegeven in de drie-dimensionale grafieken in figuur 4.11. De resultaten in dit hoofdstuk zijn de eerste voorspellingen van de combinatie van de twee metingen die hier worden beschouwd. Deze specifieke combinatie van metingen is experimenteel bekeken en kan ook worden gebruikt om computersimulaties van botsingen te verbeteren.

Ook in hoofdstuk 5 wordt de factorisatie en hersommatie van twee metingen beschreven. Wederom is een van de metingen de transversale impuls. Hoewel het niet voor het eerst is dat de metingen in dit hoofdstuk tegelijkertijd worden gefactoriseerd en gehersommeerd, leidt de ontwikkelde procedure wel tot een accurater resultaat dan de al bestaande methodes. Dit kan worden toegepast op de productie van Higgs bosonen, of dat van hypothetische, zware, onbe-

kende deeltjes die niet door het Standaardmodel worden voorspeld.

De factorisatie die wordt afgeleid in hoofdstuk 6 is een meer algemene versie dan bekend in de literatuur en heeft vele toepassingen in het verschiet. Het is de eerste factorisatie die zowel het zachte als het collineaire gedrag van een bepaalde klasse van processen beschrijft.

Tot slot wordt in hoofdstuk 7 de vraag gesteld hoeveel metingen er eigenlijk tegelijkertijd gehersommeerd kunnen worden. Het idee achter deze vraag is het feit dat alle metingen uiteindelijk iets meten aan dezelfde set deeltjes (de eindtoestand). Na een bepaald aantal metingen zou het dus zo kunnen zijn dat alle eigenschappen van de eindtoestand al bekend zijn en dat nieuwe metingen geen nieuwe informatie meer verschaffen. Dit betekent dat er bij het doen van extra metingen geen nieuwe verhoudingen tussen energieën meer tevoorschijn komen in de coefficiënten in vergelijking (2). Zodoende zal er dus ook geen hersommatie van deze extra metingen meer nodig zijn. De resultaten van dit hoofdstuk impliceren dat het hersommeren van twee metingen een grote verbetering geeft ten opzichte van het hersommeren van slechts één meting, een geruststellende conclusie gezien het onderwerp van de andere hoofdstukken in dit proefschrift. Daarnaast laat het resultaat zien dat het hersommeren van verdere metingen een steeds kleiner voordeel oplevert.

Het onderzoek in dit proefschrift is kort gezegd dus gericht op het verbeteren van de precisie van de voorspellingen die het Standaardmodel doet. Door de waarschijnlijkheid van deze bekende processen met een grotere nauwkeurigheid te bepalen, wordt het hopelijk mogelijk om nieuwe, onbekende deeltjes waar te nemen. Immers, om een speld in een hooiberg te vinden moet men eerst exact weten hoe het hooi eruit ziet.

Acknowledgements

This thesis and the scientific research that it represents could never have been realized without the aid of a large number of people. For this reason, I would like to dedicate these last few pages to all those who played a part in the development of this manuscript.

First and foremost, I would like to thank my supervisor, Wouter Waalewijn. I can honestly say that I could not have wished for a better mentor. Over the past four years you have guided me through the principles of conducting scientific research, taught me an enormous amount of physics and were always available to answer my questions. Most importantly, you managed to do so in a kind, patient and understanding manner, creating a very relaxed atmosphere in which I have always felt at ease. Besides instructing me, you also gave me plenty of opportunity to develop myself as a scientist and grow into a more independent researcher. Over the years, your role in our joined research projects slightly shifted from taking the lead to letting me figure things out by myself and offering council and guidance where needed. I am very grateful for all the input and feedback that you have provided me with over the past four years. Your extensive checking of the contents of this thesis has been vital in the realization of its final version. Thank you for four great years, in which I have both professionally and personally immensely enjoyed our collaboration. I would like to extend my gratitude to my formal promotor, Eric Laenen. Your door was always open and you were always willing to help me with both scientific questions and bureaucratic issues. In addition, I would like to thank you for the useful feedback on the first few chapters that you provided me with. My gratitude also goes to the members of the doctorate committee, who took the time to read this manuscript.

Each research project that has been incorporated in this thesis is the product of a collaboration with a number of other people. I would like to take this opportunity to express my thanks to my collaborators. Lisa, besides our joint work on joint resummation, you helped me navigate the maze that SCET can be at the beginning. Thank you for guiding me through the first steps of my PhD and for taking the time to answer my SCET-related questions, no matter how

naive, ill-phrased or tedious they might have been. Frank, your enthusiasm has been an inspiration for me in both of the projects we collaborated on. Thank you for all the meetings and discussions we had during the past few years, they were both educational and productive. Also, without your critical eye, the plots in our papers (and by extension in this thesis) would not have looked remotely as good as they do now. Johannes, our collaboration was probably the most extensive and intensive one. It has been a great pleasure to share both successes and setbacks, and to jointly tackle the latter in order to turn them into the former. Many thanks for the numerous hours spend debugging over skype together, for being my own personal `SCETlib`/`GIT` helpdesk and of course for having an uncanny way of submitting articles at exactly the right time. Besides working together, I have greatly enjoyed hanging out with you in Hamburg and Amsterdam as well as in San Diego. Andreas, I have learned a great deal from you during our work on the boundary between analytical and numerical resummation. Thank you for a very enjoyable and rewarding collaboration, for sharing your expertise in Monte Carlo parton showers with me and of course for the many interesting, fruitful and pleasant discussions we have had over coffee over the past few years.

Besides the fact that none of the results presented in this thesis could have been obtained without any of you, I have also greatly enjoyed working with each and all of you on a personal level.

Furthermore, I would like to express my gratitude towards Melissa, Solange, Sanne and Remco, for reading parts of this thesis and providing me with useful feedback. Without your help, the current version of this manuscript would be far less understandable and contain far more errors, inaccuracies, mistakes and typos.

At Nikhef, I have had the privilege of sharing my office with a number of amazing people. Ruben, Jacopo, Gilberto, Rubén, Sonia and Jake, thank you for the great atmosphere in our office, for the little chitchats, for your compassion at times, but mostly for your company and for all the laughs we shared. I would also like to thank Lorenzo and Pedro, who accompanied me on the intercontinental trips to the SCET conferences in Detroit and San Diego respectively. Traveling with you has been an amazing experience.

I would like to thank the whole Nikhef theory group for making me feel at home right from start. The communal lunches and coffee breaks were always very enjoyable and the annual day out has been something to look forward to year after year.

My thanks also go to my friends, both from highschool and from university. You guys provided me with the necessary distractions in the form of sports (both watching and playing), games, drinks or just having a good time in general.

I would like to express my thanks to my family for all the support they have given me and the interest they have shown in my research. A particular thank you goes to my sister and brother, Jamie and Morrison. Thank you for all the inside jokes and for the good times we continue to share.
I want to especially thank my parents, who have always been there for me and inspired me to develop myself. Neither this thesis, nor any of the steps that preceded it would have been possible without the loving environment that you have always provided. I am extremely grateful for everything you have done for me throughout the years and for all the encouragement and support you have always given me.

Finally, I would like to express my gratitude towards my wife. Sanne, thank you for always being there for me, for your endless support and for listening to my enthusiastic talks about particle physics. I am grateful for your never-ending encouragement and for your interest in my research. The summary in this thesis has greatly benefited from your expertise in the communication of science. Thank you for always bringing out the best of me, for being the color in my life and for continuing to share your love with me.

Bibliography

[1] G. Lustermans, W. J. Waalewijn and L. Zeune, *Joint transverse momentum and threshold resummation beyond NLL*, Phys. Lett. **B762** (2016) 447 [1605.02740].

[2] G. Lustermans, J. K. L. Michel, F. J. Tackmann and W. J. Waalewijn, *Joint two-dimensional resummation in q_T and 0-jettiness at NNLL*, JHEP **03** (2019) 124 [1901.03331].

[3] G. Lustermans, J. K. L. Michel and F. J. Tackmann, *Generalized Threshold Factorization with Full Collinear Dynamics*, 1908.00985.

[4] G. Lustermans, A. Papaefstathiou and W. J. Waalewijn, *How much joint resummation do we need?*, JHEP **10** (2019) 130 [1908.07529].

[5] J. J. Thomson, *Cathode rays*, Phil. Mag. Ser.5 **44** (1897) 293.

[6] E. Rutherford, *The scattering of alpha and beta particles by matter and the structure of the atom*, Phil. Mag. Ser.6 **21** (1911) 669.

[7] J. Chadwick, *The Existence of a Neutron*, Proc. Roy. Soc. Lond. **A136** (1932) 692.

[8] M. Gell-Mann, *A Schematic Model of Baryons and Mesons*, Phys. Lett. **8** (1964) 214.

[9] G. Zweig, *An SU(3) model for strong interaction symmetry and its breaking; Version 1*, Tech. Rep. CERN-TH-401, CERN, Jan, 1964.

[10] G. Zweig, *An SU(3) model for strong interaction symmetry and its breaking; Version 2*, in *Developments in the Quark Theory of Hadrons, Volume 1. 1964 - 1978* (D. Lichtenberg and S. P. Rosen, eds.), pp. 22–101. Hadronic Press, Nonantum, Mass., 1964.

[11] C.-N. Yang and R. L. Mills, *Conservation of Isotopic Spin and Isotopic Gauge Invariance*, Phys. Rev. **96** (1954) 191.

[12] S. L. Glashow, *Partial Symmetries of Weak Interactions*, Nucl. Phys. **22** (1961) 579.

[13] S. Weinberg, *A Model of Leptons, Phys. Rev. Lett.* **19** (1967) 1264.

[14] A. Salam, *Weak and Electromagnetic Interactions, Conf. Proc.* **C680519** (1968) 367.

[15] E. Fermi, *An attempt of a theory of beta radiation. 1., Z. Phys.* **88** (1934) 161.

[16] C. L. Cowan, F. Reines, F. B. Harrison, H. W. Kruse and A. D. McGuire, *Detection of the free neutrino: A Confirmation, Science* **124** (1956) 103.

[17] F. Englert and R. Brout, *Broken Symmetry and the Mass of Gauge Vector Mesons, Phys. Rev. Lett.* **13** (1964) 321.

[18] P. W. Higgs, *Broken Symmetries and the Masses of Gauge Bosons, Phys. Rev. Lett.* **13** (1964) 508.

[19] ATLAS collaboration, G. Aad et al., *Observation of a new particle in the search for the Standard Model Higgs boson with the ATLAS detector at the LHC, Phys. Lett.* **B716** (2012) 1 [1207.7214].

[20] CMS collaboration, S. Chatrchyan et al., *Observation of a New Boson at a Mass of 125 GeV with the CMS Experiment at the LHC, Phys. Lett.* **B716** (2012) 30 [1207.7235].

[21] L. D. Faddeev and V. N. Popov, *Feynman Diagrams for the Yang-Mills Field, Phys. Lett.* **B25** (1967) 29.

[22] H. Fritzsch, M. Gell-Mann and H. Leutwyler, *Advantages of the Color Octet Gluon Picture, Phys. Lett.* **47B** (1973) 365.

[23] C. G. Bollini and J. J. Giambiagi, *Dimensional Renormalization: The Number of Dimensions as a Regularizing Parameter, Nuovo Cim.* **B12** (1972) 20.

[24] G. 't Hooft and M. J. G. Veltman, *Regularization and Renormalization of Gauge Fields, Nucl. Phys.* **B44** (1972) 189.

[25] J. C. Collins, *Renormalization*, vol. 26 of *Cambridge Monographs on Mathematical Physics*. Cambridge University Press, Cambridge, 1986, 10.1017/CBO9780511622656.

[26] G. 't Hooft, *Renormalizable Lagrangians for Massive Yang-Mills Fields, Nucl. Phys.* **B35** (1971) 167.

[27] G. 't Hooft, *Dimensional regularization and the renormalization group*, *Nucl. Phys.* **B61** (1973) 455.

[28] S. Weinberg, *New approach to the renormalization group*, *Phys. Rev.* **D8** (1973) 3497.

[29] C. G. Callan, Jr., *Broken scale invariance in scalar field theory*, *Phys. Rev.* **D2** (1970) 1541.

[30] K. Symanzik, *Small distance behavior in field theory and power counting*, *Commun. Math. Phys.* **18** (1970) 227.

[31] PARTICLE DATA GROUP collaboration, M. Tanabashi et al., *Review of Particle Physics*, *Phys. Rev.* **D98** (2018) 030001.

[32] D. J. Gross and F. Wilczek, *Ultraviolet Behavior of Non-Abelian Gauge Theories*, *Phys. Rev. Lett.* **30** (1973) 1343.

[33] H. D. Politzer, *Reliable Perturbative Results for Strong Interactions?*, *Phys. Rev. Lett.* **30** (1973) 1346.

[34] A. Zee, *Study of the renormalization group for small coupling constants*, *Phys. Rev.* **D7** (1973) 3630.

[35] S. R. Coleman and E. J. Weinberg, *Radiative Corrections as the Origin of Spontaneous Symmetry Breaking*, *Phys. Rev.* **D7** (1973) 1888.

[36] F. Bloch and A. Nordsieck, *Note on the Radiation Field of the electron*, *Phys. Rev.* **52** (1937) 54.

[37] T. Kinoshita, *Mass singularities of Feynman amplitudes*, *J. Math. Phys.* **3** (1962) 650.

[38] T. D. Lee and M. Nauenberg, *Degenerate Systems and Mass Singularities*, *Phys. Rev.* **133** (1964) B1549.

[39] S. Dulat, T.-J. Hou, J. Gao, M. Guzzi, J. Huston, P. Nadolsky et al., *New parton distribution functions from a global analysis of quantum chromodynamics*, *Phys. Rev.* **D93** (2016) 033006 [1506.07443].

[40] L. A. Harland-Lang, A. D. Martin, P. Motylinski and R. S. Thorne, *Parton distributions in the LHC era: MMHT 2014 PDFs*, *Eur. Phys. J.* **C75** (2015) 204 [1412.3989].

[41] NNPDF collaboration, R. D. Ball et al., *Parton distributions for the LHC Run II*, *JHEP* **04** (2015) 040 [1410.8849].

[42] K. G. Wilson, *Confinement of Quarks*, *Phys. Rev.* **D10** (1974) 2445.

[43] X. Ji, *Parton Physics on a Euclidean Lattice*, *Phys. Rev. Lett.* **110** (2013) 262002 [`1305.1539`].

[44] X. Ji, *Parton Physics from Large-Momentum Effective Field Theory*, *Sci. China Phys. Mech. Astron.* **57** (2014) 1407 [`1404.6680`].

[45] J. C. Collins, D. E. Soper and G. F. Sterman, *Factorization of Hard Processes in QCD*, *Adv. Ser. Direct. High Energy Phys.* **5** (1989) 1 [`hep-ph/0409313`].

[46] R. P. Feynman, *Very high-energy collisions of hadrons*, *Phys. Rev. Lett.* **23** (1969) 1415.

[47] J. D. Bjorken and E. A. Paschos, *Inelastic Electron-Proton and γ-Proton Scattering, and the Structure of the Nucleon*, *Phys. Rev.* **185** (1969) 1975.

[48] S. D. Drell and T.-M. Yan, *Massive Lepton Pair Production in Hadron-Hadron Collisions at High-Energies*, *Phys. Rev. Lett.* **25** (1970) 316.

[49] J. C. Collins and D. E. Soper, *Parton Distribution and Decay Functions*, *Nucl. Phys.* **B194** (1982) 445.

[50] V. N. Gribov and L. N. Lipatov, *Deep inelastic e p scattering in perturbation theory*, *Sov. J. Nucl. Phys.* **15** (1972) 438.

[51] Y. L. Dokshitzer, *Calculation of the Structure Functions for Deep-Inelastic Scattering and e^+e^- Annihilation by Perturbation Theory in Quantum Chromodynamics.*, *Sov. Phys. JETP* **46** (1977) 641.

[52] G. Altarelli and G. Parisi, *Asymptotic Freedom in Parton Language*, *Nucl. Phys.* **B126** (1977) 298.

[53] S. Weinberg, *Effective Gauge Theories*, *Phys. Lett.* **91B** (1980) 51.

[54] S. R. Coleman, J. Wess and B. Zumino, *Structure of phenomenological Lagrangians. 1.*, *Phys. Rev.* **177** (1969) 2239.

[55] C. G. Callan, Jr., S. R. Coleman, J. Wess and B. Zumino, *Structure of phenomenological Lagrangians. 2.*, *Phys. Rev.* **177** (1969) 2247.

[56] S. Weinberg, *Baryon- and Lepton-Nonconserving Processes*, *Phys. Rev. Lett.* **43** (1979) 1566.

[57] Buchmüller, W. and Wyler, D., *Effective Lagrangian Analysis of New Interactions and Flavor Conservation*, Nucl. Phys. **B268** (1986) 621.

[58] L. F. Abbott and M. B. Wise, *The Effective Hamiltonian for Nucleon Decay*, Phys. Rev. **D22** (1980) 2208.

[59] B. Grzadkowski, M. Iskrzynski, M. Misiak and J. Rosiek, *Dimension-Six Terms in the Standard Model Lagrangian*, JHEP **10** (2010) 085 [`1008.4884`].

[60] R. Alonso, E. E. Jenkins, A. V. Manohar and M. Trott, *Renormalization Group Evolution of the Standard Model Dimension Six Operators III: Gauge Coupling Dependence and Phenomenology*, JHEP **04** (2014) 159 [`1312.2014`].

[61] W. Heisenberg and H. Euler, *Consequences of Dirac's theory of positrons*, Z. Phys. **98** (1936) 714 [`physics/0605038`].

[62] E. Fermi, *Trends to a Theory of beta Radiation. (In Italian)*, Nuovo Cim. **11** (1934) 1.

[63] N. Isgur and M. B. Wise, *Weak Decays of Heavy Mesons in the Static Quark Approximation*, Phys. Lett. **B232** (1989) 113.

[64] B. Grinstein, *The Static Quark Effective Theory*, Nucl. Phys. **B339** (1990) 253.

[65] E. Eichten and B. R. Hill, *An Effective Field Theory for the Calculation of Matrix Elements Involving Heavy Quarks*, Phys. Lett. **B234** (1990) 511.

[66] H. Georgi, *An Effective Field Theory for Heavy Quarks at Low-energies*, Phys. Lett. **B240** (1990) 447.

[67] W. E. Caswell and G. P. Lepage, *Effective Lagrangians for Bound State Problems in QED, QCD, and Other Field Theories*, Phys. Lett. **167B** (1986) 437.

[68] C. Cheung, P. Creminelli, A. L. Fitzpatrick, J. Kaplan and L. Senatore, *The Effective Field Theory of Inflation*, JHEP **03** (2008) 014 [`0709.0293`].

[69] W. D. Goldberger and I. Z. Rothstein, *An Effective field theory of gravity for extended objects*, Phys. Rev. **D73** (2006) 104029 [`hep-th/0409156`].

[70] G. Benfatto and G. Gallavotti, *Renormalization-group approach to the theory of the Fermi surface*, *Phys. Rev.* **B42** (1990) 9967.

[71] R. Shankar, *Renormalization group for interacting fermions in $d > 1$*, *Physica A: Statistical Mechanics and its Applications* **177** (1991) 530.

[72] S. Weinberg, *Effective action and renormalization group flow of anisotropic superconductors*, *Nucl. Phys.* **B413** (1994) 567 [`cond-mat/9306055`].

[73] A. Kapustin, T. McKinney and I. Z. Rothstein, *Wilsonian effective field theory of two-dimensional Van Hove singularities*, *Phys. Rev.* **B98** (2018) 035122 [`1804.01713`].

[74] H. Georgi, *On-shell effective field theory*, *Nucl. Phys.* **B361** (1991) 339.

[75] C. W. Bauer, S. Fleming and M. E. Luke, *Summing Sudakov logarithms in $B \to X_s\gamma$ in effective field theory*, *Phys. Rev.* **D63** (2000) 014006 [`hep-ph/0005275`].

[76] C. W. Bauer, S. Fleming, D. Pirjol and I. W. Stewart, *An Effective field theory for collinear and soft gluons: Heavy to light decays*, *Phys. Rev.* **D63** (2001) 114020 [`hep-ph/0011336`].

[77] C. W. Bauer and I. W. Stewart, *Invariant operators in collinear effective theory*, *Phys. Lett.* **B516** (2001) 134 [`hep-ph/0107001`].

[78] C. W. Bauer, D. Pirjol and I. W. Stewart, *Soft-collinear factorization in effective field theory*, *Phys. Rev.* **D65** (2002) 054022 [`hep-ph/0109045`].

[79] C. W. Bauer, D. Pirjol and I. W. Stewart, *Power counting in the soft-collinear effective theory*, *Phys. Rev.* **D66** (2002) 054005 [`hep-ph/0205289`].

[80] A. V. Manohar, T. Mehen, D. Pirjol and I. W. Stewart, *Reparameterization invariance for collinear operators*, *Phys. Lett.* **B539** (2002) 59 [`hep-ph/0204229`].

[81] C. W. Bauer, S. Fleming, D. Pirjol, I. Z. Rothstein and I. W. Stewart, *Hard scattering factorization from effective field theory*, *Phys. Rev.* **D66** (2002) 014017 [`hep-ph/0202088`].

[82] C. W. Bauer, D. Pirjol and I. W. Stewart, *Power suppressed operators and gauge invariance in SCET*, *Phys. Rev.* **D68** (2003) 034021 [`hep-ph/0303156`].

[83] A. V. Manohar and I. W. Stewart, *The Zero-Bin and Mode Factorization in Quantum Field Theory*, Phys. Rev. **D76** (2007) 074002 [`hep-ph/0605001`].

[84] M. Beneke, A. P. Chapovsky, M. Diehl and T. Feldmann, *Soft-collinear effective theory and heavy-to-light currents beyond leading power*, Nucl. Phys. **B643** (2002) 431 [`hep-ph/0206152`].

[85] M. Beneke and T. Feldmann, *Multipole-expanded soft-collinear effective theory with non-Abelian gauge symmetry*, Phys. Lett. **B553** (2003) 267 [`hep-ph/0211358`].

[86] I. W. Stewart, *Lectures on the Soft-Collinear Effective Theory.* MIT OpenCourseWare, `https://ocw.mit.edu/courses/physics/ 8-851-effective-field-theory-spring-2013/index.htm`, 2013.

[87] T. Becher, A. Broggio and A. Ferroglia, *Introduction to Soft-Collinear Effective Theory*, Lect. Notes Phys. **896** (2015) pp.1 [`1410.1892`].

[88] M. Beneke and T. Feldmann, *Factorization of heavy-to-light form factors in soft-collinear effective theory*, Nucl. Phys. **B685** (2004) 249 [`hep-ph/0311335`].

[89] C. Marcantonini and I. W. Stewart, *Reparameterization Invariant Collinear Operators*, Phys. Rev. **D79** (2009) 065028 [`0809.1093`].

[90] J. S. R. Chisholm, *Change of variables in quantum field theories*, Nucl. Phys. **26** (1961) 469.

[91] S. Kamefuchi, L. O'Raifeartaigh and A. Salam, *Change of variables and equivalence theorems in quantum field theories*, Nucl. Phys. **28** (1961) 529.

[92] V. V. Sudakov, *Vertex parts at very high-energies in quantum electrodynamics*, Sov. Phys. JETP **3** (1956) 65.

[93] A. V. Manohar, *Deep inelastic scattering as $x \to 1$ using soft-collinear effective theory*, Phys. Rev. **D68** (2003) 114019 [`hep-ph/0309176`].

[94] G. Parisi and R. Petronzio, *Small Transverse Momentum Distributions in Hard Processes*, Nucl. Phys. **B154** (1979) 427.

[95] J. C. Collins and D. E. Soper, *Back-To-Back Jets in QCD*, Nucl. Phys. **B193** (1981) 381.

[96] S. Fleming, A. H. Hoang, S. Mantry and I. W. Stewart, *Jets from massive unstable particles: Top-mass determination*, Phys. Rev. **D77** (2008) 074010 [`hep-ph/0703207`].

[97] K. S. M. Lee and I. W. Stewart, *Factorization for power corrections to $B \to X_s\gamma$ and $B \to X_u\ell\bar{\nu}$*, Nucl. Phys. **B721** (2005) 325 [`hep-ph/0409045`].

[98] T. T. Jouttenus, I. W. Stewart, F. J. Tackmann and W. J. Waalewijn, *The Soft Function for Exclusive N-Jet Production at Hadron Colliders*, Phys. Rev. **D83** (2011) 114030 [`1102.4344`].

[99] I. W. Stewart, F. J. Tackmann and W. J. Waalewijn, *Factorization at the LHC: From PDFs to Initial State Jets*, Phys. Rev. **D81** (2010) 094035 [`0910.0467`].

[100] I. W. Stewart, F. J. Tackmann and W. J. Waalewijn, *The Quark Beam Function at NNLL*, JHEP **09** (2010) 005 [`1002.2213`].

[101] J. R. Gaunt, M. Stahlhofen and F. J. Tackmann, *The Quark Beam Function at Two Loops*, JHEP **04** (2014) 113 [`1401.5478`].

[102] J. Gaunt, M. Stahlhofen and F. J. Tackmann, *The Gluon Beam Function at Two Loops*, JHEP **08** (2014) 020 [`1405.1044`].

[103] R. Abbate, M. Fickinger, A. H. Hoang, V. Mateu and I. W. Stewart, *Thrust at N^3LL with Power Corrections and a Precision Global Fit for $\alpha_s(m_Z)$*, Phys. Rev. **D83** (2011) 074021 [`1006.3080`].

[104] C. W. Bauer, D. Pirjol and I. W. Stewart, *Factorization and endpoint singularities in heavy-to-light decays*, Phys. Rev. **D67** (2003) 071502 [`hep-ph/0211069`].

[105] J.-Y. Chiu, A. Jain, D. Neill and I. Z. Rothstein, *A Formalism for the Systematic Treatment of Rapidity Logarithms in Quantum Field Theory*, JHEP **05** (2012) 084 [`1202.0814`].

[106] J.-y. Chiu, A. Jain, D. Neill and I. Z. Rothstein, *The Rapidity Renormalization Group*, Phys. Rev. Lett. **108** (2012) 151601 [`1104.0881`].

[107] C. W. Bauer, F. J. Tackmann, J. R. Walsh and S. Zuberi, *Factorization and Resummation for Dijet Invariant Mass Spectra*, Phys. Rev. **D85** (2012) 074006 [`1106.6047`].

[108] M. Procura, W. J. Waalewijn and L. Zeune, *Resummation of Double-Differential Cross Sections and Fully-Unintegrated Parton Distribution Functions*, JHEP **02** (2015) 117 [`1410.6483`].

[109] I. W. Stewart, F. J. Tackmann and W. J. Waalewijn, *N-Jettiness: An Inclusive Event Shape to Veto Jets*, Phys. Rev. Lett. **105** (2010) 092002 [`1004.2489`].

[110] J. R. Gaunt and M. Stahlhofen, *The Fully-Differential Quark Beam Function at NNLO*, JHEP **12** (2014) 146 [`1409.8281`].

[111] M. Dasgupta, F. A. Dreyer, K. Hamilton, P. F. Monni and G. P. Salam, *Logarithmic accuracy of parton showers: a fixed-order study*, JHEP **09** (2018) 033 [`1805.09327`].

[112] T. Sjöstrand, S. Mrenna and P. Z. Skands, *PYTHIA 6.4 Physics and Manual*, JHEP **05** (2006) 026 [`hep-ph/0603175`].

[113] T. Sjöstrand, S. Ask, J. R. Christiansen, R. Corke, N. Desai, P. Ilten et al., *An Introduction to PYTHIA 8.2*, Comput. Phys. Commun. **191** (2015) 159 [`1410.3012`].

[114] M. Bahr et al., *Herwig++ Physics and Manual*, Eur. Phys. J. **C58** (2008) 639 [`0803.0883`].

[115] J. Bellm et al., *Herwig 7.0/Herwig++ 3.0 release note*, Eur. Phys. J. **C76** (2016) 196 [`1512.01178`].

[116] J. Bellm et al., *Herwig 7.1 Release Note*, `1705.06919`.

[117] T. Gleisberg, S. Höche, F. Krauss, M. Schönherr, S. Schumann, F. Siegert et al., *Event generation with SHERPA 1.1*, JHEP **02** (2009) 007 [`0811.4622`].

[118] J. C. Collins, D. E. Soper and G. F. Sterman, *Factorization for Short Distance Hadron-Hadron Scattering*, Nucl. Phys. **B261** (1985) 104.

[119] J. C. Collins, D. E. Soper and G. F. Sterman, *Soft Gluons and Factorization*, Nucl. Phys. **B308** (1988) 833.

[120] A. Banfi, G. P. Salam and G. Zanderighi, *Semi-numerical resummation of event shapes*, JHEP **01** (2002) 018 [`hep-ph/0112156`].

[121] A. Banfi, G. P. Salam and G. Zanderighi, *Principles of general final-state resummation and automated implementation*, JHEP **03** (2005) 073 [`hep-ph/0407286`].

[122] A. Banfi, H. McAslan, P. F. Monni and G. Zanderighi, *A general method for the resummation of event-shape distributions in e^+e^- annihilation*, *JHEP* **05** (2015) 102 [1412.2126].

[123] W. Bizón, P. F. Monni, E. Re, L. Rottoli and P. Torrielli, *Momentum-space resummation for transverse observables and the Higgs $p_\perp$ at $N^3LL+NNLO$*, *JHEP* **02** (2018) 108 [1705.09127].

[124] H.-n. Li, *Unification of the k_T and threshold resummations*, *Phys. Lett.* **B454** (1999) 328 [hep-ph/9812363].

[125] E. Laenen, G. F. Sterman and W. Vogelsang, *Recoil and threshold corrections in short-distance cross sections*, *Phys. Rev.* **D63** (2001) 114018 [hep-ph/0010080].

[126] A. Kulesza, G. F. Sterman and W. Vogelsang, *Joint resummation in electroweak boson production*, *Phys. Rev.* **D66** (2002) 014011 [hep-ph/0202251].

[127] A. Kulesza, G. F. Sterman and W. Vogelsang, *Joint resummation for Higgs production*, *Phys. Rev.* **D69** (2004) 014012 [hep-ph/0309264].

[128] S. Marzani and V. Theeuwes, *Vector boson production in joint resummation*, *JHEP* **02** (2017) 127 [1612.01432].

[129] C. Muselli, S. Forte and G. Ridolfi, *Combined threshold and transverse momentum resummation for inclusive observables*, *JHEP* **03** (2017) 106 [1701.01464].

[130] S. Marzani, *Combining Q_T and small-x resummations*, *Phys. Rev.* **D93** (2016) 054047 [1511.06039].

[131] P. Pietrulewicz, F. J. Tackmann and W. J. Waalewijn, *Factorization and Resummation for Generic Hierarchies between Jets*, *JHEP* **08** (2016) 002 [1601.05088].

[132] A. J. Larkoski, I. Moult and D. Neill, *Toward Multi-Differential Cross Sections: Measuring Two Angularities on a Single Jet*, *JHEP* **09** (2014) 046 [1401.4458].

[133] M. Procura, W. J. Waalewijn and L. Zeune, *Joint resummation of two angularities at next-to-next-to-leading logarithmic order*, *JHEP* **10** (2018) 098 [1806.10622].

[134] D. W. Kolodrubetz, P. Pietrulewicz, I. W. Stewart, F. J. Tackmann and W. J. Waalewijn, *Factorization for Jet Radius Logarithms in Jet Mass Spectra at the LHC*, JHEP **12** (2016) 054 [1605.08038].

[135] A. Hornig, D. Kang, Y. Makris and T. Mehen, *Transverse Vetoes with Rapidity Cutoff in SCET*, JHEP **12** (2017) 043 [1708.08467].

[136] J. K. L. Michel, P. Pietrulewicz and F. J. Tackmann, *Jet Veto Resummation with Jet Rapidity Cuts*, JHEP **04** (2019) 142 [1810.12911].

[137] X. Liu, S.-O. Moch and F. Ringer, *Threshold and jet radius joint resummation for single-inclusive jet production*, Phys. Rev. Lett. **119** (2017) 212001 [1708.04641].

[138] X. Liu, S.-O. Moch and F. Ringer, *Phenomenology of single-inclusive jet production with jet radius and threshold resummation*, Phys. Rev. **D97** (2018) 056026 [1801.07284].

[139] D. Bertolini, D. Kolodrubetz, D. Neill, P. Pietrulewicz, I. W. Stewart, F. J. Tackmann et al., *Soft Functions for Generic Jet Algorithms and Observables at Hadron Colliders*, JHEP **07** (2017) 099 [1704.08262].

[140] M. Dasgupta and G. P. Salam, *Resummation of non-global QCD observables*, Phys. Lett. **B512** (2001) 323 [hep-ph/0104277].

[141] A. Banfi, G. Marchesini and G. Smye, *Away-from-jet energy flow*, JHEP **08** (2002) 006 [hep-ph/0206076].

[142] Y. Hatta and T. Ueda, *Resummation of non-global logarithms at finite N_c*, Nucl. Phys. **B874** (2013) 808 [1304.6930].

[143] A. J. Larkoski, I. Moult and D. Neill, *Non-Global Logarithms, Factorization, and the Soft Substructure of Jets*, JHEP **09** (2015) 143 [1501.04596].

[144] S. Caron-Huot, *Resummation of non-global logarithms and the BFKL equation*, JHEP **03** (2018) 036 [1501.03754].

[145] T. Becher, M. Neubert, L. Rothen and D. Y. Shao, *Effective Field Theory for Jet Processes*, Phys. Rev. Lett. **116** (2016) 192001 [1508.06645].

[146] I. W. Stewart, F. J. Tackmann and W. J. Waalewijn, *The Beam Thrust Cross Section for Drell-Yan at NNLL Order*, Phys. Rev. Lett. **106** (2011) 032001 [1005.4060].

[147] ATLAS collaboration, G. Aad et al., *Measurement of event-shape observables in $Z \to \ell^+\ell^-$ events in pp collisions at $\sqrt{s} = 7$ TeV with the ATLAS detector at the LHC*, *Eur. Phys. J.* **C76** (2016) 375 [1602.08980].

[148] S. Alioli, C. W. Bauer, C. J. Berggren, A. Hornig, F. J. Tackmann, C. K. Vermilion et al., *Combining Higher-Order Resummation with Multiple NLO Calculations and Parton Showers in GENEVA*, *JHEP* **09** (2013) 120 [1211.7049].

[149] S. Alioli, C. W. Bauer, C. Berggren, F. J. Tackmann and J. R. Walsh, *Drell-Yan production at NNLL′+NNLO matched to parton showers*, *Phys. Rev.* **D92** (2015) 094020 [1508.01475].

[150] A. Jain, M. Procura and W. J. Waalewijn, *Fully-Unintegrated Parton Distribution and Fragmentation Functions at Perturbative k_T*, *JHEP* **04** (2012) 132 [1110.0839].

[151] J. R. Gaunt, *Glauber Gluons and Multiple Parton Interactions*, *JHEP* **07** (2014) 110 [1405.2080].

[152] M. Zeng, *Drell-Yan process with jet vetoes: breaking of generalized factorization*, *JHEP* **10** (2015) 189 [1507.01652].

[153] I. Z. Rothstein and I. W. Stewart, *An Effective Field Theory for Forward Scattering and Factorization Violation*, *JHEP* **08** (2016) 025 [1601.04695].

[154] Z. Ligeti, I. W. Stewart and F. J. Tackmann, *Treating the b quark distribution function with reliable uncertainties*, *Phys. Rev.* **D78** (2008) 114014 [0807.1926].

[155] S. Gangal, M. Stahlhofen and F. J. Tackmann, *Rapidity-Dependent Jet Vetoes*, *Phys. Rev.* **D91** (2015) 054023 [1412.4792].

[156] I. W. Stewart, F. J. Tackmann, J. R. Walsh and S. Zuberi, *Jet p_T resummation in Higgs production at NNLL'+NNLO*, *Phys. Rev.* **D89** (2014) 054001 [1307.1808].

[157] J. C. Collins, D. E. Soper and G. F. Sterman, *Transverse Momentum Distribution in Drell-Yan Pair and W and Z Boson Production*, *Nucl. Phys.* **B250** (1985) 199.

[158] T. Becher and M. Neubert, *Drell-Yan Production at Small q_T, Transverse Parton Distributions and the Collinear Anomaly*, *Eur. Phys. J.* **C71** (2011) 1665 [1007.4005].

[159] J. Collins, *Foundations of perturbative QCD*. Cambridge University Press, 2013.

[160] M. G. Echevarría, A. Idilbi and I. Scimemi, *Factorization Theorem For Drell-Yan At Low q_T And Transverse Momentum Distributions On-The-Light-Cone*, JHEP **07** (2012) 002 [`1111.4996`].

[161] S. Frixione, P. Nason and G. Ridolfi, *Problems in the resummation of soft-gluon effects in the transverse-momentum distributions of massive vector bosons in hadronic collisions*, Nucl. Phys. **B542** (1999) 311 [`hep-ph/9809367`].

[162] P. F. Monni, E. Re and P. Torrielli, *Higgs Transverse-Momentum Resummation in Direct Space*, Phys. Rev. Lett. **116** (2016) 242001 [`1604.02191`].

[163] M. A. Ebert and F. J. Tackmann, *Resummation of Transverse Momentum Distributions in Distribution Space*, JHEP **02** (2017) 110 [`1611.08610`].

[164] J. C. Collins and D. E. Soper, *Back-To-Back Jets: Fourier Transform from b to k_T*, Nucl. Phys. **B197** (1982) 446.

[165] M. A. Ebert, I. W. Stewart and Y. Zhao, *Determining the Nonperturbative Collins-Soper Kernel From Lattice QCD*, Phys. Rev. **D99** (2019) 034505 [`1811.00026`].

[166] D. Neill, I. Z. Rothstein and V. Vaidya, *The Higgs Transverse Momentum Distribution at NNLL and its Theoretical Errors*, JHEP **12** (2015) 097 [`1503.00005`].

[167] U. D'Alesio, M. G. Echevarría, S. Melis and I. Scimemi, *Non-perturbative QCD effects in q_T spectra of Drell-Yan and Z-boson production*, JHEP **11** (2014) 098 [`1407.3311`].

[168] P. V. Landshoff and J. C. Polkinghorne, *Calorimeter Triggers for Hard Collisions*, Phys. Rev. **D18** (1978) 3344.

[169] C. Goebel, F. Halzen and D. M. Scott, *Double Drell-Yan Annihilations in Hadron Collisions: Novel Tests of the Constituent Picture*, Phys. Rev. **D22** (1980) 2789.

[170] F. Takagi, *Multiple Production of Quark Jets Off Nuclei*, Phys. Rev. Lett. **43** (1979) 1296.

[171] H. D. Politzer, *Power Corrections at Short Distances*, *Nucl. Phys.* **B172** (1980) 349.

[172] L. G. Almeida, S. D. Ellis, C. Lee, G. Sterman, I. Sung and J. R. Walsh, *Comparing and counting logs in direct and effective methods of QCD resummation*, *JHEP* **04** (2014) 174 [`1401.4460`].

[173] D. Bertolini, M. P. Solon and J. R. Walsh, *Integrated and Differential Accuracy in Resummed Cross Sections*, *Phys. Rev.* **D95** (2017) 054024 [`1701.07919`].

[174] M. A. Ebert, J. K. L. Michel, F. J. Tackmann et al., *SCETlib: A C++ Package for Numerical Calculations in QCD and Soft-Collinear Effective Theory*, *DESY-17-099* (2018) .

[175] J. M. Campbell and R. K. Ellis, *An Update on vector boson pair production at hadron colliders*, *Phys. Rev.* **D60** (1999) 113006 [`hep-ph/9905386`].

[176] J. M. Campbell, R. K. Ellis and C. Williams, *Vector boson pair production at the LHC*, *JHEP* **07** (2011) 018 [`1105.0020`].

[177] J. M. Campbell, R. K. Ellis and W. T. Giele, *A Multi-Threaded Version of MCFM*, *Eur. Phys. J.* **C75** (2015) 246 [`1503.06182`].

[178] E. Laenen, G. F. Sterman and W. Vogelsang, *Higher-order QCD corrections in prompt photon production*, *Phys. Rev. Lett.* **84** (2000) 4296 [`hep-ph/0002078`].

[179] A. Banfi and E. Laenen, *Joint resummation for heavy quark production*, *Phys. Rev.* **D71** (2005) 034003 [`hep-ph/0411241`].

[180] G. Bozzi, B. Fuks and M. Klasen, *Joint resummation for slepton pair production at hadron colliders*, *Nucl. Phys.* **B794** (2008) 46 [`0709.3057`].

[181] J. Debove, B. Fuks and M. Klasen, *Joint Resummation for Gaugino Pair Production at Hadron Colliders*, *Nucl. Phys.* **B849** (2011) 64 [`1102.4422`].

[182] Y. Li, D. Neill and H. X. Zhu, *An Exponential Regulator for Rapidity Divergences*, *Submitted to: Phys. Rev. D* (2016) [`1604.00392`].

[183] T. Kasemets, W. J. Waalewijn and L. Zeune, *Calculating Soft Radiation at One Loop*, *JHEP* **03** (2016) 153 [`1512.00857`].

[184] S. Mantry and F. Petriello, *Factorization and Resummation of Higgs Boson Differential Distributions in Soft-Collinear Effective Theory*, *Phys. Rev.* **D81** (2010) 093007 [`0911.4135`].

[185] G. T. Bodwin, *Factorization of the Drell-Yan Cross Section in Perturbation Theory*, *Phys. Rev.* **D31** (1985) 2616.

[186] C. Lee and G. F. Sterman, *Momentum Flow Correlations from Event Shapes: Factorized Soft Gluons and Soft-Collinear Effective Theory*, *Phys. Rev.* **D75** (2007) 014022 [`hep-ph/0611061`].

[187] A. Idilbi and T. Mehen, *On the equivalence of soft and zero-bin subtractions*, *Phys. Rev.* **D75** (2007) 114017 [`hep-ph/0702022`].

[188] T. Becher, M. Neubert and G. Xu, *Dynamical Threshold Enhancement and Resummation in Drell-Yan Production*, *JHEP* **07** (2008) 030 [`0710.0680`].

[189] T. Becher, M. Neubert and B. D. Pecjak, *Factorization and Momentum-Space Resummation in Deep-Inelastic Scattering*, *JHEP* **01** (2007) 076 [`hep-ph/0607228`].

[190] M. Procura and W. J. Waalewijn, *Fragmentation in Jets: Cone and Threshold Effects*, *Phys. Rev.* **D85** (2012) 114041 [`1111.6605`].

[191] A. Vogt, F. Herzog, S. Moch, B. Ruijl, T. Ueda and J. A. M. Vermaseren, *Anomalous dimensions and splitting functions beyond the next-to-next-to-leading order*, *PoS* **LL2018** (2018) 050 [`1808.08981`].

[192] T. van Ritbergen, J. A. M. Vermaseren and S. A. Larin, *The Four-loop β-function in quantum chromodynamics*, *Phys. Lett.* **B400** (1997) 379 [`hep-ph/9701390`].

[193] M. Czakon, *The Four-loop QCD β-function and anomalous dimensions*, *Nucl. Phys.* **B710** (2005) 485 [`hep-ph/0411261`].

[194] A. Idilbi, X.-d. Ji and F. Yuan, *Transverse momentum distribution through soft-gluon resummation in effective field theory*, *Phys. Lett.* **B625** (2005) 253 [`hep-ph/0507196`].

[195] A. Idilbi, X.-d. Ji and F. Yuan, *Resummation of threshold logarithms in effective field theory for DIS, Drell-Yan and Higgs production*, *Nucl. Phys.* **B753** (2006) 42 [`hep-ph/0605068`].

[196] A. Idilbi, X.-d. Ji, J.-P. Ma and F. Yuan, *Threshold resummation for Higgs production in effective field theory*, Phys. Rev. **D73** (2006) 077501 [hep-ph/0509294].

[197] V. Ahrens, T. Becher, M. Neubert and L. L. Yang, *Renormalization-Group Improved Prediction for Higgs Production at Hadron Colliders*, Eur. Phys. J. **C62** (2009) 333 [0809.4283].

[198] S. Moch, J. A. M. Vermaseren and A. Vogt, *Three-loop results for quark and gluon form-factors*, Phys. Lett. **B625** (2005) 245 [hep-ph/0508055].

[199] S. Moch, J. A. M. Vermaseren and A. Vogt, *The Quark form-factor at higher orders*, JHEP **08** (2005) 049 [hep-ph/0507039].

[200] S. Catani and M. Grazzini, *Higgs Boson Production at Hadron Colliders: Hard-Collinear Coefficients at the NNLO*, Eur. Phys. J. **C72** (2012) 2013 [1106.4652].

[201] S. Catani, L. Cieri, D. de Florian, G. Ferrera and M. Grazzini, *Vector-boson production at hadron colliders: hard-collinear coefficients at the NNLO*, Eur. Phys. J. **C72** (2012) 2195 [1209.0158].

[202] T. Gehrmann, T. Lübbert and L. L. Yang, *Transverse parton distribution functions at next-to-next-to-leading order: the quark-to-quark case*, Phys. Rev. Lett. **109** (2012) 242003 [1209.0682].

[203] T. Gehrmann, T. Lübbert and L. L. Yang, *Calculation of the transverse parton distribution functions at next-to-next-to-leading order*, JHEP **06** (2014) 155 [1403.6451].

[204] M. G. Echevarría, I. Scimemi and A. Vladimirov, *Universal transverse momentum dependent soft function at NNLO*, Phys. Rev. **D93** (2016) 054004 [1511.05590].

[205] T. Lübbert, J. Oredsson and M. Stahlhofen, *Rapidity renormalized TMD soft and beam functions at two loops*, JHEP **03** (2016) 168 [1602.01829].

[206] M. G. Echevarría, I. Scimemi and A. Vladimirov, *Unpolarized Transverse Momentum Dependent Parton Distribution and Fragmentation Functions at next-to-next-to-leading order*, JHEP **09** (2016) 004 [1604.07869].

[207] Y. Li, S. Mantry and F. Petriello, *An Exclusive Soft Function for Drell-Yan at Next-to-Next-to-Leading Order*, Phys. Rev. **D84** (2011) 094014 [1105.5171].

[208] S. Moch, J. A. M. Vermaseren and A. Vogt, *The three-loop splitting functions in QCD: The non-singlet case*, *Nucl. Phys.* **B688** (2004) 101 [hep-ph/0403192].

[209] P. A. Baikov, K. G. Chetyrkin, A. V. Smirnov, V. A. Smirnov and M. Steinhauser, *Quark and gluon form factors to three loops*, *Phys. Rev. Lett.* **102** (2009) 212002 [0902.3519].

[210] A. A. Vladimirov, *Correspondence between Soft and Rapidity Anomalous Dimensions*, *Phys. Rev. Lett.* **118** (2017) 062001 [1610.05791].

[211] Y. Li and H. X. Zhu, *Bootstrapping Rapidity Anomalous Dimensions for Transverse-Momentum Resummation*, *Phys. Rev. Lett.* **118** (2017) 022004 [1604.01404].

[212] G. F. Sterman, *Summation of large corrections to short-distance hadronic cross sections*, *Nucl. Phys.* **B281** (1987) 310.

[213] S. Catani and L. Trentadue, *Resummation of the QCD Perturbative Series for Hard Processes*, *Nucl. Phys.* **B327** (1989) 323.

[214] V. Ravindran, J. Smith and W. L. van Neerven, *QCD threshold corrections to di-lepton and Higgs rapidity distributions beyond N^2LO*, *Nucl. Phys.* **B767** (2007) 100 [hep-ph/0608308].

[215] D. Westmark and J. F. Owens, *Enhanced threshold resummation formalism for lepton pair production and its effects in the determination of parton distribution functions*, *Phys. Rev.* **D95** (2017) 056024 [1701.06716].

[216] P. Banerjee, G. Das, P. K. Dhani and V. Ravindran, *Threshold resummation of the rapidity distribution for Higgs production at NNLO+NNLL*, *Phys. Rev.* **D97** (2018) 054024 [1708.05706].

[217] P. Banerjee, G. Das, P. K. Dhani and V. Ravindran, *Threshold resummation of the rapidity distribution for Drell-Yan production at NNLO+NNLL*, *Phys. Rev.* **D98** (2018) 054018 [1805.01186].

[218] D. Appell, G. F. Sterman and P. B. Mackenzie, *Soft Gluons and the Normalization of the Drell-Yan Cross-section*, *Nucl. Phys.* **B309** (1988) 259.

[219] L. Magnea, *All-order summation and two-loop results for the Drell-Yan cross section*, *Nucl. Phys.* **B349** (1991) 703.

[220] G. P. Korchemsky and G. Marchesini, *Structure function for large x and renormalization of Wilson loop*, *Nucl. Phys.* **B406** (1993) 225 [`hep-ph/9210281`].

[221] H. Contopanagos, E. Laenen and G. F. Sterman, *Sudakov factorization and resummation*, *Nucl. Phys.* **B484** (1997) 303 [`hep-ph/9604313`].

[222] S. Catani, M. L. Mangano, P. Nason and L. Trentadue, *The Resummation of soft gluons in hadronic collisions*, *Nucl. Phys.* **B478** (1996) 273 [`hep-ph/9604351`].

[223] A. V. Belitsky, *Two-loop renormalization of Wilson loop for Drell-Yan production*, *Phys. Lett.* **B442** (1998) 307 [`hep-ph/9808389`].

[224] S. Moch and A. Vogt, *Higher-order soft corrections to lepton pair and Higgs boson production*, *Phys. Lett.* **B631** (2005) 48 [`hep-ph/0508265`].

[225] E. Laenen and L. Magnea, *Threshold resummation for electroweak annihilation from DIS data*, *Phys. Lett.* **B632** (2006) 270 [`hep-ph/0508284`].

[226] A. Mukherjee and W. Vogelsang, *Threshold resummation for W-boson production at RHIC*, *Phys. Rev.* **D73** (2006) 074005 [`hep-ph/0601162`].

[227] P. Bolzoni, *Threshold resummation of Drell-Yan rapidity distributions*, *Phys. Lett.* **B643** (2006) 325 [`hep-ph/0609073`].

[228] M. Bonvini, S. Forte and G. Ridolfi, *Soft gluon resummation of Drell-Yan rapidity distributions: Theory and phenomenology*, *Nucl. Phys.* **B847** (2011) 93 [`1009.5691`].

[229] M. Bonvini, S. Marzani, J. Rojo, L. Rottoli, M. Ubiali, R. D. Ball et al., *Parton distributions with threshold resummation*, *JHEP* **09** (2015) 191 [`1507.01006`].

[230] B. Fuks, M. Klasen, D. R. Lamprea and M. Rothering, *Precision predictions for electroweak superpartner production at hadron colliders with Resummino*, *Eur. Phys. J.* **C73** (2013) 2480 [`1304.0790`].

[231] M. Bonvini and S. Marzani, *Resummed Higgs cross section at N^3LL*, *JHEP* **09** (2014) 007 [`1405.3654`].

[232] T. Schmidt and M. Spira, *Higgs Boson Production via Gluon Fusion: Soft-Gluon Resummation including Mass Effects*, *Phys. Rev.* **D93** (2016) 014022 [`1509.00195`].

[233] A. A H, A. Chakraborty, G. Das, P. Mukherjee and V. Ravindran, *Resummed prediction for Higgs boson production through $b\bar{b}$ annihilation at N^3LO+N^3LL*, 1905.03771.

[234] D. Bonocore, E. Laenen, L. Magnea, L. Vernazza and C. D. White, *Non-abelian factorisation for next-to-leading-power threshold logarithms*, *JHEP* **12** (2016) 121 [1610.06842].

[235] V. Del Duca, E. Laenen, L. Magnea, L. Vernazza and C. D. White, *Universality of next-to-leading power threshold effects for colourless final states in hadronic collisions*, *JHEP* **11** (2017) 057 [1706.04018].

[236] M. Beneke, A. Broggio, M. Garny, S. Jaskiewicz, R. Szafron, L. Vernazza et al., *Leading-logarithmic threshold resummation of the Drell-Yan process at next-to-leading power*, *JHEP* **03** (2019) 043 [1809.10631].

[237] C. Anastasiou, C. Duhr, F. Dulat, E. Furlan, T. Gehrmann, F. Herzog et al., *Higgs boson gluon–fusion production at threshold in N^3LO QCD*, *Phys. Lett.* **B737** (2014) 325 [1403.4616].

[238] T. Ahmed, M. Mahakhud, N. Rana and V. Ravindran, *Drell-Yan Production at Threshold to Third Order in QCD*, *Phys. Rev. Lett.* **113** (2014) 112002 [1404.0366].

[239] T. Ahmed, M. K. Mandal, N. Rana and V. Ravindran, *Rapidity Distributions in Drell-Yan and Higgs Productions at Threshold to Third Order in QCD*, *Phys. Rev. Lett.* **113** (2014) 212003 [1404.6504].

[240] D. de Florian, J. Mazzitelli, S. Moch and A. Vogt, *Approximate N^3LO Higgs-boson production cross section using physical-kernel constraints*, *JHEP* **10** (2014) 176 [1408.6277].

[241] Y. Li, A. von Manteuffel, R. M. Schabinger and H. X. Zhu, *Soft-virtual corrections to Higgs production at N^3LO*, *Phys. Rev.* **D91** (2015) 036008 [1412.2771].

[242] C. Anastasiou, C. Duhr, F. Dulat, E. Furlan, T. Gehrmann, F. Herzog et al., *High precision determination of the gluon fusion Higgs boson cross-section at the LHC*, *JHEP* **05** (2016) 058 [1602.00695].

[243] F. Dulat, B. Mistlberger and A. Pelloni, *Differential Higgs production at N^3LO beyond threshold*, *JHEP* **01** (2018) 145 [1710.03016].

[244] F. Dulat, B. Mistlberger and A. Pelloni, *Precision predictions at N^3LO for the Higgs boson rapidity distribution at the LHC*, Phys. Rev. **D99** (2019) 034004 [1810.09462].

[245] S. Fleming and O. Z. Labun, *Rapidity Divergences and Deep Inelastic Scattering in the Endpoint Region*, Phys. Rev. **D91** (2015) 094011 [1210.1508].

[246] A. H. Hoang, P. Pietrulewicz and D. Samitz, *Variable Flavor Number Scheme for Final State Jets in DIS*, Phys. Rev. **D93** (2016) 034034 [1508.04323].

[247] C. Anastasiou, L. J. Dixon and K. Melnikov, *NLO Higgs boson rapidity distributions at hadron colliders*, Nucl. Phys. Proc. Suppl. **116** (2003) 193 [hep-ph/0211141].

[248] C. Anastasiou, L. J. Dixon, K. Melnikov and F. Petriello, *Dilepton rapidity distribution in the Drell-Yan process at NNLO in QCD*, Phys. Rev. Lett. **91** (2003) 182002 [hep-ph/0306192].

[249] C. Anastasiou, L. J. Dixon, K. Melnikov and F. Petriello, *High-precision QCD at hadron colliders: Electroweak gauge boson rapidity distributions at next-to-next-to leading order*, Phys. Rev. **D69** (2004) 094008 [hep-ph/0312266].

[250] J. Kubar, M. Le Bellac, J. L. Meunier and G. Plaut, *QCD Corrections to the Drell-Yan Mechanism and the Pion Structure Function*, Nucl. Phys. **B175** (1980) 251.

[251] P. Mathews, V. Ravindran, K. Sridhar and W. L. van Neerven, *Next-to-leading order QCD corrections to the Drell-Yan cross section in models of TeV-scale gravity*, Nucl. Phys. **B713** (2005) 333 [hep-ph/0411018].

[252] R. V. Harlander, S. Liebler and H. Mantler, *SusHi: A program for the calculation of Higgs production in gluon fusion and bottom-quark annihilation in the Standard Model and the MSSM*, Comput. Phys. Commun. **184** (2013) 1605 [1212.3249].

[253] R. V. Harlander, S. Liebler and H. Mantler, *SusHi Bento: Beyond NNLO and the heavy-top limit*, Comput. Phys. Commun. **212** (2017) 239 [1605.03190].

[254] C. F. Berger, T. Kucs and G. F. Sterman, *Event shape–energy flow correlations*, Phys. Rev. **D68** (2003) 014012 [hep-ph/0303051].

[255] E. Farhi, *A QCD Test for Jets*, *Phys. Rev. Lett.* **39** (1977) 1587.

[256] P. E. L. Rakow and B. R. Webber, *Transverse Momentum Moments of Hadron Distributions in QCD Jets*, *Nucl. Phys.* **B191** (1981) 63.

[257] S. Catani, G. Turnock and B. R. Webber, *Jet broadening measures in e^+e^- annihilation*, *Phys. Lett.* **B295** (1992) 269.

[258] D. Bertolini, T. Chan and J. Thaler, *Jet Observables Without Jet Algorithms*, *JHEP* **04** (2014) 013 [`1310.7584`].

[259] A. J. Larkoski, D. Neill and J. Thaler, *Jet Shapes with the Broadening Axis*, *JHEP* **04** (2014) 017 [`1401.2158`].

[260] R. Kleiss, W. J. Stirling and S. D. Ellis, *A New Monte Carlo Treatment of Multiparticle Phase Space at High Energies*, *Comput. Phys. Commun.* **40** (1986) 359.

[261] S. Plätzer, *RAMBO on diet*, `1308.2922`.

[262] S. Catani, Y. L. Dokshitzer, M. Olsson, G. Turnock and B. R. Webber, *New clustering algorithm for multi-jet cross-sections in e^+e^- annihilation*, *Phys. Lett.* **B269** (1991) 432.

[263] G. Salam, E_t^∞ *Scheme*, *Unpublished* .

[264] M. Cacciari, G. P. Salam and G. Soyez, *FastJet User Manual*, *Eur. Phys. J.* **C72** (2012) 1896 [`1111.6097`].

[265] B. Andersson, G. Gustafson, L. Lönnblad and U. Pettersson, *Coherence Effects in Deep Inelastic Scattering*, *Z. Phys.* **C43** (1989) 625.

[266] M. G. Echevarría, T. Kasemets, J.-P. Lansberg, C. Pisano and A. Signori, *Matching factorization theorems with an inverse-error weighting*, *Phys. Lett.* **B781** (2018) 161 [`1801.01480`].

[267] J.-L. Lagrange, *Mécanique Analytique*. Veuve Desaint, rue du Foin S. Jacques, Paris, 1788.

[268] C. W. Bauer, C. Lee, A. V. Manohar and M. B. Wise, *Enhanced nonperturbative effects in Z decays to hadrons*, *Phys. Rev.* **D70** (2004) 034014 [`hep-ph/0309278`].

[269] F. Wilczek, *Decays of Heavy Vector Mesons Into Higgs Particles*, *Phys. Rev. Lett.* **39** (1977) 1304.

[270] M. A. Shifman, A. I. Vainshtein and V. I. Zakharov, *Remarks on Higgs-Boson Interactions with Nucleons*, Phys. Lett. **B78** (1978) 443.

[271] T. Inami, T. Kubota and Y. Okada, *Effective Gauge Theory and the Effect of Heavy Quarks in Higgs Boson Decays*, Z. Phys. **C18** (1983) 69.

[272] V. P. Spiridonov and K. G. Chetyrkin, *Nonleading mass corrections and renormalization of the operators $m\bar{\psi}\psi$ and $G^2_{\mu\nu}$*, Sov. J. Nucl. Phys. **47** (1988) 522.

[273] T. Gehrmann, E. W. N. Glover, T. Huber, N. Ikizlerli and C. Studerus, *Calculation of the quark and gluon form factors to three loops in QCD*, JHEP **06** (2010) 094 [`1004.3653`].

[274] C. F. Berger, C. Marcantonini, I. W. Stewart, F. J. Tackmann and W. J. Waalewijn, *Higgs Production with a Central Jet Veto at NNLL+NNLO*, JHEP **04** (2011) 092 [`1012.4480`].

[275] M. Ritzmann and W. J. Waalewijn, *Fragmentation in Jets at NNLO*, Phys. Rev. **D90** (2014) 054029 [`1407.3272`].

[276] S. Mantry and F. Petriello, *Transverse Momentum Distributions from Effective Field Theory with Numerical Results*, Phys. Rev. **D83** (2011) 053007 [`1007.3773`].

[277] M. Höschele, J. Hoff, A. Pak, M. Steinhauser and T. Ueda, *MT: A Mathematica package to compute convolutions*, Comput. Phys. Commun. **185** (2014) 528 [`1307.6925`].

[278] M. D. Schwartz, *Resummation and NLO matching of event shapes with effective field theory*, Phys. Rev. **D77** (2008) 014026 [`0709.2709`].

[279] S. Fleming, A. H. Hoang, S. Mantry and I. W. Stewart, *Top jets in the peak region: Factorization analysis with next-to-leading-log resummation*, Phys. Rev. **D77** (2008) 114003 [`0711.2079`].

[280] O. V. Tarasov, A. A. Vladimirov and A. Yu. Zharkov, *The Gell-Mann-Low Function of QCD in the Three-Loop Approximation*, Phys. Lett. **B93** (1980) 429.

[281] S. A. Larin and J. A. M. Vermaseren, *The three-loop QCD β-function and anomalous dimensions*, Phys. Lett. **B303** (1993) 334 [`hep-ph/9302208`].

[282] G. P. Korchemsky and A. V. Radyushkin, *Renormalization of the Wilson Loops Beyond the Leading Order*, Nucl. Phys. **B283** (1987) 342.

[283] A. Vogt, S. Moch and J. A. M. Vermaseren, *The three-loop splitting functions in QCD: The singlet case*, Nucl. Phys. **B691** (2004) 129 [hep-ph/0404111].